UNIVERSITY OF SOUTHAMPTON

THE DEVELOPMENT OF HIGH POWER, PULSED FIBER LASER SYSTEMS AND THEIR APPLICATIONS

by Jonathan Hugh Vaughan Price

A thesis submitted for the degree of

DOCTOR OF PHILOSOPHY

OPTOELECTRONICS RESEARCH CENTRE

FACULTY OF ENGINEERING AND APPLIED SCIENCE

DEPARTMENT OF ELECTRONICS AND COMPUTER SCIENCE

JULY 2003

University of Southampton

ABSTRACT

FACULTY OF ENGINEERING AND APPLIED SCIENCE
OPTOELECTRONICS RESEARCH CENTRE

Doctor of Philosophy

THE DEVELOPMENT OF HIGH POWER, PULSED FIBER LASER SYSTEMS AND THEIR APPLICATIONS

by Jonathan Hugh Vaughan Price

Rare-earth doped silica fibers have been used for many years to create continuous-wave lasers, and Er-doped fiber amplifiers are now widely used in telecommunications. In addition, cladding pumped fiber allows the efficient conversion of multimode radiation from high power, low cost, broad-stripe semiconductor laser diodes into the single-mode emission of fiber lasers. With its broad gain bandwidth and high optical conversion efficiency, Yb-doped silica fiber represents an attractive medium for the generation and amplification of high energy ultrashort optical pulses. However, these potential advantages of Yb-doped silica fiber as a gain and nonlinear medium for mode-locked lasers and ultrashort pulse amplifiers have been less well studied, and it was not until 1999 that significant research interest first appeared in Yb-fiber chirp pulse amplifier (CPA) systems. This thesis describes the development of the first practical and stable, femtosecond, Yb-fiber oscillator, and of an Yb-fiber amplifier based CPA system (pulses ~10 μJ, <500 fs). Novel aspects of the system include the use of a high extinction ratio Electro-Optic modulator for pulse selection, and the development of a compact chirped-fiber-Bragg-grating (CFBG) pulse stretcher that provides both 2nd and 3rd order chirp compensation.

Recently published theoretical results have demonstrated that the asymptotic solution for ultrashort pulses in a high gain fiber amplifier is a linearly chirped pulse, which can therefore be recompressed with a standard grating compressor. This thesis reports the first experimental comparison of nonlinear pulse evolution towards the asymptotic form using a cascaded amplifier system. The 'direct amplification' system was constructed by removing the CPA stretcher grating, which also enabled the use of a less dispersive and more compact compressor. Further system development should lead to the generation of ultrashort pulses at high average power levels and >100 kHz repetition rates.

Holey fiber (HF) is a recently developed technology that uses rings of air holes around a solid core to confine the optical field by average-index effects. Fibers are highly suitable for applications using nonlinear optics because of the tightly confined mode and long interaction lengths. The increased mode confinement possible using HF means that small-core, high air-fill fraction HF are an attractive nonlinear medium. Furthermore, the high index contrast in such fibers can create a strong (anomalous) waveguide contribution to the dispersion, and such HFs can have anomalous dispersion at wavelengths <1.3 μm, where conventional fiber has normal dispersion. Therefore HFs can support solitons in new wavelength bands.

This thesis reports the first demonstration of linear dispersion compensation, soliton transmission, and visible continuum generation seeded by a 1.06 μm Yb-fiber source. In addition, an experimental study is reported that used HF seeded from a Ti:Sapphire laser to generate continuum in distinct transverse spatial modes of a HF. Numerical simulations suggested that the observed enhancement in UV generation from a higher order mode could be due to differences in the dispersion profiles of the fundamental and higher order transverse modes.

Finally, the development of a novel source of <200 fs pulses, continuously tuneable in wavelength from 1.06-1.33 μm, based on the soliton self-frequency-shift principle, is described. The source was constructed from a diode-pumped Yb-doped HF amplifier, and the Yb-fiber oscillator described above. The diode pump power controlled the output wavelength.

Acknowledgements

I would like to thank my supervisor, Professor David Richardson for his constant guidance, encouragement and patience.

There are many other people who have helped with and encouraged my studies; they are too numerous to list, but I am grateful to them all.

In addition, I would like to thank those who have directly helped with the work presented in this thesis. I acknowledge the contribution of all my co-workers for the laser and amplifier development. In particular, I thank Dr Laurent Lefort, Dr Johan Nilsson, Dr Andrew Malinowski and Andy Piper. I am grateful for the contribution of Dr Morten Ibsen in fabricating the chirped fiber Bragg gratings. I thank Dr Chris Barty, who shared his experience designing CPA compressors. I thank Dr Neil Broderick and Anna Peacock for numerical modelling of parabolic pulses, and for useful explanations about both parabolic pulses and solitons. Thanks are also due to Walter Belardi, and Dr Tanya Monro, who designed and fabricated the passive holey fiber used for the work in this thesis, and to Kentaro Furusawa, who fabricated the Yb-doped holey fiber and who helped with many of the holey fiber experiments. I thank Joanne Baggett for her assistance with recording the images from supercontinuum generation in subsidiary cores of a holey fiber. I thank Dr Andy Clarkson for his helpful comments, and I thank Professor David Hanna for encouraging the work using Yb-doped holey fiber as a wavelength tuneable source. I am also grateful to Dr Rüdiger Paschotta of ETH Zurich for enabling me to use his numerical modelling program ‘ProPulse’.

I thank Professor Jeremy Baumberg for making available his group’s femtosecond Ti:Sapphire laser laboratory for the UV supercontinuum experiments presented in this thesis. I also thank Caterina Netti, Steve Coyle and the other members of Professor Baumberg’s group for their help in enabling me to work effectively with the laser system.

I thank the other members of Professor Richardson’s group with whom I have had the pleasure of discussing ideas, borrowing equipment and who generally helped things along: Periklis Petropoulos, Peh-Chong Teh, JuHan Lee, Ron Haaksman, Hermann Offerhaus, Anoma McCoy, Ami Ljungström, Benn Thomsen, Zul Yusoff. I also thank those with whom I have shared an office in Room 4107.

I thank Simon Butler for machining several mounts for my experiments and for general advice about making the mechanical aspects of our experiments work, and I thank Chris Nash for his help with preparing figures for presentations. I thank David Oliver, and Arthur Longhurst for their cheerful help with computer troubles. I thank Professor Rob Eason, Eve Smith and Joyce Aburrow for being so energetic in their support of the ORC PhD students.

I acknowledge the support of an EPSRC studentship, and project funding from a commercial sponsor.

I would like to thank my family for their support throughout my studies.

List of Contents

List of abbreviations

AOM	Accousto-Optic Modulator
AOTF	Accousto-Optic Tunable Filter
ASE	Amplified Spontaneous Emission
CFBG	Chirped Fiber Bragg Grating
CPA	Chirped Pulse Amplification
CW	Continuous Wave
DDL	Dispersive Delay Line
EDFA	Erbium Doped Fiber Amplifier
EOM	Electro-Optic Modulator
ESA	Excited State Absorption
FP	Fabry-Perot
FROG	Frequency-Resolved Optical Gating
FWHM	Full Width at Half Maximum
FWM	Four Wave Mixing
GDD	Group Delay Dispersion
GVD	Group Velocity Dispersion
HF	Holey fiber
LMA	Large Mode Area
MCVD	Modified Chemical Vapour Deposition
NA	Numerical Aperture
NLPE	Nonlinear Polarisation Evolution
OPO	Optical Parametric Oscillator
ORC	Optoelectronics Research Centre
PBS	Polarising Beam Splitter
PC	Polarisation Controller
PPLN	Periodically Poled Lithium Niobate
RMS	Root Mean Square
SBS	Stimulated Brillouin Scattering
SEM	Scanning Electron Micrograph
SHG	Second Harmonic Generation
SNR	Signal to Noise Ratio
SPM	Self-Phase Modulation
SRS	Stimulated Raman Scattering
UV	Ultra-violet
WDM	Wavelength Division Multiplexing
ZDW	Zero Dispersion Wavelength

emerging practical applications of ultrafast technology. The development of compact and robust sources of high energy femtosecond pulses has therefore generated strong research interest.

Ytterbium (Yb) doped silica fiber, with its broad gain bandwidth, high optical conversion efficiency and large saturation fluence, represents an extremely attractive medium for both the generation and subsequent amplification of ultrashort optical pulses [7]. Moreover, Yb-fiber systems can be power scaled by the addition of diode-pumped amplifier stages to provide a compact, all-fiber, high power, short-pulse system [8, 9]. My supervisor, Professor Richardson, obtained industrial funding to develop a practical and robust, high-power short-pulse diode-pumped Yb-doped fiber based laser and amplifier system. The system would use the CPA technique, whereby pulses are first temporally stretched, then amplified, then finally recompressed in order to avoid nonlinear distortion due to high peak powers within the amplifiers. The agreed approach was to develop a passively mode-locked fiber-based oscillator to produce ~100 fs pulses as a seed for high power fiber amplifiers. The final amplified pulses would have energy of ~10-50 μJ, and average power of ~500 mW, with pulse duration ~500 fs. The system would make use of the ability of the ORC to fabricate specialty chirped fiber-Bragg gratings (CFBGs) with both 2^{nd} and 3^{rd} order dispersion in order to create a pulse stretcher, and also the ability of the ORC to fabricate large-mode-area (LMA) fiber to develop the final amplifier for the system. The development of this system formed the majority of this PhD thesis research.

For applications requiring high average power but at high repetition rates, and hence lower pulse energies, the use of a pulse stretcher is not required since the pulse peak powers, and hence nonlinear effects are less significant. This enables simplified 'direct amplification' systems to be used, in which the pulse stretcher is omitted, and consequently a much more compact compressor can be used. Recent theoretical research on short pulse evolution in fiber amplifiers with normal dispersion (e.g. using Yb-doped fiber), has demonstrated that pulses with parabolic temporal and spectral profiles and a linear chirp are the analytic asymptotic solution to the propagation equation (modified nonlinear Schrödinger equation (NLSE) with gain) [10]. The linear chirp allows such parabolic pulses to be recompressed using a standard diffraction grating compressor, and 125 fs recompressed pulses have been demonstrated experimentally in single amplifier systems at high average powers (17W, 75MHz repetition rate, and 230 nJ pulse energy [11]). However, using a single amplifier limits the maximum potential gain to ~35 dB, so to investigate the possibility of obtaining femtosecond pulses from a direct amplification system but with much higher gain, a system was developed based on the oscillator and cascaded amplifiers used for the CPA. This work is presented following the description of the CPA research.

HFs are a class of microstructured fiber which have a solid core surrounded by a cladding region that is defined by a fine array of air holes that extend along the full fiber length [12-14]. HF technology has developed rapidly in recent years and, due to their far broader range of fabrication parameters compared to conventional fiber, HFs have been produced with dispersion and nonlinear properties beyond those previously possible. In particular, high air-fill fraction HF can have a much higher index contrast than is possible with conventional fiber, and if this is combined with a small core size, the strong waveguide contribution to the dispersion can produce an overall anomalous dispersion at wavelengths <1.3 μm, where standard fibers have normal dispersion. Therefore HF can support temporal solitons in new wavelength bands. A small core naturally leads to the fiber having an exceptionally high effective nonlinearity, which is ideal for soliton generation. Moreover, as a result of the increased range of fiber properties, new results such as visible supercontinuum generation seeded directly from mode-locked Ti:Sapphire lasers have been demonstrated [15], and these results have led to tremendous advances in spectroscopy and metrology. Due to the wide range of applications of such a broadband collimated source, there has also been much interest in developing less complex, less expensive, seed laser systems.

The ORC is one of the world-leading centers in HF fabrication and HF applications research, and this thesis presents results showing a variety of novel applications of this technology using small core high nonlinearity HFs fabricated at the ORC. Experiments are described which demonstrate linear dispersion compensation (low-power), soliton formation (requiring nonlinear interaction) and soliton transmission in anomalously dispersive HF using ~20 pJ pulses in a <2 m fiber length. The fiber lengths and power requirements are orders of magnitude smaller than comparable experiments in standard silica fiber at telecommunications wavelengths. Further experiments are described which used the direct amplification system (described above) to seed HF in order to demonstrate the first all-fiber source of visible continuum generation.

Using HF with a zero dispersion wavelength (ZDW) ~800 nm, with a high-energy Ti:Sapphire laser system as the source, the extension of supercontinuum generation in the UV to wavelengths as short as 300 nm is reported. It was observed that the UV intensity was enhanced when seed pulses were coupled into a higher-order transverse spatial mode of the HF. A significant difference between the fundamental and higher order mode of the HF is the dispersion properties of these modes; in particular the higher order mode has a shorter ZDW. Numerical simulations are presented which suggest that the differences in dispersion profiles could lead to increased power transfer to short wavelengths. Using the same Ti:Sapphire source and HF, and with suitable detuning of the launch coupling into the HF, visible-supercontinuum generation in several subsidiary cores of a HF was demonstrated for the first time.

Wavelength tuneable, femtosecond optical pulse sources have applications in areas as diverse as ultrafast spectroscopy, materials processing, optoelectronics, nonlinear optics and optical chemistry. Traditionally, femtosecond pulse sources have been based on bulk crystal materials (most commonly Ti:sapphire). Whilst excellent performance characteristics have been achieved, and successful commercial products and application areas have been developed, these traditional sources offer a limited range of directly accessible wavelengths and continuous broadband tuning ranges, particularly above 1.1 μm. In general, extending this femtosecond technology to obtain broader tuning ranges and longer wavelengths requires the use of bulk parametric nonlinear devices such as OPOs, Optical Parametric Generators (OPGs), or Amplifiers (OPAs), pumped by a bulk femtosecond-laser. Such devices add to the complexity and cost, and increase the physical size of the overall system. The discovery of the soliton-self-frequency shift (SSFS) in optical fibers was first reported in 1985-1986 [16-18], and opened up the exciting possibility of obtaining widely wavelength tuneable femtosecond soliton pulses from fiber-based sources (ideally incorporating a fiber based pump laser)[19]. To obtain the SSFS effect, the frequency shifting fiber must exhibit anomalous dispersion at both the initial seed wavelength and across the required tuning range. Yb-doped HF has been developed [20-22], and by using a small core and a high air fill-fraction, these active HFs can, like passive HFs, have anomalous dispersion at 1 μm. Using such a fiber as an amplifier for seed pulses from the Yb-fiber mode-locked oscillator (above), a source of ~200 fs pulses, tuneable in wavelength from 1.06–1.33 μm was demonstrated. Wavelength tuning was based on the SSFS, and with the output wavelength controlled by the pump power applied to the Yb-doped HF amplifier.

The contents of each chapter of this thesis are summarised as follows. Chapter 2 provides a background summary of the nonlinear fiber optics theory as necessary to understand the research presented in the following chapters. The work in this thesis is predominantly based on Yb-doped fiber amplifiers, and Chapter 2 therefore also provides a brief summary of the spectroscopy of Yb-doped silica fiber, and describes the procedure used to calculate the properties of such amplifiers. In addition, due to the rapid development of HF technology in recent years, and considering that the ORC is one of only a handful of worldwide centres developing such fibers, Chapter 2 concludes with a brief overview of HF technology.

The development of a high power cascaded Yb-fiber amplifier system for ultrashort pulse generation is described in Chapters 3-8. Chapter 3 provides a review of previously reported fiber-based CPA research and describes the principal outstanding technological challenges to be addressed before practical systems can be developed for a wide range of applications. The specifications and resulting overall approach adopted for the commercially sponsored development of an Yb-fiber based CPA system is described, and an overview of the CPA

system is presented. A simplified 'direct amplification' system, operating at similar average power but higher repetition rate, hence lower pulse energy, is also described. The direct amplification system omits the pulse stretcher and therefore uses a more compact compressor compared with the CPA system, but by using the cascade of amplifiers has higher gain than previously reported direct amplification systems which have been based on a single amplifier stage.

Chapter 4 describes the development of a highly stable Yb-fiber based, mode-locked oscillator. The oscillator is based on the stretched-pulse principle, and incorporates a semiconductor saturable absorber mirror (SESAM) to enable robust self-start mode-locking. This oscillator was subsequently used for the seed in our high power systems. The operating principles are presented, then the characterisation of each component in the cavity is described. The characteristics of the laser output are presented, including pulse spectrum, autocorrelation, and RF noise.

Chapter 5 reports the development of the pulse stretcher and compressor used for the Yb-fiber CPA system. The effects of uncompensated 3^{rd} order dispersion on the quality of the recompressed pulses are demonstrated by numerical calculations. The design process for the bulk grating compressor is described, and experimental measurements of the temporal response vs. wavelength are presented. The development and characterisation of a CFBG stretcher incorporating both 2^{nd} and 3^{rd} order dispersion compensation is presented. The chapter concludes by suggesting a future CFBG design to enable shorter pulses to be produced from the CPA system e.g. 300 fs pulses, compared to the 500 fs pulses demonstrated using the initially developed CFBG.

Chapter 6 describes the development of the individual amplifier stages for the CPA system. First the characteristics of the core-pumped pre-amplifiers are described. Results of numerical modelling are reported that demonstrate the expected increase in gain that could be obtained by using modified core-pumped pre-amplifier designs in future systems. The design and measured operating characteristics of the final stage high-power cladding-pumped amplifier are then described.

Chapter 7 presents the performance of the CPA system as a whole. The output pulse spectra are presented at several pulse energies up to a maximum of 80 μJ (before temporal recompression). Stimulated Raman Scattering (SRS) was observed to limit the maximum pulse energy from the system. Results of numerical calculations are presented in order to demonstrate that increasing the core size and reducing the length of the fiber used for the final amplifier should enable pulse energies >100 μJ to be obtained. The extent of Self-phase modulation

(SPM) induced phase distortion for 100 μJ pulses is calculated, and the high quality of the recompressed pulses is shown.

Chapter 8 presents measurements on ultrashort pulses produced from a direct amplification system. The system was based on the oscillator and amplifier components developed for the CPA system of Chapter 7, but was simplified by removing the pulse stretcher, which then enabled a more compact compressor to be used. Pulse spectra and autocorrelation data are shown. Second Harmonic Generation (SHG) Frequency Resolved Optical Gating (FROG) measurements are presented, which provide the full temporal phase profile of the pulses. Numerical simulations of the pulses from the system are presented, and are shown to be in close agreement with the measured pulse parameters. In addition, the theoretical asymptotic 'parabolic' pulse solution to the modified NLSE with gain is described, and the characteristics of the measured pulses are compared to the characteristics predicted for parabolic pulses.

Chapters 9, 10, and 11 present the research performed using small-core HF with anomalous dispersion at wavelengths <1.3 μm. Chapter 9 describes linear dispersion compensation, and the generation and transmission of solitons. Linear dispersion compensation was demonstrated by launching strongly attenuated, positively chirped pulses from the oscillator of Chapter 4 into a length of passive HF. Solitons were produced using the same arrangement except by increasing the power launched into the HF. Further results are presented showing visible supercontinuum generation obtained by launching pulses from the direct amplification system of Chapter 8 into a similar HF.

Chapter 10 describes supercontinuum generation extending to 300 nm in the UV produced by launching high energy pulses from a Ti:Sapphire laser system into a short length of small-core HF. The UV generation was enhanced by coupling the seed pulses into a higher order transverse mode. Results of full-vector numerical calculations of the dispersion profiles of both the fundamental and higher order mode of the HF are presented for the first time. Results of pulse-propagation simulations (using the calculated dispersion profiles of the fundamental and higher order mode) are presented; the results suggest that the dispersion profile of the higher order mode is responsible for generating increased power at shorter wavelengths. Visible supercontinuum generation in several subsidiary cores of the fiber is demonstrated for the first time, and suggestions are presented for the fabrication of a multi-core fiber specifically for producing tailored supercontinuum spectra from different sized cores (different dispersion profiles) but using a single fiber.

Chapter 11 describes the development of a source of <200 fs pulses continuously tuneable in wavelength from 1.06-1.33 μm, based on the SSFS principle. The source is based on a diode-pumped Yb-doped HF amplifier, seeded by pulses from the mode-locked Yb-fiber oscillator

described in Chapter 4. The diode pump power was demonstrated to control the output wavelength. The calculated HF characteristics are presented, then the experimental setup is described. Next, the wavelength tuning results are shown. Finally, results demonstrating broadband continuum generation, and pulse compression to ~65 fs are presented.

Chapter 12 provides a summary of the work in this thesis and describes possible areas for further research.

The thesis concludes with three appendices. Appendix I describes the method used to measure the amplitude noise and timing jitter of a CW mode-locked laser. Appendix II summarises the performance of the mode-locked laser described in Chapter 4, when tested with a range of SESAMs in order to identify the optimum modulation depth and saturation fluence for robust self-start and stable CW mode-locking. Appendix III is a list of publications arising from my thesis work.

The work in this thesis consists primarily of the author's own research, undertaken whilst the author was a registered postgraduate student at the University of Southampton. Any material from other sources is referenced accordingly.

References

1. D. Du, X. Liu, G. Korn, J. Squier and G. Mourou, "Laser-Induced Breakdown by Impact Ionization in SiO_2 with Pulse Widths from 7 ns to 150 fs," Applied Physics Letters **64,** 3071-3073 (1994).
2. B. N. Chichkov, C. Momma, S. Nolte, F. von Alvensleben and A. Tunnermann, "Femtosecond, picosecond and nanosecond laser ablation of solids," Applied Physics A-Materials Science & Processing **63,** 109-115 (1996).
3. C. B. Schaffer, A. Brodeur, J. F. Garcia and E. Mazur, "Micromachining bulk glass by use of femtosecond laser pulses with nanojoule energy," Optics Letters **26,** 93-95 (2001).
4. F. Korte, S. Adams, A. Egbert, C. Fallnich and A. Ostendorf, "Sub-diffraction limited structuring of solid targets with femtosecond laser pulses," Optics Express **7,** 41-49 (2000).
5. D. Strickland and G. Mourou, "Compression of Amplified Chirped Optical Pulses," Optics Communications **56,** 219-221 (1985).
6. J. Squier, G. Korn, G. Mourou, G. Vaillancourt and M. Bouvier, "Amplification of Femtosecond Pulses at 10-kHz Repetition Rates in Ti-Sapphire," Optics Letters **18,** 625-627 (1993).
7. V. Cautaerts, D. J. Richardson, R. Paschotta and D. C. Hanna, "Stretched pulse Yb^{3+} silica fiber laser," Optics Letters **22,** 316-318 (1997).
8. H. M. Pask, R. J. Carman, D. C. Hanna, A. C. Tropper, C. J. Mackechnie, P. R. Barber and J. M. Dawes, "Ytterbium-Doped Silica Fiber Lasers - Versatile Sources for the 1-1.2 micron Region," IEEE Journal of Selected Topics in Quantum Electronics **1,** 2-13 (1995).
9. R. Paschotta, J. Nilsson, A. C. Tropper and D. C. Hanna, "Ytterbium-doped fiber amplifiers," IEEE Journal of Quantum Electronics **33,** 1049-1056 (1997).
10. M. E. Fermann, V. I. Kruglov, B. C. Thomsen, J. M. Dudley and J. D. Harvey, "Self-similar propagation and amplification of parabolic pulses in optical fibers," Physical Review Letters **84,** 6010-6013 (2000).
11. J. Limpert, T. Schreiber, T. Clausnitzer, K. Zollner, H. J. Fuchs, E. B. Kley, H. Zellmer and A. Tünnermann, "High-power femtosecond Yb-doped fiber amplifier," Optics Express **10,** 628-638 (2002).
12. J. C. Knight, T. A. Birks, P. St.J.Russell and D. M. Atkin, "All-silica single-mode optical fiber with photonic crystal cladding," Optics Letters **21,** 1547-1549 (1996).
13. J. C. Knight, T. A. Birks, P. St.J.Russell and D. M. Atkin, "All-silica single-mode optical fiber with photonic crystal cladding: Errata," Optics Letters **22,** 484-485 (1997).
14. T. M. Monro, D. J. Richardson, N. G. R. Broderick and P. J. Bennett, "Holey optical fibers: An efficient modal model," Journal of Lightwave Technology **17,** 1093-1102 (1999).
15. J. K. Ranka, R. S. Windeler and A. J. Stentz, "Visible continuum generation in air-silica microstructure optical fibers with anomalous dispersion at 800 nm," Optics Letters **25,** 25-27 (2000).
16. F. M. Mitschke and L. F. Mollenauer, "Discovery of the soliton self-frequency shift," Optics Letters **11,** 659-661 (1986).
17. J. P. Gordon, "Theory of the soliton self-frequency shift," Optics Letters **11,** 662-664 (1986).
18. E. M. Dianov, A. Y. Karasik, P. V. Mamyshev, A. M. Prokhorov, V. N. Serkin, M. F. Stel'makh and A. A. Fomichev, "Stimulated-Raman conversion of multisoliton pulses in quartz optical fibers," JETP Lett. **41,** 294-297 (1985).

19. N. Nishizawa and T. Goto, "Compact system of wavelength-tunable femtosecond soliton pulse generation using optical fibers," IEEE Photonics Technology Letters **11,** 325-327 (1999).

20. W. J. Wadsworth, J. C. Knight, W. H. Reeves, P. St.J.Russell and J. Arriaga, "Yb-doped photonic crystal fibre laser," Electronics Letters **36,** 1452-1454 (2000).

21. K. Furusawa, T. M. Monro, J. C. Baggett, P. Petropoulos, P. W. Turner and D. J. Richardson, "A mode-locked ytterbium doped holey fiber laser," *Conference on Lasers and Electro Optics (CLEO), paper CWC2*, (2001).

22. K. Furusawa, T. M. Monro, P. Petropoulos and D. J. Richardson, "Modelocked laser based on ytterbium doped holey fibre," Electronics Letters **37,** 560-561 (2001).

Chapter 2 Nonlinear fiber optics

2.1 Introduction

Nonlinear pulse evolution in fiber is of critical importance for the devices described in this thesis. This chapter provides the nonlinear fiber optics background used to develop these devices. The work in this thesis is predominantly based on Yb-doped fiber amplifiers, and this chapter also provides a brief summary of the spectroscopy of Yb-doped silica fiber, and describes the procedure used to calculate the properties of fiber amplifiers. Holey fibers (HFs) were used to enable various of the nonlinear experiments described in the latter chapters of this thesis. This chapter describes the procedure used to fabricate HF and provides a brief overview of the extended range of dispersion and nonlinear properties that are made possible by HF technology.

This chapter is organised as follows. In Section 2.2 a brief introduction to the main nonlinear optical effects in optical fiber is presented. In Section 2.3 the spectroscopy of Yb and methods for calculating the characteristics of Yb-fiber amplifiers are described. Section 2.4 provides an overview of holey fiber technology.

2.2 Nonlinear effects in optical fibers

This section is intended to provide an overview of the relevant theory to enable a thorough consideration of the experiments described in this thesis. Starting from Maxwell's equations, the principal dispersive and nonlinear effects relevant to silica fiber are discussed, and the derivation of the basic propagation equation, called the nonlinear Schrödinger equation (NLSE), is described.

Ultrashort pulses have broad bandwidths, so the dispersion of the propagating medium must be considered, and such pulses can also have high peak powers, which may excite a nonlinear response in the propagating medium. Dispersion arises due to the linear response of the bound electrons in silica, and due to the waveguide dispersion of the fiber. The Kerr nonlinearity causes self-phase modulation and cross-phase modulation, and is due to the elastic response (no energy exchanged) of the bound electrons to an intense optical field. Raman and Brillouin scattering are caused by inelastic scattering whereby energy is exchanged with the medium through the creation or annihilation of phonons. The nonlinear and dispersive effects can be

beneficial, for example when the dispersion is anomalous, the dispersion and nonlinearity can combine to support stable pulse forms (solitons) that can propagate without broadening. However, the nonlinear effects can also be detrimental, for example with normal dispersion, nonlinear effects can distort the pulse profile and significantly increase the minimum duration of the pulses produced from an amplifier system. In this section, the equations describing these effects are briefly reviewed.

This section is organised as follows. Section 2.2.1 introduces the wave equation and the concept of induced polarisation which are essential to understanding nonlinear properties in optical fiber. In Section 2.2.2, the effects of purely linear dispersion are described. In Section 2.2.3 an overview of nonlinear effects is presented, including the effects of self-phase modulation (SPM). Cross-phase modulation (XPM) is described in Section 2.2.4, and stimulated Raman and Brillouin scattering are described in Section 2.2.5. Section 2.2.6 describes the split-step Fourier method that is typically used to numerically calculate the profiles of ultrashort pulses propagating in optical fibers.

2.2.1 Pulse propagation in optical fiber

The propagation of optical fields in optical fiber is governed by Maxwell's equations:

$$\nabla \times \vec{E} = -\frac{\partial \vec{B}}{\partial t} \qquad \text{Eqn. 2.2:1}$$

$$\nabla \times \vec{H} = \vec{J} + \frac{\partial \vec{D}}{\partial t} \qquad \text{Eqn. 2.2:2}$$

$$\nabla \cdot \vec{D} = \rho \qquad \text{Eqn. 2.2:3}$$

$$\nabla \cdot \vec{B} = 0 \qquad \text{Eqn. 2.2:4}$$

where $\vec{E}$ and $\vec{H}$ are electric and magnetic field vectors, respectively, and $\vec{D}$ and $\vec{B}$ are corresponding electric and magnetic flux densities. The current density vector $\vec{J}$ and the charge density ρ represent the sources for the electromagnetic field. In optical fiber there are no free charges, and $\vec{J} = 0$ and $\rho = 0$.

The relationship of the flux densities $\vec{D}$ and $\vec{B}$ to the electric and magnetic fields ($\vec{E}$ and $\vec{H}$) inside the medium and can be expressed through the constitutive relations given by

$$\vec{D} = \varepsilon_0 \vec{E} + \vec{P} \qquad \text{Eqn. 2.2:5}$$

$$\vec{B} = \mu_0 \vec{H} + \vec{M} \qquad \text{Eqn. 2.2:6}$$

where ε_0 is the vacuum permittivity, μ_0 is the vacuum permeability, and $\vec{M}$ is the induced magnetic polarisation. $\vec{M}$ = 0 in optical fiber because silica is a nonmagnetic medium. By taking the curl of Eqn. 2.2:1, the above equations can be converted into the wave equation that describes light propagation

$$\nabla \times \nabla \times \vec{E} = -\frac{1}{c^2}\frac{\partial^2 \vec{E}}{\partial t^2} - \mu_0 \frac{\partial^2 \vec{P}}{\partial t^2} \qquad \text{Eqn. 2.2:7}$$

where c $\left(=1/\sqrt{\mu_0 \varepsilon_0}\right)$ is the velocity of light in vacuum.

To solve Eqn. 2.2:7, a relation between $\vec{P}$ and $\vec{E}$ is needed. Optical fiber has a nonlinear response to intense electromagnetic fields due to the anharmonic motion of bound electrons under the influence of the applied field. The induced polarisation $\vec{P}$ is thus not linear in the electric field, but is described by the more general relation

$$\vec{P} = \varepsilon_0\left(\chi^{(1)} \cdot \vec{E} + \chi^{(2)} : \vec{E}\vec{E} + \chi^{(3)} \vdots \vec{E}\vec{E}\vec{E} + \cdots\right) \qquad \text{Eqn. 2.2:8}$$

where $\chi^{(j)}(j = 1,2,3,\cdots)$, is j$^{\text{th}}$ order susceptibility (tensor of rank j+1). (This relationship assumes that the response is both instantaneous and local, and in order to correctly describe Raman and Brillouin scattering we relax the assumption of an instantaneous response, and consider the delayed response of the medium as described in Section 2.2.5.) The linear susceptibility $\chi^{(1)}$ is the dominant contribution to $\vec{P}$, and its effects are included through the refractive index n, and the attenuation coefficient α. The second-order susceptibility $\chi^{(2)}$ is responsible for second-harmonic generation and sum-frequency generation. However, centro-symmetric materials such as amorphous SiO_2 show a zero value for $\chi^{(2)}$ (neglecting surface effects), and therefore silica fiber does not exhibit second-order nonlinear effects. The lowest order nonlinear effects in optical fiber originate from the third-order susceptibility $\chi^{(3)}$, which is responsible for phenomena such as third-harmonic generation, four-wave mixing, and the intensity dependence of the refractive index. To obtain significant third-harmonic generation or four-wave mixing requires special efforts to achieve phase matching and these processes are not considered further in this thesis. It is then usual to make several simplifying assumptions to enable the solution of Eqn. 2.2:7 and Eqn. 2.2:8. First, the nonlinear contribution to the polarisation ($\vec{P}_{NL}$) is assumed to be a small perturbation to the linear contribution ($\vec{P}_L$) to the total induced polarisation. We then write the total induced polarisation as $\vec{P} = \vec{P}_L + \vec{P}_{NL}$, and including only the third-order nonlinear effects governed by $\chi^{(3)}$, we obtain:

$$\vec{P}_L(\vec{r},t) = \varepsilon_0 \int_{-\infty}^{\infty} \chi^{(1)}(t-t') \cdot \vec{E}(\vec{r},t')dt' \quad , \qquad \text{Eqn. 2.2:9}$$

$$\vec{P}_{NL}(\vec{r},t) = \varepsilon_0 \int_{-\infty}^{+\infty}\iiint \chi^{(3)}(t-t_1,t-t_2,t-t_3) \vdots \vec{E}(\vec{r},t_1)\vec{E}(\vec{r},t_2)\vec{E}(\vec{r},t_3)\, dt_1 dt_2 dt_3 \quad . \qquad \text{Eqn. 2.2:10}$$

These relations are valid in the electric-dipole approximation such that the response of the medium is local. Eqn. 2.2:7 can then be simplified by using the mathematical relation $\nabla \times \nabla \times \vec{E} = \nabla(\nabla \cdot \vec{E}) - \nabla^2 \vec{E} = -\nabla^2 \vec{E}$ (where $\nabla \cdot \vec{D} = \varepsilon \nabla \cdot \vec{E} = 0$ and where ε represents the dielectric constant) to give

$$\nabla^2 \vec{E} - \frac{1}{c^2}\frac{\partial^2 \vec{E}}{\partial t^2} = -\mu_0 \frac{\partial^2 \vec{P}_L}{\partial t^2} - \mu_0 \frac{\partial^2 \vec{P}_{NL}}{\partial t^2} \quad . \qquad \text{Eqn. 2.2:11}$$

The following sections demonstrate that by considering the waveguide geometry of an optical fiber, and by assuming the spectral width of the pulse is much less than the central carrier frequency (slowly varying envelope approximation), the three dimensional wave equation (Eqn. 2.2:11) can be reduced to a one dimensional propagation equation for the temporal profile of the pulse envelope. The resulting equation is normally called the nonlinear Schrödinger equation (NLSE) and it is possible to solve the equation numerically (and even analytically in the special case of solitons) to determine the evolution of a pulse propagating in an optical fiber.

2.2.2 Linear propagation and dispersion

Starting from the nonlinear wave equation derived above (Eqn. 2.2:11), this section considers the case where the nonlinear polarisation can be neglected. The result then describes the effects of dispersion on a pulse propagating in a fiber with a linear response. The nonlinear polarisation will then be re-introduced in the following section using perturbation theory. With $\vec{P}_{NL} = 0$, Eqn. 2.2:11 is linear in $\vec{E}$ and takes the following simple form in the Fourier domain:

$$\nabla^2 \tilde{\vec{E}} + \varepsilon(\omega) k_0^2 \tilde{\vec{E}} = 0 \qquad \text{Eqn. 2.2:12}$$

where $\varepsilon = (n + i\alpha / 2k_0)^2$, and due to the low loss of silica fiber ε is initially simplified to $\varepsilon(\omega) = n^2(\omega)$. Far from material resonances, as is the case in silica fiber in the wavelength range 0.5-2.0 μm relevant to the work in this thesis, the linear response of the material can be represented by the Sellmeier equation (in contrast to a full quantum mechanical description):

$$n^2(\omega) = 1 + \sum_{j=1}^{m} \frac{B_j \omega_j^2}{\omega_j^2 - \omega^2} \quad . \qquad \text{Eqn. 2.2:13}$$

In the cylindrical symmetry of a fiber, we use co-ordinates ρ, ϕ, z to write $\tilde{E}_z(\vec{r},\omega) = \tilde{A}(\omega)F(\rho)\exp(im\phi)\exp(i\beta z)$ (i.e. assuming initially no z-dependence of the pulse envelope). A similar equation exists for $\tilde{H}_z$ (the other four components $\tilde{E}_\rho, \tilde{E}_\phi, \tilde{H}_\rho, \tilde{H}_\phi$ are not independent variables and can be obtained using Maxwell's equations). Matching the (Bessel function) solutions for $F(\rho)$ at the core:cladding boundary, an Eigenvalue equation is obtained that must be solved numerically to yield the propagation constants for the various fiber modes, $\beta_{nm}(\omega)$, and hence the transverse mode profile $F_m(\kappa_{mn}\rho)$, where $\kappa_{mn}^2 = n^2k_0^2 - \beta_{mn}^2$ at a given frequency. In a standard step-index fiber the number of guided modes is determined by the normalised frequency, or V value $V = {2\pi}/{\lambda} \cdot \rho_{co} \cdot \sqrt{(n_{co}^2 - n_{cl}^2)}$, where n_{co} and n_{cl} represent core and cladding indices, respectively, and ρ_{co} is the core radius [1]. Single mode guidance is obtained for $V < 2.405$. For V values of ~2.0 (typical for single-mode fibers) the field distribution of the fundamental mode is approximately Gaussian: $F(\rho) \sim \exp(-\rho^2/\mathrm{w}^2)$, where $\mathrm{w} \approx$ core radius, and the effective mode area is $A_{eff} = \pi \mathrm{w}^2$. For weakly guiding fibers [2], an approximate expression for the propagation constant of the fundamental mode is obtained from: $\beta(\omega) = \sqrt{(\omega/c)^2 n^2(\omega) - \rho_{co}^{-2}u^2(\omega)}$ where $u(\omega) = \left[\left(1-\sqrt{2}\right)V(\omega)\right] \Big/ \left[1+\left(4+V^4(\omega)\right)^{1/4}\right]$, where we have expressed the normalised frequency as a function of ω.

A single mode fiber actually supports two modes that are dominantly polarised in orthogonal directions. Due to small departures from cylindrical symmetry or small fluctuations in material anisotropy, the mode propagation constant (effective index) becomes slightly different for the x and y polarisation modes and it can be shown that the power between the two modes is exchanged periodically with a characteristic "beat length" [3] period: $L_B = 2\pi/\left(\left|\beta_x - \beta_y\right|\right) = \lambda/\left(\left|n_x - n_y\right|\right)$.

Having obtained the mode-profile, we derive the basic propagation equation. We assume that the optical field is launched on one polarisation axis and maintains its polarisation along the fiber length, and that the spectral width $\Delta\omega$ is such that $\Delta\omega << \omega_0$, where ω_0 is the central frequency (slowly varying envelope approximation). The rapidly varying part of the electric field can then be separated by writing

$$\vec{E}(\vec{r},t) = \frac{1}{2}\hat{x}[E(\vec{r},t)\exp(-i\omega_0 t) + c.c.] \qquad \text{Eqn. 2.2:14}$$

where c.c. stands for complex conjugate, $\hat{x}$ is the polarisation unit vector, and the amplitude $E(\vec{r},t)$ is a slowly varying function of time. Using separation of variables, we write $\tilde{E}_z(r,\omega-\omega_0)=F(x,y)\tilde{A}(z,\omega-\omega_0)\exp(i\beta_0 z)$ in Eqn. 2.2:12, which then gives both an equation for $F(x,y)$ (solved to obtain the propagation constant, and hence the mode-profile via an Eigenvalue equation, as discussed above); and the following equation for the slowly varying envelope:

$$2i\beta_0\frac{\partial\tilde{A}}{\partial z}+\left(\tilde{\beta}^2-\beta_0^2\right)\tilde{A}=0\ . \qquad \text{Eqn. 2.2:15}$$

We then introduce a small loss as a perturbation and write $\varepsilon=\left(n+\Delta n\right)^2\approx n^2+2n\Delta n$, where $\Delta n=\frac{i\alpha}{2k_0}$ and write $\tilde{\beta}=\left(\beta(\omega)+\Delta\beta\right)$, where the small change $\Delta\beta$ can be evaluated using first order perturbation theory. We use the approximation $\tilde{\beta}^2-\beta_0^2=2\beta_0(\tilde{\beta}-\beta_0)$ to obtain:

$$\frac{\partial\tilde{A}}{\partial z}=i\left[\beta(\omega)+\Delta\beta-\beta_0\right]\tilde{A}\ . \qquad \text{Eqn. 2.2:16}$$

To transform Eqn. 2.2:16 to the time domain, we first expand $\beta(\omega)$ using a Taylor series expansion about the carrier frequency ω_0,

$$\beta(\omega)=\beta_0+\beta_1(\omega-\omega_0)+\tfrac{1}{2}\beta_2(\omega-\omega_0)^2+\tfrac{1}{6}\beta_3(\omega-\omega_0)^2+\ldots \qquad \text{Eqn. 2.2:17}$$

where $\beta_m=(d^m\beta/dT^m)_{\omega=\omega_0}$, and $(m=0,1,2\ldots)$. After returning to the time domain (using the inverse Fourier transform) and using co-moving co-ordinates, $T=(t-z/\mathrm{v}_g)=(t-\beta_1 z)$, we obtain the propagation equation

$$\frac{\partial A}{\partial z}=-\frac{i}{2}\beta_2\frac{\partial^2 A}{\partial T^2}+\frac{1}{6}\beta_3\frac{\partial^3 A}{\partial T^3}-\frac{\alpha}{2}A\ . \qquad \text{Eqn. 2.2:18}$$

This one dimensional propagation equation enables us to study the effects of dispersion. In most cases β_2 is the dominant term in Eqn. 2.2:18. The dispersion length is defined as the length over which an initially unchirped pulse doubles its temporal width and is calculated using $L_D=\left(T_0^2/|\beta_2|\right)$. For the specific case of a Gaussian pulse envelope, the effects of β_2,β_3 can be studied analytically, but for the general case, Eqn. 2.2:18 must be solved numerically. However, even for an arbitrary initial pulse profile it can be shown that after propagating for several dispersion lengths, the principal effect of 2nd order dispersion is a symmetric broadening of the pulse and the creation of a linear chirp, whereas the principal effect of 3rd order dispersion is asymmetric broadening of the pulse and the creation of a quadratic chirp.

The second derivative, $\beta_2(\omega_0)$, is called the group-velocity dispersion (GVD) at frequency ω_0. In the normal dispersion regime $\beta_2 > 0$, and in the anomalous dispersion regime $\beta_2 < 0$. The magnitude of β_2 gives the pulse broadening per unit length of the medium and per unit bandwidth of the pulse. Note that the GVD concept is straightforward in application only for a homogeneous medium (e.g. a single type of fiber). The group-delay dispersion (GDD) is the absolute time delay accumulated between components per unit frequency difference, and for a specific length of material: GDD = $\beta_2(\omega_0) \times$ Length of material. For a multi component system, GDD is easier to consider because it can be calculated for each component, and summed to obtain a total delay.

2.2.3 Nonlinear polarisation effects

In addition to the effects of linear dispersion described above, nonlinear polarisation effects are an essential component of the work presented in this thesis. Essentially, the refractive index increases slightly with increasing pulse intensity. To obtain the required quantitative solution, we use the expression for the electric field envelope of the pulse (Eqn. 2.2:14) and write $\vec{P}_L(\vec{r},t) = (1/2)\,\hat{x}\,[P_L(\vec{r},t)\exp(-i\omega_0 t) + c.c.]$ and $\vec{P}_{NL}(\vec{r},t) = (1/2)\,\hat{x}\,[P_{NL}(\vec{r},t)\exp(-i\omega_0 t) + c.c.]$. Substituting these relations into Eqn. 2.2:10, we observe that $\vec{P}_{NL}(\vec{r},t)$ has a term at a frequency of ω_0 and another term at the third-harmonic frequency of $3\omega_0$. However the latter term is negligible unless special efforts are made at phase-matching this process and it is not considered further. The nonlinear absorption coefficient (which defines 2-photon absorption) is also weak in silica and is neglected. We assume (initially) an instantaneous nonlinear response of the medium, and $\vec{P}_{NL}(\vec{r},t)$ can be then expressed as follows:

$$P_{NL}(\vec{r},t) = \varepsilon_0 \varepsilon_{NL} E(\vec{r},t) \quad , \qquad \text{Eqn. 2.2:19}$$

where ε_{NL} is the nonlinear part of the dielectric constant defined by

$$\varepsilon_{NL} = \frac{3}{4}\chi^{(3)}_{xxxx}\left|E(\vec{r},t)\right|^2 \quad . \qquad \text{Eqn. 2.2:20}$$

Since n is found to be intensity dependent because of ε_{NL}, it is customary to introduce $n = n_0 + n_2\left|E\right|^2 = n_0 + n_2 I$, where in silica at wavelengths close to 1 μm, the linear refractive index n_0 is ~1.46, and n_2 (Kerr nonlinearity coefficient) is ~3 x 10^{-20} m^2/W, and I represents the intensity of the signal. Writing $\Delta n = n_2\left|E\right|^2 + i\alpha/2k_0$, and following the same overall procedure as described for determining the effects of linear dispersion, the propagation equation (Eqn. 2.2:16) for the pulse envelope is transformed to the time domain, and becomes:

$$\frac{\partial A}{\partial z} = -\frac{i}{2}\beta_2 \frac{\partial^2 A}{\partial T^2} + \frac{1}{6}\beta_3 \frac{\partial^3 A}{\partial T^3} - \frac{\alpha}{2}A + i\gamma \left| A \right|^2 A \qquad \text{Eqn. 2.2:21}$$

where $\gamma = n_2 \omega_0 / (cA_{eff})$. This equation (Eqn. 2.2:21) is the fundamental equation used to study nonlinear pulse evolution in fibers and it is called the nonlinear Schrödinger equation (NLSE). The NLSE has been found to be applicable to the study of nonlinear systems in many branches of physics. Due to the assumption of instantaneous nonlinear response that was made when deriving Eqn. 2.2:21, it describes accurately the propagation of pulses that have durations ($\tau_{FWHM} \geq 1$ ps), that are longer than the nonlinear response time in silica. For pulses of duration $\tau_{FWHM} \leq 1$ ps , the delayed response of $\chi^{(3)}$ must usually be included, as described in Section 2.2.5.

The NLSE can be used to study self-phase modulation (SPM): the nonlinear response to the changing intensity of the pulse envelope itself induces a phase change across the pulse. To study the effects of SPM, the dispersion is initially ignored and the NLSE may then be solved analytically. The temporal phase of a signal pulse propagating through optical fiber due to SPM is found to be:

$$\phi^{NL}(z = L, t) = \frac{2\pi L_{eff} n_2 \left| E(z = 0, t) \right|^2}{\lambda} \qquad \text{Eqn. 2.2:22}$$

where λ is the signal wavelength, and $L_{eff} = \frac{1}{\alpha}\left(1 - \exp(-\alpha L)\right)$, where L is the actual fiber length. The nonlinear length L_{NL} is defined as $L_{NL} = 1/\gamma P_0$, where P_0 is the pulse peak power. The nonlinear length provides a length scale over which nonlinear effects become important for pulse evolution along the fiber. We also define $N^2 = L_D / L_{NL}$, which for a given pulse duration and peak power provides a measure of the relative importance of dispersive vs. nonlinear effects. When $N^2 << 1$ dispersion is dominant, and when $N^2 >> 1$ nonlinear effects are dominant.

The time dependent phase change experienced by an optical pulse may be regarded as a change in the instantaneous frequency, which is referred to as a frequency chirp. The SPM induced spectral broadening is thus a consequence of the time dependence of the induced nonlinear phase changes. At the leading edge of a bright pulse, red-shifted wavelengths are produced, and at the trailing edge, blue-shifted wavelengths are produced. The generation of new spectral components if coupled with normal dispersion in the fiber, will lead to increased temporal broadening of the pulse. By contrast, in the anomalous dispersion regime pulse compression can be achieved. With $N^2 = 1$, the balance of dispersive and nonlinear effects leads to stable pulse forms which propagate without broadening. These pulses are called

fundamental solitons and they are an analytical solution to the NLSE, with pulse amplitude profile:

$$A = \sqrt{P_0}\,\mathrm{sech}\left(T / T_0\right)\exp\left(i\,z/\left(2\,L_D\right)\right)\ , \qquad \text{Eqn. 2.2:23}$$

where T_0 is the pulse width ($T_0 = 1.763 T_{FWHM}$). The soliton period is defined as $Z_0 = (\pi/2)L_D$.

2.2.4 Coupling between different pulses

When two optical signals propagate inside a fiber they can interact with each other through the Kerr nonlinearity ($\chi^{(3)}$). Each signal experiences SPM (described above) and they also influence each other by changing the refractive index experienced by the other signal, resulting in a nonlinear phase change. This phenomenon is known as cross-phase modulation (XPM).

We first consider the nonlinear refractive index for signals with the same frequency (ω_0) but travelling on orthogonal fiber axes. The electric field associated with an elliptically polarised optical wave of central frequency ω_0 can be written in the form

$$\vec{E}(\vec{r},t) = \frac{1}{2}[\,\hat{x}\,E_x + \hat{y}\,E_y\,]\exp(-i\omega_0 t) + c.c. \quad , \qquad \text{Eqn. 2.2:24}$$

where E_x and E_y are the complex amplitudes of the orthogonal polarisation components. The nonlinear part of the induced polarisation (again, ignoring 3rd harmonic components i.e. assuming no phase-matching conditions have been applied) is then

$$\vec{P}_{NL}(\vec{r},t) = \frac{1}{2}[\,\hat{x}\,P_x + \hat{y}\,P_y\,]\exp(-i\omega_0 t) + c.c. \quad , \qquad \text{Eqn. 2.2:25}$$

with P_x and P_y given by $P_i = \dfrac{3\varepsilon_0}{2}\sum_j \left(\chi^{(3)}_{xxyy}E_iE_jE_j^* + \chi^{(3)}_{xyxy}E_jE_iE_j^* + \chi^{(3)}_{xyyx}E_jE_jE_i^*\right)$. For silica fibers, the three independent components of $\chi^{(3)}$ have nearly the same magnitude in silica fibers [4], and are related by $\chi^{(3)}_{xxxx} = \chi^{(3)}_{xxyy} + \chi^{(3)}_{xyxy} + \chi^{(3)}_{xyyx}$. If $\chi^{(3)}_{xxyy}$, $\chi^{(3)}_{xyxy}$, and $\chi^{(3)}_{xyyx}$ are assumed to be identical, we obtain

$$P_x = \frac{3\varepsilon_0}{4}\chi^{(3)}_{xxxx}\left[\left(\left|E_x\right|^2 + \frac{2}{3}\left|E_y\right|^2\right)E_x + \frac{1}{3}\left(E_x^*E_y\right)E_y\right] \quad , \qquad \text{Eqn. 2.2:26}$$

$$P_y = \frac{3\varepsilon_0}{4}\chi^{(3)}_{xxxx}\left[\left(\left|E_y\right|^2 + \frac{2}{3}\left|E_x\right|^2\right)E_y + \frac{1}{3}\left(E_y^*E_x\right)E_x\right] \quad . \qquad \text{Eqn. 2.2:27}$$

If $L >> L_B$, as would be the case in strongly birefringent fibers, the last term (cross-term) in the above equations contributes negligibly because of the large phase mismatch. We then write $P_j(\omega) = \varepsilon_0 \varepsilon_j E_j$ where $\varepsilon_j = \varepsilon_j^L + \varepsilon_j^{NL} = \left(n_j^L + \Delta n\right)^2 \approx \left(n_j^L\right)^2 + 2 n_j^L \Delta n_j$. Assuming $n_x^L = n_y^L = n$ and writing $n_2 = \frac{1}{2n} \mathrm{Re}\left\{\varepsilon^{NL}\right\} \approx \frac{3}{8n} \mathrm{Re}\left\{\chi_{xxxx}^{(3)}\right\}$, we obtain (neglecting nonlinear loss)

$$\Delta n_x = n_2 \left[\, |E_x|^2 + \frac{2}{3} |E_y|^2 \, \right] \quad , \qquad \text{Eqn. 2.2:28}$$

$$\Delta n_y = n_2 \left[\, |E_y|^2 + \frac{2}{3} |E_x|^2 \, \right] \quad . \qquad \text{Eqn. 2.2:29}$$

The first terms in each of the above equations (Eqn. 2.2:28 and Eqn. 2.2:29) account for SPM, and the second terms are responsible for XPM. If the input light is elliptically polarised, the XPM induced nonlinear coupling between the field components E_x and E_y creates nonlinear birefringence.

This effect of XPM between fields of the same frequency but on orthogonal polarisation axes is particularly relevant to the operation of the fiber-based mode-locked laser described in Chapter 4 of this thesis. As illustrated schematically in Fig. 2.1, the polarisation state at the fiber output is intensity dependent [5], which can create a fast saturable absorber for mode-locking. The input polarisation state to the fiber in the laser cavity is biased such that the nonlinear ellipse rotation, which is greater for the most intense central part of the pulse, creates an output polarisation state that passes through a polarisation beam splitter with lower loss than the polarisation state of the low intensity wings of the pulse. The net result is that the pulse is slightly shortened after each round trip inside the cavity. (The technique of nonlinear polarisation rotation is a variant of additive-pulse mode locking in which orthogonally polarised components play the role of two interferometer arms.)

The XPM-induced coupling is also observed between optical waves with intensities I_i, I_j, traveling on the same polarisation axis but with different frequencies ω_i, ω_j, respectively. The refractive index for each signal can then be expressed [1] as follows:

$$n_i = n_i^L + n_2 |E|_i^2 + 2 \cdot n_2 |E|_j^2 \qquad \text{Eqn. 2.2:30}$$

$$n_j = n_j^L + n_2 |E|_j^2 + 2 \cdot n_2 |E|_i^2 \qquad \text{Eqn. 2.2:31}$$

where the linear component of the refractive index has been included due to its dependence on the signal wavelength (dispersion). It is interesting that XPM between the two waves of different frequencies is more effective than that between two waves of the same frequency but

orthogonal polarisation as it shows a factor of 2 in Eqn. 2.2:30 and Eqn. 2.2:31, rather than 2/3 as in Eqn. 2.2:28 and Eqn. 2.2:29 (although the qualitative behaviour is same).

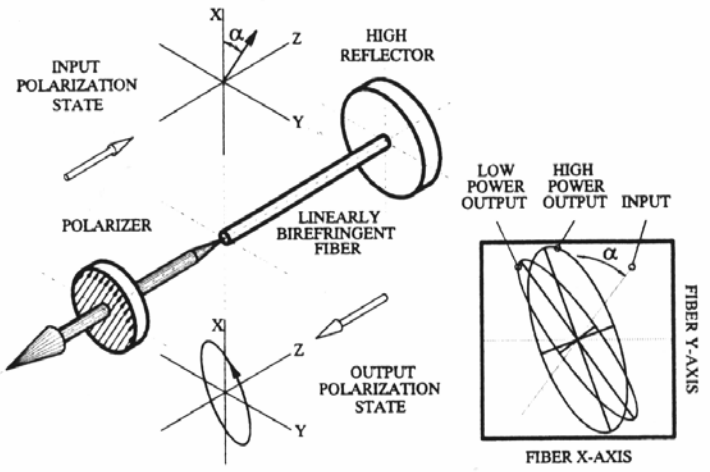

Fig. 2.1. Nonlinear ellipse rotation used to create a fast saturable absorber (from [5]).

This effect of XPM between fields of different frequencies is relevant to the work presented in this thesis because the high pulse peak powers in the final fiber amplifier of the CPA system (described in Chapters 3-8) result in the creation of a Raman pulse co-propagating with the original signal pulse (see Section 2.2.5.2 for calculation of walk-off length of pump and Stokes pulses). Coupling between the pulses is induced by XPM and distorts the signal pulse. (In practice, the CPA system has been designed to minimise stimulated Raman scattering (SRS).)

2.2.5 Stimulated Raman Scattering

A consideration of stimulated inelastic scattering from phonons is also important for understanding the work presented in this thesis. SRS can be regarded as scattering from optical phonons, and stimulated Brillouin scattering (SBS) can be regarded as scattering from acoustic phonons. Both processes result in a Stokes wave generated at a longer wavelength.

The Brillouin gain occurs at a frequency shift of ~10 GHz and has a peak gain of ~$6\text{x}10^{-11}$ m/W for silica. However the Brillouin gain spectrum is extremely narrow with a bandwidth of $\Delta\nu_B$ ~10 MHz. For a broad bandwidth ($\Delta\nu_P$) pump, the peak gain decreases by a factor $\Delta\nu_B/\Delta\nu_P$. Therefore, for pulses relevant to the work in this thesis with minimum bandwidth of $\Delta\lambda_P$ >8 nm ($\Delta\nu_P$ > 2 THz considering a central wavelength of 1 μm), the effective Brillouin gain coefficient is reduced by ~10^6, and hence SBS is not observed.

In contrast, the Raman gain spectrum is very broad, extending up to ~30 THz, as shown in Fig. 2.2 [6]. The measured Raman gain peak is g_R ~ $1\text{x}10^{-13}$ m/W (pump wavelength 1 μm) and occurs at a Stokes shift $\Delta\nu$ ~13.2 THz. The Raman gain is directly related to the delayed nonlinear response of the heavy nuclei (slower than the almost instantaneous electronic response

which is responsible for elastic scattering) and this delayed temporal response has been calculated from the Raman gain profile [6] as shown in Fig. 2.2 (b).

SRS can be considered for two regimes of pump pulse bandwidth. For narrow and moderate bandwidth pulses (e.g. $\Delta\nu_P < 0.5$ THz, $\tau_{FWHM} > 1$ ps). The principal effect of SRS is that the pulses can act as a pump and transfer energy to a longer wavelength Stokes signal e.g. at a frequency offset close to the Raman gain peak (13.2 THz). The pump pulse is described by the NLSE, but with an intensity dependent loss term to account for the energy transfer to the Stokes pulse, and perhaps including a term to account for the influence of the Stokes pulse on the pump pulse through XPM. In contrast, for broad bandwidth pulses (e.g. $\Delta\nu_P \approx 4.4$ THz , corresponding to a transform limited 100 fs pulse), in addition to the possible energy transfer to an independent Stokes pulse, the long wavelength spectral components may experience significant Raman gain pumped by the short wavelength components. This is the phenomenon of intra-pulse SRS, and the NLSE should then be modified to include the delayed temporal response of the medium (Fig. 2.2(b)), as follows [1](Eqn. 2.2:32)

$$\frac{\partial A}{\partial z} = -\frac{i}{2}\beta_2\frac{\partial^2 A}{\partial T^2} + \frac{1}{6}\beta_3\frac{\partial^3 A}{\partial T^3} - \frac{\alpha}{2}A + i\gamma\left(1 + \frac{i}{\omega_0}\frac{\partial}{\partial T}\right)\times\left[A(z,T)\int_{-\infty}^{+T} R(T')\left|A(z,T-T')\right|^2 dT'\right].$$

Eqn. 2.2:32

The response function $R(T) = (1 - f_R)\delta(t) + f_R h_R(T)$ includes both instantaneous and delayed nonlinear response of the fiber, where $f_R = 0.18$ is the fractional contribution of the delayed Raman response, and the experimentally determined Raman response of silica (Fig. 2.2(b)) is used for $h_R(T)$, normalised such that $\int_{-\infty}^{+\infty} h_R(T')\,dT' = 1$. In order to conserve photon number Eqn. 2.2:32 also includes the so-called self-steepening term that results from including the first derivative of the slowly varying envelope of the nonlinear polarisation, $\vec{P}_{NL}$, in Eqn. 2.2:7. The likely significance of the delayed response of the medium can also be considered in the time domain (see Fig. 2.2(b)), by assessing whether the pulse duration is comparable to the response time of the medium.

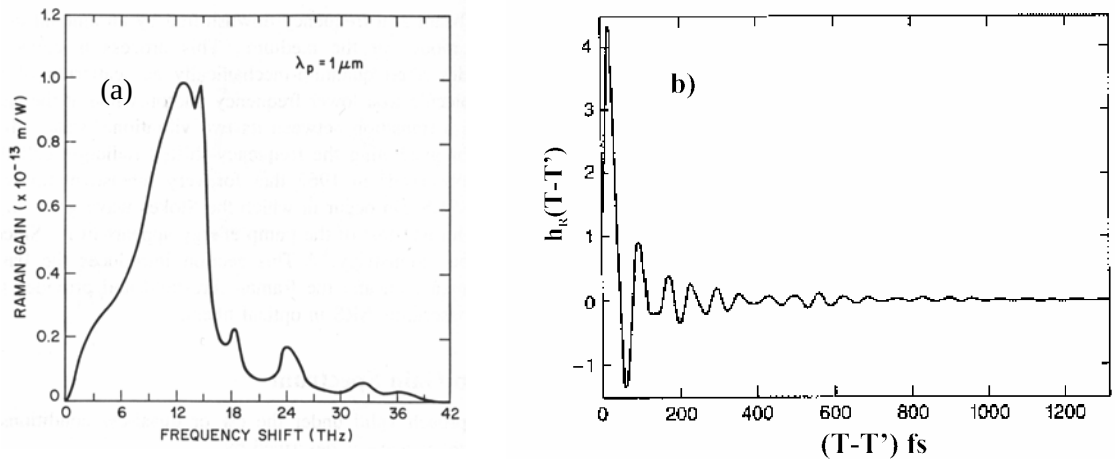

Fig. 2.2 Raman gain spectrum and delayed time response for silica. (a) Measured Raman gain. (b) Delayed time response, $h_R(T)$, as described in above text. (From [1].)

2.2.5.1 Soliton self-frequency-shift

For the solitons in holey fibers described in the later part of this thesis (Chapters 9-11) the peak powers are sufficiently low, and the fiber lengths sufficiently short, that the generation of a strong Stokes pulse from quantum noise does not occur, and the principal effect of SRS is intra-pulse scattering. In particular because solitons are stable against small perturbations this effect leads to the soliton self-frequency-shift (SSFS), which causes a continuous downshift of the soliton frequency as it propagates along the fiber (as illustrated by the results of Chapter 11).

The approximate functional dependence of the rate of frequency shifting $d(\Delta f)/dz$ on the soliton duration can be explained as follows. The Raman gain is proportional to the pump intensity, which scales as $1/\tau^2$ for a soliton of duration τ. The Raman gain can be seen (Fig. 2.2(a)) to be approximately proportional to the frequency offset $\Delta\nu$ (for $\Delta\nu$ <<13 THz), and is therefore proportional to $1/\tau$. The overall Raman gain therefore depends on $1/\tau^3$. The rate of frequency downshift is approximately proportional to the frequency width of the pulse (~$1/\tau$), which gives an overall rate of frequency downshift $d(\Delta f)/dz \sim 1/\tau^4$ [7]. This is a useful approximate analytic relationship, but for detailed studies, numerical simulations are usually performed.

2.2.5.2 Threshold power for Stokes pulse generation

For the pulses in the CPA and direct amplification systems described in the first part of this thesis, the peak power is sufficient to create a strong SRS generated Stokes pulse from quantum noise. The main consequence of SRS is that energy is transferred to a longer wavelength Stokes pulse ($\Delta\nu_R$=13.2 THz corresponding to a 45 nm wavelength shift at a wavelength of 1 μm) and

this presents a limit on the maximum pulse peak power that can be produced from these systems. The initial growth of the Stokes signal can be described by

$$\frac{dI_S}{dz} = g_R I_P I_S + g_S I_S \quad , \qquad \text{Eqn. 2.2:33}$$

where g_S is the amplifier gain for the Stokes signal, g_R is the Raman gain coefficient, I_S and I_P are the Stokes and pump intensities. Neglecting pump depletion due to the Stokes wave, the evolution of the pump signal follows

$$\frac{dI_P}{dz} = g_P I_P \quad , \qquad \text{Eqn. 2.2:34}$$

where g_P is the amplifier gain at the seed pulse wavelength. For a seed pulse intensity at the amplifier output $(z = L)$ of $I_P(L)$, we obtain the solution for $I_P(z)$ (Eqn. 2.2:35) which can be substituted into Eqn. 2.2:33 to obtain a further equation for $I_S(z)$ (Eqn. 2.2:36).

$$I_P(z) = I_P(L)\exp\big(-g_P(L-z)\big) \quad , \qquad \text{Eqn. 2.2:35}$$

$$\frac{dI_S}{dz} = g_R I_P(L)\exp\big(-g_P(L-z)\big)I_S + g_S I_S \quad , \qquad \text{Eqn. 2.2:36}$$

Assuming $g_P = g_S = g$ we then obtain the solution for $I_S(z)$

$$I_S(z) = I_S(0)\exp\big(g_R I_P(L)\ z_{eff} + gz\big) \quad , \qquad \text{Eqn. 2.2:37}$$

where $z_{eff} = (1/g)[1-\exp(-gz)]$. The Stokes wave can build up from quantum noise occurring throughout the fiber length, and Smith [8] has shown that this is equivalent to injecting one fictitious photon per mode at the fiber input. Integration over all frequencies gives:

$$P_S(z) = \int_{-\infty}^{\infty} \hbar\omega \exp\big(g_R(\omega) I_P(L)\ z_{eff} + g\ z\big) d\omega \quad . \qquad \text{Eqn. 2.2:38}$$

The Raman threshold power (P_0^{cr}) is defined as the pump power at the amplifier output which generates the same amount of Stokes power at the amplifier output. The Raman gain is strongly peaked at frequency offset of 13.2 THz from the pump, and by assuming that the Raman gain profile can be approximated by a strongly peaked Lorentzian gain profile, Smith [8] has calculated P_0^{cr} to be given, to a good approximation, by

$$\big(g_R P_0^{cr} L_{eff}\big)\big/A_{eff} \approx 16 \quad . \qquad \text{Eqn. 2.2:39}$$

Due to the wavelength offset the pump and Stokes pulses travel at different group velocities, and the walk-off length is calculated to be $L_W = T \Big/ \left| v_{g\_P}^{-1} - v_{g\_S}^{-1} \right| = T \Big/ \left| \beta_{1\_P} - \beta_{1\_S} \right|$ $= T \Big/ \left| (\omega_P - \omega_S) \times \beta_2 \right|$ where T is the pulse duration. For T =5 ps, which corresponds to the pulse duration for the directly amplified pulses in Chapter 8, we have (using $\left| \omega_P - \omega_S \right| = 2\pi \times 13.2 \text{ THz}$) L_W ~2.4 m, and since the interaction between the pump and Stokes pulses occurs over a distance of $\sim 3 \times L_W$ [9], the walk-off of the pulses does not affect the calculated Raman threshold for the ~4.5 m long fiber amplifiers in this thesis. (A similar conclusion applies for the CPA system where the pulse duration is ~300 ps.) In principle, SRS can also occur for counter-propagating pulses, but the interaction time (length) is much shorter so that the effect is not significant.

2.2.6 Numerical solution of the nonlinear Schrödinger equation

Except in certain special cases e.g. solitons, the NLSE (Eqn. 2.2:21) does not have analytic solutions, and numerical methods are generally used to propagate an initial pulse form. A technique commonly implemented is called the split-step Fourier method. To understand the method, we write the propagation equation for the pulse envelope, $A(z,T)$, as

$$\frac{\partial A}{\partial z} = \left(\hat{N} + \hat{D} \right) A \qquad \text{Eqn. 2.2:40}$$

where $\hat{N}$ is the nonlinear operator, and $\hat{D}$ is the dispersion operator,

$$\hat{N} = i \gamma \left| A \right|^2 - \frac{\alpha}{2} \qquad \text{Eqn. 2.2:41}$$

$$\hat{D} = -\frac{i}{2} \beta_2 \frac{\partial^2}{\partial T^2} + \frac{1}{6} \beta_3 \frac{\partial^3}{\partial T^3} \ . \qquad \text{Eqn. 2.2:42}$$

Here $\hat{N}$ includes only the SPM nonlinear term and a loss term, but higher order nonlinear terms can be included as necessary. By assuming that the dispersion and nonlinearity act approximately independently over a small propagation distance Δz, the split-step Fourier method applies the two operators sequentially

$$A(z + \Delta z, T) = \exp(\Delta z \, \hat{N}) \exp(\Delta z \, \hat{D}) \, A(z,T) \ . \qquad \text{Eqn. 2.2:43}$$

Differentiation with respect to time equates to multiplication by $i\omega$ in the frequency domain, so the dispersion operator is more easily treated in the frequency domain by using a fast Fourier transform (FFT), before returning to the time domain using the inverse transform (IFFT) in order to apply the nonlinear operator. This procedure is illustrated below for one propagation step:

$$\tilde{A}(\nu) = FFT\{A(T)\}$$
$$\tilde{A}(\nu) = \tilde{A}(\nu)\exp\left[\left(\tfrac{i}{2}\beta_2\omega^2 + \tfrac{i}{6}\beta_3\omega^3\right)\Delta z\right]$$
$$A(t) = IFFT\left\{\tilde{A}(\nu)\right\}$$
$$A(t) = A(t)\exp\left[\left(i\gamma|A(t)|^2 - \alpha/2\right)\Delta z\right]$$
... repeat until $\sum \Delta z = \mathrm{L}$.

2.3 Ytterbium doped silica fiber

Yb-doped silica fiber has been used as the gain medium for the majority of the work reported in this thesis. This section provides a summary of the spectroscopic properties of Yb-doped silica. The Yb spectroscopy governs the range of possible pump and signal wavelengths, and the variation in characteristics with temperature. Results are presented in subsequent chapters of this thesis that demonstrate how our Yb-fiber amplifiers were optimised for maximum gain. The work was mainly done by experimental optimisation, but supported where necessary by numerical calculations. This section therefore describes briefly the model and computational method used to produce the numerical results.

This section is organised as follows. In Section 2.3.1, the Yb spectroscopy is briefly described. The following three sections describe the computational method used in order to calculate the optimum amplifier length. Section 2.3.2 provides an overview of the model. Section 2.3.3 describes the procedure for calculating the inversion density in a fiber piece which is sufficiently short that the inversion density does not vary along the length. Section 2.3.4 presents an algorithm that uses the inversion density from the short fiber piece to calculate the power at the output of an amplifier of arbitrary length. Use of that result to optimise the amplifier design (e.g. fiber length) is described.

2.3.1 Ytterbium fiber spectroscopy

This section provides a brief description of the spectroscopy of Yb-doped silica. Yb is a member of the rare-earth (lanthanide) group of elements within the periodic table [10], all of which have the general electronic structure $4f^N5s^25p^65d^06s^2$. In particular, Yb has the structure $(Xe)4f^{14}5d^06s^2$. When inserted into a host material, e.g. silica, the outer two 6s electrons of the Yb atom, and one of the 4f electrons are used for ionic binding, so Yb becomes triply ionized. The spectroscopy of the Yb^{3+} ion is simple compared to other rare-earth ions [11]. For all optical wavelengths, only two manifolds are relevant: the $^2F_{7/2}$ ground-state manifold and the $^2F_{5/2}$ excited-state manifold as shown in Fig. 2.3(a). Coulomb interactions split the 4f states into terms, spin-orbit coupling splits each term into manifolds, and crystal-field (Stark) interaction splits each manifold into sublevels (shown in Fig. 2.3). Electric dipole transitions within the 4f

shell are partly-forbidden so Yb^{3+} has a long upper state lifetime [11] (~0.8 ms). (Mixing of wave-functions with opposite parity is brought about by the crystal-field interaction which creates weak, but non-zero, transition probabilities.)

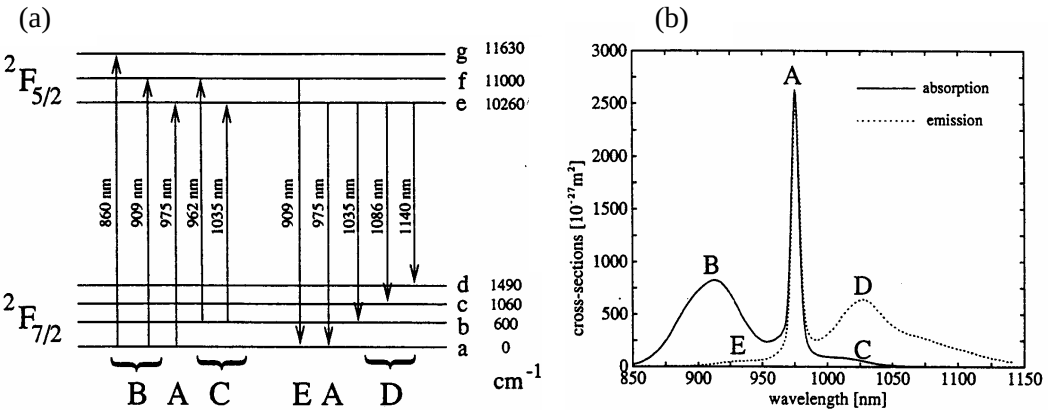

Fig. 2.3 (a) The Yb energy level structure, consisting of two manifolds, the ground manifold $^2F_{7/2}$ (with four Stark levels labelled a-d), and a well separated excited state manifold $^2F_{5/2}$ (with three Stark levels labelled e-g). Approximate energies in wavenumbers above ground energy are indicated. (b) Absorption and emission cross sections for a germanosilicate host. The principal features of the spectra have been labelled A-E, and are discussed in the text. (From [12] .)

The large energy gap between the manifolds precludes non-radiative decay via multi-phonon emission, even in a host with high phonon energy such as silica. Excited state absorption (ESA) of pump or signal light, or concentration quenching by ion-ion energy transfer processes, does not occur with Yb due to the absence of other energy levels (in contrast e.g. to Er), and co-operative up-conversion (whereby two excited Yb^{3+} ions emit a single green photon) is a very weak process (negligible). The transitions between sublevels are not fully resolved for Yb^{3+} ions in a glass at room temperature due predominantly to strong homogeneous broadening, although weaker inhomogeneous broadening is also observed [13]. It has been pointed out by others that the details of absorption and emission spectra depend to some extent on the host glass composition [13, 14]. Comparison of various Yb-doped germanosilicate fibers with differing content of germanium, aluminium and boron show typical deviations from the cross sections shown in Fig. 2.3 by up to ~30%. The measured fluorescence decay times are typically around 0.8 ms and also vary by ~30% between different fibers; fibers with higher germanium content in the core (introduced to achieve a higher numerical aperture) tend to have comparatively shorter lifetimes while Yb in a pure silicate glass has a longer lifetime of around 1.5 ms.

The absorption and emission spectra of Yb-doped silica are shown in Fig. 2.3 (b). Following Pask et al. [12], the most obvious features have been labeled (A)-(E). Pumping at the strong absorption peak (A) at 975nm enables efficient pump absorption in a short fiber length. We

note that pumping at the broader feature (B), at 915nm, has several disadvantages for applications at 1.06 μm, because it leads to high gain at 975 nm, which can result in ASE if the signal is weak, and the reduced absorption cross-section results in a longer absorption length for the pump and correspondingly longer devices. The peak in the emission spectrum (D) from 1030 nm out to beyond 1100 nm corresponds to transitions from level e to levels b, c and d. These transitions can become quasi 4-level in character at longer wavelengths due to the small thermal populations of the Stark split lower levels. To minimise the absorption length, the majority of the experiments in this thesis have used diode pumping at wavelengths close to the 975 nm absorption peak.

2.3.2 Overview of numerical model

This section describes a numerical model that is suitable for optimising the Yb-fiber amplifier parameters e.g. changing the length to maximise the gain at a given wavelength. In the most general case of unguided pump and signal beams in a bulk gain medium, calculating the power distribution at the amplifier output is a complex problem that could require calculation of the inversion density in individual small elements throughout the gain volume, which would have both transverse and longitudinal variation along the signal propagation direction. Furthermore, gain guiding or antiguiding could cause changes in the mode profile of the signal beam. Fortunately, the small-core waveguide geometry of a fiber amplifier has the result that the pump, signal, and ASE all propagate along the fiber with constant mode-profiles. Therefore calculating the optimum amplifier parameters decouples to enable independent optimisation of the transverse doping/refractive index profile (2 D) and of the fiber length (1D).

The transverse refractive index profile and Yb-doping geometry are both variable parameters for the design of the fiber. Indeed, this freedom was used by previous researchers at the ORC when optimising large mode area (LMA) fiber for power amplifiers and high energy Q-switched lasers. However, optimisation of the fiber refractive index profile and Yb-doping geometry has not formed part of the research in this thesis, and therefore further description of the necessary calculations are not presented here. The modelling presented in this thesis was used to optimise the fiber length and core size (hence pump/signal intensity) in order to obtain maximum gain.

A further simplification typically applied when modelling the fiber geometry is to average out the radial variation of the inversion density of the active ions (caused by the radial variation of the pump, signal, and ASE intensity profiles), by considering the doped region to interact with beams of uniform “effective” intensity. The “effective” intensity calculated by the following overlap integral Γ_q (q = Pump (P), Signal (S), ASE (A)), which can vary from zero (no overlap of intensity and doping profiles) to one (exact overlap):

$$\Gamma_q = \int_0^{2\pi}\int_0^{\infty} i_q(r,\phi)\, n_t(r,\phi)\, r\, dr\, d\phi \Big/ \int_0^{2\pi}\int_0^{\infty} n_t(r,\phi)\, r\, dr\, d\phi \quad , \qquad \text{Eqn. 2.3:1}$$

where $i_q(r,\phi) = I_q(r,\phi,z)/P_q(z)$, and n_t = total density of Yb^{3+} ions. In core-pumped fiber, the high-brightness pump has a similar mode-profile (hence overlap fraction) compared to the signal and ASE. However, cladding-pumped fiber (also called double-clad fiber) is used for high power applications because it enables pumping with higher power but lower brightness, multimode laser-diodes. In cladding-pumped fiber, the pump is guided in a multimode "inner-cladding" and only the signal and ASE are guided in the single or few-moded core. Pump power is absorbed from the inner-cladding (passive) to the core (doped with active-ions) along the fiber length, but the transverse pump mode-profile along the fiber can remain approximately constant provided that asymmetries in the inner-cladding shape continually mix the inner-cladding modes. (Double-clad fiber designs used to achieve efficient mode-mixing are described in Chapter 6.) The calculation of overlap fractions for a double-clad fiber are illustrated in Fig. 2.4, for both signal (core-guided) and pump (guided by inner-cladding).

Having reduced the required calculation from 3D to 1D, it is then necessary to set-up and solve the rate equations in order to determine the population inversion in a given fiber section $z \to (z + \Delta z)$. However, because these attributes result in rapid ASE build-up, both forward and backward propagating ASE must be included in the model since the ASE power can be comparable to the signal or pump power.

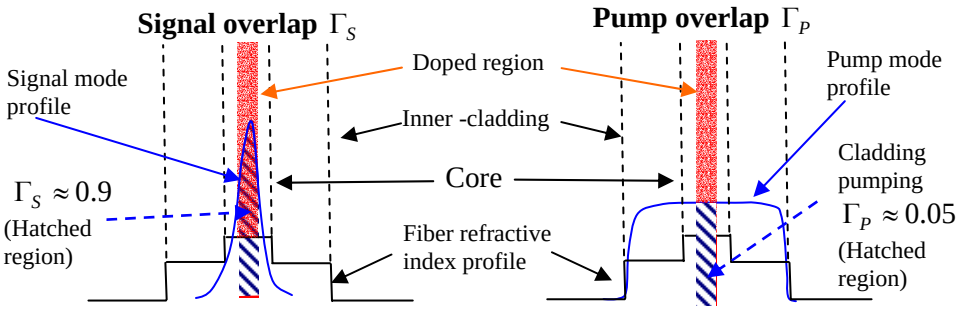

Fig. 2.4. Schematic of fiber profile showing various effective overlap integrals.

Calculating the population inversion requires considering the spectroscopy of the Yb^{3+} ion, and this is typically modelled as a two-level system. Considering Yb-as a two level system is valid because of the simplicity of the Yb-manifolds involved in optical transitions (as described above). This model assumes a homogeneously broadened lineshape, and homogeneous broadening is indeed the dominant broadening mechanism in Yb-doped silica, although there is some component of inhomogeneous broadening. The thermalisation time (establishment of Boltzmann distribution within the upper or lower manifolds) is extremely rapid in Yb, and can

usually be considered to be instantaneous. Also the fiber temperature is usually considered to be constant because Yb has a small quantum defect and a fiber amplifier has a large surface area to volume ratio and naturally dissipates heat efficiently. Hence the emission and absorption cross sections, which are dependent on the Boltzmann thermal population fractions within the sublevels, are considered as constants regardless of pump and signal power levels. Considering all of these features, the two-level model is therefore appropriate for Yb-doped silica fiber.

2.3.3 Calculating the inversion in a short fiber section

The simplifications described in the previous sections reduce the problem of calculating the amplifier parameters (e.g. gain), to a one dimensional problem in a two-level system. However, the tightly confined mode and long interaction length in a fiber amplifier can result in strong gain, which results in a large variation in the population inversion density along the amplifier length. One aspect of the model that it is not often possible to simplify is the consideration of ASE propagation along the fiber length. The tightly confined optical mode and long interaction length that result from the fiber geometry naturally lead to rapid ASE build-up in both forward and backward directions. The calculation of ASE build-up is described further in Section 2.3.4 below. In this section, we consider a length of amplifier sufficiently short that the inversion can be considered uniform, and then in the following section we describe a procedure that uses the results obtained for this short amplifier section in order to calculate the performance of the amplifier as a whole.

To calculate the population inversion for the short fiber section it is first necessary to select the appropriate system of rate equations. In the CPA system, the time interval between pulses (20 ns at 50 MHz rep. rate, increasing to 0.1 ms at 10 kHz rep. rate) is shorter than the upper state lifetime of Yb, and the signal can be considered as quasi continuous wave (CW). The rate equations are therefore solved by setting $\frac{dN_1}{dt} = \frac{dN_2}{dt} = 0$, to obtain the population inversion.

For a signal power P_{Sr} at wavelength λ_r, the transition rate from level 1 (lower level) to level 2 (upper level) is $\frac{N_1 \sigma_{ar} P_{Sr} \Gamma_{Sr}}{Ah\nu_r}$ where N_1 = number of ions in level 1, σ_{ar} = absorption cross section (at wavelength λ_r) and Γ_{Sr} = overlap integral for the signal, and A is the area of the fiber core. The transition rate from level 2 to level 1 is $\frac{N_2 \sigma_{er} P_{Sr} \Gamma_{Sr}}{Ah\nu_r} + \frac{N_2}{\tau}$, where σ_{er} = emission cross section (at wavelength λ_r), N_2 = number of ions in level 2, and τ is the upper level lifetime.

Assuming an amplifier configuration with end-reflections suppressed at both ends of the fiber, there are in general four beams propagating in the fiber, namely: the signal, the pump (which we will assume to be co-propagating, but could also be counter-propagating), and the forward (+) and backward (-) propagating ASE. The ASE is normally considered to be core-guided, and therefore to have the same overlap integral as the signal. For a broad bandwidth signal, as is the case for ultrashort pulses considered in this thesis, it is useful to obtain the spectral dependence of the gain. Spectral dependence is included by using the experimentally measured wavelength dependence of the absorption and emission cross sections, and then modelling the signal as a series of spectral slices of width $\Delta\lambda$ with central wavelength λ_r, and signal power P_{Sr}, where $r = 1 \ldots n$. The ASE can be modelled either approximately by considering an effective ASE bandwidth and appropriate absorption/emission cross sections, or by spectral slicing as suggested for the signal (but perhaps with broader slices than for the signal). In the rate equations below, different wavelength band subscripts, r, k, are used for the signal and ASE summation indices to allow for the possibility of different width spectral slices being used for the computations of signal and ASE. In addition, the pump is assumed to be forward propagating, but it would be equally possible to consider a backward propagating pump. The rate equations are then:

$$\frac{dN_1}{dt} = -\left[\sum_r \frac{\sigma_{ar}(\lambda_r)\Gamma_{Sr}(\lambda_r)}{h\nu_r A} P_{sr} + \sum_k \frac{\sigma_{ak}(\lambda_k)\Gamma_{Sk}(\lambda_k)}{h\nu_k A}\left(P_{Ak}^{+} + P_{Ak}^{-}\right) + \frac{\sigma_{aP}(\lambda_P)\Gamma_P(\lambda_P)}{h\nu_P A} P_P\right] N_1$$
$$+\left[\sum_r \frac{\sigma_{er}(\lambda_r)\Gamma_{Sr}(\lambda_r)}{h\nu_r A} P_{Sr} + \sum_k \frac{\sigma_{ek}(\lambda_k)\Gamma_{Sk}(\lambda_k)}{h\nu_k A}\left(P_{Ak}^{+} + P_{Ak}^{-}\right) + \frac{\sigma_{eP}(\lambda_P)\Gamma_P(\lambda_P)}{h\nu_P A} P_P + \frac{1}{\tau}\right] N_2$$

Eqn. 2.3:2

$$\frac{dN_2}{dt} = +\left[\sum_r \frac{\sigma_{ar}(\lambda_r)\Gamma_{Sr}(\lambda_r)}{h\nu_r A} P_{Sr} + \sum_k \frac{\sigma_{ak}(\lambda_k)\Gamma_{Sk}(\lambda_k)}{h\nu_k A}\left(P_{Ak}^{+} + P_{Ak}^{-}\right) + \frac{\sigma_{aP}(\lambda_P)\Gamma_P(\lambda_P)}{h\nu_P A} P_P\right] N_1$$
$$-\left[\sum_r \frac{\sigma_{er}(\lambda_r)\Gamma_{Sr}(\lambda_r)}{h\nu_r A} P_{Sr} + \sum_k \frac{\sigma_{ek}(\lambda_k)\Gamma_{Sk}(\lambda_k)}{h\nu_k A}\left(P_{Ak}^{+} + P_{Ak}^{-}\right) + \frac{\sigma_{eP}(\lambda_P)\Gamma_P(\lambda_P)}{h\nu_P A} P_P + \frac{1}{\tau}\right] N_2$$

Eqn. 2.3:3

and by conservation $N_t = N_1 + N_2$. Eqn. 2.3:4

2.3.4 Calculating the optimum amplifier length

This section describes a typical algorithm that uses the solution for the population inversion for the short section of fiber, considered above, in order to calculate the pump, signal, and ASE at the output of the complete amplifier.

We write the linear absorption (loss) coefficients of the pump, signal and ASE as α_P, α_S and α_A respectively. The convective equations describing the spatial development of the power in the pump, signal, and forward (+) and reverse (-) ASE beams are:

$$\frac{dP_P(z,t)}{dz} = P_P\Gamma_P\left(\sigma_{aP}N_1 - \sigma_{eP}N_2\right) - \alpha_P P_P \quad , \qquad \text{Eqn. 2.3:5}$$

$$\frac{dP_{Sr}(z,t)}{dz} = P_{Sr}\Gamma_{Sr}\left(\sigma_{er}N_2 - \sigma_{ar}N_1\right) - \alpha_S P_{Sr} \quad , \qquad \text{Eqn. 2.3:6}$$

$$\frac{dP^{\pm}_{Ak}(z,t)}{dz} = \mp P^{\pm}_{Ak}\Gamma_{Sk}\left(\sigma_{ak}N_1 - \sigma_{ek}N_2\right) \pm 2\sigma_{ek}N_2 h\nu_k\Delta\nu_k \mp \alpha_A P^{\pm}_{Ak} \ . \qquad \text{Eqn. 2.3:7}$$

The second term on the right hand side in Eqn. 2.3:7 represents spontaneous emission produced in the amplifier in the bandwidth $\Delta\nu_k$ for both polarisation states. For an end-pumped amplifier with co-propagating pump, boundary conditions for the pump, signal and forward ASE are: $P_P(0) = P_{P\_input}$, $P_s(0) = P_{s\_input}$, $P^+_A(0) = 0$, and $P^-_A(0) = P^-_A(0)_{initial\_estimate}$. Starting at the fiber input ($z = 0$), it is then computationally straightforward to propagate the convective equations stepwise along the fiber by calculating the inversion ($\Delta N = N_2 - N_1$) after each step. The equations are propagated forward to calculate $P_S(L)$, $P_P(L)$, and $P^+_A(L)$. Using these calculated values and the boundary condition $P^-_A(L) = 0$ (which is appropriate because the end reflections are assumed to be suppressed), the pump, signal and ASE (-) are then propagated in the reverse direction to $z = 0$ to find $P_S(0)$, $P_P(0)$, and $P^-_A(0)$. The calculated powers obtained for each beam will be different from the input conditions because the initial estimate for $P^-_A(0)_{initial\_estimate}$ was incorrect. A standard iterative numerical technique (e.g. shooting or relaxation) must then be applied to repeat the calculation using a revised estimate for $P^-_A(0)_{revised\_estimate}$ until a self-consistent solution is obtained that satisfies the boundary conditions at both the input and the output of the amplifier. With this solution established, the gain, ASE (noise) and lost pump power $P_P(L)$ are then known, which gives the amplifier performance (e.g. gain = $P_S(L)/P_S(0)$) for the given amplifier configuration (fiber length, pump power, and signal input power). The optimum amplifier configuration can be determined by using the algorithm iteratively with several variations of the parameter to be varied.

From the extensive modelling and practical work that has been performed with the established EDFA technology, the general properties of fiber amplifiers are now well established. Forward pumping (co-propagating) provides higher inversion density at the beginning of the amplifier, and is appropriate for small signal (high gain) applications because it

results in low noise operation. Forward pumping is appropriate for the low-noise pre-amplifiers in the CPA system because of the small signal strength from the oscillator. With small input signals, high gain is still possible because the power at the amplifier output typically does not saturate the gain. In contrast, reverse pumping (counter-propagating) provides higher inversion density at the end of the amplifier, which results in increased output power with the large signals (saturated gain). However, reverse pumping can produce a significant noise fraction for very weak input signals if care is not taken to avoid this. Reverse pumping is appropriate for the power amplifier in the CPA system, because a strong input signal has been established by using pre-amplifiers, and power extraction is most critical.

2.4 Holey fiber technology

Holey fibers (HFs) are a class of microstructured fiber which have a solid core surrounded by a cladding region that is defined by a fine array of air holes that extend along the full fiber length [15, 16]. HF technology has developed rapidly in recent years, and due to the broader range of fabrication parameters compared to conventional fiber, HFs have been produced with dispersion and nonlinear properties beyond those previously possible [16, 17]. As a result of the extended range of dispersion and nonlinear properties, HFs have led to new applications in spectroscopy [18], metrology [19], and communications [20, 21]. Several experiments reported in this thesis demonstrate novel applications made possible due to the unique properties of HFs, and this section provides an overview of HF technology.

This section is organised as follows. The physical structure and guidance mechanism of HF is first described. Then Section 2.4.1 describes the HF fabrication process. Section 2.4.2 describes the range of dispersion properties possible using HFs. The nonlinear properties of HF are briefly discussed in Section 2.4.3.

Fig. 2.5. shows an idealised HF structure. HFs are typically made of a single material, usually pure silica, and guide light through a modified form of total internal reflection since volume average index in the core region of the fiber is greater than that of the surrounding microstructured cladding. The hole diameter (d) and pitch (Λ=hole to hole spacing), which are the critical design parameters used to specify the structure of an HF, are typically on the scale of the wavelength of light. Fig. 2.6. shows scanning electron microscope (SEM) images of various HFs fabricated at the University of Southampton.

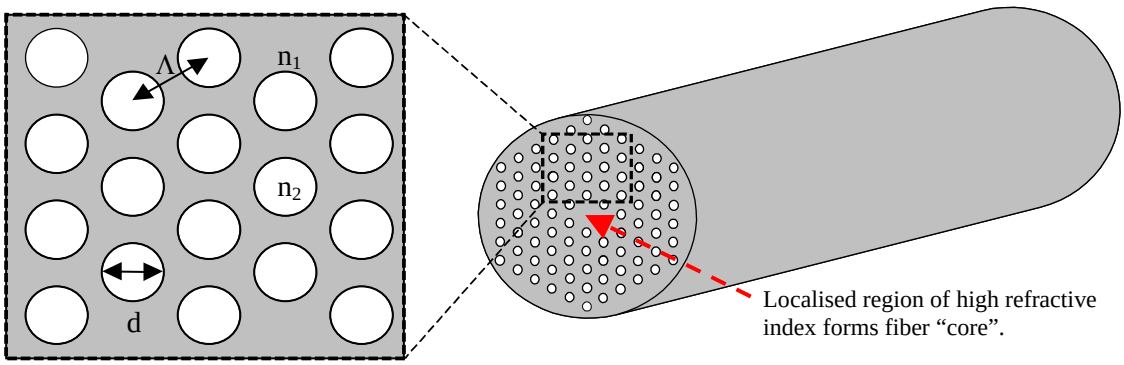

Fig. 2.5.An idealised HF structure.

The physical differences between HFs and conventional fiber types arise from the way that the guided mode experiences the cladding region. In a conventional fiber, this is largely independent of wavelength to first-order. However, in a HF, the large index contrast between glass and air and the small structure dimensions combine to make the effective cladding index a strong function of wavelength. Short wavelengths remain tightly confined to the core, and so the effective cladding index is only slightly lower than the core index. However, at longer wavelengths, the mode samples more of the cladding, and so the effective index contrast is larger.

An unusual modal property of HFs with a low air fill fraction ($(d/\Lambda) < 0.4$) is that such fibers can be single-moded regardless of operating wavelength [22]. The broad bandwidth single-mode operation of HF with a low air fill fraction ($(d/\Lambda) < 0.4$) can be understood qualitatively as follows. The V value (defined earlier) should be less than 2.405 for single mode operation in fiber, which means most of standard single mode fibers produced for telecommunications applications are multi-mode for short wavelengths. For example, SMF28 has a single mode cut-off wavelength of ~ 1.2 μm. In HF the light field at shorter wavelengths is confined within the silica core area rather than being distributed across the air cladding as is the case for longer wavelengths. Thus, the corresponding effective cladding index increases at the shorter wavelengths, keeping the V value nearly constant and extending the single mode bandwidth.

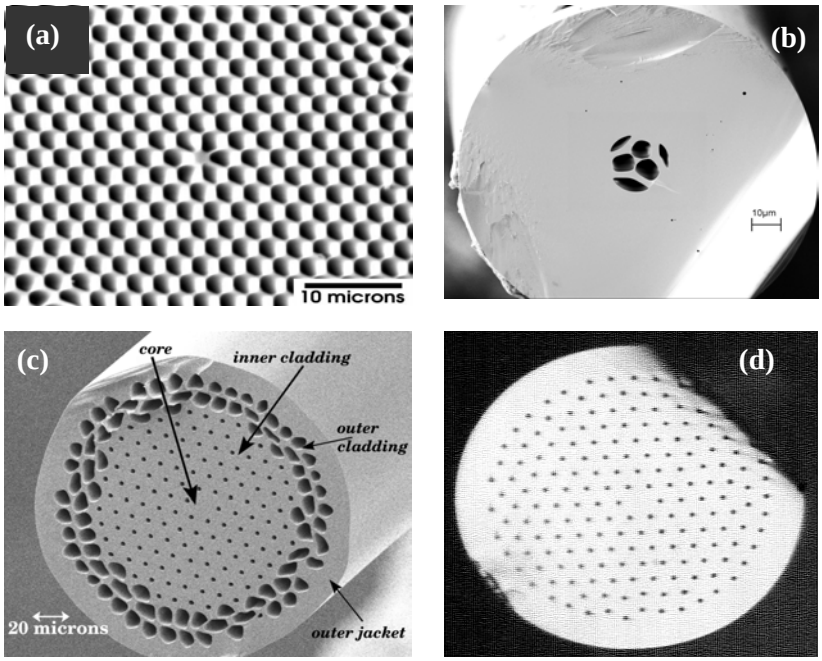

Fig. 2.6. SEMs of various HFs fabricated at University of Southampton: (a) small effective area silica HF, (b) high nonlinearity HF in Schott SF57 glass, (c) Yb-doped, air-clad, Large Mode Area HF for high power cladding-pumping applications, (d) Large Mode Area - HF.

2.4.1 Fabrication of holey fibers

HFs are typically fabricated by stacking an array of capillaries in a hexagonal configuration around a solid rod, which defines a core. The resulting stack (preform), is then drawn down to fiber dimensions using a conventional fiber drawing tower. By selecting the wall thickness and tube diameter of the capillaries and by controlling the conditions under which the fiber is drawn, a wide range of HFs with different optical properties can be produced. To fabricate an active HF, a doped core must be used for the solid central rod when the preform is stacked. Fig. 2.7. shows an outline of the procedure used to fabricate an active HF. This technique was used to fabricate the Yb-doped HF for the experiments presented in Chapter 11. A rare-earth doped core may be obtained by using an ultrasonic drill to remove the core from a conventionally fabricated MCVD fiber preform. The well established technology used to fabricate the conventional preform enables a low loss core rod to be obtained. HFs can be jacketed by inserting the capillary stack into a thick walled silica tube before drawing into fiber, and the resulting fibers can be polymer coated which gives the HF robust handling properties that are similar to those of conventional fibers. To further extend the range of possible structures, alternatives to the capillary stacking technique have been developed and recently the University of Southampton demonstrated the first HF preform fabricated by extrusion of a glass with a lower softening temperature (~600 °C for SF57 versus ~2000 °C for silica) [23].

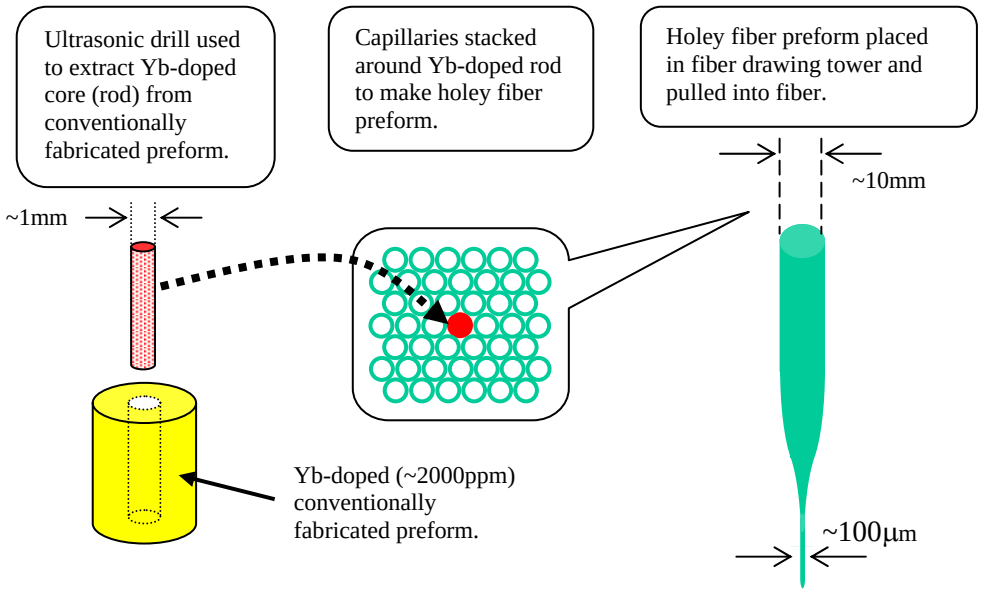

Fig. 2.7 Procedure used for active holey fiber fabrication.

2.4.2 Dispersion properties of holey fiber

The unusual wavelength dependence of the effective refractive index in HF leads to a range of novel dispersion properties which are relevant for applications [20]. For example, silica fibers with a small pitch (Λ<2 μm) and large air holes ($d/\Lambda > 0.5$) can exhibit anomalous dispersion down to wavelengths as low as 550 nm [17] because the exceptionally strong (anomalous) waveguide contribution to the dispersion can dominate the (normal) material dispersion of silica to provide fiber with overall anomalous dispersion at these short wavelengths. This has made the generation and propagation of optical solitons in the near-IR and visible regions of the spectrum a reality [24, 25], something not possible in conventional single mode fibers. Fig. 2.8. shows the GVD of a HF as a function of wavelength for a range of different hole sizes when the hole spacing is fixed [16]. We also note that small core, high air-fill fraction holey fibers are typically polarisation maintaining because small asymmetries in the fiber geometry result in a strong modal birefringence of the orthogonal polarisation modes. Full vector models are therefore essential in order to properly numerically calculate the properties (dispersion, mode area) of such fibers.

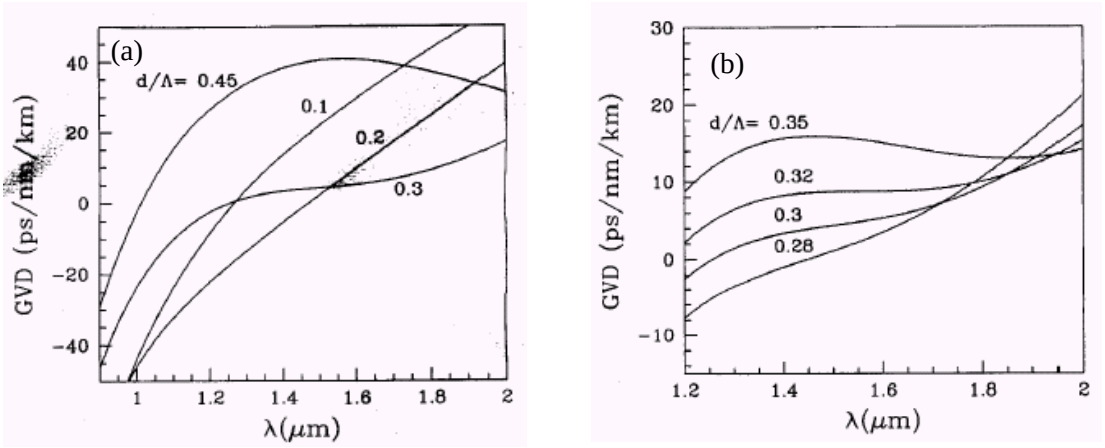

Fig. 2.8. (a) GVD for holey fibers with d/Λ = 0.1, 0.2, 0.3, and 0.45 for Λ = 2.3 μm. Both waveguide and material dispersion have been included. (b) GVD for holey fibers with d/Λ = 0.28, 0.3, 0.32, and 0.35 in order of increasing GVD at a wavelength of 1.4 μm for Λ = 2.3 μm. Both waveguide and material dispersion have been included [16].

2.4.3 Nonlinearity of holey fiber

Due to the tightly confined optical mode, small core, HFs with a high air-fill-fraction in the cladding naturally have tightly confined optical mode, and hence a high effective nonlinearity, $\gamma = (2\pi n_2)/(\lambda A_{eff})$. Further increases in fiber nonlinearity should be achievable using fibers made of other glasses, such as the Chalcogenides [26], which have around two orders of magnitude higher nonlinear optical coefficient compared to silica. Recently researchers at the ORC produced the first results in this direction and demonstrated a HF in SF57 lead glass with γ = 550 $W^{-1}.km^{-1}$, approximately 500 times more nonlinear than conventional SMF28 fiber [23]. (The SF57 fiber shown in Fig. 2.6(b) was produced using the extrusion technique.) With the continuing development of fibers fabricated from high nonlinearity glasses, and new HF structures made possible by the extrusion technique, the field of HF research offers many opportunities for developing future applications based on fiber technology.

References

1. G. P. Agrawal, *Nonlinear Fiber Optics*, Academic Press (San Diego), 2nd (1995).
2. D. Gloge, "Weakly Guiding Fibers," Applied Optics **10,** 2252-2258 (1971).
3. I. P. Kaminow, "Polarization in Optical Fibers," IEEE Journal of Quantum Electronics **17,** 15-22 (1981).
4. M. A. Duguay and J. W. Hansen, "An Ultrafast Light Gate," Applied Physics Letters **15,** 192-194 (1969).
5. M. E. Fermann, "Ultrashort-Pulse Sources Based on Single-Mode Rare-Earth-Doped Fibers," Applied Physics B-Lasers and Optics **58,** 197-209 (1994).
6. R. H. Stolen, J. P. Gordon, W. J. Tomlinson and H. A. Haus, "Raman Response Function of Silica-Core Fibers," Journal of the Optical Society of America B-Optical Physics **6,** 1159-1166 (1989).
7. J. P. Gordon, "Theory of the soliton self-frequency shift," Optics Letters **11,** 662-664 (1986).
8. R. G. Smith, "Optical power handling capacity of low loss optical fibers as determined by stimulated Raman and Brillouin scattering," Applied Optics **11,** 2489 - 2494 (1972).
9. R. H. Stolen and A. M. Johnson, "The Effect of Pulse Walkoff on Stimulated Raman-Scattering in Fibers," IEEE Journal of Quantum Electronics **22,** 2154-2160 (1986).
10. O. Svelto, *Principles of Lasers*, Kluwer Academic / Plenum Publishers (New York), 2nd Edition (1998).
11. R. Paschotta, J. Nilsson, A. C. Tropper and D. C. Hanna, "Ytterbium-doped fiber amplifiers," IEEE Journal of Quantum Electronics **33,** 1049-1056 (1997).
12. H. M. Pask, R. J. Carman, D. C. Hanna, A. C. Tropper, C. J. Mackechnie, P. R. Barber and J. M. Dawes, "Ytterbium-Doped Silica Fiber Lasers - Versatile Sources for the 1-1.2 micron Region," IEEE Journal of Selected Topics in Quantum Electronics **1,** 2-13 (1995).
13. M. J. Weber, J. E. Lynch, D. H. Blackburn and D. J. Cronin, "Dependence of the Stimulated-Emission Cross-Section of Yb^{3+} on Host Glass Composition," IEEE Journal of Quantum Electronics **19,** 1600-1608 (1983).
14. H. Takebe, T. Murata and K. Morinaga, "Compositional dependence of absorption and fluorescence of Yb in oxide glasses," Journal of the American Ceramic Society **79,** 681-687 (1996).
15. J. C. Knight, T. A. Birks, P. St.J.Russell and D. M. Atkin, "All-silica single-mode optical fiber with photonic crystal cladding: Errata," Optics Letters **22,** 484-485 (1997).
16. T. M. Monro, D. J. Richardson, N. G. R. Broderick and P. J. Bennett, "Holey optical fibers: An efficient modal model," Journal of Lightwave Technology **17,** 1093-1102 (1999).
17. J. C. Knight, J. Arriaga, T. A. Birks, A. Ortigosa-Blanch, W. J. Wadsworth and P. St.J.Russell, "Anomalous dispersion in photonic crystal fiber," IEEE Photonics Technology Letters **12,** 807-809 (2000).
18. R. Holzwarth, T. Udem, T. W. Hansch, J. C. Knight, W. J. Wadsworth and P. St.J.Russell, "Optical frequency synthesizer for precision spectroscopy," Physical Review Letters **85,** 2264-2267 (2000).
19. D. J. Jones, S. A. Diddams, J. K. Ranka, A. Stentz, R. S. Windeler, J. L. Hall and S. T. Cundiff, "Carrier-envelope phase control of femtosecond mode-locked lasers and direct optical frequency synthesis," Science **288,** 635-639 (2000).

20. J. H. Lee, Z. Yusoff, W. Belardi, M. Ibsen, T. M. Monro and D. J. Richardson, "Investigation of Brillouin effects in small-core holey optical fiber: lasing and scattering," Optics Letters **27,** 927-929 (2002).

21. Z. Yusoff, J. H. Lee, W. Belardi, T. M. Monro, P. C. Teh and D. J. Richardson, "Raman effects in a highly nonlinear holey fiber: amplification and modulation," Optics Letters **27,** 424-426 (2002).

22. T. A. Birks, J. C. Knight and P. S. Russell, "Endlessly single-mode photonic crystal fiber," Optics Letters **22,** 961-963 (1997).

23. T. M. Monro, M. Kiang, J. H. Lee, K. Frampton, Z. Yusoff, R. C. Moore, J. A. Tucknott, D. W. Hewak, H. N. Rutt and D. J. Richardson, "High nonlinearity extruded single-mode holey optical fibers," *Proc. Optical Fiber Communications Conference (OFC 2002)*, (March, 2002).

24. W. J. Wadsworth, J. C. Knight, A. Ortigosa-Blanch, J. Arriaga, E. Silvestre and P. St.J.Russell, "Soliton effects in photonic crystal fibres at 850 nm," Electronics Letters **36,** 53-55 (2000).

25. J. H. Price, K. Furusawa, T. M. Monro, L. Lefort and D. J. Richardson, "A tuneable, femtosecond pulse source operating in the range 1.06-1.33 microns based on an Yb doped holey fiber amplifier," Conference on Lasers and Electro Optics (CLEO), Vol. 56 of OSA Trends in Optics and Photonics Series (Optical Society of America, Washington, D.C., 2001) paper CPD1 (2001).

26. T. M. Monro, Y. D. West, D. W. Hewak, N. G. R. Broderick and D. J. Richardson, "Chalcogenide holey fibres," Electronics Letters **36,** 1998-2000 (2000).

Chapter 3 Yb fiber based pulse sources

3.1 Introduction

There are a wide variety of new and rapidly emerging applications that rely on high peak powers and femtosecond interaction times, e.g. two-photon absorption microscopy, materials processing, and supercontinuum generation in small core HFs. Despite the proven capabilities of solid state laser systems, there are significant intrinsic limitations on the long-term stability, compactness and cost of such systems, which hampers the successful implementation of the emerging practical applications of ultrafast technology. Developing compact and robust sources of high energy femtosecond pulses has therefore generated strong research interest, and fiber based sources in particular, have developed rapidly during the past ten years. Optical fibers are intrinsically robust and compact components because they are waveguides and they are suitable for high average power applications because their geometry leads to efficient heat dissipation [1].

This chapter presents a summary of results previously reported from fiber based systems. The principal outstanding areas for further research are then described, followed by an overview of the industrially-sponsored CPA system development (the detailed development work is presented in Chapters 4 – 8).

3.2 Summary of related research

The fiber laser was first demonstrated by Elias Snitzer in 1963 using Neodymium (Nd)-doped fiber operating at 1.06 μm. After much development, the first commercial fiber devices appeared in the late 1980s. These lasers used single-mode diode pumping, emitted a few tens of milliwatts, and attracted users because of their large gains and the feasibility of single mode CW lasing for many transitions of rare-earth ions that are not readily achievable in the more-usual crystal-laser version. The most well-known application of fiber-laser technology is in 1550 nm Er-doped fiber amplifiers used in telecommunications.

Cladding-pumped fiber, which was first proposed in 1974, allows the efficient conversion of multimode output radiation from high power, low cost, broad-stripe semiconductor laser diodes into the single-mode emission of fiber lasers [2-4]. More than 110 W has been obtained from a single mode CW Yb-fiber laser [5], and power of up to 6 kW has been demonstrated from a

commercially available multimode fiber laser [6]. Furthermore, diode-pumped double-clad fiber lasers can provide broad gain bandwidths (> 100 nm [7]), with optical pumping efficiencies as high as 80% [8]. These properties, combined with high optical gain, suggest that fiber based systems have many positive attributes compared to bulk crystal or bulk glass systems for high power applications.

However, as other authors have noted [9], the same attributes that make optical fiber advantageous (confined mode, long length), constitute a problem for achieving high peak powers inside the fiber. The relatively small mode size (10 μm versus 1–3 mm) and long interaction length (1–10 m versus 1–10 cm) of a fiber compared to a bulk solid-state system, respectively, means that fiber systems are relatively sensitive to nonlinear effects despite the low inherent nonlinearity of silica, and fibers are perhaps not best suited to pulsed operation. As discussed in Chapter 2 of this thesis, nonlinear effects such as SPM and ultimately SRS limit the maximum energy of pulses that can be obtained from fiber based systems. However, technological developments in the design of doped fibers, coupled to advances in diode brightness mean that reasonable pulse energies and peak powers can now be reached with fiber systems. Within many application areas, particularly those that benefit from high average power levels (high repetition rate, modest pulse energies) fiber technology can now compete and indeed in some cases outperform bulk-laser technology

3.2.1 High energy CPA systems

To increase the pulse energies from fiber systems requires that the nonlinear effects should be controlled and the basic approach has been to scale down the peak intensity inside the fiber core. The CPA technique, as used in bulk solid state ultrashort pulse systems, has also been applied to fiber systems; the pulses are temporally stretched before launch into the fiber amplifiers, then recompressed after the final amplifier stage. However, the largest practical stretched pulse duration of ~1 ns is insufficient to overcome the limiting effects of SRS in standard core-size fibers. To produce higher pulse energies, the core size (mode size) is increased, which reduces the peak intensity.

Fiber-CPA work started with Er-doped fibers using established telecommunications technology. Pulse energies of 1 μJ were produced [10], which was approximately the limit achievable with standard single-mode fibers. Using cladding-pumping then enabled higher average powers, and the first femtosecond fiber systems with 1 W output was demonstrated in 1996 [11]. Then large-core single-mode fibers were developed by using a low NA for the fiber core to maintain single-mode guidance, with a 16 μm diameter mode [12]. Such fibers were used to produce 10 μJ pulses from a single-mode fiber-based CPA system [13] at 1550 nm.

The experimental arrangement of a typical fiber-based CPA system is shown in Fig. 3.1. In 1997 [14], the system was the first fiber-based setup to produce 100 μJ picosecond pulses. The system is described in some detail because it demonstrates the various components that are necessary in order to obtain high energy pulses. Due to the tightly confined mode in a fiber amplifier, amplified spontaneous emission (ASE) build-up limits the maximum gain that is possible from a single amplifier to ~35-40 dB. The experiment required 50–60 dB total gain for boosting pulse energies from an initial 0.1–1 nJ to 100 μJ and therefore used an amplifier cascade to achieve the required gain. The system comprised a femtosecond fiber oscillator, a bulk-grating based pulse stretcher and a compressor, and three main amplifier stages (a fourth pre-amplifier is not shown). Acousto-optic modulators (AOMs) between the amplification stages were used as optical gates, allowing control of the pulse repetition rate down to the kHz range required for achieving maximum pulse energies compared to the MHz repetition rate of the mode-locked oscillator. AOM time gates also prevented cascaded ASE build-up due to the feedback between different amplification stages (in a high repetition rate system, optical isolators would be necessary).

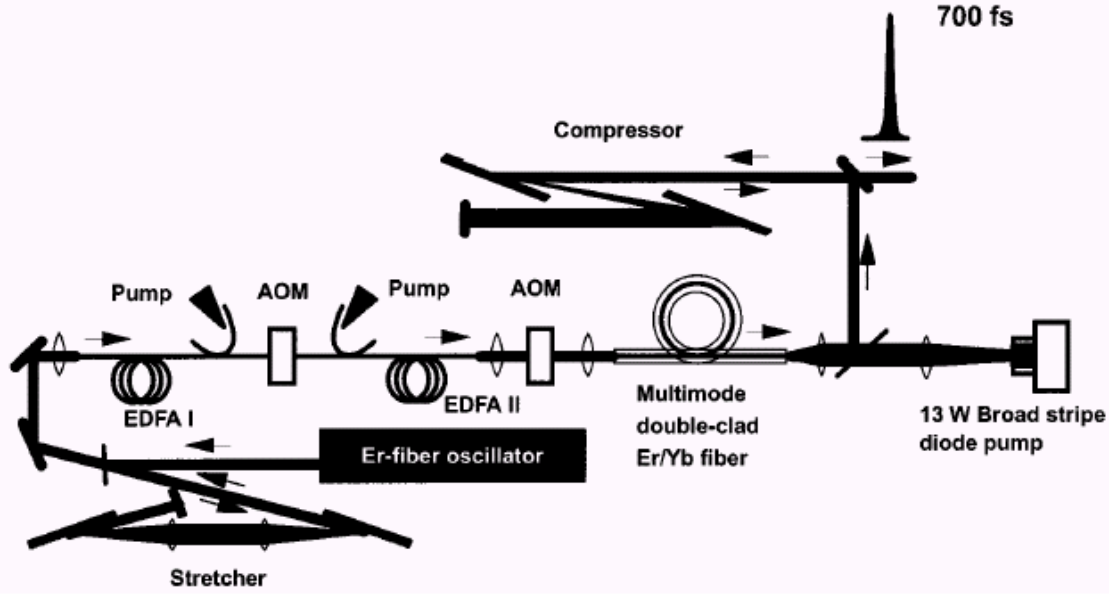

Fig. 3.1 Typical fiber based CPA setup. (System illustrated is based Er/Yb-doped 30 micron core fiber for the final amplifier. From [14]].].)

The increase in pulse energy was enabled by using a larger core fiber. The final amplifier was double-clad Er/Yb-fiber, with a 200 μm cladding and a 30 μm core, and 1.5 m in length. This fiber was heavily doped in order to achieve maximum gain in a short fiber length. The maximum pulse energy of 250 μJ (before compressor) was reached at repetition rates below 1 kHz. The average output power at high repetition rates was up to 1.2 W. After recompression, pulse energies of up to 100 μJ were achieved, with a pulse duration of 0.7 ps.

The output beam had measured M^2 ~1.5 and so was approximately single mode. The core was multimode, but single mode output was obtained by using launch from a single-mode source that was carefully aligned such that only the fundamental mode of the fiber was excited at the input and by using a short fiber length to avoid mode-mixing.

Until this point, all fiber-based CPA development had used Er-fiber as the gain medium. However, Yb-doped silica fiber, with its broad gain bandwidth, high optical conversion efficiency and large saturation fluence [15, 16], represents an extremely attractive medium for both the generation [17, 18] and subsequent amplification of ultra short optical pulses. Two main advantages of Yb-doped over Er-doped fibers are the significantly broader amplification bandwidth (50–100 nm compared to 10–30 nm) and significantly higher optical pumping efficiencies (60–80% compared to 30–40%). In addition, the maximum achievable active-ion concentrations in the Yb-doped fiber core can be significantly higher than for Er-doping, thus enabling very high optical gain in a relatively short fiber length. In 1998, a commercial sponsor entered into negotiation with Professor Richardson to develop an Yb-fiber based CPA system. Professor Richardson had previously demonstrated an Yb-fiber mode-locked oscillator [17], and the ORC was a leading research group in field of Yb-fiber fabrication and applications [15, 16]. The negotiations resulted in a contract to develop a compact, all Yb-fiber, CPA system.

Since the contract with Professor Richardson was negotiated, several other research groups have also recognised and demonstrated the advantages of Yb-fiber for high power pulsed applications, and this parallel work is reviewed here for completeness. Results were presented at CLEO 2000 demonstrating 100 μJ, femtosecond pulses [19]. This Yb-fiber CPA system produced pulses at 1050 nm using a 25 μm core fiber for the final amplifier. Due to higher pumping efficiencies (compared to Er-fiber systems), average output powers up to 5.5 W at 1 MHz, were obtained (before recompression), and the broad amplification bandwidth provided pulses as short as 220 fs, compared to the 500–700 fs typical from previous Er-fiber CPA systems. (Mode-quality results were not presented.) Further progress was reported in 2001 [20] with the demonstration of pulse energies up to 1.2 mJ at a repetition rate of 1667 Hz using an experimental arrangement similar to that shown in Fig. 3.1, including the use of a bulk-grating based pulse stretcher. The seed-pulse source was comprised of a stretched-pulse Er-fiber mode-locked oscillator operating at 1550 nm, followed by a length of single mode fiber used to frequency-shift the pulses to ~2.1 μm (using SSFS), then a chirped periodically poled Lithium Niobate (PPLN) frequency doubling crystal to convert the wavelength to 1050 nm and finally a Yb-fiber pre-amplifier was used to increase the seed average power to 330 mW at a 50 MHz repetition rate. The seed pulse bandwidth was 20 nm, and the pulses were linearly chirped with 2 ps duration [21]. A 2.6 m length of double-clad fiber with 50 μm diameter core, and 350 μm inner cladding diameter (NA~0.4) was used for the final amplifier and was pumped with a 20W

diode laser array. The pump for the final amplifier was counter propagated with respect to the signal, which reduced the effective propagation length. The measured output-beam mode profile was M^2 ~1.16. The final 1.2 mJ recompressed pulses had duration of 380 fs. The maximum pulse energy was limited by the onset of SRS.

3.2.2 High average power systems

In contrast to the high energy pulses at low repetition rates discussed above, there has been parallel research interest in developing fiber systems suitable for applications that require high average powers at high repetition rates. For example, material processing speeds may be increased; synchronously pumped OPO cavities could be made more compact at higher repetition rates, and in spectroscopy, data acquisition rates or statistical accuracy could be aided by higher repetition rates. A high average power CPA system with up to four amplifier stages, and using time-gating between the amplifier stages to obtain variable repetition rates has been demonstrated [22]. The seed oscillator was a mode-locked Nd:glass solid-state laser and produced 1.2 nJ pulses at a repetition rate of 82 MHz. The maximum average power achieved was ~22 W at 1 MHz (fiber core diameter = 55 μm, M^2=7), and at a lower repetition rate of 32 kHz, pulse energies of 100 μJ (average power ~3.2 W) were achieved (fiber core diameter = 11 μm, M^2=1.7).

However, it has also been demonstrated that much simpler system designs can produce high average power ultrashort pulses if the required maximum pulse energy is somewhat lower. The comparative simplicity of high average power systems is because with lower pulse energies, they require lower total gain compared to a high energy CPA system and so use significantly shorter stretched-pulse durations while still providing suitable management of nonlinear effects. The fiber dispersion is an important consideration for direct amplification systems. Standard silica fiber has normal dispersion at wavelengths appropriate for Yb-fiber systems at (1 μm), and the action of nonlinear effects (SPM) is to further increase the pulse broadening caused by dispersion. It has been shown that by carefully selecting a suitable combination of fiber core diameter and fiber length, that the combined effects of SPM and GVD can produce pulses with a linear chirp [23], which facilitates compression with a diffraction grating pair. (This effect has been used with passive fiber for pulse compression [24].) It has been demonstrated experimentally and numerically, and most recently analytically (asymptotic solution) [25, 26] that pulses in a fiber amplifier (i.e. experiencing gain) can develop a parabolic temporal and spectral profile with a highly linear chirp after sufficient propagation distance. The rate of convergence to the asymptotic form depends on the input pulse profile in comparison with the asymptotic pulse profile. These so-called “parabolic” pulses have been recompressed to <100 fs durations [25], and 125 fs duration recompressed pulses have been demonstrated at an average

power of 17 W (75 MHz) [27]. At a wavelength of ~ 1.5 μm, standard telecommunications fiber has anomalous dispersion, and the maximum pulse energy is then limited by soliton formation or modulation instability. Therefore Er-fiber based systems are unsuitable for direct amplification systems. Dispersion shifted fiber (DSF) can have normal dispersion at wavelengths suitable for Er-doped fiber amplifiers. However, the very low dispersion value could result in rather short pulse durations and hence low SRS threshold pulse energies. In addition, DSF has a small core which is again unsuitable for high power applications.

The experimental arrangement for a high repetition rate direct amplification system is simplified compared to that of a fiber based CPA system, because typically one amplifier stage is used and the pulse stretcher is omitted. Time-gating is not required in a high repetition rate system, so AOMs are not required before the amplifier and coupling losses are reduced. Although a diffraction grating compressor is still required at the system output in order to compensate for the linear chirp of the pulses, the compressor is more compact in comparison to a CPA system due to the dramatically reduced stretched pulse duration. Overall, the direct amplification systems can provide high average power, yet are simpler, lower loss, and more compact, compared to CPA based systems.

3.3 Remaining technological challenges

The above review considered the impressive results so-far obtained from fiber based CPA and direct amplification systems. However, there remain several technical challenges to be addressed before truly compact, practical, straightforward to manufacture systems can be produced for wide application. Yb-doped fiber appears now to be the preferred gain medium for both high pulse energy and high average power sources. The first technical challenge is therefore to produce a practical ultrashort seed oscillator at 1 μm. Existing oscillators are either based on bulk Yb crystals (e.g. product from “TimeBandwidth”), which results in a cavity that can be costly to manufacture and requires precise alignment, or (e.g. product from “IMRA”) use complex multi-stage systems (start with Er-fiber oscillator, then use the soliton self-frequency-shift to tune the pulses to 2.1 μm, followed by frequency doubling in PPLN to generate pulses at 1.05 μm [21]). Professor Richardson’s research started to address this challenge with the development of an Yb-fiber oscillator in 1997 [17], but despite good performance (~65 fs pulses), the laser was Ti:sapphire pumped, and employed a complex cavity. This thesis describes (Chapter 4) our development of a much more practical, robust, and very stable diode-pumped Yb-fiber oscillator. This oscillator is now commercially available through Positive Light Inc., and initial sales have been made [18, 28, 29].

Another outstanding challenge is to develop compact stretcher/compressor technologies. The conventional fiber CPA layout is to use diffraction-grating based stretchers and compressors, which are typically large and require careful alignment. For applications which require a frequency doubled output, chirped quasi-phase matching gratings may be appropriate [30]. Alternatively, chirped fiber Bragg gratings (CFBGs) are highly dispersive and can provide suitable time delays in only centimetre lengths of fiber. Indeed, Neil Broderick et al. at the ORC have demonstrated 4-ps pulses with energy of 0.9 μJ using CFBG stretcher and compressor gratings in an all fiber CPA system based on large mode area (LMA) fiber components [31]. The principal limit on the use of CFBGs is that due to the high peak power in the compressor (~100 MW for 50 μJ, 500 fs recompressed pulses), the nonlinearity of the grating fiber degrades the pulse quality. A bulk-grating based compressor is therefore required for high energy CPA systems, but it is still possible to use a CFBG stretcher.

Both 2nd order (GDD) and 3rd order dispersion of a bulk-grating compressor are proportional to the grating separation [32]. Therefore, using a long (~0.3 ns) stretched pulse duration that requires large GDD, also adds large 3rd order dispersion. For recompressed pulse durations <500 fs, uncompensated 3rd order dispersion would result in a significant pedestal on the recompressed pulse. CFBGs incorporating both 2nd and 3rd order dispersion compensation have not previously been reported in CPA systems at 1 μm, and the development of a CFBG pulse stretcher with both the correct 2nd and 3rd order dispersion to compensate for the bulk-grating compressor is presented in Chapter 5 of this thesis. The CFBG was fabricated using the uniquely flexible CFBG writing technology developed at the ORC [33]. Using the CFBG stretcher should provide a robust, compact, and alignment-free stretcher. As an alternative technology, single mode fiber was also considered for the stretcher, but because fiber has the same sign of 3rd order dispersion as the bulk grating compressor, it is unsuitable for CPA systems producing <500 fs pulses.

In our CPA and direct amplification systems described in Chapters 3-8, we have included a fiberised, 3 GHz bandwidth, electro-optic modulator (EOM) (phase modulator with a $LiNbO_3$ crystal in one arm) to select single pulses from the 50 MHz pulse train from the mode-locked oscillator. An EOM has several advantages compared to using an AOM for pulse selection. First, an EOM can easily accommodate repetition rates above 1 GHz, whereas an AOM has a maximum repetition rate of ~50MHz (due to the slow rise time of the acoustic wave), and it is typically necessary to sacrifice AOM diffraction efficiency in order to achieve operation above ~20MHz. Second, our EOM has a 50 dB extinction ratio, compared to a typical extinction ratio of ~ 30dB for an AOM. In addition, if the amplification system were reconfigured to produce longer pulses by temporally slicing from a CW laser source, the EOM would enable <1 ns

pulses to be produced, compared to >20 ns pulses if an AOM were used. Moreover, the EOM would also enable pulse generation at higher repetition rates.

While direct amplification systems are attractive for high average power applications, at the time of writing, such systems have only been demonstrated using a single amplifier stage. This restricts the maximum gain to <35 dB, which, depending on the pulse energy from the initial source, could restrict the maximum output pulse energy to below that required for certain applications. To avoid this restriction, further research using direct amplification systems, with more than one amplification stage, would be interesting. In addition, it may be useful to use time gating in order to introduce the flexibility of a variable repetition rate, both to suit the requirements of possible applications, and in order to demonstrate the ultimate pulse energies that might be possible from such systems. SRS will limit the maximum energy, but as with CPA systems, pulse energy can be increased by enlarging the fiber core size. The results from an investigation of a direct amplification system using cascaded amplifiers are presented in Chapter 8 of this thesis.

3.4 Overview of CPA and direct amplification system

3.4.1 Background

The agreed target specification for our CPA system was for pulses with duration ~500 fs, energy 10-50 μJ, and average power ~500 mW (repetition rate ~ 50 kHz). When the scope of the research was being agreed, there had been no published reports of Yb-fiber based amplifier short pulse systems, and the target pulse peak powers were higher than those reported from existing fiber based research (i.e. the system specification represented the state-of the art, although results demonstrating pulse energy >1 mJ have since been reported by other researchers using a less compact and commercially practical system). The work developing this industrially funded system formed a large proportion of this PhD thesis and is described in Chapters 3-7.

We note that the initial industrial contract specified a very demanding development timetable. As a result, it was not always possible to perform as detailed a characterisation of the individual system components as would have been desirable and on occasion, initially unpromising results were not followed up with more extensive research efforts. Our approach was rewarded by the rapid development of a highly-stable oscillator, which has since been commercialised, and has also been used to seed several of the experiments reported in this thesis. In combination with the amplifier cascade, the system has also been used to pump a femtosecond OPO.

3.4.2 Detailed system configuration

A schematic representation of the industrially funded CPA system is shown in Fig. 3.2. To address the outstanding technological challenges described above, the agreed research approach was to develop a passively mode-locked Yb-fiber-based oscillator to produce ~100 fs pulses to be used as a seed for a fiber amplifier cascade. As with previously reported fiber systems, a multi-stage amplifier design was necessary because ASE limits the gain from a single fiber amplifier to ~30-35 dB [34]. The system incorporated a high extinction ratio (>50 dB) EOM for pulse selection; and used a CFBG pulse stretcher. ASE build-up was prevented by incorporating isolators and AOM time gating (synchronised to the arrival of each pulse) between amplifier stages. These additional components created coupling losses (total ~20 dB). We required ~60 dB net gain in order to obtain pulses with an energy of ~50 μJ from our oscillator, and it was expected that a cascade of three amplifiers would be necessary to produce the required gain, and reasonable overall noise performance. The subsequent oscillator development (Chapter 4) resulted in a stable oscillator with output pulse energy ~50 pJ, which confirmed that three amplifiers would be required.

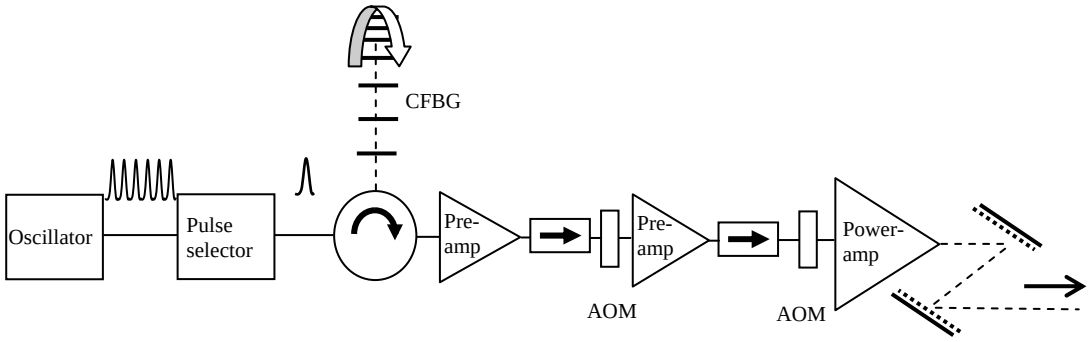

Fig. 3.2. Schematic of the CPA system

The desire to obtain a robust and straightforward-to-manufacture system would suggest that core-pumping would be the preferred approach. High-brightness pig-tailed pump diodes, spliced directly to WDM couplers, and then to the Yb-doped fiber gain medium, would create an integrated fiber system. However, the core-pumping approach has limited scope for power-scaling, e.g. the maximum available power from reliable pigtailed diodes is ~350 mW, which is below the output power required from the CPA system. Cladding pumping was therefore necessary for the final amplifier stage and possibly for the penultimate amplifier. Cladding pumping has the advantage of using less expensive, low brightness pump diodes. It was decided that the best aspects of both pumping technologies could be exploited by developing a core-pumped oscillator and at least one core-pumped pre-amplifier, followed by a cladding-pumped power amplifier. However, selecting a suitable operating wavelength to successfully integrate these two technologies in the quasi-three level Yb system is challenging.

The emission cross section of 975 nm pumped, Yb-doped silica fiber is peaked at 1030 nm (see Chapter 2). The absorption cross section is highest at wavelengths below ~1030 nm and decreases more rapidly than the emission cross section at longer wavelengths e.g. 1060 nm. Therefore, high pump intensity can lead to peak gain at wavelengths close to 1030 nm, whereas lower pump intensities result in gain at wavelengths >1070 nm. Core-pumped amplifiers result in very high pump-intensities due to ~100% overlap fraction of pump and doped region (doping is typically confined to the core), which tends to favour peak Yb gain at 1020-1040 nm. If necessary, the gain can be extended to ~1050-1060 nm by using a longer fiber length because the Yb gain at 1060 nm can be pumped by re-absorbed 1030 nm ASE. In contrast, cladding-pumped amplifiers result in much lower pump intensities due to reduced pump overlap with the doped-region (core). Low pump intensity creates peak Yb gain at 1070-1100 nm. In addition, relatively long fiber lengths are needed to fully absorb the pump, and thus create an efficient amplifier, which again favours operation at long wavelengths due to reabsorption of short wavelength ASE. Shorter fiber lengths are not ideal because they can reduce the amplifier efficiency. Pumping at the 976 nm Yb-absorption peak assists in obtaining the most rapid pump absorption in short fiber lengths, and therefore pushes the gain towards shorter wavelengths. In a pulsed system, use of the shortest possible fiber length also minimises detrimental nonlinear interactions. The gain at 1040-1070 nm is also increased by using a lower cladding: core area ratio (big core, small cladding) to create higher pump intensities. The difference between the optimally efficient operating wavelengths of core-pumped and cladding-pumped amplifiers suggested that a central wavelength of ~1050-1060 nm would enable most effective integration of the two technologies within the CPA system. This wavelength window became the design specification for the system, and since the system operating wavelength is determined by the oscillator wavelength, this was an important specification for the oscillator. The final system comprised a cascade of two core-pumped pre-amplifiers and a LMA quasi-single mode cladding-pumped fiber for the final stage power amplifier.

Obtaining ultrashort (<500 fs) pulses at the system output required careful consideration of the combined effects of group velocity dispersion and nonlinear processes (SPM and SRS) that would distort the pulse due to the high peak powers at the system output. SPM can produce a strongly nonlinear chirp such that the recompressed pulse exhibits a broad pedestal containing much of the pulse energy. Avoiding such nonlinear broadening limits the maximum achievable pulse energy from a fiber-based system, and in order to increase the pulse energy at which nonlinear distortion arises, we used two techniques which reduced the peak intensity within the amplifiers. We use the CPA technique to temporally stretch the initial pulse. The maximum stretched pulse duration is limited by the size of the bulk-grating compressor (grating size and grating separation). To achieve a truly compact system, our industrial sponsor specified the

grating size (see Chapter 5 for details), which resulted in a maximum stretched pulse duration of ~0.3 ns for our system. With the stretched-pulse duration fixed by the compressor, the maximum achievable pulse energy is limited by the onset of SRS in the final amplifier. Using LMA fiber for the final amplifier, decreases the peak intensity (W/cm^2) and therefore increases the maximum achievable pulse energy that can be cleanly recompressed.

The detailed development work on this CPA system has formed a major part of this PhD thesis research, and is described in the following chapters. Chapter 4 describes the design and realisation of the passively mode-locked, diode-pumped, Yb-fiber laser. The development of the grating stretcher and compressor are described in Chapter 5. Next, the amplifier development is reported in Chapter 6. The overall performance of the CPA system is described in Chapter 7. The practical implementation of directly amplifying the pulses from the oscillator, without temporal stretching, to create a simplified high power source (based on the amplifiers developed for the CPA system) has also been investigated. For this direct amplification system, multiple amplifier stages were used in order to obtain higher gain than had been reported previously from direct amplification – all previous reports have used a single amplifier stage. The performance of the direct amplification system (without pulse stretching) is described in Chapter 8.

References

1. M. K. Davis, M. J. F. Digonnet and R. H. Pantell, "Thermal effects in doped fibers," Journal of Lightwave Technology **16,** 1013-1023 (1998).
2. Maurer, U.S. Patent 3,808,549 (April 30, 1974).
3. J. Kafka, U.S. Patent 4,829,529 (May 9, 1989).
4. E. Snitzer, H. Po, F. Hakimi, R. Tumminelli and B. C. McCollum, "Double Clad, Offset Core Nd Fiber Laser," Proceedings, OFS conference, New Orleans Post-deadline paper PD5 (1988).
5. V. Dominick, S. MacCormack, R. Waarts, S. Sanders, S. Bicknese, R. Dohle, E. Wolak, P. S. Yeh and E. Zucker, "110W fiber laser," Electronics Letters **35,** 1158-1160 (1999).
6. *IPG Photonics press release, Dec16 2002 (http://www.ipgphotonics.com).*
7. J. K. Sahu, C. C. Renaud, K. Furusawa, R. Selvas, J. A. Alvarez-Chavez, D. J. Richardson and J. Nilsson, "Jacketed air-clad cladding pumped Ytterbium-doped fibre laser with wide tuning range," Electronics Letters **37,** 1116-1117 (2001).
8. L. Goldberg, J. P. Koplow and D. A. V. Kliner, "Highly efficient 4-W Yb-doped fiber amplifier pumped by a broad-stripe laser diode," Optics Letters **24,** 673-675 (1999).
9. A. Galvanauskas, "Mode-scalable fiber-based chirped pulse amplification systems," IEEE Journal of Selected Topics in Quantum Electronics **7,** 504-517 (2001).
10. A. Galvanauskas, M. E. Fermann, P. Blixt, J. A. Tellefsen and D. Harter, "Hybrid Diode-Laser Fiber-Amplifier Source of High-Energy Ultrashort Pulses," Optics Letters **19,** 1043-1045 (1994).
11. A. Galvanauskas, M. E. Fermann, D. Harter, J. D. Minelly, G. G. Vienne and J. E. Caplen, "Broad-area diode-pumped 1 W femtosecond fiber system," Tech. Dig. Conf. Lasers and Electro-Optics, Vol. 9, Washington DC, pp. 495-496 (1996).
12. D. Taverner, D. J. Richardson, L. Dong, J. E. Caplen, K. Williams and R. V. Penty, "158 μJ pulses from a single-transverse-mode, large-mode-area Erbium-doped fiber amplifier," Optics Letters **22,** 378-380 (1997).
13. D. Taverner, A. Galvanauskas, D. Harter, D. J. Richardson and L. Dong, "Generation of high-energy pulses using a large-mode-area Erbium-doped fiber amplifier," Tech. Dig. Conf. Lasers and Electro-Optics, Vol. 9, Washington DC, pp. 496-497 (1996).
14. J. D. Minelly, A. Galvanauskas, D. Harter, J. E. Caplen and L. Dong, "Cladding-pumped fiber laser/amplifier system generating 100 micro-Joule energy picosecond pulses," Tech. Dig. Conf. Lasers and Electro-Optics, Vol. 11, Washington DC pp. 475-476 (1997).
15. H. M. Pask, R. J. Carman, D. C. Hanna, A. C. Tropper, C. J. Mackechnie, P. R. Barber and J. M. Dawes, "Ytterbium-Doped Silica Fiber Lasers - Versatile Sources for the 1-1.2 micron Region," IEEE Journal of Selected Topics in Quantum Electronics **1,** 2-13 (1995).
16. R. Paschotta, J. Nilsson, A. C. Tropper and D. C. Hanna, "Ytterbium-doped fiber amplifiers," IEEE Journal of Quantum Electronics **33,** 1049-1056 (1997).
17. V. Cautaerts, D. J. Richardson, R. Paschotta and D. C. Hanna, "Stretched pulse Yb^{3+} silica fiber laser," Optics Letters **22,** 316-318 (1997).
18. J. H. Price, L. Lefort, D. J. Richardson, G. J. Spuhler, R. Paschotta, U. Keller, C. Barty, A. Fry and J. Weston, "A practical, low noise, stretched pulse Yb^{3+}-doped fiber laser," Conference on Lasers and Electro-Optics (CLEO 2001), paper CTuQ6 (2001).

19. G. C. Cho, A. Galvanauskas, M. E. Fermann, M. L. Stock and D. Harter, "100 micro-Joule and 5.5 W Yb-fiber femtosecond chriped pulse amplifier system," Tech. Dig. Conf. Lasers and Electro-Optics, Washington DC, p. 118 (2000).

20. A. Galvanauskas, Z. Sartania and M. Bischoff, "Millijoule femtosecond fiber CPA system," in *Advanced Solid-State Lasers, Proceedings*, vol. 50, *OSA Trends in Optics and Photonics*, C. Marshall, Ed. Washington, 2001, pp. 679-681.

21. M. E. Fermann, A. Galvanauskas, M. L. Stock, K. K. Wong, D. Harter and L. Goldberg, "Ultrawide tunable Er soliton fiber laser amplified in Yb-doped fiber," Optics Letters **24,** 1428-1430 (1999).

22. A. Liem, D. Nickel, J. Limpert, H. Zellmer, U. Griebner, S. Unger, A. Tünnermann and G. Korn, "High average power ultra-fast fiber chirped pulse amplification system," Applied Physics B-Lasers and Optics **71,** 889-891 (2000).

23. D. Anderson, M. Desaix, M. Karlsson, M. Lisak and M. L. Quirogateixeiro, "Wave-Breaking-Free Pulses in Nonlinear-Optical Fibers," Journal of the Optical Society of America B-Optical Physics **10,** 1185-1190 (1993).

24. G. P. Agrawal, *Nonlinear Fiber Optics*, Academic Press (San Diego), 2nd (1995).

25. M. E. Fermann, V. I. Kruglov, B. C. Thomsen, J. M. Dudley and J. D. Harvey, "Self-similar propagation and amplification of parabolic pulses in optical fibers," Physical Review Letters **84,** 6010-6013 (2000).

26. K. Tamura and M. Nakazawa, "Pulse compression by nonlinear pulse evolution with reduced optical wave breaking in Erbium-doped fiber amplifiers," Optics Letters **21,** 68-70 (1996).

27. J. Limpert, T. Schreiber, T. Clausnitzer, K. Zollner, H. J. Fuchs, E. B. Kley, H. Zellmer and A. Tünnermann, "High-power femtosecond Yb-doped fiber amplifier," Optics Express **10,** 628-638 (2002).

28. D. J. Richardson, J. Nilsson, L. Lefort, J. H. Price, A. Malinowski and M. Ibsen, "Pulsed Light Sources," U.S. Patent Application 10/146,219 (May 13, 2002).

29. L. Lefort, J. H. Price, D. J. Richardson, G. J. Spuhler, R. Paschotta, U. Keller, A. Fry and J. Weston, "Practical Low-Noise stretched-pulse Yb-doped fiber laser," Optics Letters **27,** 291-293 (2002).

30. A. Galvanauskas, D. Harter, M. A. Arbore, M. H. Chou and M. M. Fejer, "Chirped-pulse amplification circuits for fiber amplifiers, based on chirped-period quasi-phase-matching gratings," Optics Letters **23,** 1695-1697 (1998).

31. N. G. R. Broderick, D. J. Richardson, D. Taverner, J. E. Caplen, L. Dong and M. Ibsen, "High-power chirped-pulse all-fiber amplification system based on large-mode-area fiber gratings," Optics Letters **24,** 566-568 (1999).

32. R. L. Fork, C. H. B. Cruz, P. C. Becker and C. V. Shank, "Compression of Optical Pulses to 6 femtoseconds by Using Cubic Phase Compensation," Optics Letters **12,** 483-485 (1987).

33. M. Ibsen, M. K. Durkin, M. J. Cole, M. N. Zervas and R. I. Laming, "Recent Advances in Long Dispersion Compensating Fiber Bragg Gratings.," (IEE Colloquium on Optical Fiber Gratings) IEE, London, U.K. (1999).

34. B. Desthieux, R. I. Laming and D. N. Payne, "111 kW (0.5 mJ) Pulse Amplification at 1.5-microns Using a Gated Cascade of 3 Erbium-Doped Fiber Amplifiers," Applied Physics Letters **63,** 586-588 (1993).

Chapter 4 Mode locked fiber laser

4.1 Introduction

This chapter describes the development of a compact, and highly stable stretched pulse laser operating at 1.06 μm, based on Yb-doped fiber. As described in Chapter 3, the laser was developed as a seed laser for a CPA system for an industrial sponsor. Important criteria were that the laser should be compact, robust, and stable, and that it should have low noise operation.

We constructed the oscillator using a Fabry-Perot cavity design, with grating based dispersive delay line [1, 2], and SESAM to initiate self-start mode locking [3]. The oscillator uses nonlinear polarisation rotation switching to sustain mode-locking. The oscillator has robust, reliable self start, single pulse, mode-locked operation with no Q-switching instabilities, with a launched pump power of ~60 mW, and delivers ~30 pJ pulses that are compressible to ~110 fs (54 MHz repetition rate; 2.5 mW average output power). The initial development work on the oscillator was performed jointly with Dr. Laurent Lefort, a research fellow working in Professor Richardson's group during the early stages of the CPA project, and his contribution is gratefully acknowledged.

The excellent performance (robust self-start operation with minimal (<0.05%) amplitude jitter) of our research prototype, has since enabled us to perform several nonlinear optics experiments using this source (e.g. see Chapters 9,10). The system stability is largely attributable to the use of a grating-stabilised, telecommunications-qualified, 976 nm diode pump laser. Pump coupling is both conveniently and reliably achieved using a 980nm/1054nm, fused-tapered WDM coupler.

This chapter is structured as follows. Section 4.2 provides a review of previous mode-locked fiber laser research and describes the operating principles of our laser. Section 4.3 provides a description of the cavity. Section 4.4 discusses the characteristics of the Yb-doped fiber. Section 4.5 describes the passive fiber components in the cavity and Section 4.6 describes various SESAMs that we tested. The laser performance is described in Section 4.7, and Section 4.8 presents our conclusions.

4.2 Mode-locked fiber laser operating principles

Ultrashort pulse generation requires either an ultrafast switch, or an environment in which such pulses are the most stable state. Ultrafast sources in the visible are typically based on bulk crystal gain media, e.g. Ti:Sapphire, use Kerr lens mode locking as an ultrafast nonlinear switch. An intra-cavity aperture results in relatively high losses for the large diameter CW beam, whereas Kerr self-focussing of the high-intensity pulses reduces the beam diameter and decreases the loss. However, such bulk-optics-based cavities require precise alignment and are therefore difficult and expensive to construct. Previous work at a wavelength of 1.5 μm, has demonstrated that the anomalous dispersion of standard single mode fiber produces modulation instability for a CW beam, and hence initiates pulse formation. Ultrashort soliton pulses can be supported by balancing the effects of GVD and SPM. The gain medium used at this wavelength is Er-doped fiber, and this enables the use of established technology from the telecommunications industry. Whilst modulation instability and soliton effects can generate ultrashort pulses, the amplification that occurs every round trip leads to a background continuum of wavelengths being produced that can destabilise the circulating soliton. Therefore a filter or ultrafast switch is required, and the first soliton fiber lasers used a nonlinear loop mirror fiber (uses SPM as the nonlinearity) as a fast saturable absorber in a figure of eight cavity geometry [4-6]. Later work used a simpler ring cavity geometry with a nonlinear polarisation evolution (NLPE) based fast saturable absorber (uses XPM as the nonlinearity) [7-10]. The soliton power increases with the magnitude of the dispersion, so dispersion shifted fiber (providing low total cavity round trip dispersion) has been used to encourage self-starting at low powers. However, the maximum energy from soliton lasers was limited to very low pulse energies by the generation of spectral side-bands that resulted in pulse instability and breakup into multiple solitons.

A breakthrough came when, again at 1.5 μm, the group at MIT [11-13] demonstrated that quasi-soliton operation was possible in a cavity with lumped sections of large positive and negative dispersion, provided that the overall round trip dispersion was close to zero. (In fact, the shortest pulses were obtained with small net normal dispersion.) In this “stretch-pulse” configuration, the pulses broaden because of the excess GVD in one section of the cavity, before being recompressed in the section of the cavity with opposite sign GVD. The dispersion managed cavity idea leads to the possibility of using bulk optics for the anomalous dispersion section, and so it was applicable to wavelengths below 1.3 μm, where conventional fiber has normal dispersion. A passively mode-locked stretched pulse laser based on Nd-doped fiber was previously reported in 1993 in a Fabry-Perot cavity with prism-based dispersive delay-line (DDL) [14]. NLPE was used as a fast saturable absorber mechanism, and a SESAM was used

to induce self-start mode-locking [15]. Although the laser performance in terms of pulse duration and quality seemed very good, no data was presented on system stability and reliability. Moreover, this system was end-pumped with two polarisation-multiplexed 150 mW laser diodes (808 nm), or with a Kr^{3+} laser (to obtain the shortest pulses), so the system was still not practical for wide application.

Yb-doped silica fiber offers the advantage of broader gain bandwidth, and in 1996 Professor Richardson's group demonstrated the first mode-locked Yb-doped fiber oscillator [16]. A unidirectional cavity design was used that incorporated an optical circulator arrangement and an intracavity prism based DDL. NLPE in the fiber acted as the fast saturable absorber. The laser exhibited good self-starting performance and generated ~65 fs pulses. However, the cavity was large and complex and was pumped with a Ti:sapphire laser. There have also been a number of reports of stretched-pulse lasers operating at 1 μm using high power broad-stripe pump diodes and cladding pumped Yb or Nd-doped fiber. Cladding pumped fiber readily allows scaling of the pulse energies achievable from diode-pumped cavities to the nJ regime, but high power diode-pump sources are typically not stable against wavelength drift, and are noisier when compared to the grating stabilised, high-brightness, single-mode diodes developed over many years for core-pumping of erbium doped fiber amplifiers. Moreover, due to the reduced overlap of the pump and signal fields in dual clad fibers, cladding pumped fiber lasers are ordinarily much longer in length than core-pumped fiber laser. Cladding pumped lasers are thus inherently likely to be far less stable than cavities based on core-pumped fiber.

For the new cavity design it was decided that Yb-fiber would be used for the gain medium. To ensure low-noise operation, a grating stabilised telecommunications grade laser diode would be the preferred pump laser, and using a pigtailed pump diode coupled to the Yb-fiber using a WDM coupler would create an all fiber gain-unit. A Fabry-Perot design would enable a simple and compact cavity to be constructed, in preference to the complex ring cavity used previously [16]. However, in Fabry-Perot cavities the standing wave pattern of the electric field creates a refractive-index grating in the gain medium which creates uneven frequency spacing between cavity modes. This effect increases the threshold power at which mode-beating fluctuations build up into a stable pulse i.e. increases the threshold power for self-start mode-locking [17]. We therefore decided to try incorporating a SESAM into the cavity to enable reliable self-start mode-locking. A bulk grating or prism based dispersive delay line (DDL) would be used to compensate for the normal disperison introduced by the fiber.

4.3 Description of the cavity

A photograph and schematic of our laser is shown in Fig. 4.1. The cavity contains a grating-based intracavity dispersion compensator [1, 2], ~1.0 m of high-concentration, moderately

birefringent Yb-doped fiber with angle polished ends to suppress intracavity reflections, and a 976/1050 nm WDM coupler. Two polarisers and associated wave plates are included to (1) control the bias of the polarisation switch, and (2) adjust the output coupling. A suitably optimised SESAM device (InGaAs MQW absorber, with a rear Bragg mirror made from AlAs-GaAs quarter layers) is also incorporated to facilitate reliable self-start mode-locking [3]. (The SESAM is described in more detail in Section 4.6.) All intra-cavity optics were anti-reflection coated to avoid etalon effects which could disrupt self-starting [15]. The laser is pumped with a telecommunications qualified, grating stabilised, 976 nm pump diode (~65mW). The output from the oscillator is extracted from either PBS1 or PBS2. The axis for the polarisation switch is defined at PBS1, where the rejected part of the pulse appears at Port 1. The half wave plate between PBS1 and PBS2 provides adjustable output coupling for the circulating pulses; positively chirped pulses are output from PBS2 at Port 3, and negatively chirped pulses are output from PBS1 at Port 2. Having a linear chirp, the pulses are compressible external to the cavity, for example using a diffraction grating pair at Port 3 or by propagating the pulses from Port 2 along an ~80 cm length of single mode fiber.

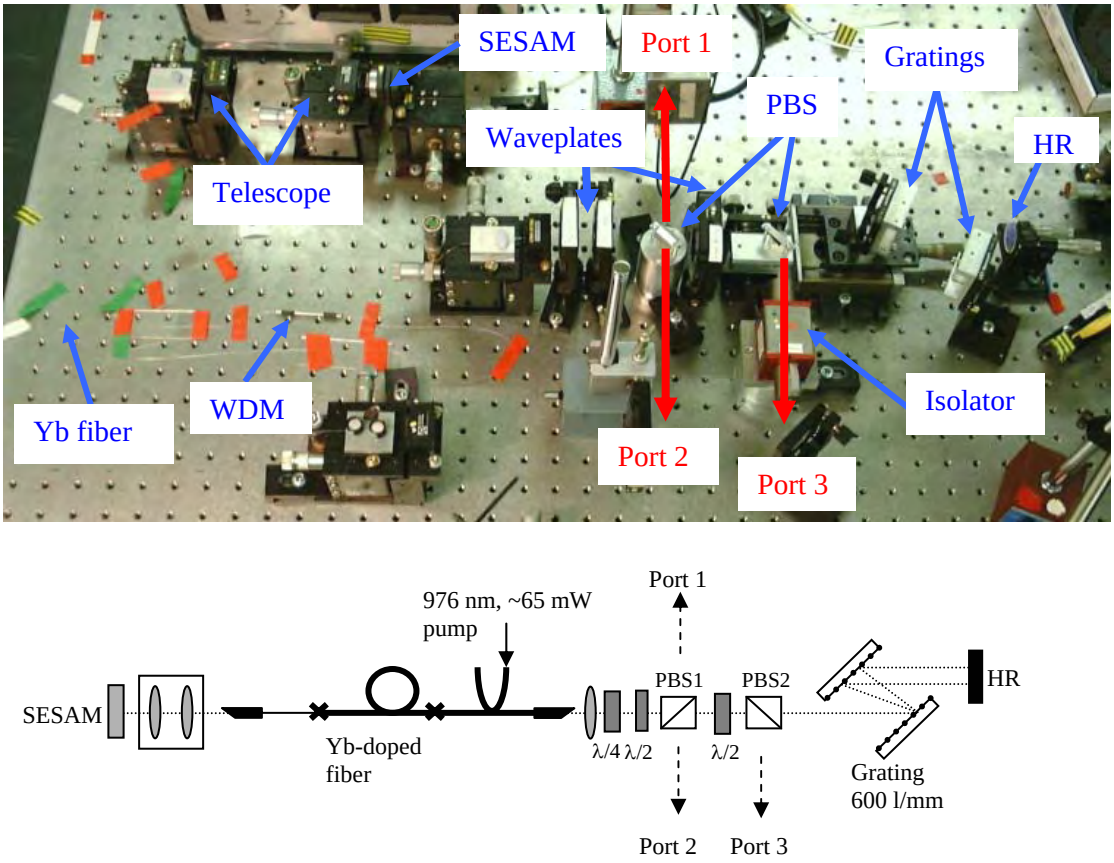

Fig. 4.1 Experimental configuration (photograph and schematic). PBS, polarising beam splitter; HR, high reflectivity mirror.

We obtained successful mode locking with both a prism-based and grating-based DDL [16], but the prism separation was > 1 m, so we finally adopted the more compact grating based design. The DDL comprised a 600 lines/mm diffraction grating pair, with the beam incident at a 30-degree angle with respect to the grating normal.

4.4 Characteristics of the Yb doped fiber

The requirements for the Yb-doped fiber are that it should be single mode, should efficiently absorb the 975 nm pump, and provide sufficient round trip gain and should have broad gain-bandwidth (for ultrashort pulses). The 3rd order dispersion, unlike the 2nd order dispersion, is increased rather than compensated by the diffraction grating based DDL; therefore, to minimise pulse-distorting effects, we needed to minimise the length of active fiber within the cavity. In order to minimise the length of fiber required for efficient pump-absorption, we used high concentration (2,300 parts in 10^6 by weight) Yb-doped silica fiber (NA 0.21; cutoff ~940 nm) pumped at 976 nm (close to the Yb^{3+} absorption maximum at 975 nm). The fiber length used for all the results presented below was ~1m. The total length of fiber in the cavity, including the WDM, was 1.46 m, and the second and 3rd order dispersion of the 1.46 m length of fiber were estimated to be 5.1 x 10^4 fs^2 and 2.9 x 10^4 fs^3, respectively at 1056 nm.

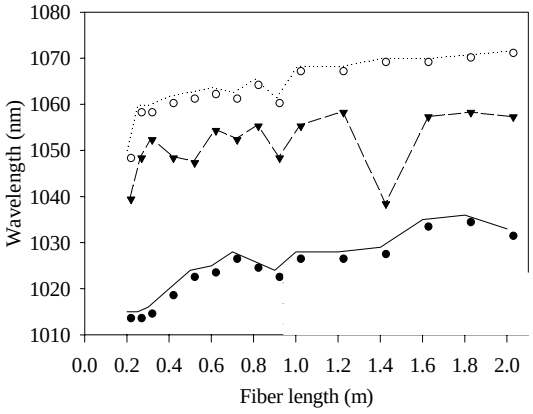

Fig. 4.2 Maximum (open circles) and minimum (closed circles) lasing wavelengths vs. length of Yb-fiber (linear cavity with grating for wavelength tuning). The centre curve (closed triangles) shows the wavelength at which the laser gave maximum output power.

To assess the minimum fiber length that would support a broad gain bandwidth, we tested the wavelength tuning range of a CW laser as a function of fiber length using a Fabry-Perot cavity with a 4% flat cleave reflection at one end and a lens coupling the beam onto a diffraction grating (mounted on a rotation stage) at the other end. By rotating the grating, we were able to tune the lasing wavelength. We found that the laser wavelength would reliably tune to 1064nm for Yb-doped fiber lengths as short as 40 cm. For a fiber length of 40 cm, the slope efficiency

was 56% and the threshold pump power was 40 mW. Fig. 4.2. shows the minimum and maximum lasing wavelengths as the length of Yb-doped fiber is varied from 20 cm to 2 m. The fiber is doped with ~1,500 ppm Yb^{3+} ions, NA ~ 0.18, cut-off wavelength ~ 940 nm (calculated). In our mode-locked laser cavity, we use ~1.0 m of Yb-doped fiber, which gives excellent laser performance.

4.5 Characteristics of the WDM and birefringence of cavity fiber

There are two passive fiber components in the laser cavity: the WDM (used to couple the pump into the cavity), and boron doped fiber (used in one of the angle polished ends). This section shows the measured characteristics of those components as relevant to the laser.

The requirements for the WDM are that it should be low loss around 1055 nm, and that it should have good pump coupling into the cavity at 976 nm. At wavelengths that strongly couple across the WDM ports i.e. out of the laser cavity, there will be a high cavity loss. This wavelength dependent filter could narrow the oscillator bandwidth, so the WDM should have as broad a bandwidth as possible around the 1055 nm central wavelength. Fig. 4.3. shows the reasonably flat transmission from 1020 – 1060 nm, and the efficient out-coupling (for the pump) around 980nm.

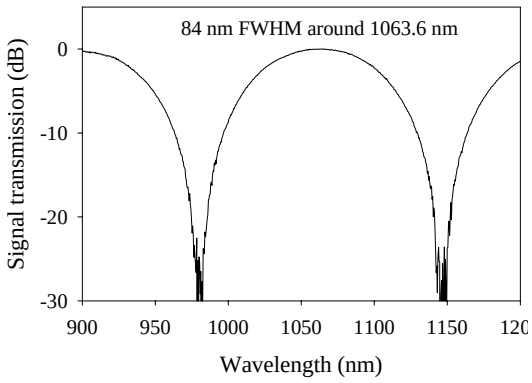

Fig. 4.3 WDM transmission vs. wavelength

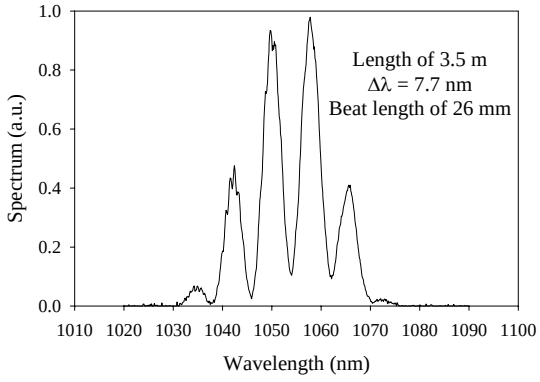

Fig. 4.4 Spectrum from oscillator after passing through a polariser, then the Boron doped fiber, then another polariser.

The fiber for the polished ends should be single mode and low loss. Although we could have polished the WDM and Yb-doped fiber ends directly (avoids splicing), we initially found it more convenient (easier to change fiber lengths) to make separate polished ends, and we used Boron doped fiber for this because it was readily available since it was used to make the fiber gratings for the project, and it was also single mode at 1 μm. We observed that when using the boron fiber the oscillator self-started more reliably, so we characterised the fiber. By launching polarised light from the oscillator and measuring the transmitted intensity viewed through an

analyser polariser, (Fig. 4.4.) the fiber birefringence beatlength was measured to be 2.6 cm i.e. significantly shorter than the 29.7 cm beatlength of the Yb-doped fiber (measured at a wavelength of 1510 nm). We believe that the strong birefringence of the Boron fiber may assist the nonlinear polarisation rotation switching since it provides more strongly defined fast and slow axes for the orthogonal polarisation modes.

4.6 Characteristics of the SESAM

To reduce the self-start threshold power, we incorporated a SESAM to initiate pulsed operation [3]. The SESAM modulation depth has conflicting design requirements with regard to avoiding Q-switching whilst providing sufficient modulation depth for our high loss cavity. The tendency for SESAM induced Q-switched mode locking (laser output consists of mode locked pulses underneath a Q-switched envelope) is avoided if the intracavity pulse energy exceeds a critical value E_p, described by following expression (derived by Professor Ursula Keller's group at ETH in Zurich) [18],

$$E_p = \left(F_{sat,L} A_{eff,L} F_{sat,A} A_{eff,A} \Delta R\right)^{1/2}$$

where $F_{sat,L} = h\nu / \left[2\left(\sigma_{em} + \sigma_{abs}\right)\right]$ is the gain saturation fluence ($h\nu =$ photon energy), $F_{sat,A}$ is the SESAM saturation fluence, and $A_{eff,L}$ and $A_{eff,A}$ are the effective laser mode areas in the gain medium and on the SESAM, respectively and ΔR is the modulation depth Therefore, the critical energy to obtain CW-mode-locking increases with increasing modulation depth. In contrast, we require a high modulation depth to provide a sufficient perturbation in our high loss cavity.

It was not obvious which SESAM modulation depth would be the best for initiating robust self start mode-locking with single pulse in the cavity. Professor Keller was therefore kind enough to lend us a selection of eleven SESAMs with different modulation depths and recovery times to test within our cavity. The SESAMs were of the low finesse antiresonant Fabry Perot type (AFPSA) [3, 19] as typically used in ultrashort pulse sources (see Appendix II for a description of the SESAM design and operation). Before deciding which SESAM to use, we characterised the performance of the entire range of SESAMs as described in Appendix II. The SESAM finally chosen was sample Z367. Whilst the pulse energy in the cavity is largely controlled by the peak power necessary for the nonlinear polarisation rotation switching, the fluence incident on the SESAM also depends on the spot size of the incident beam, which can be optimised by using a telescope with appropriate focal length lenses. We experimented with 1:1 focusing and directly butting the fiber end to the SESAM, but obtained the most reliable Q-

switch free operation and robust self-starting using a telescope to reduce the spot size on the SESAM (f=11mm lens nearest to the fiber, and f=6mm lens nearest to the SESAM).

The SESAM (Z367) found to give optimal operation of the oscillator had similar construction to SESAM Z273, and the oscillator had almost identical performance with these two SESAMs. We therefore believe that the characteristics of the two SESAMs were very closely matched. Full characterisation of the SESAM parameters required returning the device to Professor Keller's group, and in order to enable us to continue research using Z367 without interruption, we therefore decided to send SESAM Z273 for characterisation. For Z273, the modulation depth vs. wavelength, and the saturation fluence required for bleaching are shown in Fig. 4.5. The slow time constant is ~3ps, the fast time constant is ~100fs, and the modulation in reflectivity is ~16%.

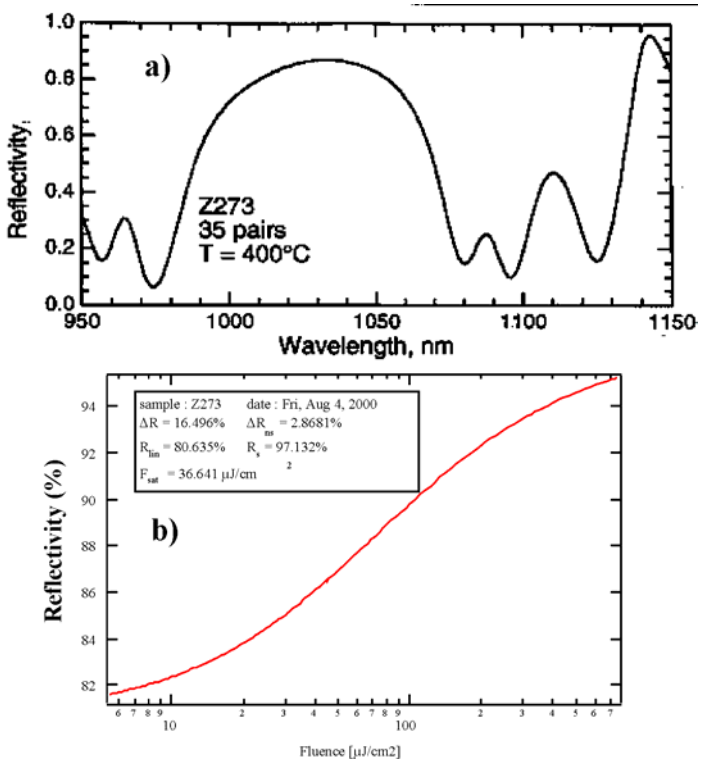

Fig. 4.5 SESAM reflectivity: a) Spectral response. b) As a function of incident intensity. (Figures provided by Professor U. Keller, ETH, Zurich.)

4.7 Laser performance

The laser performance was characterised in the spectral domain using an optical spectrum analyser, and in the temporal domain using a non-collinear second harmonic generation autocorrelator. We also present RF spectra which gives information about the amplitude noise and timing jitter of the laser.

The dispersion of the DDL was adjusted by varying the grating separation, and we investigated the laser performance with various grating separations. Highly stable operation was achieved with a grating separation of 5.4 cm, corresponding to 2nd and 3rd order dispersion (double pass) of –8.3 x 10^4 fs^2, and 1.5 x10^5 fs^3 respectively. The total 2nd and 3rd order dispersion in the cavity, including a double pass of the 1.46 m of fiber and the DDL set with the optimum grating separation of 5.4 cm, were estimated to be 1.9 x10^4 fs^2 and 2.1 x10^5 fs^3, respectively at 1056 nm, which corresponds to a small, net normal group velocity dispersion, typical for stretched-pulse cavities [12]. With suitable adjustment of the wave plates, and at increased pump powers, the oscillator would also mode-lock with either larger grating separation (soliton regime), or with smaller grating separation (substantial net normal dispersion). The soliton regime was characterised by stable mode-locking, but often with multiple pulses circulating in the cavity. With substantial net normal dispersion, mode-locked operation was typically more difficult to initiate and was less stable. Reliable and stable, self-start, stretched-pulse mode-locking was observed for pump powers as low as 62 mW. The maximum average output power of the laser was 3 mW (~60 pJ pulse energy). We note that there was almost no hysteresis for the range of pump powers below the self-start threshold for which mode-locking could be maintained. At lower pump powers Q-switched mode-locking and CW operation were observed.

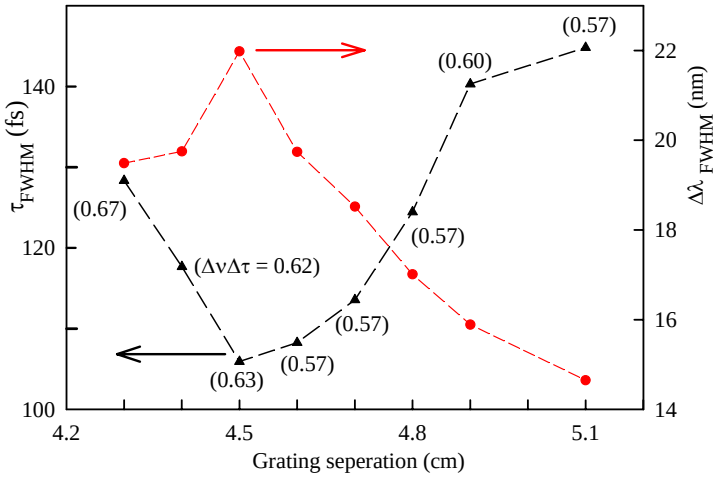

Fig. 4.6 Variation of laser performance with net cavity dispersion. (See text for details.)

The laser has been in constant use, so we have not had the opportunity to characterise its performance in detail with varying grating separation i.e. varying net dispersion. Instead, we have characterised the performance of a "clone" cavity, but which uses a total fiber length of 1.15 m (WDM = 30 cm, boron fiber = 10 cm, Yb-doped fiber =75 cm), which is slightly shorter than the 1.46 m of fiber in the original cavity. The development and characterisation of the clone oscillator was performed jointly with Andy Piper, a graduate student in Professor

Richardson's group. The measured bandwidth, compressed pulse duration (externally compressed from Port 2 using single mode fiber), and time-bandwidth product are shown in Fig. 4.6. Scaling the optimised grating separation of 4.5 cm used in the clone cavity according to the ratio of the fiber lengths in each cavity (1.15m:1.46m) suggests that the optimum grating separation of the working cavity should be 5.7 cm, which is close to the 5.4 cm actually used.

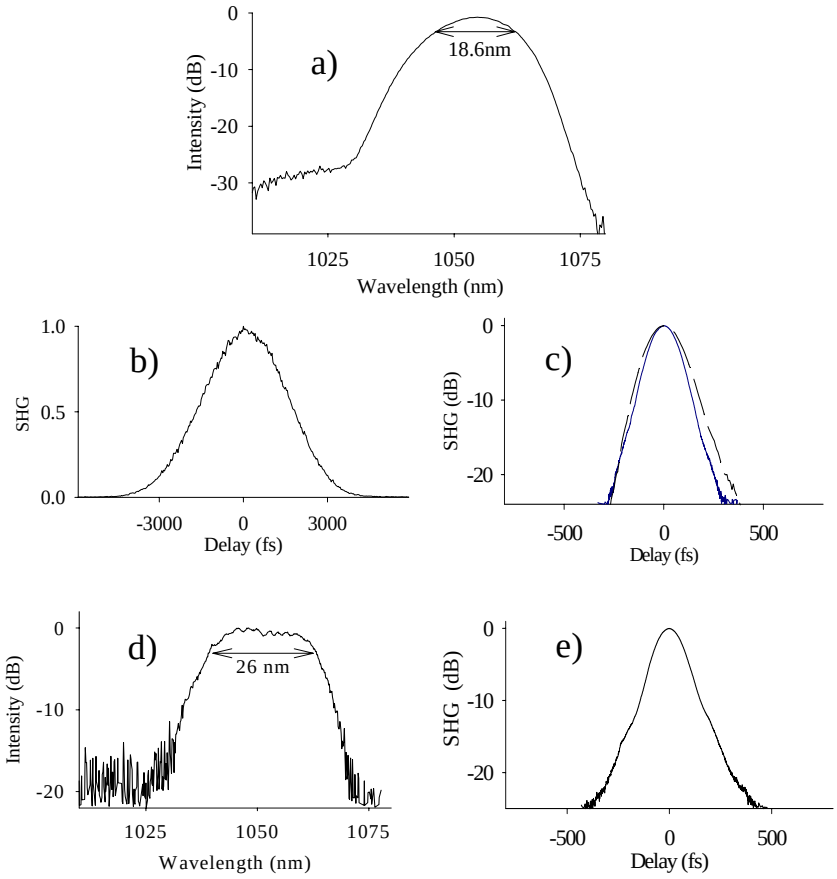

Fig. 4.7 a) Spectrum of pulses extracted from Port 2 or Port 3; b) Autocorrelation of uncompressed pulses from Port 3 (FWHM 2.4 ps); c) Autocorrelation of compressed pulses from Port 2 (dashed line; FWHM 136 fs), and Port 3 (solid line; FWHM 108 fs); d) Spectrum of pulses extracted from Port 1 (rejected by polarisation switch); e) Autocorrelation of compressed pulses from Port 1 (rejected by polarisation switch; FWHM ~110 fs).

The output pulse spectrum from Ports 2 and 3 of the laser is shown in Fig. 4.7.a). The spectrum is centred at 1056 nm, and the spectral bandwidth is 18.6 nm. Fig. 4.7.b) shows the autocorrelation of the uncompressed pulses directly from Port 3 (measured to be similar at output Ports 1 and 2). The output pulses have a strong temporal chirp, and the pulse duration was measured using SHG autocorrelation to be ~2.4 ps. To compress the pulses from Port 3 by elimination of the positive temporal chirp, we used a diffraction grating pair and recorded the autocorrelation duration to optimise the compressor grating separation. To compress the pulses from Port 2 by elimination of the negative temporal chirp, we coupled the pulses into varying lengths of normally dispersive fiber.

The dashed and solid lines in Fig. 4.7.c) show the autocorrelation of the compressed pulses from Ports 2 and 3, respectively. The shortest pulses have an estimated FWHM of 108 fs (assuming a Gaussian pulse shape) indicating a compression factor of order 20. The corresponding time bandwidth product of the compressed pulses is ~0.54, typical for a stretched-pulse laser. By comparison, the time bandwidth product for a transform-limited Gaussian pulse is 0.44. Both the autocorrelation and spectrum are seen to be extremely clean over the available dynamic range of the measurement equipment.

We used an external diffraction grating pair to demonstrate that the pulses rejected from Port 1 of our laser were also compressible. The spectrum of these pulses is shown in Fig. 4.7.d); and the compressed pulse autocorrelation is shown in Fig. 4.7.e). The spectrum is slightly less smooth compared to the circulating pulses, but the compressed pulses are seen to be of a similar quality (FWHM ~110 fs). Following Tamura's earlier work [20], we may therefore be able to eliminate other outputs in order to extract higher power (and still short) rejected pulses at Port 1, or to reduce even further the pump power required for self-start mode-locking. To produce higher powers, we used Port 2 of the oscillator as a seed for amplification (see Chapters 3, 5, 7, 8), and only used Port 1 (rejected output) to trigger the pulse selector and the time gating between amplifier stages. We also note that the grating pair passes the first-order diffracted beam, which leaves the zero order beam available as a monitor port or as an additional output.

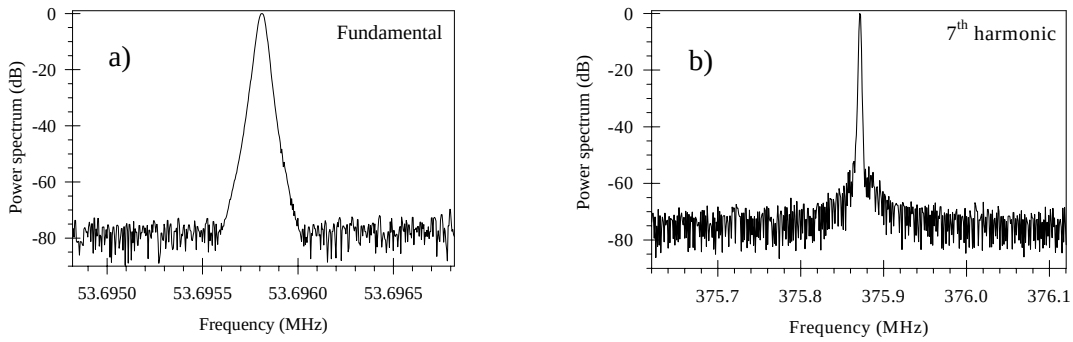

Fig. 4.8 RF spectra: a): At the cavity round trip frequency highlighting the low amplitude noise of the laser. b): Seventh harmonic, used to calculate the timing jitter.

Fig. 4.8. shows the RF spectrum at the cavity's fundamental frequency (53.7 MHz) measured by directing the laser output onto a low noise detector (~3 GHz bandwidth), and analysing the pulse intensity signal [21] with an RF spectrum analyser (Marconi Instruments model no. 2382). The resolution bandwidth for the scan shown in Fig. 4.8(a) was 10Hz (span 2 kHz), which highlights the low amplitude noise of the laser (calculated to be ~0.05%). From the pedestal on the 7^{th} harmonic peak (Fig. 4.8(b), resolution bandwidth 1 kHz) we calculate the time jitter of the pulses to be ~2ps. The method for calculating the amplitude noise and the time

jitter are explained in Appendix I [21]. We note that no effort has been made to stabilise the laser against external environmental changes. However, our daily startup procedure has not required adjustment of the intra-cavity wave plates provided that the laboratory air conditioning maintained similar ambient temperature, and we envisage that enclosing the cavity in a temperature controlled housing, would lead to adjustment-free operation.

If the pump power is high, then there is sufficient gain that the energy of the pulse exceeds the threshold for breaking into multiple pulses (a common feature in soliton lasers). Fig. 4.9. shows that the threshold launched pump power is >60 mW and that multiple pulses are observed for launched pump powers >80 mW.

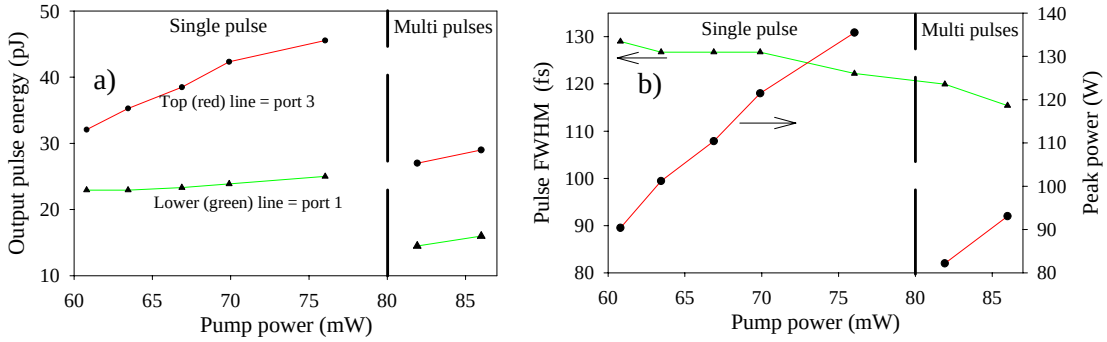

Fig. 4.9 Single and multi-pulsing regimes: a) output energy, b) pulse width and peak power.

4.8 Conclusion

In conclusion, we have developed a practical and stable stretched pulse laser operating at 1.06 µm based on Yb-doped silica fiber. The Fabry-Perot cavity incorporates a SESAM to initiate self-start mode-locking, a diffraction grating based dispersive delay line for dispersion compensation, and is pumped with a grating-stabilised telecommunications-qualified single-mode laser-diode. Highly reliable and stable, stretched-pulse mode locking (employing nonlinear polarisation evolution) could be achieved for pump powers as low as 62 mW. The maximum average output power of the laser in this instance was 3 mW, at a repetition rate of 53.7 MHz, corresponding to ~60 pJ pulse energy. The pulses are demonstrated to have a smooth spectrum, are compressible externally to 108 fs (assuming a Gaussian pulse profile) and have minimal amplitude jitter (~0.05%).

The setup is based on bulk optical components and XYZ adjustment stages, but in future it may be possible to use GRIN lenses directly butted to the fiber ends, and holey fiber instead of bulk diffraction gratings for dispersion compensation so as to greatly simplify the cavity set-up. We also note that the pulse width was not limited by the Yb^{3+} gain bandwidth, which has been demonstrated to support at least 65fs pulses experimentally [16] and ~30 fs theoretically. We

did not seek to obtain shorter pulses from our cavity, but would consider that this should have been possible with further optimisation of fiber length and overall dispersion compensation.

We believe that laser will prove useful for a wide range of future applications; indeed it has already provided useful service in a range of projects at the ORC [22-29]. The laser has now been commercialised by our industrial sponsor, and at least one unit is in use with a customer.

References

1. R. L. Fork, C. H. B. Cruz, P. C. Becker and C. V. Shank, "Compression of Optical Pulses to 6 femtoseconds by Using Cubic Phase Compensation," Optics Letters **12,** 483-485 (1987).
2. M. Hofer, M. H. Ober, F. Haberl and M. E. Fermann, "Characterization of Ultrashort Pulse Formation in Passively Mode-Locked Fiber Lasers," IEEE Journal of Quantum Electronics **28,** 720-728 (1992).
3. U. Keller, K. J. Weingarten, F. X. Kartner, D. Kopf, B. Braun, I. D. Jung, R. Fluck, C. Honninger, N. Matuschek and J. A. derAu, "Semiconductor saturable absorber mirrors (SESAM's) for femtosecond to nanosecond pulse generation in solid-state lasers," IEEE Journal of Selected Topics in Quantum Electronics **2,** 435-453 (1996).
4. E. Yoshida, Y. Kimura and M. Nakazawa, "Laser Diode-Pumped Femtosecond Erbium-Doped Fiber Laser with a Sub-Ring Cavity for Repetition Rate Control," Applied Physics Letters **60,** 932-934 (1992).
5. D. J. Richardson, R. I. Laming, D. N. Payne, M. W. Phillips and V. J. Matsas, "320 fs Soliton Generation with Passively Mode-Locked Erbium Fiber Laser," Electronics Letters **27,** 730-732 (1991).
6. I. N. Duling, "Subpicosecond All-Fiber Erbium Laser," Electronics Letters **27,** 544-545 (1991).
7. K. Tamura, H. A. Haus and E. P. Ippen, "Self-Starting Additive Pulse Mode-Locked Erbium Fiber Ring Laser," Electronics Letters **28,** 2226-2228 (1992).
8. D. U. Noske, N. Pandit and J. R. Taylor, "Subpicosecond Soliton Pulse Formation from Self-Mode-Locked Erbium Fiber Laser Using Intensity Dependent Polarization Rotation," Electronics Letters **28,** 2185-2186 (1992).
9. V. J. Matsas, T. P. Newson, D. J. Richardson and D. N. Payne, "Self-Starting Passively Mode-Locked Fiber Ring Soliton Laser Exploiting Nonlinear Polarization Rotation," Electronics Letters **28,** 1391-1393 (1992).
10. C. J. Chen, P. K. A. Wai and C. R. Menyuk, "Soliton Fiber Ring Laser," Optics Letters **17,** 417-419 (1992).
11. K. Tamura, L. E. Nelson, H. A. Haus and E. P. Ippen, "Soliton Versus Nonsoliton Operation of Fiber Ring Lasers," Applied Physics Letters **64,** 149-151 (1994).
12. K. Tamura, E. P. Ippen, H. A. Haus and L. E. Nelson, "77-fs Pulse Generation from a Stretched-Pulse Mode-Locked All- Fiber Ring Laser," Optics Letters **18,** 1080-1082 (1993).
13. H. A. Haus, K. Tamura, L. E. Nelson and E. P. Ippen, "Stretched-Pulse Additive-Pulse Mode-Locking in Fiber Ring Lasers - Theory and Experiment," IEEE Journal of Quantum Electronics **31,** 591-598 (1995).
14. M. H. Ober, M. Hofer, U. Keller and T. H. Chiu, "Self-Starting Diode-Pumped Femtosecond Nd Fiber Laser," Optics Letters **18,** 1532-1534 (1993).
15. H. A. Haus and E. P. Ippen, "Self-Starting of Passively Mode-Locked Lasers," Optics Letters **16,** 1331-1333 (1991).
16. V. Cautaerts, D. J. Richardson, R. Paschotta and D. C. Hanna, "Stretched pulse Yb^{3+} silica fiber laser," Optics Letters **22,** 316-318 (1997).
17. F. Krausz and T. Brabec, "Passive-Mode Locking in Standing-Wave Laser Resonators," Optics Letters **18,** 888-890 (1993).
18. C. Honninger, R. Paschotta, M. Graf, F. Morier-Genoud, G. Zhang, M. Moser, S. Biswal, J. Nees, A. Braun, G. A. Mourou, I. Johannsen, A. Giesen, W. Seeber and U. Keller, "Ultrafast ytterbium-doped bulk lasers and laser amplifiers," Applied Physics B-Lasers and Optics **69,** 3-17 (1999).

19. C. Honninger, F. Morier-Genoud, M. Moser, U. Keller, L. R. Brovelli and C. Harder, "Efficient and tunable diode-pumped femtosecond Yb : glass lasers," Optics Letters **23,** 126-128 (1998).

20. K. Tamura, C. R. Doerr, L. E. Nelson, H. A. Haus and E. P. Ippen, "Technique for Obtaining High-Energy Ultrashort Pulses from an Additive-Pulse Mode-Locked Erbium-Doped Fiber Ring Laser," Optics Letters **19,** 46-48 (1994).

21. D. Von der linde, "Characterization of the Noise in Continuously Operating Mode-Locked Lasers," Applied Physics B-Photophysics and Laser Chemistry **39,** 201-217 (1986).

22. J. H. V. Price, K. Furusawa, T. M. Monro, L. Lefort and D. J. Richardson, "Tunable, femtosecond pulse source operating in the range 1.06- 1.33 microns based on an Yb^{3+}-doped holey fiber amplifier," Journal of the Optical Society of America B-Optical Physics **19,** 1286-1294 (2002).

23. J. H. V. Price, W. Belardi, T. M. Monro, A. Malinowski, A. Piper and D. J. Richardson, "Soliton transmission and supercontinuum generation in holey fiber, using a diode pumped Ytterbium fiber source," Optics Express **10,** 382-387 (2002).

24. J. H. Price, L. Lefort, D. J. Richardson, G. J. Spuhler, R. Paschotta, U. Keller, C. Barty, A. Fry and J. Weston, "A practical, low noise, stretched pulse Yb^{3+}-doped fiber laser," Conference on Lasers and Electro-Optics (CLEO 2001), paper CTuQ6 (2001).

25. J. H. Price, K. Furusawa, T. M. Monro, C. Netti, A. Malinowski, J. J. Baumberg and D. J. Richardson, "Phase matched UV Generation in a silica holey fiber," Conference on Lasers and Electro Optics (CLEO), Vol. 73 of OSA Trends in Optics and Photonics Series (Optical Society of America, Washington, D.C., 2002) paper CTuB5 (2002).

26. J. H. Price, K. Furusawa, T. M. Monro, L. Lefort and D. J. Richardson, "A tuneable, femtosecond pulse source operating in the range 1.06-1.33 microns based on an Yb doped holey fiber amplifier," Conference on Lasers and Electro Optics (CLEO), Vol. 56 of OSA Trends in Optics and Photonics Series (Optical Society of America, Washington, D.C., 2001) paper CPD1 (2001).

27. J. H. Price, W. Belardi, L. Lefort, T. M. Monro and D. J. Richardson, "Nonlinear pulse compression, dispersion compensation, and soliton propagation in holey fiber at 1 micron," Nonlinear Guided Waves and Their Applications (NLGW 2001), paper WB1-2 (2001).

28. M. V. O'Connor, M. A. Watson, D. C. Hanna, D. P. Shepherd, L. Lefort, J. H. V. Price, A. Malinowski, J. Nilsson, N. G. Broderick and D. J. Richardson, "Fibre-laser pumped femtosecond PPLN OPO," *Quantum Electronics and Photonics 15 (QEP 15), Glasgow, September 3-6, pp139*, Institute of Physics, (2001).

29. L. Lefort, J. H. Price, D. J. Richardson, G. J. Spuhler, R. Paschotta, U. Keller, A. Fry and J. Weston, "Practical Low-Noise stretched-pulse Yb-doped fiber laser," Optics Letters **27,** 291-293 (2002).

Chapter 5 CPA Stretcher and compressor

5.1 Introduction

An important aspect of our industrially funded CPA system, which differs from previously published fiber CPA work, is the use of a compact bulk-grating based compressor, and a matched chirped fiber Bragg grating stretcher. The compact compressor design results in significant 3rd order dispersion, which must be compensated by the pulse stretcher if high quality <500 fs final recompressed pulses are to be obtained. This chapter describes our work to design an efficient pulse compressor, and a CFBG stretcher with matching 2nd and 3rd order dispersion.

CPA is a technique widely used with high power solid-state laser systems in which a short, transform-limited optical pulse is first chirped to stretch the pulse duration, then amplified to a high energy, then recompressed to the initial duration by a device of opposite dispersion to the pulse stretcher. This technique avoids high peak intensity in the amplifiers, and hence avoids the limiting effects of nonlinearity (SPM, SRS, and self-focusing) thus massively extending the peak powers that are attainable from laser systems. Since the effects of the fiber nonlinearity depend on the peak intensity, the design criteria for the stretcher/compressor is for as long a stretched pulse duration as possible, within the constraints created by the dimensions of the selected pulse stretcher and compressor components.

Pulse stretching and compression are usually performed with bulk optic devices such as a diffraction grating pair, e.g. Galvanauskas et al. demonstrated an Yb-fiber CPA that produced 380 fs pulses with energies of 1.2 mJ [1] using bulk gratings for both stretcher and compressor. However, obtaining the required temporal stretching factors requires grating separations of the order of 1 m, which make such systems large and cumbersome. CFBGs are highly dispersive and can provide suitable time delays in only centimetre lengths of fiber. Indeed, Neil Broderick et al. at the ORC have demonstrated 4 ps pulses with energy of 0.9 μJ using CFBG stretcher and compressor gratings in an all Er-doped fiber CPA system based on LMA fiber components [2]. The principal limit on the use of CFBGs is that due to the high peak power in the compressor, the nonlinearity of the grating fiber degrades the pulse quality. In our system, the target final (recompressed) pulses with energy of 50 μJ and duration of 500 fs would have a peak power of ~100 MW and therefore a bulk-grating based compressor is required. However, it is still

possible to use a CFBG stretcher. Both GDD and 3rd order dispersion of a bulk-grating compressor are proportional to the grating separation. Therefore, using a long (~0.3 ns) stretched pulse duration that requires large GDD, also adds large 3rd order dispersion. For recompressed pulse durations <500 fs, uncompensated 3rd order dispersion would result in a significant pedestal on the recompressed pulse. CFBGs incorporating both 2nd and 3rd order dispersion compensation have not previously been reported at 1 μm, but using the uniquely flexible CFBG writing technology developed at the ORC [3] has enabled us to fabricate a CFBG with both the correct 2nd and 3rd order dispersion to compensate for the bulk-grating compressor. Using this CFBG technology should provide a robust, compact, and alignment-free pulse stretcher for use in future systems. The development of this CFBG pulse stretcher is presented in this chapter. Due to the flexibility of the CFBG writing process, we first optimised the compressor design for the grating specified by our industrial sponsor, then designed the CFBG stretcher to have the required (mirror) dispersion profile.

This chapter is organised as follows. Section 5.2 illustrates the effect of uncompensated 3rd order dispersion on pulses with bandwidths corresponding to transform limited durations of 500 fs and 200 fs. In Section 5.3, we describe the design of the bulk grating compressor. In Section 5.4 we describe the design and development of the CFBG stretcher. Then in Section 5.5 we present our conclusions.

5.2 Effect of uncompensated third order dispersion

As described above, the high peak powers of the recompressed pulses from the CPA system require a bulk grating based pulse compressor, which inherently introduces 3rd order dispersion in proportion to the 2nd order dispersion (both are proportional to the diffraction grating separation). To illustrate the effect of uncompensated 3rd order dispersion, we have calculated (formula from Agrawal [4]) the effects of uncompensated 3rd order dispersion on Gaussian pulses with bandwidths of 7.5 nm and 3 nm, which correspond to transform-limited FWHM pulse durations of 200 fs and 500 fs at a wavelength of 1 μm. We considered two values of uncompensated 3rd order dispersion: $dD/d\lambda$ x Length = 1.5 ps/nm^2, and $dD/d\lambda$ x Length = 0.5 ps/nm^2 (i.e. one third of the value of the first case). The larger value of 3rd order dispersion corresponds to that introduced by the grating compressor design described in Section 5.3. The smaller value of 3rd order dispersion corresponds to the maximum that can be fabricated into a CFBG that has both the 2nd order dispersion of the compressor, and also has sufficient spectral window (15 nm) to support 300 fs recompressed pulses (see Section 5.4.3 for more details about this constraint).

The results of our calculations are shown in Fig. 5.1. For each case we have shown the pulse intensity on a linear scale, and the SHG autocorrelation on both a linear and a dB scale. The results show that the distortion from the uncompensated 3rd order dispersion of our compressor would be very severe for a 200fs pulse, but less severe for a 500fs pulse. The FWHM of the SHG autocorrelations in Fig. 5.1 b) and e), for increasing 3rd order dispersion (0, 0.5, 1.5 ps/nm^2), are 283 fs, 1.25 ps, 2.30 ps, for the 200 fs pulse, and 707 fs, 1.05 ps, 1.65 ps for the 500 fs pulse. However, the autocorrelation shape, particularly on a dB scale, gives a clearer measure of the pulse quality than the FWHM data because the shape demonstrates how uncompensated 3rd order dispersion results in an increasing fraction of the energy in a broad pedestal. We concluded from these calculations that to obtain clean pulses with durations below ~500 fs would require compensation of the 3rd order dispersion of the compressor. However, for much longer recompressed durations e.g. 1 ps (bandwidth ~1.5 nm) the distortion caused by the 3rd order dispersion of the compressor would be less significant, and compensation may then be unnecessary.

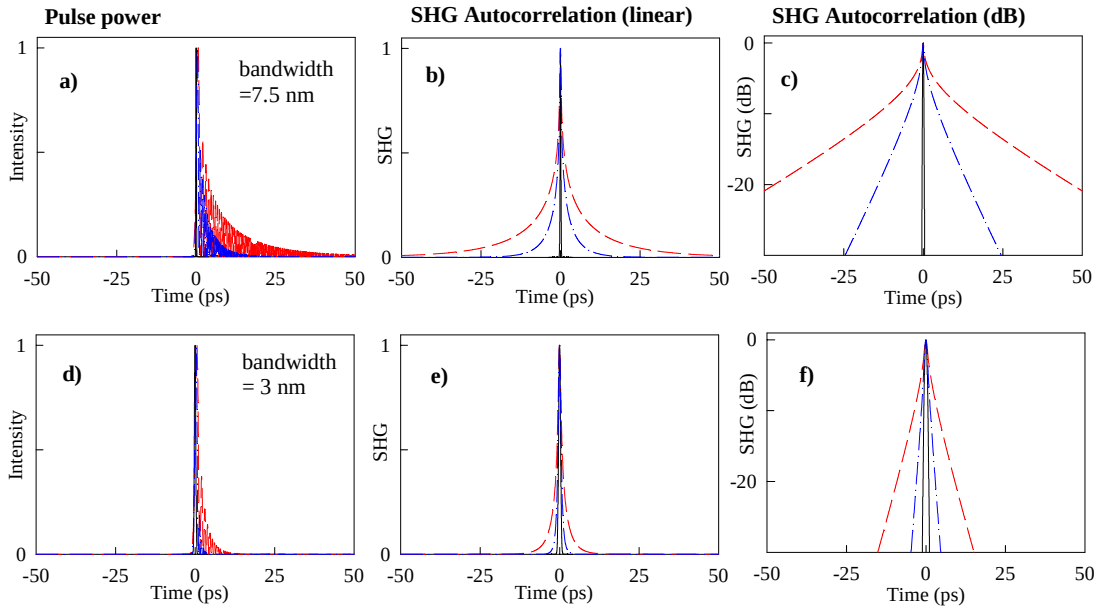

Fig. 5.1. Effect of uncompensated 3rd order dispersion on Gaussian pulse. a)-c) 200 fs pulse (7.5 nm transform limited bandwidth); d)-f) 500 fs pulse (3 nm transform limited bandwidth). Black line: transform limited pulse. Red line: 3rd order dispersion corresponding to that of bulk grating compressor. Blue line: 3rd order dispersion corresponding to ~1/3 that of the bulk grating compressor.

5.3 Bulk grating compressor

This section describes the experimental setup and the dispersion design of the bulk grating compressor used in our CPA system.

5.3.1 Overall layout

The experimental setup of the bulk-grating compressor is shown in the photograph of Fig. 5.2 and the schematic of Fig. 5.3. The photograph shows the path of the beam (outward pass shown in red, return pass shown in blue). Roof mirrors have been used to translate the beam horizontally and vertically to enable just one grating to be used. This setup has the advantage that with the roof mirrors carefully aligned, the grating "pair" is always exactly parallel. The operation of the compressor is perhaps easier to follow on the schematic, where both gratings of the equivalent grating pair are shown explicitly (no horizontal translation roof mirror). The schematic also shows the variable design parameters: the grating separation, and the grating angle. As shown in the upper schematic of Fig. 5.3, a major design constraint is that the spectrum would be clipped by the second grating once the grating pair separation is too large for the given bandwidth (i.e. the pulse spectral width) and the grating dispersion (determined by the grating groove density – lines/mm, and by the angle of incidence). There is some flexibility in designing the dispersion of the compressor because the ratio of 3rd order and 2nd order dispersion changes with grating angle as shown by the lower schematic of Fig. 5.3, and quantitatively in Fig. 5.4.

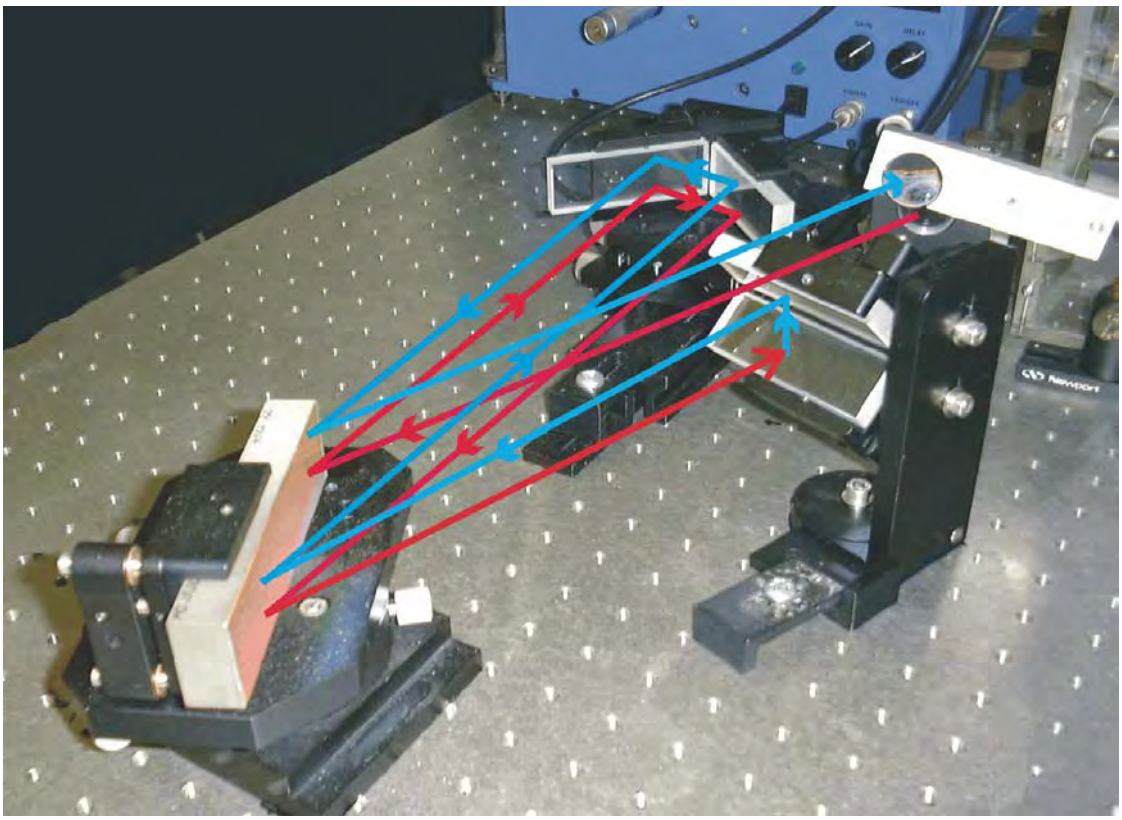

Fig. 5.2 Photograph of compressor.

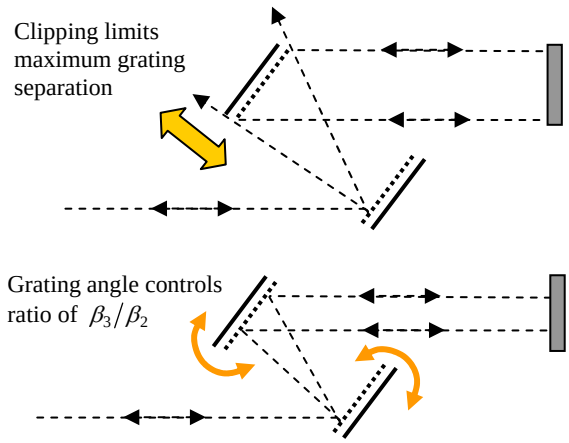

Fig. 5.3. Schematic of compressor.

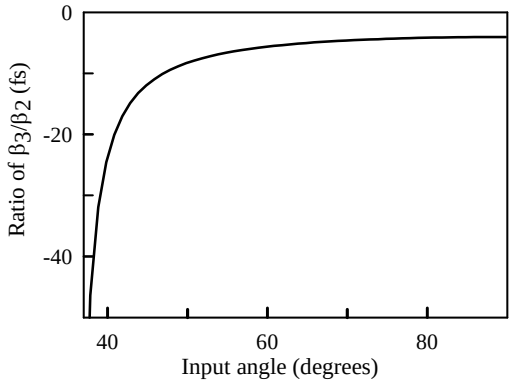

Fig. 5.4. Ratio of β_3/β_2 vs. input angle onto grating.

5.3.2 Details of design and performance

We note that the concept of FWHM bandwidth as applied to pulses is less applicable when discussing gratings, and instead we refer to "spectral window" to distinguish that a particular wavelength either is, or is not, reflected by the grating. For a bulk grating the spectral window is the wavelength range that will be transmitted through the compressor optics without clipping the edges of the grating. For a CFBG, the spectral window is determined by the range of the grating periods written within the core of the fiber. When calculating the minimum (transform limited) temporal pulse duration that would be possible from a grating with a given spectral window, we have assumed a pulse FWHM bandwidth equal to half of the spectral window.

In addition to the agreed overall CPA specifications of <500 fs recompressed pulses, which sets a minimum FWHM bandwidth of >5 nm, our sponsors also specified the bulk-grating to be used for the compressor (a grating used in some of their other CPA systems). We are grateful to Dr. C. Barty (working with our sponsor at the time of this work) for his assistance with the initial compressor design and alignment. Specifying the bulk grating imposes two additional constraints on the compressor deign. First, if at all possible the grating should be used at the angle of incidence for which it is most efficient, which specifies the ratio of (2^{nd} order dispersion)/(3^{rd} order dispersion). Second, the size of the grating (here 10cm) then fixes the stretched pulse duration, because the spectral window is already fixed by the bandwidth required for the recompressed pulse, and this in turn sets the maximum grating separation. The task of designing the compressor first required selection of the spectral window. Then, using the input angle for which the grating is most efficient, we calculated the maximum grating separation in order to avoid clipping. Finally we calculated the resulting 2^{nd} and 3^{rd} order dispersion of the compressor.

The grating provided by our sponsor was holographic, with 1500 gr/mm, sinusoidal groove profile, gold coated, 10 cm wide, and was manufactured by Richardson Grating Laboratory. The beam path through the compressor diffracts off the grating four times, which means that high diffraction efficiency is essential. For example, a diffraction efficiency of 90% leads to an overall compressor transmission of $(0.9)^4 = 0.65$, but decreasing the diffraction efficiency to 80% reduces the compressor transmission by more than a third to $(0.8)^4 = 0.41$. According to the specifications, the grating was expected to have a maximum diffraction efficiency of 89% at 41 degrees angle of incidence to the grating normal at a wavelength of 1 μm. Calculating the grating efficiency vs. angle of incidence is a specialised topic, beyond the scope of this thesis [5, 6]. Instead, we measured the diffraction efficiency as a function of angle of incidence using the light with the input polarisation found experimentally to have the highest throughput, and the results are shown in Table 5.1. The measured diffraction efficiency is high at angles of incidence between 39 degrees and 45 degrees (although our measured efficiencies are somewhat lower than the grating specifications). We conclude that if high transmission is the overriding requirement, then the grating compressor should be operated using a 41 degree angle of incidence.

Both the 2nd order and 3rd order dispersion of the compressor are proportional to the grating separation, but the ratio changes with the angle of incidence. For our grating, the ratio $|\beta_3 / \beta_2|$ has minimum value of 4 fs at 89 degrees angle of incidence, and the proportion of 3rd order dispersion increases rapidly at angles of incidence <45 degrees, as shown in Fig. 5.4. At a 41 degrees angle of incidence the ratio $|\beta_3 / \beta_2|$ is 19 fs. The varying proportion of 3rd order dispersion with angle of incidence makes it possible to compensate for small variations in either 2nd or 3rd order dispersion of the final system, by making small adjustments to the grating angle compared to the initial design. This degree of freedom does not exist with the CFBG stretcher, so it is a useful feature of the compressor. Although small changes in the angle of incidence could be useful for optimising the system, large changes could result in excess loss due to changes in diffraction efficiency with angle of incidence.

Table 5.1 Diffraction efficiency of bulk compressor grating

Angle of incidence (degrees)	Diffraction efficiency (%)
36.5	55
37	68
38.5	74
39	79
41.5	79
44	80
45	78
46.5	75
47	73

We designed the pulse compressor to operate at 41 degree angle of incidence in order to achieve maximum efficiency. We selected the spectral window of 16 nm, being twice the measured 8 nm FWHM bandwidth of the amplified pulses. We then calculated that the maximum grating separation that keeps this 8 nm spectral window from clipping the grating to be 40 cm. For a central wavelength of 1056 nm, the compressor dispersion parameters were then calculated [7] to be: D x Length = 45.5 ps/nm, (GDD = -27×10^6 fs^2/rad); and $dD/d\lambda$ x Length = 1.5 ps/nm^2 (β_3 x Length = 530×10^6 fs^3/rad^2). In calculating this dispersion, we have also included the estimated total dispersion of the fiber amplifiers (D x Length = -0.8 ps/nm, $dD/d\lambda$ x Length = 0.001 ps/nm^2), so the above values are the total system dispersion to be compensated by the CFBG.

For this compressor design, we used a network analyser to measure the phase delay vs. wavelength as illustrated by Fig. 5.5. The phase delay measurements were converted to time delay measurements by noting that at the test frequency of 1 GHz, a phase delay of 2π corresponds to a time delay of 1 ns. The measured time delay vs. wavelength is shown in Fig. 5.5, which also shows the theoretical delay characteristic. The measured response corresponds closely to the design characteristic.

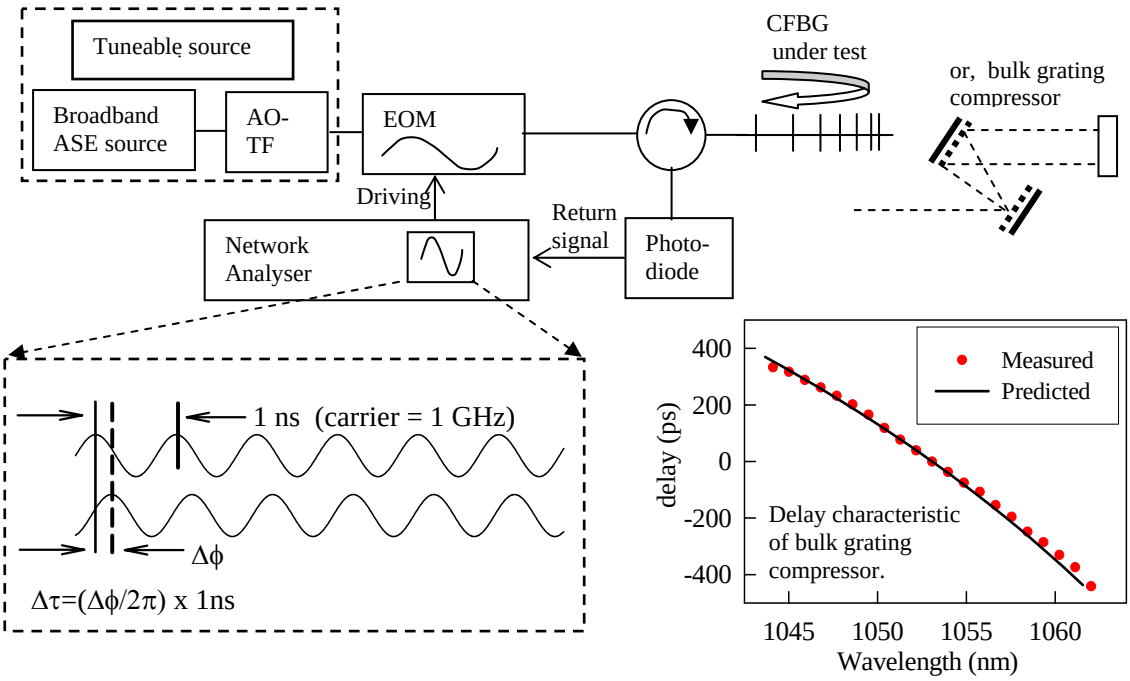

Fig. 5.5. Measurement setup and results showing time delay vs. wavelength for bulk-grating compressor. (AOTF=accousto-optic tuneable filter.)

We note that single mode fiber has been used by other researchers [8] as a simple, low-loss, alternative form of pulse stretcher. However, the 3rd order dispersion of single mode fiber has the same sign as that of the bulk grating compressor, so a fiber stretcher causes additional pulse distortion. Our conclusion that we should compensate for the 3rd order dispersion of the

compressor to obtain clean pulses with duration ~500 fs will apply to these fiber stretchers, but to consider the suitability of fiber stretchers for longer pulses, we calculated the 2nd and 3rd order dispersion to be β_2 = 24x10^6 fs^2/rad.km (D = -40 ps/nm.km); and β_3 = 15 x10^6 fs^3/rad^2.km (dD/dλ = 0.12 ps/nm^2.km), at a wavelength of 1 μm [9]. Hence, for single mode fiber the ratio $|\beta_3 / \beta_2|$=0.6 fs, compared to $|\beta_3 / \beta_2|$ = 19 fs for our grating compressor. The 2nd order dispersion of the stretcher and compressor would be matched, so the ratio $|\beta_3 / \beta_2|$ shows that the uncompensated 3rd order dispersion would be mostly due to the compressor. Our conclusions regarding the suitability of using a single mode fiber stretcher with no 3rd order dispersion compensation would therefore be similar to the above, i.e. that such a system would only be acceptable for use with longer pulses (narrower bandwidth) e.g. ~1 ps (bandwidth ~1.5 nm).

5.4 CFBG stretcher

CFBG fabrication is performed by selectively exposing the core of a germano-silicate fiber (UV sensitive) to intense light pulses from an excimer laser, which creates refractive index variations along the fiber core (typically Δn ~ 10^{-3} –10^{-4}). The reflection from each grating period is weak, but the ability to fabricate several thousand periods can result in extremely strong gratings [3, 10]. In a research environment, the strength of the refractive index variation can be relaxed to the required strength in a controlled way by annealing the grating at the required temperature. (In contrast, for commercial production the exact fabrication parameters would be developed and tested in detail, and then the gratings would be written directly to the required strength followed only by a low temperature bake to outgas the deuterium loaded fiber after writing.)

We are grateful to Morten Ibsen, of the fiber gratings group at the ORC, for his collaboration on this aspect of the CPA project. His research group, with input from Professor Zervas, has developed a uniquely flexible fiber grating fabrication technology and related grating design algorithms, which have allowed the fabrication of gratings with custom designs for 2nd and 3rd order dispersion compensation for telecommunications applications at wavelengths near 1.5 μm [3, 10]. In designing the required CFBG we have assumed, following direction from Morten Ibsen, that gratings with both a broad spectral window and high values of 2nd and 3rd order dispersion could be fabricated. Our contribution to the design process was to calculate the required relative time delay at each wavelength for the bulk grating compressor, and this information was then used by Morten Ibsen to design the appropriate CFBG stretcher.

This section describes the development and testing of a series of CFBGs in order to optimise the performance of the CPA system. As mentioned in the introduction, our goal is to compensate both the 2nd and 3rd order dispersion of the fiber amplifiers and bulk grating

compressor, in order to produce distortion-free compressed pulses at the system output. The first CFBG that we tested had high losses at shorter wavelengths due to "cladding mode losses". The second generation of CFBG was fabricated to control the cladding mode losses by using a reduced grating strength compared to the initial grating. The development process of this second generation CFBG demonstrated that due to the large 3rd order dispersion relative to 2nd order dispersion, practical constraints imposed by the writing process would limit the spectral window of the grating to ~10 nm (corresponding pulse FWHM bandwidth ~5 nm). This limited spectral window would limit the minimum recompressed pulse duration to ~500 fs. I therefore developed a design for a third generation CFBG, with reduced 3rd order dispersion, and which we expect could be fabricated with ~15 nm spectral window (i.e. matched to that of the compressor), to enable ~300 fs recompressed pulses to be produced.

This section is organised as follows. In Section 5.4.1 we present data for the first generation CFBG, and explain our observation of excess loss at short wavelengths. In Section 5.4.2 we present data for the second generation CFBG, which incorporated refinements to control the cladding mode losses and produced ~500 fs recompressed pulses. In Section 5.4.3 we propose a design for a future CFBG that should enable us to obtain ~300 fs recompressed pulses.

5.4.1 Performance of first generation CFBG

Due to the scheduled replacement of the CFBG writing rig during summer/autumn 2000, we decided to perform initial testing with an available CFBG with D x length = 18.5 ps/nm, $dD/d\lambda$ x length = 0.1 ps/nm^2.

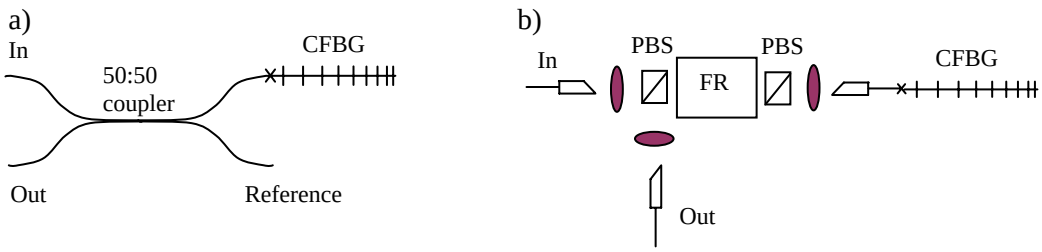

Fig. 5.6. Coupling schemes for CFBG. a) 50:50 coupler; b) Optical circulator. (FR – Faraday Rotator; PBS - Polarising Beam Splitter)

To couple light onto the CFBG, we used a 50:50 fiber coupler as shown in Fig. 5.6 a). The optical circulator arrangement shown in Fig. 5.6 b) is an alternative coupling scheme used in later experiments. The optical circulator requires more components, but it introduces lower coupling losses. Fig. 5.7 shows the reflected spectra measured from both ends of the CFBG using pulses from the mode-locked oscillator described in Chapter 4 as the broadband source. The spectra clearly show strong losses at shorter wavelengths when pulses are incident from the long wavelength (red) end.

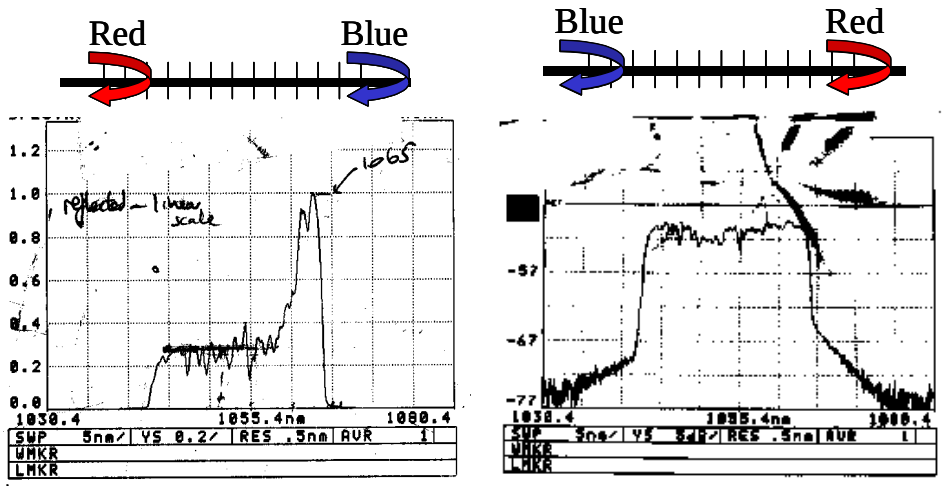

Fig. 5.7. Measured spectral response of initial CFBG

The explanation for the difference in reflected spectra for light incident from the two ends of the grating is that for such broad spectral window CFBGs, power at shorter wavelengths is transferred from the core to cladding modes and is thus lost [11]. Ideally, the CFBG would have only one scattering mechanism – when the grating wave-vector $\vec{k}_G(\nu_o)$ (matched to light of frequency ν_o in the high refractive index core) exactly couples the wave-vectors of the forward and backward propagating core modes

i.e. $\vec{k}_G(\nu_o) = \vec{k}_{backward,core}(\nu_o) - \vec{k}_{forward,core}(\nu_o)$.

However, for a given frequency, the lower index in the cladding means that the mode there has a longer wavelength (shorter wave-vector); so the grating scattering vector, $\vec{k}_G(\nu_o)$, can also couple a forward propagating core mode of slightly higher frequency $(\nu = \nu_o + \Delta\nu)$ (longer wave-vector) to a short wave-vector cladding mode (at the same frequency $\nu = \nu_o + \Delta\nu$), resulting in lost power

i.e. $\vec{k}_G(\nu_o) = \vec{k}_{backward,clad}(\nu_o + \Delta\nu) - \vec{k}_{forward,core}(\nu_o + \Delta\nu)$.

Entering the chirped grating from the low frequency (red) end (high cladding-mode loss), the high frequency (blue) components suffer significant power transfer to cladding modes before they reach the point in the grating where they are efficiently coupled into backward propagating core modes, so they appear to be only weakly reflected. The problem does not occur when entering the grating from the blue end because the blue components are reflected before entering into the portion of the grating with the correct wave-vector for coupling the light into cladding modes. Unfortunately, we must enter from the red end in order to match the dispersion of the bulk-grating compressor. We concluded that it would be necessary to control the cladding mode losses in order to obtain satisfactory performance from the CPA system. In the following section we describe two methods tested in the second generation CFBG to control these losses.

5.4.2 Performance of second generation CFBG

When designing the second generation of CFBG we decided to test two methods of controlling the cladding mode losses. The first method was to design a CFBG with a spectral window much wider than twice the pulse bandwidth, such that the pulse could be reflected from the uniform plateau (Fig. 5.7) caused by cladding mode loss that extends across all except the longest wavelengths. Reflecting the pulse from the spectrally flat plateau leaves the reflected spectrum undistorted and we considered that the additional ~5-10 dB loss may be acceptable. The second method of controlling cladding mode loss was to weaken the CFBG by annealing after writing. A weaker grating scatters less of the shorter-wavelength power to the cladding modes, and could therefore actually increase the reflectivity at shorter wavelengths to give a generally flatter spectral response.

To demonstrate the potential of a wide-spectral window grating design for controlling cladding mode loss, whilst avoiding the much greater fabrication effort required to produce a grating that incorporates large 3rd order dispersion, we initially tested a linearly chirped grating with 30nm spectral window. The reflection and transmission data for this grating are shown in Fig. 5.8 (normalised with respect to input signal).

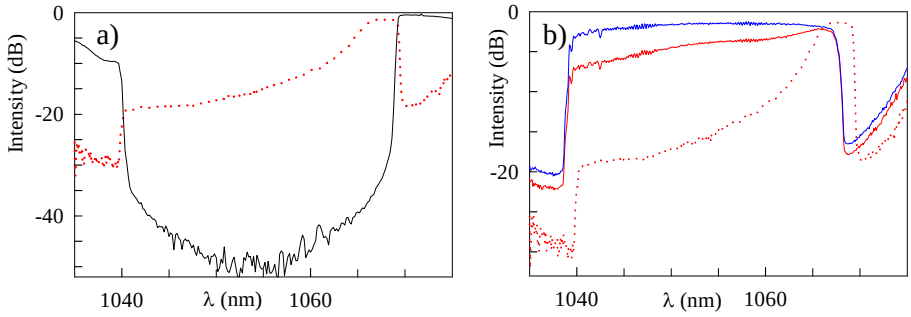

Fig. 5.8. Spectral response of linearly chirped grating, with 30 nm spectral window. a) Before annealing: Red dotted line: reflection from long wavelength side. Black line: transmitted spectrum. b) After annealing: Blue line: (flat spectrum) reflection from short wavelength side. Red solid line: reflection from long wavelength side. Red dotted line: data repeated from a) for comparison.

The transmission curve in Fig. 5.8 a) shows an extinction of >50 dB at a wavelength of 1055 nm, which demonstrates that this was initially a very strong grating. The strength of the grating also created large cladding mode losses, which are evident from the >15 dB decrease in reflection at short wavelengths compared to the peak at 1065 nm. To reduce the strength and thus decrease the cladding mode loss, we annealed the grating, with the results shown in Fig. 5.8 b). The reflection spectra from both ends of the grating are shown, which confirms that the spectral response was only affected by cladding mode losses when the grating was illuminated from the long wavelength side. The reflected spectrum from the long wavelength side of the

annealed grating was generally flatter compared to the spectrum from the grating prior to annealing. The maximum reflectivity was slightly reduced, but the reflectivity at short wavelengths was dramatically increased. The relaxation of the raised index periods that results from annealing, reduces the average refractive index of the grating, and therefore reduces the optical path length in the grating. The reduced optical path length causes the slight shift of the grating spectrum to shorter wavelengths that can be seen by comparing the reflection curves from before annealing (dotted red line) and after annealing (solid red line) in Fig. 5.8 b). From these results we concluded that by annealing to provide optimum strength, it would be possible to control the problems associated with cladding mode losses. Using this technique, the entire spectral window of the CFBG is useful, and it would therefore be unnecessary to work on the short-wavelength low-reflectivity plateau.

The next CFBG that we tested had a spectral window of 10 nm, and the full 2^{nd} and 3^{rd} order dispersion required to compensate for the compressor: D x length = 45.5 ps/nm, $dD/d\lambda$ x length = 1.5 ps/nm^2. For this CFBG design, we again used a network analyser to measure the time delay vs. wavelength, as described in Section 5.3.2. The measured time-delay vs. wavelength results and the designed delay vs. wavelength are shown in Fig. 5.9. The measured response corresponds closely to the design characteristic.

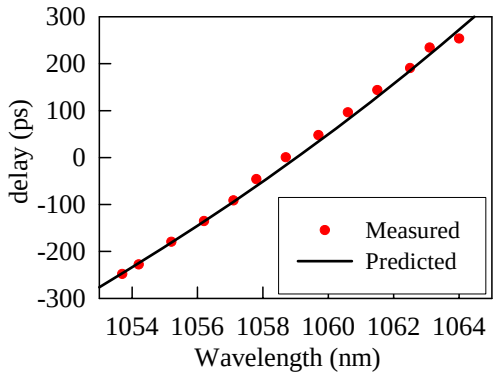

Fig. 5.9. Delay vs. wavelength for 10 nm CFBG. Both design and measured characteristics are shown.

The normalised reflection spectrum of the grating (after annealing) is shown in Fig. 5.10. We considered that the spectral response was sufficiently uniform that the grating should permit cleanly recompressed pulses. The calculated stretched pulse duration was ~ 45.5 ps/nm x 5 nm = 220 ps. Fig. 5.11 shows the SHG autocorrelation measurements of the compressed pulses (i.e. after passing through both stretcher and compressor) for both the 30 nm grating and for the 10nm grating. The autocorrelation from the 30 nm CFBG clearly shows the degradation in pulse quality caused by uncompensated 3^{rd} order dispersion of the compressor. By comparison, the performance of the 10 nm CFBG is excellent, producing τ_{FWHM} = 470 fs pulses

with 6nm bandwidth, $\Delta\nu\Delta\tau$~0.7. We conclude that this grating is suitable for producing clean pulses with the 500 fs duration required for our industrially sponsored CPA system.

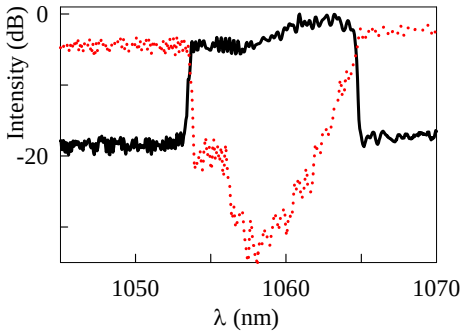

Fig. 5.10. Spectral response of 10 nm spectral window CFBG (with 3rd order dispersion). Black line: reflection from long wavelength side. Red dotted line: transmitted spectrum.

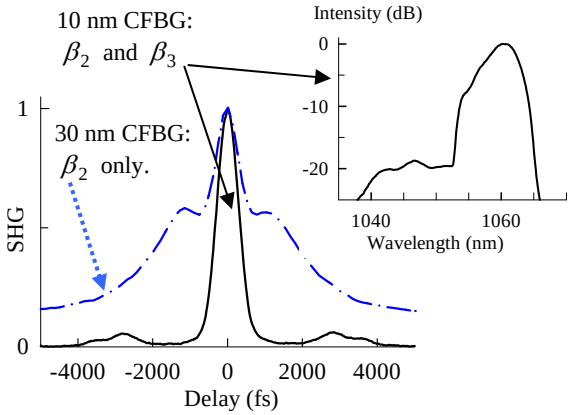

Fig. 5.11 SHG autocorrelation of recompressed pulses. Black line: Pulse FWHM=470 fs, from 10 nm CFBG. Blue dash dot line: Pulse FWHM=2000 fs from 30 nm linearly chirped CFBG. Inset: pulse spectrum after final amplifier of CPA system with 10 nm CFBG.

5.4.3 Further considerations

The 10 nm spectral window CFBG (Section 5.4.2) with the required 2nd and 3rd order dispersion to compensate for that of the compressor, enabled us to produce compressed pulses with τ_{FWHM} = 470 fs, $\Delta\nu\Delta\tau$=0.7 (bandwidth ~6nm). Due to practical constraints imposed by the CFBG writing process and the limited range of available phase-masks, 10 nm was the maximum spectral window that it was possible to fabricate for a grating that incorporated the high value of 3rd order dispersion required to compensate for the compressor. This limited spectral window would limit the minimum recompressed FWHM pulse duration to ~500 fs. Pulses of this duration should be useful for many applications of our CPA system, but to extend further the range of potential applications may require the system to produce shorter pulses.

Morten Ibsen indicated it should be possible to fabricate a larger spectral window CFBG with D x Length = 45.5 ps/nm by limiting the 3rd order dispersion to dD/dλ x Length = 0.5 ps/nm^2 i.e. ~ 1/3 of that required by the original compressor design. We noted in Section 5.3 that by changing the angle of incidence onto the grating compressor, the ratio $|\beta_3 / \beta_2|$ could be reduced, although this would potentially result in reduced transmission efficiency. To develop our technology to produce ~300 fs pulses, we have therefore designed a third generation CFBG. We first redesigned the compressor with reduced 3rd order dispersion as follows: spectral window = 15 nm (corresponds to pulse FWHM of ~7.5 nm), 58 degree angle of incidence, grating separation of 120 cm, calculated dispersion of D x Length = 40.8 ps/nm, dD/dλ x Length = 0.34 ps/nm^2 (stretched pulse duration ~ 40.8 ps/nm x 7.5 nm ~300 ps). The CFBG stretcher will be fabricated (not done at the time of writing) with 15 nm spectral window, and

dispersion to compensate for that of the redesigned compressor, and should enable us to obtain high quality pulses with duration of ~300 fs.

We noted in Section 5.3 that the diffraction efficiency of our grating reduces significantly at angles of incidence above 47 degrees (see Table 5.1). However, this reduced diffraction efficiency may not prove to be a limitation because as we move towards higher average powers from the CPA system it will be necessary to switch to a more efficient compressor grating with a reflective dielectric coating (e.g. >95% efficiency), or to use the emerging technology of silica transmission gratings that have been designed to handle >100W average power from a CPA system [8]. When selecting a new compressor grating, it may be possible to obtain efficient diffraction at the angle of incidence required to match the $|\beta_3 / \beta_2|$ ratio of the third generation design CFBG. We therefore consider that the proposed design of CFBG stretcher and compressor is a valuable development, as it should enable us to demonstrate significantly shorter (~300 fs) recompressed pulses from the system.

5.5 Conclusion

In conclusion, we designed and implemented a bulk grating compressor that transmitted a spectral window of 16 nm, had grating separation of 40 cm, operated at 41 degree angle of incidence, and produced 2nd and 3rd order dispersion of D x Length = 45.5 ps/nm, (β_2 x Length = -27x10^6 fs^2/rad); and dD/dλ x Length = 1.5 ps/nm^2 (β_3 x Length= 530 x10^6 fs^3/rad^2). Our calculations indicated that 3rd order dispersion compensation would be necessary in order to obtain high quality recompressed pulses with τ_{FWHM} <500 fs, and this was confirmed experimentally by the large pedestal on the SHG autocorrelation observed when we used a linearly chirped CFBG stretcher. Our initial CFBG tests showed highly uneven spectral reflectivity caused by cladding mode losses when light was incident from the long wavelength side of the grating. By optimising the strength of the grating (by annealing the CFBG after writing) we have now largely controlled this problem. We then designed and implemented a CFBG stretcher with 10nm spectral window and the correct 2nd and 3rd order dispersion to compensate for the parameters of this bulk grating compressor. The grating had a well controlled spectral response and the measured SHG autocorrelation showed that we obtained high quality recompressed pulses with τ_{FWHM} = 470 fs ($\Delta\nu\Delta\tau$~0.7). The stretched pulse duration from this grating was calculated to be ~220 ps. The combination of bulk grating compressor and 10 nm CFBG stretcher should satisfy the requirements of our industrial sponsor.

To develop the CFBG technology to produce τ_{FWHM} ~300 fs pulses, we have re-designed the pulse compressor to reduce the 3rd order dispersion relative to the 2nd order dispersion (D x Length = 40.8 ps/nm, dD/dλ x Length = 0.34 ps/nm^2), which should enable the fabrication of a

CFBG with spectral window >15 nm and with both 2^{nd} and 3^{rd} order dispersion to compensate for the compressor. The calculated stretched pulse duration from this CFBG is ~300 ps. The redesigned compressor will not operate at the most efficient angle of incidence for our bulk grating, but we note that to develop the compressor for use at high average power may require replacement of our gold-coated diffraction grating with a very high efficiency dielectric grating, and it may be possible to select the replacement grating to have high efficiency at the required angle of incidence. We consider that the proposed design of CFBG stretcher and bulk grating compressor should enable ~300 fs recompressed pulses and is therefore a valuable development.

References

1. A. Galvanauskas, Z. Sartania and M. Bischoff, "Millijoule femtosecond fiber CPA system," in *Advanced Solid-State Lasers, Proceedings*, vol. 50, *OSA Trends in Optics and Photonics*, C. Marshall, Ed. Washington, 2001, pp. 679-681.
2. N. G. R. Broderick, D. J. Richardson, D. Taverner, J. E. Caplen, L. Dong and M. Ibsen, "High-power chirped-pulse all-fiber amplification system based on large-mode-area fiber gratings," Optics Letters **24,** 566-568 (1999).
3. M. Ibsen, M. K. Durkin, M. J. Cole, M. N. Zervas and R. I. Laming, "Recent Advances in Long Dispersion Compensating Fiber Bragg Gratings.," (IEE Colloquium on Optical Fiber Gratings) IEE, London, U.K. (1999).
4. G. P. Agrawal, *Nonlinear Fiber Optics*, Academic Press (San Diego), 2nd (1995).
5. M. C. Hutley, *Diffraction Gratings*, Academic Press (London), (1982).
6. C. Palmer, *Diffraction Grating Handbook*, Richardson Grating Laboratory (Rochester), 4th Edition (2000).
7. R. L. Fork, C. H. B. Cruz, P. C. Becker and C. V. Shank, "Compression of Optical Pulses to 6 femtoseconds by Using Cubic Phase Compensation," Optics Letters **12,** 483-485 (1987).
8. J. Limpert, T. Schreiber, T. Clausnitzer, K. Zollner, H. J. Fuchs, E. B. Kley, H. Zellmer and A. Tünnermann, "High-power femtosecond Yb-doped fiber amplifier," Optics Express **10,** 628-638 (2002).
9. D. Gloge, "Weakly Guiding Fibers," Applied Optics **10,** 2252-2258 (1971).
10. M. Ibsen, M. K. Durkin, M. N. Zervas, A. B. Grudinin and R. I. Laming, "Custom design of long chirped Bragg gratings: Application to gain-flattening filter with incorporated dispersion compensation," IEEE Photonics Technology Letters **12,** 498-500 (2000).
11. T. Erdogan, "Fiber Grating Spectra," Journal of Lightwave Technology **15,** 1277 - 1294 (1997).

Chapter 6 Fiber Amplifier Cascade

6.1 Introduction

In this chapter, we describe the design and characterisation of the Yb-fiber amplifiers used in the CPA and direct amplification systems described in Chapter 3. We also describe the components use to suppress ASE build-up between the amplifier stages because these components are common to both systems.

A detailed schematic of the complete CPA system is shown in Fig. 6.1. The system design follows common practice by decreasing the pulse repetition rate to reduce gain saturation effects and hence achieve higher pulse energies. The multi-stage amplifier system was necessary because ASE limits the gain from a fiber amplifier to ~35 dB [1], but we required ~60 dB gain in order to obtain pulses with E>10 μJ from our (highly stable) low power oscillator with pulse energy ~ 60 pJ. If unchecked, ASE would build up along the amplifier cascade and saturate the gain of the amplifiers we therefore used isolators and time gating (synchronised to the arrival of each pulse) to avoid cascaded ASE. The necessary additional components created coupling losses that totaled ~20 dB, including: 4 dB insertion loss of our pulse selector, 3 dB coupling loss between each amplifier, and 10 dB coupling loss from the CFBG pulse stretcher. We therefore required a cascade of three amplifiers to produce the necessary gain.

As described in Chapter 3, the goal of creating a robust and straightforward-to-manufacture system suggested that using core-pumped amplifiers would be the preferred approach. However, core-pumped amplifiers have limited scope for power-scaling, e.g. the maximum available power from single-mode pump diodes is ~350 mW, and therefore cladding-pumping was necessary for the final amplifier stage in order to obtain the required high output power. We decided that the best aspects of both pumping technologies could be exploited by developing two core-pumped pre-amplifiers, followed by a cladding-pumped power amplifier.

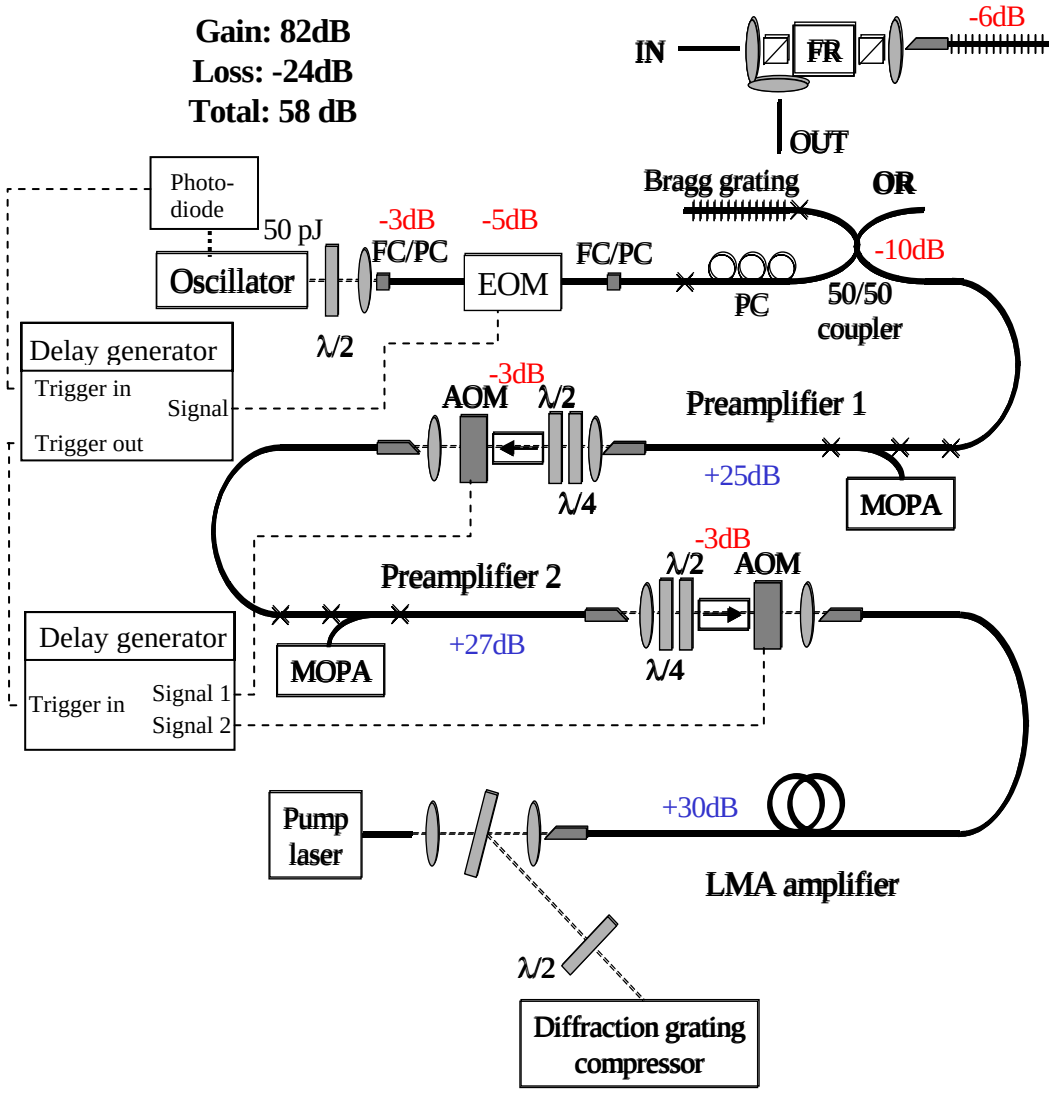

Fig. 6.1. Detailed schematic of complete CPA system. (FR = Faraday rotator. MOPA = diode pump laser, FC/PC = fiber connector type.)

This chapter is organised as follows. We first describe the components used for pulse selection and ASE suppression in Section 6.2. Next, we present our work to optimise the amplifiers. Section 6.3 describes the development of the core-pumped pre-amplifiers. Section 6.4 describes the concept of cladding-pumped amplifiers. Section 6.5 describes a 'GTWave' cladding-pumped pre-amplifier. ('GTWave' is a cladding pumping scheme patented and marketed by Southampton Photonics Inc. (SPI)) Section 6.6 describes LMA power amplifier that was cladding-pumped using a conventional end-pumping configuration. The performance of the CPA system as a whole is presented in the following chapter (Chapter 7), and the performance of the direct amplification system is presented in Chapter 8.

6.2 Pulse selection and amplifier gating

For pulse selection, we used a high extinction ratio (>50 dB) EOM. Using this device, the repetition rate could, in principle, be reduced to any sub harmonic value of the oscillator. In practice the lowest repetition rate used in our CPA system was limited to ~10 kHz by the requirement to saturate the final amplifier.

ASE build-up along the amplifier chain can be a significant problem at low repetition rates. To suppress this, both an isolator and an AOM were inserted between each amplifier. The AOMs were aligned such that the first order diffracted beam was launched into the following amplifier stage and were then activated for a only short time window to allow the pulses through but to block the ASE background. The AOMs (supplied by AA Sa., model number AA ST110_1.06) are made from TeO_2 (acoustic velocity 4200 m/s) with specified rise time of 160 ns/mm. With a beam diameter ~1.5 mm, the experimentally determined optimum time window (to just avoid clipping of the transmitted pulse) was found to be 320 ns. The electronic timing control system was comprised of a trigger and delay/pulse generators controlling the EOM (HP 8131A), and the AOMs (Stanford Research Systems DG 535). For the trigger, we used a fast photodiode at the output port of the oscillator that is not used for seeding the system. The electronic timing control system is shown schematically in Fig. 6.1. Polarisation controllers were used to ensure maximum throughput from the isolators.

6.3 Core pumped pre-amplifiers

The peak power in the pre-amplifiers is not high so, when using the CPA technique, nonlinearity management is not a concern. To achieve stable, low-noise operation, we used core pumping via a 980:1060 nm WDM in a forward pumped configuration. The measured wavelength coupling characteristics of the WDM are shown in Chapter 4. We used standard single-mode Yb-fiber for the gain medium (identical to that used in the oscillator). This section is organised as follows. Section 6.3.1 describes the performance of the initial configuration of the pre-amplifiers. Sections 6.3.2 and 6.3.3 describe design refinements that enable increased gain to be obtained.

6.3.1 Initial performance

The initial configuration of the pre-amplifiers is shown in Fig. 6.2. Angled ends were used to suppress unwanted Fresnel end-reflections. The length of the Yb-fiber was selected such that the ASE spectrum was approximately flat and centered across the wavelength band of the signal as shown in Fig. 6.3.

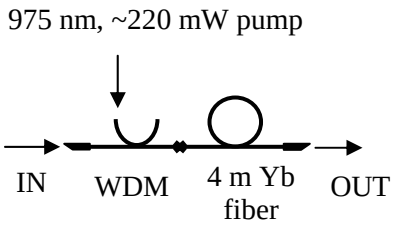

Fig. 6.2 Pre-amplifier: initial configuration

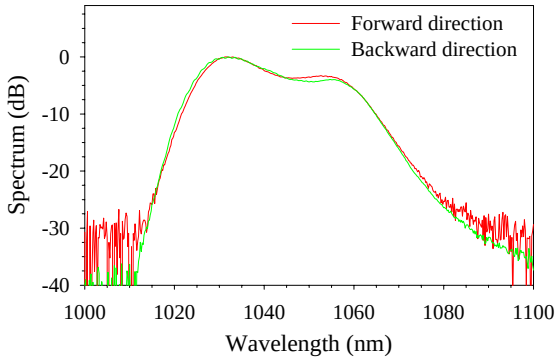

Fig. 6.3 Measured pre-amplifier ASE

The gain of the pre-amplifiers was characterised using a Nd:YLF seed laser (1047 nm), with a signal-generator-driven AOM to control the input duty cycle. The input and output pulses were measured using a photodiode, and calibrated neutral density filters were inserted at the amplifier output to match the photodiode voltage to that at the input. The launch efficiency into the WDM was measured before splicing on the Yb-fiber. For the pre-amplifier of Fig. 6.2, the measured small-signal gain was ~25 dB, and the saturated output power was ≥ 50 mW, as shown in Fig. 6.4. The gain was adequate for our requirements, but would limit future power increases in the system, so we have also considered design improvements, described below, that should enable increased gain to be obtained.

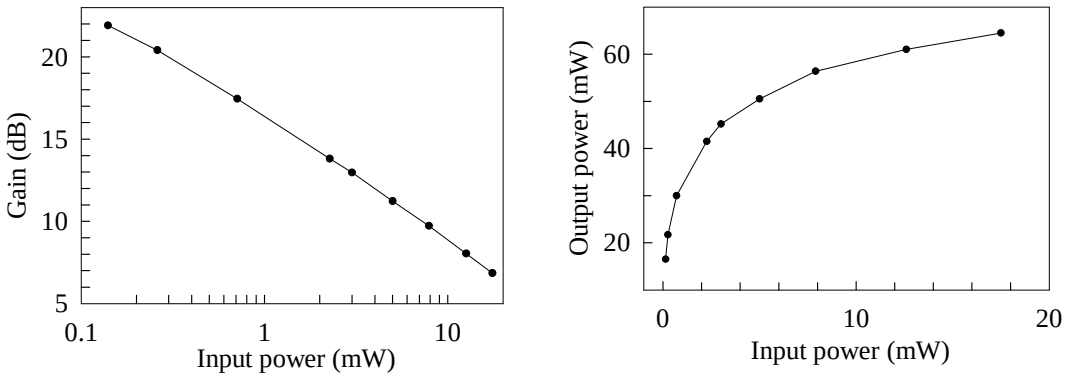

Fig. 6.4 Gain and output power characteristics of first pre-amplifier.

6.3.2 Increased gain using mid-amplifier pump injection

In this section, we describe a technique for obtaining increased gain from a core-pumped Yb-doped fiber amplifier by recycling lost short-wavelength ASE. This technique was first applied to Er-doped fiber amplifiers, but to our knowledge, has not been used previously in Yb-doped fiber amplifiers.

Recycling lost ASE exploits the details of the Yb spectroscopy (see Chapter 2). In the 1.0–1.1 μm range, the emission cross section of Yb-doped silica fiber is peaked at 1030 nm. The absorption cross section is highest at wavelengths below ~1030 nm. Consequently a high inversion fraction and strong pumping are required to create gain (and ASE) at 1030 nm; and gain at 1030 nm will only occur near the pump end of the fiber. Importantly, the absorption cross section decreases more rapidly than the emission cross section at longer wavelengths e.g. 1060 nm. Therefore a much lower inversion, possibly pumped by re-emitted 1030 nm light, can create gain at 1060 nm; and gain at 1060 nm is possible further away from the pump end of the fiber (in a part of the fiber where there is net absorption of 1030 nm light). We operate with a 1060 nm signal, so 1030 nm ASE emitted from the pump end of the fiber is "lost" power. In a paper concerning long wavelength (1570-1610 nm) Er-doped fiber amplifiers, a similar relationship between the absorption and emission cross sections at shorter and longer wavelengths also resulted in "lost" shorter wavelength (1550 nm) ASE near the pump [2]. It was demonstrated that a second length of Er-doped fiber inserted before the point where the pump was injected could absorb the "lost" ASE and provide additional gain of up to 4 dB at longer signal wavelengths. Applying this idea to our set-up, Fig. 6.5 shows the results of theoretical modelling (by Dr. J. Nilsson) for our Yb-fiber system, which confirms that by using mid-point pump injection, the gain at 1056 nm would increase by ~3 dB compared to the gain with a single length of doped fiber. Note that in Fig. 6.5. the percentage of the total fiber length either side of the pump is shown. Fig. 6.5 also shows that the peak gain does not change significantly when the pump injection point is >30% along the doped fiber length, so some variation in the exact position of the pump injection point can be tolerated. We have employed mid-point pump injection for the final design of pre-amplifier used to characterise the performance of the CPA system.

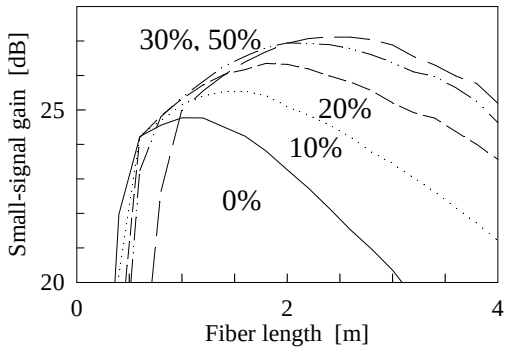

- Small-signal gain of core pumped Yb-doped fiber amplifier with midway forward pump injection.
- Pump injected at 0,10,20,30, and 50% of the YDF length.
- Signal wavelength 1056 nm

Fig. 6.5 Predicted amplifier gain; midpoint pump injection; 5 μm diameter core; 220mW pump.

6.3.3 Increased gain using small core fiber

In this section we describe the technique of using a smaller core Yb-doped fiber for obtaining increased small signal gain. Using a small core with high NA results in a tightly confined mode, and hence higher pump intensities for a given pump power. The concept of obtaining increased gain from a more tightly confined mode has previously been applied to Er-doped fiber amplifiers [3, 4]. However, to our knowledge, this is the first time that the technique has been applied to an Yb-fiber system.

Fig. 6.6 shows simulation results (by Dr. J. Nilsson) for a 3 μm core fiber, using the same pump power as the simulations for a 5 μm core fiber shown in Fig. 6.5. Using the smaller core fiber causes the maximum gain to increase by ~10 dB. Fig. 6.7 shows simulated results for the 3 μm core fiber but with an increased pump power of 400 mW; the gain has increased by a further 4 dB to 41 dB. In practice, it will be necessary to splice the 3 μm core fiber to the WDM coupler (~5 μm core fiber), which will create a theoretical [5] splice loss of ~0.6 dB per splice. It may be possible to reduce the splicing loss by inserting a short length of fiber with intermediate core size to create a quasi-adiabatic taper, or by using tapered splices. There may also be an increased coupling loss at the launch to the LMA power amplifier. Even after taking into account the expected splice/coupling losses, the net gain using the 3 μm core fiber is still significantly above that obtained from the 5 μm core fiber, so we intend to use such a small core fiber in the next upgrade of the system.

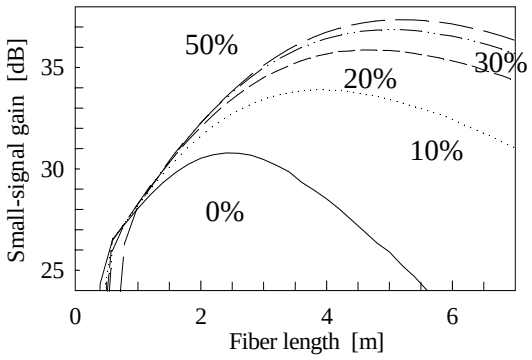

Fig. 6.6 Predicted amplifier gain: midpoint pump injection; 3 μm core fiber; 220mW pump.

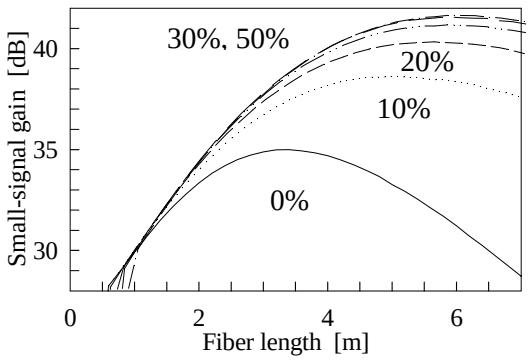

Fig. 6.7 Predicted amplifier gain: midpoint pump injection; 3 μm core fiber; 400mW pump.

6.4 Cladding pumped amplifiers

Cladding-pumped fiber enables low brightness but high power pump diodes to efficiently pump high brightness fiber lasers and amplifiers. To obtain the required power at the CPA system output, it was essential that we used a cladding pumped final stage power-amplifier. In the future, we may wish to upgrade the CPA system to produce much higher average power e.g. ~10 W. We therefore evaluated a cladding-pumped pre-amplifier that would potentially

provide sufficient input power to saturate the final amplifier even when producing such a high average output power. Section 6.5 describes the evaluation of a cladding-pumped pre-amplifier, and Section 6.6 describes the design and performance of the cladding-pumped final stage power-amplifier.

6.5 GTWave pre-amplifier

This section describes the charactersitics of a cladding pumped pre-amplifier that could produce much higher average power compared to a core-pumped pre-amplifier. The usual arrangement for launching the pump into the fiber inner cladding is to use a lens pair and dichroic mirror, and is shown in Fig. 6.11, and this technique was used for the LMA power-amplifier. However, this arrangement is bulky, and requires precise alignment. An ingenious alternative developed by Dr. Anatoly Grudinin and Paul Turner (ORC/SPI: European patent application number W0067350) called GTWave fiber, is shown schematically in Fig. 6.8. A fiber with a doped core is held in contact with a pure silica dummy fiber, encased together in a low refractive index outer clad. The fiber pigtailed pump diode is spliced directly to the dummy fiber, from which the power transfers across to the doped fiber and into the Yb-doped core.

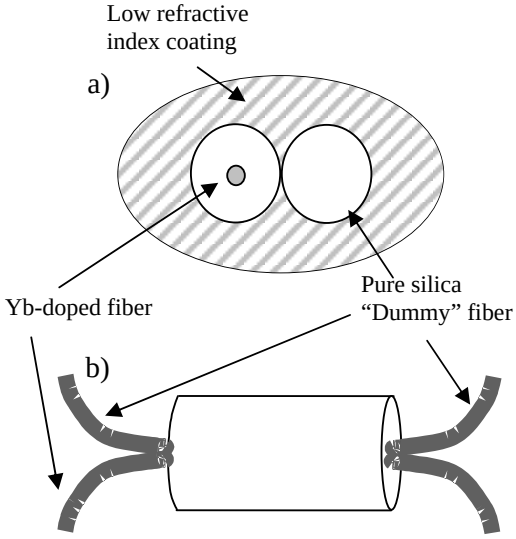

Fig. 6.8 Schematic of GTWave fiber: a) cross section view (Yb-doping confined to active fiber core (shaded)), b) side view.

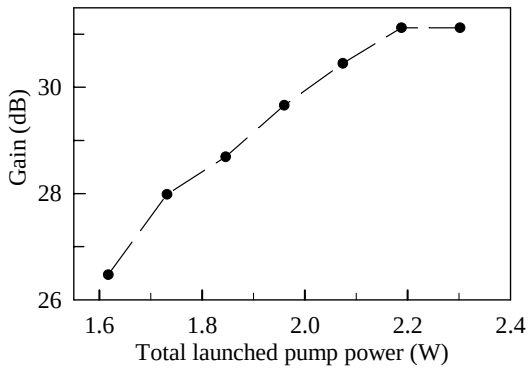

Fig. 6.9. Gain characteristics of GTWave amplifier. Maximum output power = 200 mW. Bi-directional pumping with maximum pump power from each end of ~1.2W.

We measured the small signal gain of a GTWave amplifier using pump power >2 W, and using an AOM gated Nd:YLF seed (1047 nm). We obtained ~31 dB small signal gain from an amplifier with ~2.5 m doped fiber length as shown in Fig. 6.9. However the amplifier we tested was an early prototype and the pump to signal optical efficiency was only ~10%, due to pump leakage from the dummy fiber and incomplete absorption. GTWave amplifiers using Er-doped

fibers are now a standard product produced by SPI, and GTWave Yb-fiber amplifiers are scheduled to become a standard product shortly. We have been unable, as yet, to test a suitably optimised Yb-fiber GTWave amplifier, but we plan to return to this technology in the future to enable the CPA system to produce higher average power. For the initial prototype of our industrially sponsored CPA system, core pumped pre-amplifiers were used.

6.6 Power amplifier

This section describes the pump configuration and fiber design developed for the power amplifier used in the CPA and direct amplification systems. As described in Section 6.4, cladding pumping is necessary in order to obtain the >1 W power required at the output of our CPA system. To obtain maximum output power from the amplifier, counter propagating pump is used, although this increases the noise figure, and requires a strong input signal (saturated gain regime) if acceptably low ASE levels are to be obtained at the amplifier output. Simply using standard single-mode core fiber designs in a cladding pumped configuration would not enable us to achieve the required output pulse energy because SRS in the final amplifier would limit the maximum pulse energy. We therefore used a larger core fiber design to increase the maximum pulse energy that could be produced by the system.

This section is organised as follows. In Section 6.6.1 we review how the maximum pulse energy that avoids unacceptable nonlinear distortion scales with the fiber core area and with the reciprocal of the fiber effective length. Then. in Section 6.6.2 we calculate the maximum pulse energy possible for a given fiber core geometry due to energy storage limitations. In Section 6.6.3 we describe the fiber design used in our system, and in Section 6.6.4 we describe the experimental setup used to measure the fiber efficiency when operating as a laser.

6.6.1 Fiber nonlinearity constraints

The nonlinear process that limits the maximum pulse energy is SRS. As described in Chapter 2, the threshold pulse peak power for the onset of SRS is approximately $(16 \times A_{eff}) / (g_{Raman} \times L_{eff})$, where g_{Raman} is the Raman gain coefficient, A_{eff} is the effective mode area, and L_{eff} is the effective length of fiber [6]. This is the threshold power for forward Raman scattering; the threshold power for reverse Raman scattering is higher. As an example, for a stretched pulse FWHM duration of 0.3 ns, an amplifier fiber length = 2 m, gain = 20 dB, and fibers with core diameters = 5, 15 and 30 μm, the Raman threshold power corresponds to a pulse with energy of 3, 28 and 113 μJ respectively. The limiting effects of SRS are considered in greater detail in the following chapter.

Even below the threshold for SRS, nonlinear pulse phase distortion arises due to SPM, and this can increase the duration of the recompressed pulse and decrease the peak to pedestal contrast ratio [7]. Although in a CPA system the phase-distortion introduced by SPM can, in principle, be pre-compensated by purely linear devices [8], e.g. a spatial light modulator [9], we would prefer to avoid this complexity by preventing excessive SPM induced pulse distortion from occurring. Using large core fibers decreases the intensity and hence increases the pulse energy threshold for unacceptable SPM induced distortion. In our system we used LMA fiber for the final amplifier with a 15 μm core diameter.

6.6.2 Energy storage constraints

As an estimate of the maximum extractable energy, we consider the maximum energy Q-switched pulse that can be obtained from a given fiber. As a direct result of the high gain and tightly confined optical mode, rapid energy loss in the form of ASE limits the Q-switched pulse energy from conventional single-mode Er and Yb-doped fibers to ~ 10 μJ [10] and 100 μJ [11] respectively. The extractable pulse energy is influenced by the spectroscopic properties of the dopant, the available pump power, and the fiber geometry, and a good estimate for the maximum energy obtainable from a fiber is E_{max}~10 x saturation energy. The saturation energy is calculated as $E_{sat}= h\nu_s A/((\sigma_{es}+\sigma_{as})\Gamma_s)$, where $h\nu_s$ is the signal photon energy, A is the doped area, Γ_s is the signal overlap with the active dopant, and σ_{es} and σ_{as} are the signal emission and absorption cross sections [12]. For fibers that have the active dopant confined within the core, that E_{sat} is then approximately proportional to the signal mode area [11], and by using large core Yb-doped fibers, single-mode Q-switched pulses with >5 mJ have been produced [12]. We conclude that whereas the extractable energy from a conventional single-mode fiber would probably prove problematic for our target of 10-50 μJ, this limitation would be avoided by using LMA fiber.

6.6.3 Fiber design

As described above, to overcome the constraints imposed by energy storage and nonlinear pulse distortion, we used a large mode design for the fiber core and this section provides details of the core design. Earlier work using large core multimode fiber amplifiers demonstrated increased pulse energy and increased threshold for nonlinear distortion, although without necessarily maintaining M^2 = 1 beam quality [1]. More recently, Fermann et al. at IMRA used large core multimode fibers to obtain increased pulse energies, whilst attempting to maintain single-mode beam quality by exciting only the fundamental mode at the fiber input [13]. However, the mode quality obtained this multi-mode fiber approach is perhaps less inherently robust against

exciting higher order modes due to launch alignment drift or fiber perturbation compared to using a single-mode fiber.

Our group has previously demonstrated 0.5 mJ pulses directly from a Q-switched, quasi-single-mode LMA fiber. LMA fiber combines a low NA core to reduce the number of guided modes to ~3, and a strategic doping pattern designed to greatly enhance the gain of the fundamental mode compared to higher order modes to give quasi single-mode output [14]. The minimum core NA is set by the ability to reliably fabricate a small index difference, and is typically ~0.06. The addition of a raised index ring within the LMA fiber core significantly reduces bend losses, and increases further the size of the fundamental mode. The increased sensitivity to bending loss compared to standard (higher NA) fibers is managed by using fiber coils with ~30cm diameter. Fig. 6.10. shows the refractive index profile of our Yb-doped LMA preform. The Yb-doped gain region is confined to the central core, which overlaps with a larger fraction of the fundamental mode power (intensity maximum at fiber centre), compared to the low overlap fraction with the second order mode power (intensity node at fiber centre). The differential overlap encourages single-mode operation. For many applications, robust M^2=1 mode quality is required, and we therefore chose an LMA power amplifier [14, 15] for the initial CPA design.

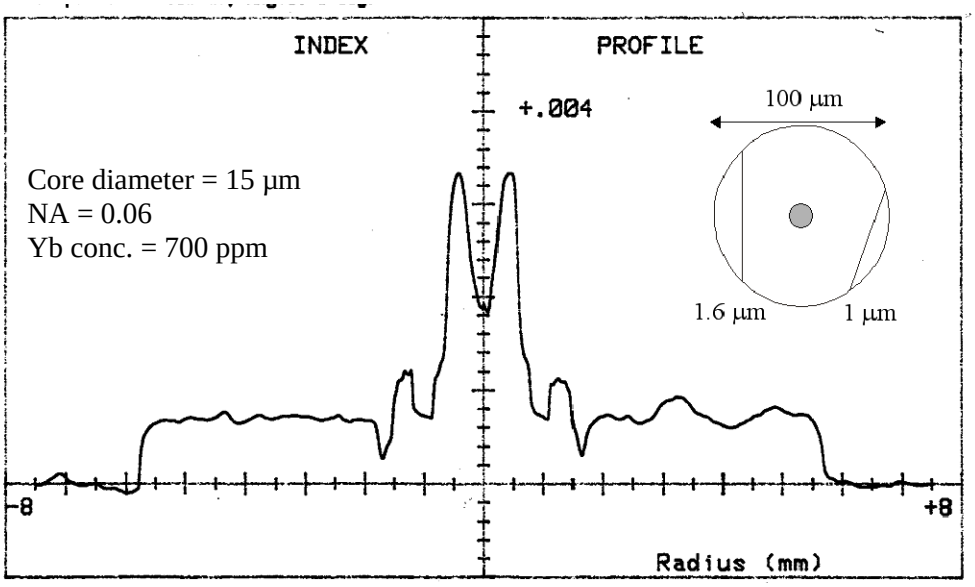

Fig. 6.10. Refractive index profile of LMA preform (fiber code number: HD605).

The length of the amplifier is controlled by the efficiency of power transfer from the cladding to the core, which depends on the extent of overlap of the inner-cladding modes with the Yb-doped core. Inefficient power transfer can arise because the higher order modes supported by the inner-cladding, e.g. helical modes, can have nodes at the fiber centre, leading to unabsorbed pump. Standard techniques to improve the coupling from inner-cladding modes to core modes

are to increase the core to inner-cladding area ratio, to use an offset core, and to use an irregular shaped inner-cladding (encourages mode-coupling). We used a preform with milled flat sides, which destroyed the cylindrical symmetry of the inner cladding and encouraged mode-mixing [16]. A schematic cross section of the preform geometry with milled flat sides is shown inset to Fig. 6.10. The milled preform is coated with a polymer jacket with lower refractive index to create a waveguide for the pump light.

6.6.4 Experimental setup and results

The experimental setup used for the power amplifier is shown in Fig. 6.11. To obtain maximum output power and minimise the effective length (minimum nonlinear distortion) we reverse pumped the power amplifier. The pump diode laser was a Boston Laser Inc. model ML430: 6 W, 915 nm, fiber coupled into 100 μm diameter, NA = 0.2 core fiber. The pump was free-space coupled into the LMA fiber inner cladding (diameter 100 μm; NA ~0.2), and we used a dichroic to separate the pump and signal beams.

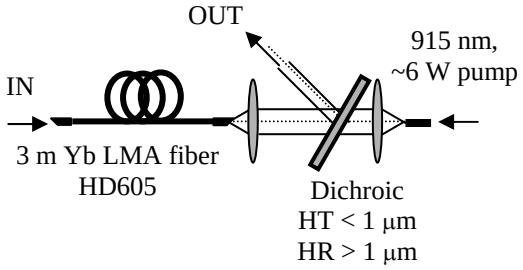

Fig. 6.11 Schematic of LMA amplifier showing the pump configuration.

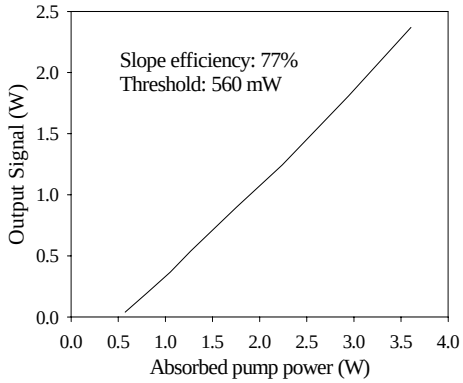

Fig. 6.12. Laser characteristic of LMA (HD605). (Length = 3 m; Flat-cleaved ends).

We first measured the efficiency of a 3 m length LMA fiber by constructing a laser with 4% cleaved end reflections. Fig. 6.12. shows the laser threshold power of 560 mW and slope efficiency of 77%, which demonstrated that the fiber efficiency was acceptable (quantum efficiency = 915nm/1030 nm = 89%). The performance of this fiber as an amplifier is demonstrated as part of the overall CPA and direct amplification systems, as presented in Chapters 7 and 8.

References

1. B. Desthieux, R. I. Laming and D. N. Payne, "111 kW (0.5 mJ) Pulse Amplification at 1.5-microns Using a Gated Cascade of 3 Erbium-Doped Fiber Amplifiers," Applied Physics Letters **63,** 586-588 (1993).
2. J. H. Lee, U. C. Ryu, S. J. Ahn and N. K. Park, "Enhancement of power conversion efficiency for an L-band EDFA with a secondary pumping effect in the unpumped EDF section," IEEE Photonics Technology Letters **11,** 42-44 (1999).
3. C. R. Giles and E. Desurvire, "Modeling Erbium-Doped Fiber Amplifiers," Journal of Lightwave Technology **9,** 271-283 (1991).
4. B. Pedersen, A. Bjarklev, J. H. Povlsen, K. Dybdal and C. C. Larsen, "The Design of Erbium-Doped Fiber Amplifiers," Journal of Lightwave Technology **9,** 1105-1112 (1991).
5. P. K. Cheo, *Fiber Optics and Optoelectronics*, Prentice Hall 2nd (1990).
6. R. G. Smith, "Optical power handling capacity of low loss optical fibers as determined by stimulated Raman and Brillouin scattering," Applied Optics **11,** 2489 - 2494 (1972).
7. Y. H. Chuang, D. D. Meyerhofer, S. Augst, H. Chen, J. Peatross and S. Uchida, "Suppression of the Pedestal in a Chirped-Pulse-Amplification Laser," Journal of the Optical Society of America B-Optical Physics **8,** 1226-1235 (1991).
8. A. Galvanauskas, "Mode-scalable fiber-based chirped pulse amplification systems," IEEE Journal of Selected Topics in Quantum Electronics **7,** 504-517 (2001).
9. F. G. Omenetto, A. J. Taylor, M. D. Moores and D. H. Reitze, "Adaptive control of femtosecond pulse propagation in optical fibers," Optics Letters **26,** 938-940 (2001).
10. H. L. Offerhaus, N. G. Broderick, D. J. Richardson, R. Sammut, J. Caplen and L. Dong, "High-energy single-transverse-mode Q-switched fiber laser based on a multimode large-mode-area erbium-doped fiber," Optics Letters **23,** 1683-1685 (1998).
11. C. C. Renaud, H. L. Offerhaus, J. A. Alvarez-Chavez, J. Nilsson, W. A. Clarkson, P. W. Turner, D. J. Richardson and A. B. Grudinin, "Characteristics of Q-switched cladding-pumped ytterbium-doped fiber lasers with different high-energy fiber designs," IEEE Journal of Quantum Electronics **37,** 199-206 (2001).
12. C. C. Renaud, J. A. Alvarez-Chavez, J. K. Sahu and J. Nilsson, "7.7 mJ pulses from a large core Yb-doped Cladding pumped Q-switched fibre laser," Conference on Lasers and Electro Optics (CLEO), Vol. 56 of OSA Trends in Optics and Photonics Series (Optical Society of America, Washington, D.C., 2001) paper CTuQ5 (2001).
13. M. E. Fermann, A. Galvanauskas, M. L. Stock, K. K. Wong, D. Harter and L. Goldberg, "Ultrawide tunable Er soliton fiber laser amplified in Yb-doped fiber," Optics Letters **24,** 1428-1430 (1999).
14. N. G. R. Broderick, H. L. Offerhaus, D. J. Richardson and R. A. Sammut, "Power scaling in passively mode-locked large-mode area fiber lasers," IEEE Photonics Technology Letters **10,** 1718-1720 (1998).
15. N. G. R. Broderick, H. L. Offerhaus, D. J. Richardson, R. A. Sammut, J. Caplen and L. Dong, "Large mode area fibers for high power applications," Optical Fiber Technology **5,** 185-196 (1999).
16. H. Zellmer, A. Tünnermann, H. Welling and V. Reichel, Optical Amplifiers and their Applications, OSA Trends in Optics and Photonics Series **16,** 137 (1997).

Chapter 7 Overall CPA System Performance

7.1 Introduction

In this chapter, we describe the performance of the complete CPA system developed for our industrial sponsors. The overall design of the system was described in Chapter 3, and the characteristics of the individual components were described in Chapters 4, 5, and 6. This chapter is structured as follows. We first describe the pre-amplifier configuration in Section 7.2, and the design of pulse stretcher in Section 7.3. In Section 7.4 we present results showing characteristics of the final output pulses from the system at repetition rates from the maximum of 54 MHz, and as low as 10 kHz (the minimum repetition rate for good signal to ASE ratio). Pulses generated with energy ~10 μJ have been cleanly recompressed to ~500 fs. Section 7.5 presents calculations which show that by slightly reducing the length, and increasing the core diameter of the the fiber for the final amplifier, it should be possible to reduce the effects of SRS and SPM sufficiently to enable the system to produce pulses with energy ~100 μJ. Section 7.6 presents our conclusions.

7.2 Configuration of pre-amplifiers

The core-pumped design of the pre-amplifiers was described in Chapter 6, and gain and ouptut power characteristics were presented for core-pumped pre-amplifiers in an end-pumped configuration. It was also shown in Chapter 6, that by using mid-point pump injection in preference to end-pumping, it should be possible to obtain increased gain. When characterising the CPA performance for our industrial sponsors, we first converted the pre-amplifiers to this configuration as shown in Fig. 7.1. The two pre-amplifiers have almost identical construction, differing mainly due to different wavelength pump sources. We assessed the appropriate length of Yb-doped fiber by tuning the ASE spectrum. The total fiber lengths are similar to the end pumped pre-amplifiers for which the gain charactersistics were presented in Chapter 6.

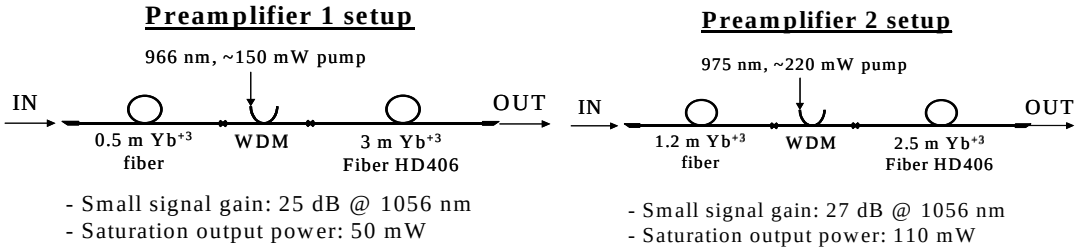

Fig. 7.1 Schematic of preamplifiers as used for complete CPA characterisation.

7.3 Configuration of pulse-stretcher

The targeted stretched pulse duration for the final CFBG stretcher design described in Chapter 5 was 300 ps. Due to delays in obtaining our CFBG pulse stretcher, we performed initial tests on our amplifier system using ~500 m of single mode fiber as a pulse stretcher. Using a 20 GHz photodiode and sampling oscilloscope, we measured the stretched pulse FWHM to be 322 ps as shown in Fig. 7.2. The measured duration is very close to the 300 ps that should be obtained from the CFBG, and therefore the CPA pulse energy results that we obtain using the fiber stretcher are therefore a valuable guide to the expected performance of the final system using a CFBG pulse stretcher. Using single mode fiber as the pulse stretcher has the advantage of transmitting the full bandwidth of the pulses, and because the fiber stretcher is spliced directly to the pre-amplifier without requiring a circulator, it results in comparatively low-losses. The disadvantage of using a fiber-stretcher is that it has the same sign of 3rd order dispersion as the bulk grating compressor, and the accumulated 3rd order dispersion results in a "ringing" structure on the trailing edge of the re-compressed pulse (see Chapter 5).

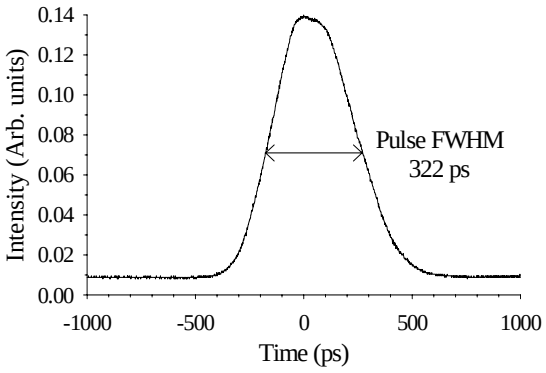

Fig. 7.2 Duration of stretched pulse after ~500 m of single mode fiber.

7.4 Experimental results

This section shows the performance of the CPA system as a whole. Beam quality (M^2) measurements were performed on the final amplified pulses using a "Modemaster" supplied by Coherent. The measured beam quality was $M^2 = 1.3$ (fiber core diameter of 19 μm, and outer diameter of 100 μm). We have since found that the mode quality at the amplifier output is strongly influenced by the signal launch at the fiber input. The fraction of the power in the higher order mode could be observed directly using an autocorrelation measurement because pulses in the fundamental and higher order modes propagated at different velocities along the LMA fiber and therefore separated temporally, and which enabled us to see satellite pulses on the autocorrelation measurements of the recompressed pulses. We observed that the intensity of the satellite pulses was strongly influenced by the signal launch into the LMA. We would therefore expect that quasi single-mode operation would be obtainable from this 19 μm core diameter LMA fiber by optimising the signal launch.

The average output power and pulse energy vs. repetition rate for a constant pump power of 3.5 W (>2.0 W launched) are shown in Fig. 7.3.

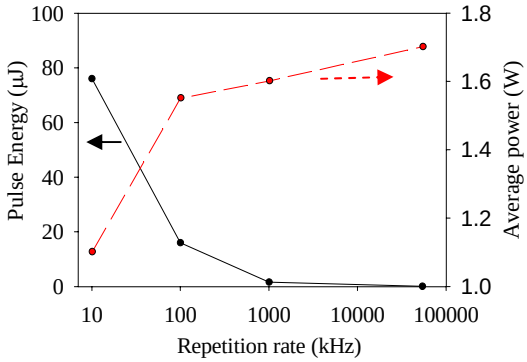

Fig. 7.3. System output power and pulse energies after the LMA amplifier.

The corresponding output spectra are shown in Fig. 7.4. At high repetition rates the signal spectrum is clean and >10 dB above the ASE, as shown by Fig. 7.4 (a) and (b). However, ASE at ~1030 nm started to become more prominent at a repetition rate of 100 kHz as shown in Fig. 7.4 (c). Raman scattering is evident at the highest pulse energies (lowest repetition rates) and has transferred a significant fraction of the energy to a broad longer-wavelength band as shown by Fig. 7.4 (c) and (d). From these spectral measurements we concluded that when considered as a practical limitation on the acceptable performance of the system, the SRS threshold pulse energy for our 15 μm core LMA is above 16 μJ but not as high as 76 μJ.

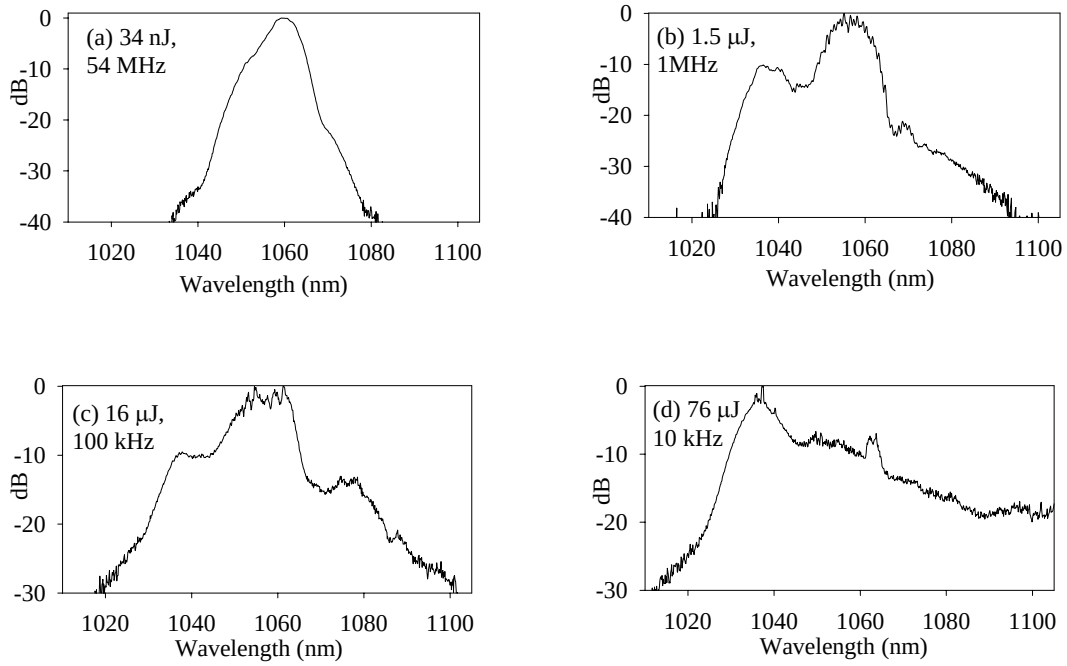

Fig. 7.4. Amplified pulse spectra for increasing pulse energies.

The temporal characteristics of the recompressed pulses are not presented because the additional 3rd order dispersion of the fiber stretcher results in poor pulse recompressed pulse quality (as demonstrated numerically in Chapter 5). However, more recent results have been obtained using CFBG pulse stretcher (spectral window of 7 nm), with the full 2nd and 3rd order dispersion required to compensate for the compressor: D x length = 45.5 ps/nm, $dD/d\lambda$ x length = 1.5 ps/nm^2). A typical autocorrelation of a recompressed pulse, after passing through this CFBG stretcher and the whole CPA system, is shown in Fig. 7.5. At low energies the FWHM pulse duration was measured to be 0.5 ps with 5 nm bandwidth, $\Delta\nu\Delta\tau\sim0.7$. Pulse energies of ~10 μJ have been demonstrated with this setup (limited by the onset of SRS).

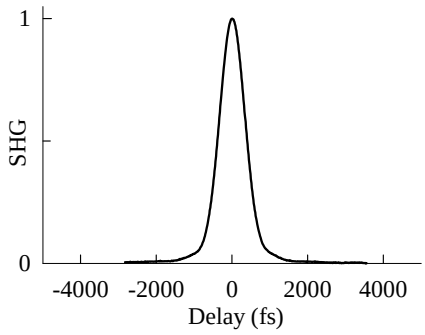

Fig. 7.5. Autocorrelation of recompressed pulse after passing through the entire CPA system using a 7 nm CFBG pulse stretcher. Pulse duration ~0.5 ps.

7.5 Extending the system capabilities

As described in Chapter 3, the target pulse energy for our industrial sponsors is 10-50 μJ, at a repetition rate of 10 kHz (average power 0.5 W). The grating compressor has a transmission loss of ~3 dB, so the target pulse energy immediately after the LMA amplifier is 20-100 μJ. The maximum pulse energy demonstrated with this system configuration of section 7.4 was limited by SRS to ~50 μJ, and in this section we present calculations showing that increasing the core diameter of the LMA fiber should enable 100 μJ pulses to be produced. Having established the required system parameters to avoid SRS, we then show numerical simulation results used to consider the possible effects of SPM on the quality of the re-compressed pulses.

We first compare the energy for which SRS was observed experimentally to be unacceptable with the calculated SRS threshold energy. Considering the system configuration with the characteristics described above, (measured pulse duration 0.32 ns, 2 m long amplifier fiber, 15 μm core diameter, and 20 dB gain), the calculated SRS threshold energy is ~30 μJ. The 2 m fiber length used in this calculation corresponds to longer physical length of fiber because reverse pumping significantly reduces the effective length of the fiber. The calculated SRS threshold energy is approximately equal to the measured (>16 μJ) threshold energy that was estimated from the data in Section 7.4 to correspond to the limit for acceptable spectral distortion.

We used a 915nm pump in our initial setup due to short-term diode availability. However, the strongest absorption peak of Yb-doped fiber is at 975 nm (four times stronger absorption compared to 915 nm), so we would like to pump at 975 nm to minimise the fiber length needed to absorb the pump. Switching to a 975 nm source should enable us to use a shorter final amplifier in order to achieve pulse energies at least double those presented in Fig. 7.4. For example, using an estimated final fiber length of L~1.5 m, and a 0.3 ns stretched pulse duration, with amplifier gain=20 dB, would result in an increased pulse energy threshold for SRS of 38 μJ for a 15 μm diameter core (compared to the L=2 m configuration SRS threshold of 30μJ). Increasing the core diameter to 29 μm would further increase the SRS threshold pulse energy to 100 μJ for an amplifier with gain =15 dB, and to 131 μJ for an amplifier with gain=20 dB.

To estimate the effects of SPM on the quality of the re-compressed pulse, we performed numerical modelling. In performing this modelling, I am grateful to Dr. Rüdiger Paschotta for allowing me to use "ProPulse", which is a numerical modelling package he has written for simulating pulse propagation in fibers, lasers, and OPO cavities. One difficulty of modelling stretched (i.e. chirped) pulses is that the number of grid points is proportional to the product of (Time Range x Frequency Range), so increases with the chirp. As explained in Chapter 2, the

nonlinear phase-shift due to SPM is proportional to the peak power, so the pulse energy and duration can be scaled provided that the original peak power is preserved. To reduce the grid size, a shorter pulse with 1/60 of the original duration, i.e. FWHM = 5 ps, was considered but without changing the 8 nm bandwidth (bandwidth = half of the final CFBG spectral window). The input pulse was a linearly chirped, and has the same peak power as for the 100 μJ, 0.3 ns stretched pulse. The relative importance of SPM and GVD will be slightly different for the shorter pulse, but as the fiber length is short, and the 5 ps pulse is still highly chirped ($\Delta\nu\Delta\tau\sim$ 25 times transform limit), the results from the modelling should provide a good indication of the behaviour of the longer pulse. A second simplification is to model propagation in passive fiber (no gain) by scaling the length of passive fiber to equal L_{eff} of the amplifier fiber (L_{eff} calculated assuming constant gain per unit length). We believe that this length scaling should provide a good indication of the results that would be obtained for a longer fiber which has gain. The simulation parameters were $L_{amplifier}$ = 1.5 m, G=15 dB (L_{eff} = 0.42 m), core diameter = 29 μm, fiber dispersion: D= - 40 ps/(nm.km) throughout. The re-compression was performed by applying a linear chirp (optimised to maximise the peak power), so the higher-order pulse phase distortion caused by SPM remains. Table 7.1 shows the parameters of the re-compressed pulse for the various pulse energies that were simulated.

Table 7.1. Pulse parameters used for numerical simulations in Fig. 7.6.

E (μJ) for 0.3 ns chirped pulse	E (μJ) equivalent for 5 ps chirped pulse	FWHM (fs) of 5ps pulse after propagation and recompression	Peak power (kW)	Pulse quality: $(\Delta\nu\Delta\tau)/(0.44)$, where $\Delta\tau$ is the RMS width (not FWHM)	Dispersion applied by compressor (ps^2)
0.01	1.667x10-4	205	0.732	1.05	-0.379
10	0.1667	239	570	2.19	-0.341
50	0.8333	206	2580	12.2	-0.189
100	1.667	151	6170	24	-0.120

Fig. 7.6 shows the predicted shapes of the re-compressed pulses. The peak powers have been normalised to facilitate comparison of the pulse shapes. Fig. 7.6(a) shows the power of re-compressed pulses on a linear scale; and Fig. 7.6(b) shows the power of re-compressed pulses measured in dB. With power plotted on a linear scale, the duration of the compressed pulse does not appear to change drastically as the energy increases, but the higher energy pulses have distinct side lobes, which contain an increasing fraction of the pulse energy. Fig. 7.6 (b) shows the pulse on a dB scale, and more clearly demonstrates that for the highest energy pulse, there is a substantial fraction of the pulse energy in the pedestal, and that the peak:pedestal contrast ratio has decreased. The decrease in contrast could be detrimental for some applications which require a short interaction time, because the pedestal would arrive well before the peak, and due to the reduced contrast ratio, might have sufficient power to excite the relevant nonlinear process, which would effectively prolong the interaction.

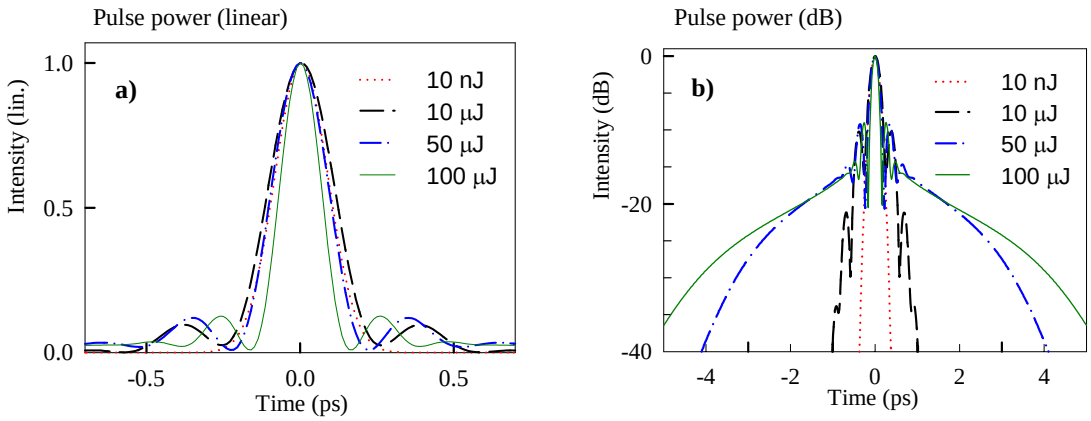

Fig. 7.6. Simulation results showing distortion due to SPM in final amplifier for pulses with 8 nm bandwidth, after recompression by applying a linear chirp. The pulse energy numbers refer to a 0.3 ns duration stretched pulse. (See Table 7.1 for details of pulse parameters.)

From the results of this numerical modelling, we conclude that the effects of SPM induced distortion do not prevent the formation of ~300 fs recompressed pulses, with high peak powers, but that a substantial fraction of the energy starts to be retained in a broad pedestal, which may reduce the range of applications for which the pulses are well suited. Extending the pulse energies to higher levels will require larger core fiber for the final amplifier. The minimum core NA that can reliably be fabricated (also, from a practical standpoint, the minimum core NA that has acceptably low bend losses) is ~0.06. For quasi-single mode fiber (V<3) this limits the core diameter to ~15 μm at a wavelength of 1 μm. However, depending on the length of the amplifier, the diameter of the inner cladding, the doping profile (gain guiding), and on the launch conditions at the input, it may be possible to use low NA multimode fibers (V~5-15) and still obtain $M^2 < 1.2$ output mode quality, as demonstrated in previously reported systems that produced output pulses with energy above 1.2 mJ [1].

7.6 Conclusion

In conclusion, we have developed a CPA system that produces pulses with energy of ~50 μJ immediately after the final amplifier. The maximum pulse energy was limited by the onset of SRS in the final amplifier. The system comprised a mode-locked fiber laser, a pulse selector, a pulse stretcher and compressor, and a cascade of three amplifiers separated by isolators and synchronously time-gated AOMs. Details of all components have been described in previous Chapters. We have described how by using a final amplifier with reduced length of 1.5 m (using 975 nm pump instead of 915 nm pump), and with 29 μm diameter core (15 μm core used initially), it should be possible to obtain 100 μJ pulses from our system assuming gain in the final amplifier of 15 dB, with the energy increasing to 131 μJ assuming 20 dB gain. We have performed numerical modelling with this revised final amplifier design, which demonstrated

that the nonlinear pulse distortion due to SPM should not result in unacceptable degradation of the quality of the recompressed 100 μJ pulses.

References

1. A. Galvanauskas, Z. Sartania and M. Bischoff, "Millijoule femtosecond fiber CPA system," *Advanced Solid-State Lasers, Proceedings*, (2001).

Chapter 8 Direct Pulse Amplification

8.1 Introduction

This chapter describes our measurements of ultrashort pulses directly launched into a cascade of Yb-fiber amplifiers without the use of a pulse stretcher. The threshold pulse energy for unacceptable SRS scales in proportion to the stretched pulse duration [1], and therefore CPA system can provide high pulse energies. However, when the highest pulse energies are unnecessary but the application still requires high average power, the direct amplification setup is highly-suitable since it is simpler (does not require a pulse stretcher and highly-dispersive compressor). The established high performance levels from diode-pumped Yb-doped fiber mean that systems producing such directly amplified pulses are of immediate practical interest. Diode-pumped direct amplification systems based on a single amplifier stage have been demonstrated to be capable of producing ultrashort pulses at average powers of >17 W [2]. However, using a single amplifier stage limits the total gain to ~30-40 dB, which restricts the range of possible applications and sources. For example, the mode-locked Yb-fiber laser described in Chapter 4 is an extremely attractive source, having robust self-start characteristics, and low amplitude noise, but the pulse energy is low (~10 pJ). Use of a single amplifier would thus limit the output pulse energy to around 10 nJ, which is insufficient for many applications. The experiments reported in this chapter demonstrate that multiple cascaded amplifiers can be used to produce pulses with higher pulse energies than single amplifier systems. Pulses have been characterised using SHG FROG in order to directly determine the full chirp profile across the pulse. High quality pulses with energy ~150 nJ and compressed duration ~300 fs have been produced, and such pulses have been used to demonstrate an all fiber pumped femtosecond OPO [3].

Due to the increased pulse peak powers, the directly amplified pulses undergo some degree of nonlinear evolution (SPM) within the amplifiers, and we have studied the effects of this nonlinear evolution on the recompressed pulses. Low energy pulses undergo mostly linear evolution due to the fiber dispersion, and develop a linear chirp which can be compensated using a grating pair at the system output. At the highest pulse energies the pulses develop a parabolic profile, which has recently been described theoretically as an asymptotic solution to the nonlinear Schrödinger equation with constant gain [4]. The theory predicts that parabolic pulses also have a linear chirp, although with different slope compared to the pulses that have

evolved linearly, and so parabolic pulses can also be recompressed to short durations using a grating compressor. The effects of SPM on the quality of the recompressed pulses from the CPA system (Chapter 7) were considered by numerical modelling. The modelling showed that the initial effect of SPM was to reduce the peak:pedestal contrast ratio of the recompressed pulses. The parabolic pulse solution suggests that by undergoing increased nonlinear evolution in the presence of continuous gain, that the chirp across the entire pulse could again become linear (although with a steeper slope) which would result in high peak:pedestal contrast ratio for the recompressed pulses. This makes parabolic pulses particularly interesting for applications where this contrast ratio is important.

The ideal theoretical model of unlimited, spectrally flat, gain bandwidth, and unlimited amplifier length (asymptotic solution) is not realised in a practical system. Finite gain bandwidth will distort the pulse if the nonlinear spectral broadening (due to SPM) creates a pulse bandwidth greater than the amplifier bandwidth. Finite amplifier length will prevent the formation of parabolic pulses if the nonlinear evolution of the pulse has not progressed sufficiently to create a linear chirp across the entire pulse by the end of the amplifier fiber. These constraints have not interrupted parabolic pulse formation in previous experimental reports, which have considered only the evolution of initially unchirped pulses in a single amplifier stage. This chapter reports our results from a system with three amplifiers, which demonstrated how the practical constraints were managed in order to obtain higher energy pulses that could be cleanly recompressed. The two main features of the system that disrupt the steady pulse evolution are that each amplifier in the chain has different parameters such as gain, dispersion and effective nonlinearity (determined by the effective area of the fiber mode); and that in order to prevent cascaded ASE from saturating the gain, it is necessary to optically isolate individual amplifier stages [5], which also introduces lumped losses between each amplifier within the chain (as high as 4.5 dB in our case). To improve our understanding of the pulse evolution towards the asymptotic parabolic shape, we compared the pulse parameters to those predicted by the asymptotic solution and also performed numerical modelling using the experimentally measured amplifier settings. Our numerical predictions of the temporal and spectral widths of the pulses and of the corresponding pulse chirp, were in close agreement with our experimental measurements. Having obtained a good understanding of the system, the next goal will be to use the numerical model to determine the most appropriate setup to obtain directly amplified parabolic pulses with energies up to the SRS threshold energy.

This chapter is structured as follows. In Section 8.2 we describe the experimental setup. In Section 8.3 we outline the numerical model that was implemented to simulate our results. In Section 8.4 we describe our experimental results and compare those results with the results of

our simulations, and with the pulse characteristics calculated from the asymptotic parabolic pulse solution. In Section 8.5 we present our conclusions.

8.2 Experimental setup

The experimental setup as shown in Fig. 8.1 was similar to the CPA system described in Chapter 7. The principal difference is that the pulse stretcher has been removed, and as a result the chirp of the pulse is reduced and a less dispersive compressor is required. Pulses from the oscillator were passed through a high-extinction-ratio EOM, which reduced the repetition rate, and thus enabled increased gain to be obtained from the amplifiers. ASE build-up along the amplifier chain was prevented by using both an isolator and an AOM between each amplifier stage. Polarisation controllers (either wave-plates, or fiber based) were used at each amplifier stage to ensure maximum transmission through the isolators. The AOMs were activated for a short time window in order to transmit the pulses, but block most of the continuous ASE background.

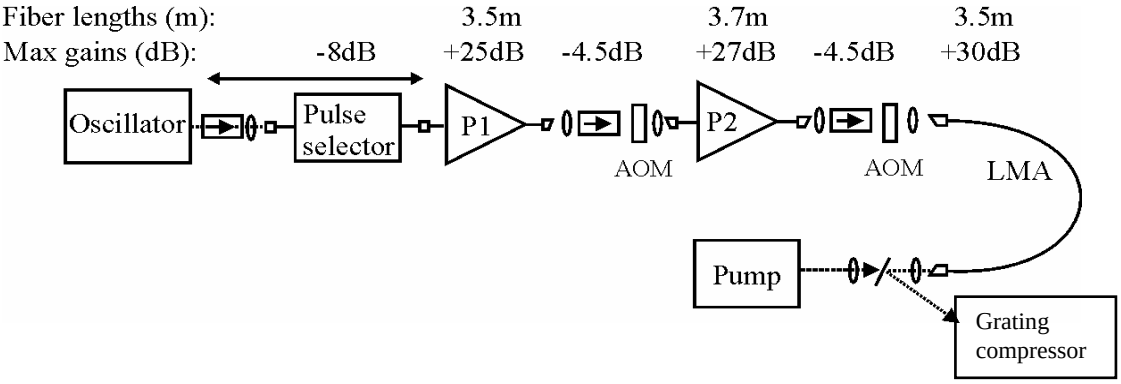

Fig. 8.1. Schematic of the cascaded amplifier system used to study parabolic pulse formation.

The two pre-amplifiers were constructed from conventional single mode Yb-doped fiber, core-pumped via WDM couplers, in a forward pumping configuration for low-noise operation. The power amplifier was constructed from double-clad, LMA fiber (ORC fiber code number HD 406-02), end-pumped by a 6 W, 915 nm fiberised diode source [6]. The coupling losses between each amplifier stage, and the fiber length and maximum gain of each amplifier stage are shown in Fig. 8.1. Details of all of the above components have been described in Chapters 3-7. For the grating compressor we used a pair of 820 groove/mm ruled gratings from Richardson Gratings Laboratory, blazed for a wavelength of 1.2 μm (>80% efficiency at 1.0-1.1 μm). The system produced output pulses with energies in the range 10-340 nJ. Throughout this chapter the individual amplifier stages are referred to as P1 (first pre-amplifier), P2 (second pre-amplifier), and LMA (large mode area power amplifier).

The pulses were characterised both temporally and spectrally as they propagated through the amplifier cascade. The characteristics of the pulses from the oscillator are described in Chapter 4. The pulse FWHM duration at the output from the oscillator was 2.5 ps, with a bandwidth (FWHM) of 18.6 nm, with a positive linear chirp. Due to the normal GVD of the amplifier fiber, the pulses broadened temporally at each amplifier stage, and reached a duration of ~8 ps after the final amplifier. The pulses were then recompressed by propagation through a diffraction grating pair which has anomalous dispersion. The spectral evolution of the pulses was controlled both by the nonlinear action of SPM, which acted to broaden the spectrum, and by gain-filtering due to the finite gain bandwidth of the amplifiers, and which ultimately limits the pulse bandwidth. We measured the pulse spectrum after every amplifier stage using an optical spectrum analyser. Using a 'Modemaster' supplied by Coherent Inc., we measured the beam quality at the output of the LMA to be M^2~1.2. The pulses were also characterised directly after the LMA amplifier using SHG FROG. In addition, non-collinear SHG autocorrelation measurements were recorded for the recompressed pulses (after the grating compressor).

We characterised the system with five different gain (dB) settings to determine which proportion of gain in the various amplifier stages would produce high energy pulses that could be cleanly recompressed. Increased gain was obtained by changing the duty cycle using the EOM. A 20% duty cycle was obtained by using a 200 ns window with a 1 ms period (allows 10 pulses in every 50 to pass through the system). A 5% duty cycle was obtained by passing a single pulse in every twenty (window= 20 ns, period = 370 ns). The gain was calculated by comparing the average input and output powers from each amplifier stage. The gain settings, labelled I-V, are shown in Table 8.1 in order of increasing final pulse energy together with the associated pulse energies at the system output. Reference is made to these labels throughout the results section of this chapter. The gain in P1 was high for all settings. Setting I produced low energy pulses and had low gain in both P2 and LMA. Settings II and IV had relatively even gain in both P2 and LMA; the absolute gain was higher for IV than II, which led to increased energy pulses at the system output. Settings III and V had low gain in P2 and high gain in LMA; setting V had higher absolute gain and produced higher energy pulses. The proportion of total gain in the smaller core (high effective nonlinearity) P2, compared to the gain in the larger core (lower effective nonlinearity) LMA, was observed to have a strong influence on the shape of the chirp of the final pulses.

Table 8.1 Gain distribution in amplifier chain.

	Gain (dB)			Duty Cycle (%)	Average Power (W)	Pulse Energy (nJ)
	P1	P2	LMA			
I	17.0	9.5	11.5	100	0.60	11.2
II	20.4	11.3	12.6	20	0.52	48
III	22.6	4.3	22.2	5	0.39	146
IV	22.6	12.5	14.8	5	0.48	177
V	22.6	4.3	25.8	5	0.90	334

The system performance for each of these gain settings is presented in Section 8.4. However, before discussing these results we first briefly describe the numerical model that we used to simulate our system.

8.3 Numerical model

As described in Chapter 2, we use a modified nonlinear Schrödinger equation (NLSE) in order to model the system. We used a Lorentzian gain profile as shown in the equations below, and included both 2nd and 3rd order dispersion, lumped fiber losses between the individual amplifiers, and the Kerr effect [7],

$$\frac{\partial A}{\partial z} = -\frac{i}{2}\beta_2\frac{\partial^2 A}{\partial T^2} + \frac{1}{6}\beta_3\frac{\partial^3 A}{\partial T^3} - \frac{\alpha}{2}A + i\gamma\left|A\right|^2 A - \frac{i}{2}\int_{-\infty}^{+\infty}\chi_D(\nu)\tilde{A}(z,\nu)\exp(-i2\pi\nu T)\,d\nu \quad , \qquad \text{Eqn. 8.3:1}$$

where

$$\chi_D = \frac{g(z)\left(i - 2\pi T_2\right)}{1+\left(2\pi\nu T_2\right)} \quad . \qquad \text{Eqn. 8.3:2}$$

The amplifiers themselves were modelled with uniform gain per unit length, and a Lorentzian gain profile(see Eqn. 8.3:2), where T_2 is the oscillator relaxation time for the Lorentzian gain, selected to give the appropriate bandwidth. The modified NLSE was solved using the standard split-step Fourier method with an appropriate change in fiber and gain parameters for each amplifier stage. We are grateful for the assistance of Neil Broderick, who performed the numerical simulations. The dispersion parameters used for all amplifiers were: β_3 =25 x 10^{-3} ps^2/m (D= -50 ps/nm/km), β_3 =2.5 x 10^{-5} ps^3/m. The effective nonlinearity $\gamma = \left(2\pi n_2\right)/\left(\lambda A_{eff}\right)$ was calculated with n_2 =2.35 x 10^{-20} m^2/W and using the effective mode area for each amplifier as follows: A_{eff} = 15 μm^2 for both P1 and P2, and A_{eff} = 250 μm^2 for the LMA.

For the simulations, the input pulse shape to amplifier P1 was a positive-linearly chirped Gaussian pulse with duration (FWHM) of 2.5 ps, and a bandwidth (FWHM) of 13.6 nm. This pulse duration was that measured at the output of the oscillator. The pulse bandwidth (hence

chirp) was chosen such that after linear propagation through the (measured) length of the amplifiers, with the above dispersion per unit length, the pulse duration (FWHM) would be consistent with that measured after the LMA with the system operating at low power (corresponding to linear pulse evolution). The bandwidths of the three amplifiers were estimated from the measured spectra after each stage of amplification for pulses at low powers. The amplifier bandwidths chosen for modeling were 10 nm for P1, 15 nm for P2, and 40 nm for the LMA. The relatively narrow bandwidths of P1 and P2 are thought to be due to gain narrowing, and to spectral filtering from the interplay of the fiber birefringence and the polarising isolators between the amplifiers, which could be improved by the use of a less birefringent fiber. With the above parameters held fixed, the only variable parameters in our simulations were the gains of the three amplifiers. For each of the experimental pulses modelled, the gain of each amplifier stage was chosen to match the experimentally measured gain in pulse energy (Table 8.1).

The parabolic solution to the NLSE with gain is a recently discovered phenomenon resulting from a self-similarity analysis of pulse evolution in fiber with normal dispersion and constant gain. As pulses propagate towards the asymptotic parabolic form, they expand both spectrally, due to the nonlinear process of self-phase modulation (SPM), and temporally, due to group velocity dispersion (GVD), but maintain a parabolic profile. Importantly the pulses also develop a highly linear chirp across the central region of the pulse, and are therefore compressible to short durations, and so are suitable for the generation of high-energy, femtosecond pulses. The asymptotic characteristics of the parabolic pulses are determined only by the initial pulse energy, and by the amplifier characteristics, with the initial pulse shape determining only the map towards the asymptotic shape. Parabolic pulses have been demonstrated experimentally, and the expected characteristics including the parabolic spectral and temporal profile, and linear chirp have been measured [4].

The analytic asymptotic solution in an amplifier with constant gain (g) per unit length is given by the following equation:

$$A(z,T) = A_0(z)\{1-[T/T_0(z)]^2\}^{1/2}\exp\left[i\phi(z,T)\right], \quad |T| \le T_0(z) \ , \qquad \text{Eqn. 8.3:3}$$

$$A(z,T) = 0, \quad |T| > T_0(z) \ , \quad \text{where} \quad \phi(z,T) = \phi_0 + 3\gamma(2g)^{-1}A_0^2(z) - g(6\beta_2)^{-1}T^2 \ .$$

Once in the asymptotic regime, the parabolic shape is maintained, with exponential scaling of the amplitude, and of the effective width parameter according to:

$$A_0(z) = 0.5(gE_{IN})^{1/3}\left(\frac{\gamma\beta_2}{2}\right)^{-1/6}\exp\left[gz/3\right] \ , \qquad \text{Eqn. 8.3:4}$$

$$T_0(z) = 3g^{-2/3}E_{IN}{}^{1/3}\left(\frac{\gamma\beta_2}{2}\right)^{1/3}\exp[gz/3] \quad . \qquad \text{Eqn. 8.3:5}$$

The pulse chirp is linear in time: $\delta\omega = -\frac{\partial\varphi}{\partial T} = g(3\beta_2)^{-1}T$, and the slope of the chirp is constant: $g(3\beta_2)^{-1}$. In the forward or reverse pumped configuration of P2 or LMA respectively, the gain will vary along the amplifier length compared to our assumption of constant gain. However, parabolic pulses have been shown to form (using numerical simulations and self-similarity analysis) in amplifiers with both exponentially increasing and decreasing gain profiles, and the principal difference compared to the case of uniform gain was the rate of parabolic pulse formation [8]. We therefore believe that the calculations assuming uniform gain should provide an approximate indication of the chirp if the pulses were strongly evolving toward the asymptotic parabolic form, and in Section 8.4, we show a comparison of the slope of the chirp calculated for an asymptotic parabolic pulse (using the above equation) and the measured slope of the chirp of the experimental pulses.

8.4 Results and discussion

To characterise the evolution of the pulses, we measured the spectrum after the oscillator and each subsequent amplifier stage. We then used SHG FROG to measure the temporal profile and phase of the pulses at the output of the final amplifier [9]. FROG is a technique that uses a spectrally resolved autocorrelation to retrieve the phase information of the pulse. We used a grating pair to compress the pulses, and we performed SHG autocorrelation measurements on the recompressed pulses. A summary of the experimental data for a typical pulse (Energy =146 nJ) are shown in Fig. 8.2. The pulse spectrum after the LMA is shown in Fig. 8.2 (a). The temporal profile of the pulse at the output from the LMA, as retrieved from our SHG FROG measurements, is shown in Fig. 8.2 (b). The figure also shows the chirp of the pulse, which is linear across the central region of the pulse, but changes slope in the wings of the pulse. Fig. 8.2 (c) shows the non-collinear second harmonic generation (SHG) autocorrelation of the recompressed pulse after a suitably optimised grating pair compressor.

Since the grating-based compressor provides a mostly linear chirp, the quality of the recompressed pulses can be predicted from the chirp of the pulse after the final amplifier; a linear chirp across the entire pulse should lead to a pedestal-free recompressed pulse, whereas a pulse with a chirp that varies nonlinearly, e.g. with a different slope of the chirp in the wings compared to the central part of the pulse, would prevent the compression of all parts of the pulse. The nonlinear effects of SPM accumulate more rapidly in the most intense central portion of the pulse relative to the nonlinear effects in the wings of the pulse. The slope of the

chirp therefore changes first in the central portion of the pulse, and only changes in the wings of the pulse after substantial amplification. Due to the large effective mode area, LMA fiber has a low effective nonlinearity compared to standard fiber. We used LMA fiber for the final amplifier. In contrast, the pre-amplifiers were constructed from standard single mode fiber. By varying the balance of the gain between the three amplifier stages, we changed the relative strength of the nonlinear evolution of the pulses. As described in Section 8.3, we performed full numerical simulations using the experimental pulse parameters, which we also compared with the experimental data. In addition, we also calculated the slope of the chirp for an asymptotic parabolic pulse for comparison with the measured slope of chirp.

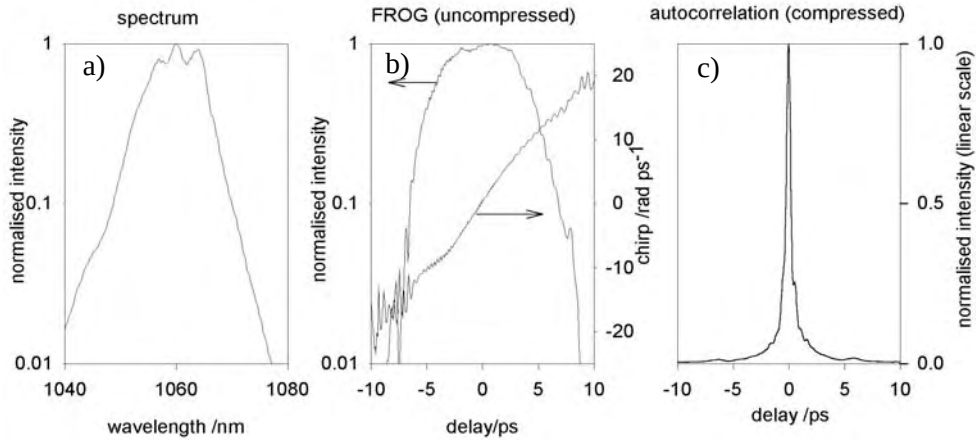

Fig. 8.2. Results summary for typical parabolic pulse with E=146 nJ (pulse III from Table 8.1). (a) Spectrum. (b) Temporal profile. (c) Autocorrelation of recompressed pulse.

The variation of the pulse parameters was investigated in detail using the five amplifier gain settings recorded in Table 8.1, and the results are presented in the following subsections. In Section 8.4.1 we present experimental spectra recorded after each section of the system. In Section 8.4.2 we present both experimental and simulation results for the temporal profile and chirp of the pulses after the final amplifier. In Section 8.4.3 we present experimentally measured SHG autocorrelation results for recompressed pulses. In Section 8.4.4 we compare the pulse parameters after the final amplifier to those calculated from the analytic asymptotic solution.

8.4.1 Spectral data after each section of the system

The spectra obtained from the oscillator, and after each amplifier stage, are shown in Fig. 8.3 for three different gain settings. The evolution of a low energy (11 nJ) pulse (I fromTable 8.1) is shown in Fig. 8.3(a). The spectrum after the amplifiers is narrower than that from the oscillator as a result of gain narrowing. Fig. 8.3(b) shows the results for a higher energy (177 nJ) pulse (IV) produced from relatively high gain in P2 compared to the LMA. The spectrum from P2 already shows the characteristic broadened spectrum associated with parabolic pulse formation

with peaks at the longest and shortest wavelengths ("batman" shape) [10]. The nonlinear evolution has continued in the LMA resulting in further broadening. Fig. 8.3(c) shows the highest energy (334 nJ) pulse (V) that was studied. This pulse was produced from relatively weak amplification in P2 and strong amplification in the LMA. The "batman" shape does not emerge until after the LMA. The shoulder in the LMA spectra at ~1040 nm which appears ~15 dB lower than the peak, as seen in Fig. 8.3(b) and (c) is due to cascaded ASE because of the reduced pulse repetition rate used to obtain such high energy pulses. ASE is less prominent in Fig. 8.3(a) because the low energy pulse was produced using a high repetition rate, so the amplifier gain was saturated by the signal.

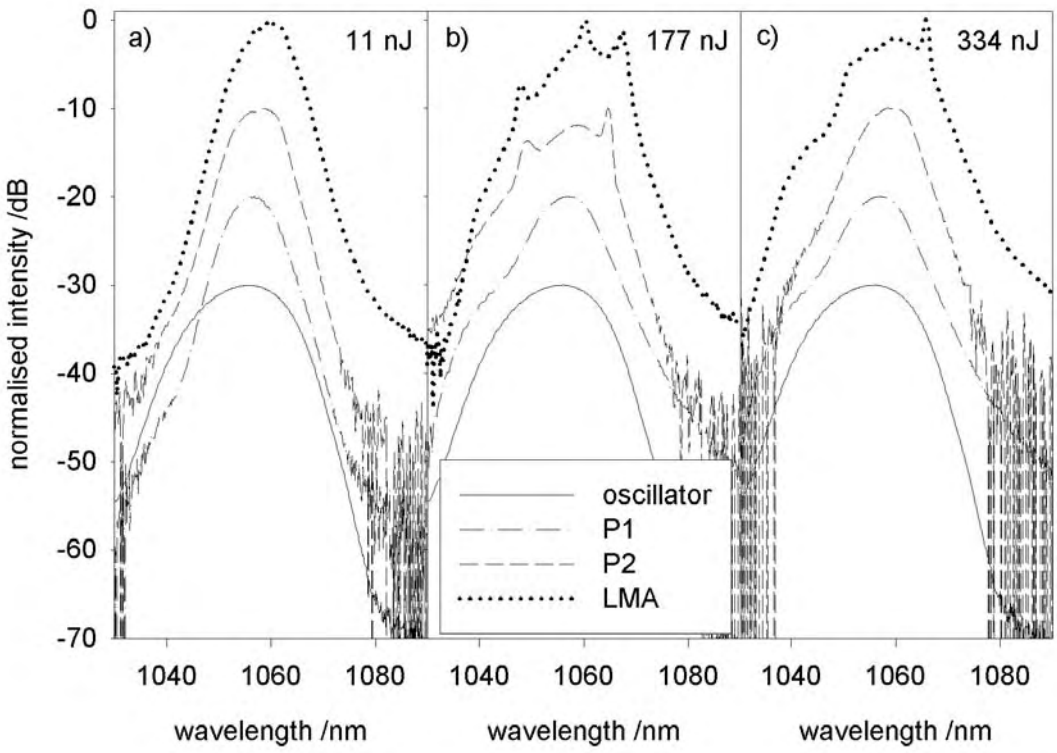

Fig. 8.3. Evolution of the pulse spectrum as it passes through the amplifier chain for; a) pulse I (11nJ), b) pulse IV (177nJ), c) pulse V (334nJ).

8.4.2 Phase characteristics after final amplifier

We investigated the properties of the pulses emerging from the LMA using SHG FROG. The FROG fitting errors [9] that we achieved ranged from 0.006 to 0.02, so represent a good fit to the data. Fig. 8.4 shows the pulse shape and chirp of (a) 11nJ pulse (I), (b) 146nJ pulse (III), and (c) 334 nJ pulse (V), as reconstructed from FROG data (solid) and from our numerical simulations (dotted). All of the essential temporal and spectral features in the pulses are present in the numerical simulations. The chirp is seen to be linear across the central region of the pulse, as is characteristic of parabolic evolution. Note that both the numerical simulations and

experimental results show that the slope of the chirp is different in the wings of the pulses as compared to the central region.

At low energies the slope of the chirp tends to 2 rad.ps^{-2}, due to the linear dispersion, determined by the total length of fiber in the system. For higher pulse energies the slope of the chirp in the central region of the pulse increases, but remains linear, as expected for parabolic evolution. Although not shown in this figure, we note that the slope of the chirp is higher for pulses where the amplification was strong in P2 than for pulses where the main amplification took place in the LMA. This is due to more prominent nonlinear effects in P2 due to the smaller core size (compared to LMA). The results from the numerical simulations are again in close agreement with the experimental data.

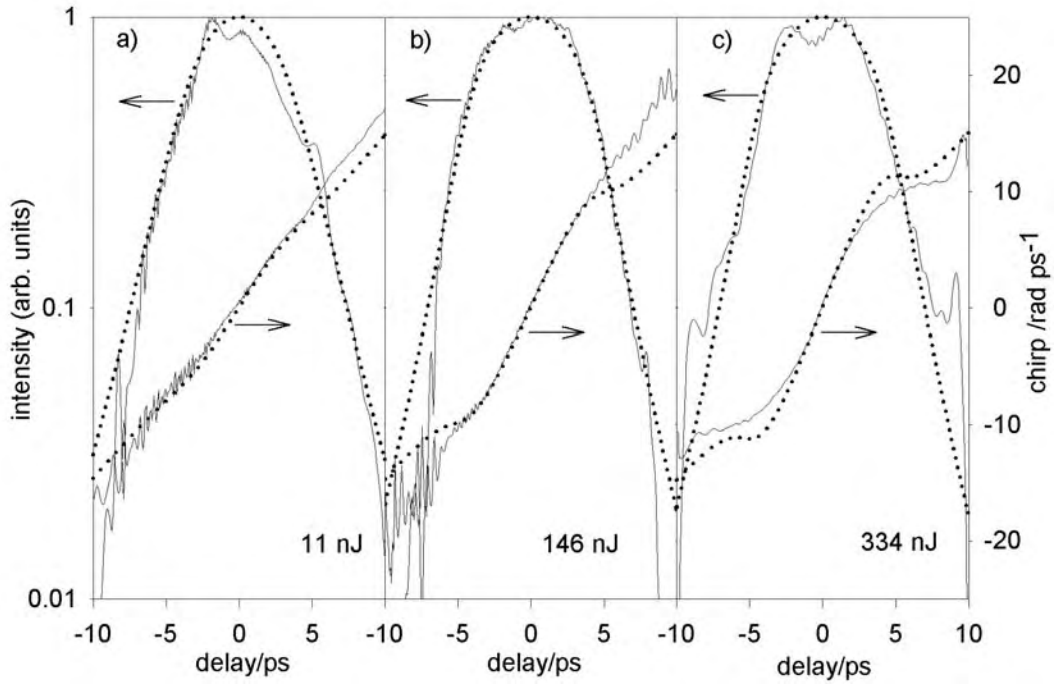

Fig. 8.4. The measured retrieved FROG data (solid) and numerical simulations (dotted) of pulse shape and chirp. a) pulse I (11 nJ), b) pulse III (146 nJ), and c) pulse V (334 nJ).

Fig. 8.5 shows plots of (a) the spectral width, (b) the temporal width, and (c) the slope of the chirp at the centre of the final pulses, as a function of pulse energy, as obtained from both FROG measurements (circles) and our numerical simulations (diamonds). The parameters displayed were chosen because they characterised the nonlinear evolution of the pulses and in a linear system they would not depend on the amplifier gain. It can be seen from Fig. 8.5 that there are two distinct regimes of pulse formation. The first regime is characterised by pulses II and IV (open circles) which, for a given pulse energy, have relatively broad spectral widths, broad temporal widths, and a high slope of the chirp; and the second regime is characterised by

pulses III and V (filled circles), which have relatively narrow spectral widths, narrow temporal widths and a low slope of the chirp. The most striking difference between these two regimes is in the spectral width of the pulses. These regimes can be clearly identified in both the numerical and experimental results. The first regime corresponds to approximately equal gain in P2 and LMA such that the nonlinear pulse formation occurs predominantly within P2. The second regime is when most of the gain is in the LMA such that the nonlinear pulse formation is predominantly within the LMA. In the first regime, the pulses see large nonlinear effects due to the high gain in P2. In the second regime, the peak powers are smaller in the preamplifiers (due to the smaller gain), and hence the nonlinear effects are less pronounced.

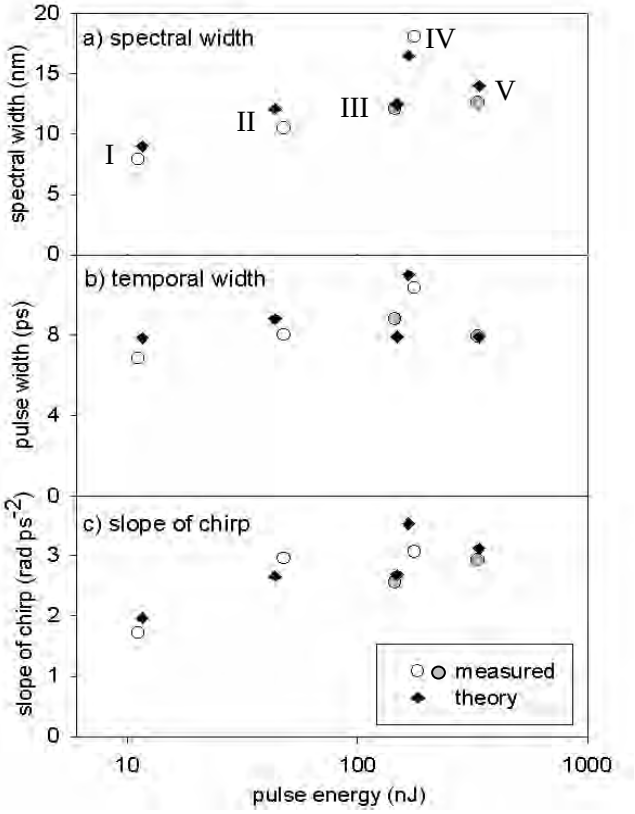

Fig. 8.5. Plots of a) spectral width, b) temporal width and c) slope of chirp (at the centre of the pulse) against pulse energy. The circles represent measured values, and the diamonds are calculated from the results of our simulations. Open circles: strong gain in P2; Filled circles: gain predominantly in LMA.

8.4.3 SHG autocorrelation measurements of compressed pulses

The pulses from the LMA were passed through a grating pair, which compensated the linear chirp. The grating separation was optimised experimentally for each pulse (I-V) in order to minimise the FWHM of the autocorrelation peak. Fig. 8.6 shows SHG autocorrelations of the compressed pulses. Autocorrelation FWHM widths were in the region of 440-490 fs, indicating compressed pulse widths of ~300 fs (assuming Gaussian profile). Fig. 8.6(a) shows how the autocorrelations vary with pulse energy in the regime where the gain is mainly in the LMA. At

the highest energies the autocorrelations have broad wings, though the width of the central peak changes little. Fig. 8.6(b) shows the autocorrelations of two pulses of similar energy, but representing the two different regimes of amplification. It can be seen that the 177 nJ pulse (IV), which was strongly amplified in P2, has more structure in the wings and a much lower fraction of its energy in the central peak compared to the pulse strongly amplified in the LMA (III), which is consistent with the more nonlinear chirp measured for the uncompressed pulse. The small features visible in several of the autocorrelations at ±6 ps are believed to be due to cross correlations between the fundamental and a higher spatial mode propagating at a different velocity in the slightly multimoded LMA.

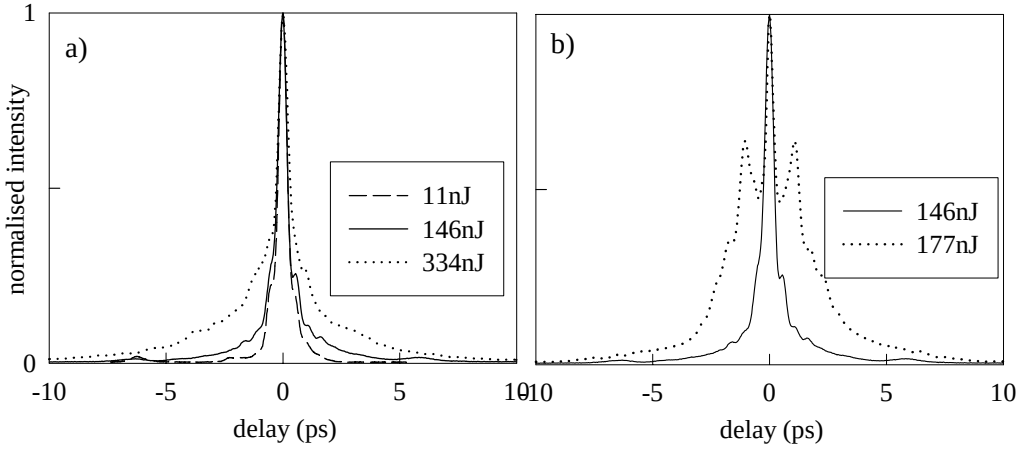

Fig. 8.6. SHG autocorrelation traces of pulses after compensation of the linear chirp using a grating pair. a) Pulses of various energies (I, III, V) where gain is predominantly in LMA, b) pulses of similar energy with gain predominantly in LMA (III solid) and with strong gain in P2 (IV dotted).

8.4.4 Comparison to asymptotic analytic solution

Here we compare the slope of the chirp and the duration of the measured pulses with those predicted by the analytic asymptotic parabolic solution (Eqn. 8.3:3). This comparison provides an indication of the extent to which the pulses have evolved towards the parabolic form.

We have calculated the slope of the chirp ($g/(3\beta_2)$) that would be expected for a parabolic pulse after P2 and LMA, using β_2 = 25 x 10^{-3} ps^2m^{-1}, and the measured gain from Table 8.2 for each of the pulses I-V (assuming constant gain per unit length). The results are shown in Table 8.2 together with the measured value of the slope of the chirp after the LMA from Fig. 8.5c). We measured the slope of chirp only after the LMA, but we have calculated the predicted value for the slope of chirp after both P2 and after the LMA because of the possibility that a parabolic pulse, having formed in the relatively high nonlinearity, smaller core of P2, may subsequently evolve linearly in the larger core LMA. Comparing the results for measured slope of the chirp with those of the calculated value expected for the asymptotic parabolic pulse form, shows that the two values are different. The results in Table 8.2 suggest that although the pulses from the

system have developed a "batman" spectrum (Fig. 8.3), and nonlinear chirp (Fig. 8.4), further evolution towards the parabolic form would be possible if increased gain or longer amplifier lengths were available.

Table 8.2 Slope of chirp: Experimental values and values calculated for parabolic pulses.

Pulse number	Gain (g) in P2 (m^{-1})	Gain (g) in LMA (m^{-1})	Theory: slope of chirp after P2 – parabolic pulse (rad/ps^2)	Theory: slope of chirp after LMA – parabolic pulse (rad/ps^2)	Experimental slope of chirp after LMA (rad/ps^2)
I	0.59	0.76	7.88	10.1	1.9
II	0.70	0.83	9.37	11.1	3.1
III	0.27	1.46	3.57	19.5	2.5
IV	0.78	0.97	10.4	13.0	3.2
V	0.25	1.70	3.6	22.6	2.9

We have also compared the duration of the measured pulses to those predicted for parabolic pulses with the corresponding energies (Eqn. 8.3:5). For given amplifier parameters g, β_2, γ, the duration of a parabolic pulse (FWHM = $1.44T_0$) is determined absolutely by the pulse energy. The pulse durations calculated the parabolic using the estimated launched pulse energy at the input to each amplifier, and at the output of the LMA are shown in Table 8.3. The table also shows the experimentally measured results which were estimated using the pulse duration at the system output and allowing for pulse dispersion based on the measured spectral widths shown in Fig. 8.5(a).

Table 8.3 Pulse duration: Experimental results and values calculated for parabolic pulses.

Pulse energy (nJ)				Experimental FWHM (ps) (estimated)				Theoretical Parabolic FWHM (ps)			
P1 input	P2 input	LMA Input	LMA output	P1 input	P2 input	LMA input	LMA output	P1 input	P2 input	LMA input	LMA output
0.01	0.22	0.79	11.2	3.5	4.5	5.5	6.8	1.43	1.79	1.04	2.5
0.01	0.49	2.63	47.8	3.5	4.5	6.5	8.0	0.38	2.07	1.45	3.8
0.01	0.81	0.87	144.3	3.5	5.0	6.4	8.7	0.36	4.67	0.69	3.8
0.01	0.81	5.74	173.5	3.5	5.0	7.5	10.2	0.36	2.29	1.70	5.3
0.01	0.81	0.87	330.5	3.5	5.0	6.4	7.9	0.36	4.67	0.62	4.5

The results from Table 8.3 show that the experimental pulse duration is longer than that predicted for a parabolic pulse at all points along the system, but that the rate of increase in pulse width as the pulse passes through the system is greater for the parabolic pulse, so that the pulse widths slowly converge. For the lowest energy pulse (I) that evolved mostly linearly, the duration increases by a factor of 2 experimentally and by a theoretic factor of 1.7 for a parabolic pulse; and for the highest energy pulse (V), the duration increases by a factor of 2.3 experimentally and by a theoretic factor of 12.5 for a parabolic pulse. Therefore the relative importance of nonlinear broadening is much greater for the parabolic pulse than for the highest energy experimental pulse, which remained mostly controlled by linear broadening (GVD). We note that previous studies of parabolic pulse formation have considered only the evolution of

unchirped pulses at the system input. Unchirped pulses converge towards the equivalent energy parabolic form because a pulse that is initially longer than the corresponding parabolic pulse has less bandwidth, and so broadens less rapidly, whereas a pulse that is initially shorter than the equivalent energy parabolic pulse has more bandwidth, and so broadens more rapidly.

One reason why our experimental pulses are longer than the parabolic form, and therefore evolve mostly linearly, is that the experimental pulses are strongly chirped at the input to P1 (duration = 35 x transform limit). We suggest that the chirped pulses in our system converge only slowly to the equivalent energy parabolic pulse duration because the larger bandwidth of our chirped pulses (compared to transform limited pulse) caused more rapid temporal broadening due to GVD. We also compared the pulse bandwidth at the system output to that of the equivalent energy parabolic pulse. High energy parabolic pulses are strongly chirped, so the bandwidth can be estimated from the chirp across the temporal FWHM, to give $\Delta\omega = g(3\beta_2)^{-1}T_{FWHM}$, which we estimated to correspond to 61 nm for a 330 nJ pulse (V). The bandwidth of the parabolic pulse is greater than that of the observed pulses, which indicates the importance of nonlinear spectral broadening for the evolution of parabolic pulses and which is relatively weaker for our experimental pulses.

We suggest that in the future, it would be interesting to model the results of some chirp compensation at the input to P2 (possibly implemented in practice using holey fiber with anomalous dispersion), or using increased gain in P2 and LMA. It may then be possible to optimise the system to produce highly nonlinear evolution towards high energy parabolic pulses. Further evolution towards the parabolic pulse form should produce a highly linear chirp across the entire pulse spectrum and result in an improved peak:pedestal intensity ratio, which could be useful for applications where this is an important consideration. Greater nonlinear evolution will also result in pulses with greater bandwidth, so to obtain true parabolic pulses from the system we may also need to consider increasing the bandwidth of our amplifiers to support those pulses.

8.5 Conclusion

In conclusion, we constructed an Yb-fiber based oscillator and amplifier system that produced good beam quality (M^2~1.2) with pulses of energies up to ~150 nJ, which could be cleanly compressed to a FWHM duration of ~300 fs. The system produced pulses of slightly longer duration with energies as high as 334 nJ. The system was robust, diode-pumped, all-fiber based and therefore suitable for wide practical application, and has been used to drive a synchronously pumped OPO that produced 330 fs pulses with an average power of 90 mW [3]. The OPO signal was tuneable across the wavelength range from 1.55-1.95 μm.

We have performed a detailed characterisation of the pulses from the system using SHG FROG, and have devised a numerical model based on the modified NLSE with gain that produced simulated pulse parameters in close agreement with the observed values. We have also compared the evolution of the pulses to the theoretically predicted asymptotic solution, which is a pulse with parabolic spectral and temporal shape and linear chirp. This is the first time, to our knowledge, that the evolution of directly amplified pulses has been studied in a multi-stage amplifier cascade. We determined that for the experimental pulses, although SPM was clearly evident, there was scope for further nonlinear evolution towards the parabolic form.

We envisage that with our improved understanding of the direct amplification process it should be possible to increase the power levels achieved whilst still producing high quality recompressed pulses. We propose to use our numerical model to investigate the capability of our system to produce higher energy pulses with an evolution that has progressed further towards the asymptotic parabolic profile, and which we expect could enable <200 fs pulses with >>500 nJ energy to be produced. As discussed in relation to the CPA system (Chapter 7), SRS will ultimately limit the maximum energy that can be obtained. For example, the SRS threshold energy would be ~0.4 μJ for 8 ps pulses with a 15 μm diameter core amplifier with L=3.5 m, and total gain of 20 dB. For the same pulse parameters and amplifier gain, the SRS threshold energy would increase to ~3 μJ for a core diameter of 30 μm, and L=2 m. We propose to use the modelling to determine the most appropriate configuration for obtaining cleanly recompressed pulses with energy approaching this SRS threshold, and then to conduct these experiments.

Finally, as a practical point to be considered for future experiments, we briefly note our observation of damage to the output facet of the LMA when running with high-energy parabolic pulses. After a period of operating the system at ~300 mW average power (measured at the output of the LMA), we observed that the output mode quality would deteriorate strongly from the initial gaussian mode profile (M^2~1.1). Examination of the end of the fiber under the microscope revealed damage to the fiber facet and the adjacent ~1 cm of the fiber. This observation of facet damage is consistent with observations by others and attributed to breakdown at the silica/air interface due to the high pulse fluence [11]. We considered that our observations were most often observed with this parabolic pulse system, rather than with the CPA system (Chapter 7), because the stochastic nature of the damage process means that a long run-time (this system was used to pump a femtosecond optical parametric oscillator [3]) resulted in increased incidence of failure. A solution to this facet damage may have to be applied in the future, and a standard technique is to splice a short length of "dummy" fiber (no core) to the end of the fiber. The diverging beam, with half angle = $\sin^{-1}(NA/n_{core})$, is expanded to just less than the dummy-fiber diameter (by cleaving the dummy-fiber to the appropriate length). The fluence

of the expanded beam is thus reduced below the damage threshold of the silica/air interface, and facet damage is prevented [11].

References

1. R. G. Smith, "Optical power handling capacity of low loss optical fibers as determined by stimulated Raman and Brillouin scattering," Applied Optics **11,** 2489 - 2494 (1972).
2. J. Limpert, T. Schreiber, T. Clausnitzer, K. Zollner, H. J. Fuchs, E. B. Kley, H. Zellmer and A. Tünnermann, "High-power femtosecond Yb-doped fiber amplifier," Optics Express **10,** 628-638 (2002).
3. M. V. O'Connor, M. A. Watson, D. P. Shepherd, D. C. Hanna, J. H. V. Price, A. Malinowski, J. Nilsson, N. G. R. Broderick and D. J. Richardson, "Synchronously pumped optical parametric oscillator driven by a femtosecond mode-locked fiber laser," Optics Letters **27,** 1052-1054 (2002).
4. M. E. Fermann, V. I. Kruglov, B. C. Thomsen, J. M. Dudley and J. D. Harvey, "Self-similar propagation and amplification of parabolic pulses in optical fibers," Physical Review Letters **84,** 6010-6013 (2000).
5. B. Desthieux, R. I. Laming and D. N. Payne, "111 kW (0.5 mJ) Pulse Amplification at 1.5-microns Using a Gated Cascade of 3 Erbium-Doped Fiber Amplifiers," Applied Physics Letters **63,** 586-588 (1993).
6. N. G. R. Broderick, H. L. Offerhaus, D. J. Richardson and R. A. Sammut, "Power scaling in passively mode-locked large-mode area fiber lasers," IEEE Photonics Technology Letters **10,** 1718-1720 (1998).
7. G. P. Agrawal, *Nonlinear Fiber Optics*, Academic Press (San Diego), 2nd (1995).
8. V. I. Kruglov, A. C. Peacock, J. M. Dudley and J. D. Harvey, "Self-similar propagation of high-power parabolic pulses in optical fiber amplifiers," Optics Letters **25,** 1753-1755 (2000).
9. R. Trebino, K. W. DeLong, D. N. Fittinghoff, J. N. Sweetser, M. A. Krumbugel, B. A. Richman and D. J. Kane, "Measuring ultrashort laser pulses in the time-frequency domain using frequency-resolved optical gating," Review of Scientific Instruments **68,** 3277-3295 (1997).
10. V. I. Kruglov, A. C. Peacock, J. D. Harvey and J. M. Dudley, "Self-similar propagation of parabolic pulses in normal- dispersion fiber amplifiers," Journal of the Optical Society of America B-Optical Physics **19,** 461-469 (2002).
11. C. C. Renaud, J. A. Alvarez-Chavez, J. K. Sahu and J. Nilsson, "7.7 mJ pulses from a large core Yb-doped Cladding pumped Q-switched fibre laser," Conference on Lasers and Electro Optics (CLEO), Vol. 56 of OSA Trends in Optics and Photonics Series (Optical Society of America, Washington, D.C., 2001) paper CTuQ5 (2001).

Chapter 9 Solitons in passive holey fiber

9.1 Introduction

This chapter describes our demonstration of linear dispersion compensation, soliton pulse formation, soliton compression, and ultra-broad supercontinuum generation in a HF that has anomalous dispersion for wavelengths above 800 nm. The HF was seeded with ultrashort pulses from the diode-pumped, Yb-doped fiber oscillator described in Chapter 4, operating with either one or a pair of amplifiers in a direct amplification configuration, as described in Chapter 8. When it was initially published, the work was the first direct demonstration of linear dispersion compensation in an anomalously dispersive HF at wavelengths below 1.3 μm [1, 2]. Soliton propagation in HF had previously been demonstrated over 3 soliton periods, seeded with a Ti:Sapphire laser at ~820 nm [3]. Our report of soliton propagation over 475 soliton periods therefore represented an advance over previous work, and demonstrated the potential for HF based ultrashort pulse transmission for practical applications requiring a wavelength below 1.3 μm e.g. ultrafast spectroscopy. Our work was novel because of the new seed wavelength provided by our Yb-fiber oscillator. The results show the compatibility of the rapidly developing HF technology with our practical Yb-doped fiber source for a wide range of potential applications.

The use of soliton effects such as nonlinear pulse compression, propagation, and the soliton self-frequency shift (SSFS) in optical fiber have been exploited in a variety of sources operating at wavelengths above 1.3 μm, most commonly using lasers based on Er-doped fiber which operate around 1550 nm [4]. However it has not been possible to exploit soliton effects within sources operating in the visible and near infrared regions of the spectrum, since conventional single mode fibers display normal dispersion at wavelengths below 1.3 μm. HF technology, has now enabled the design and fabrication of fibers with anomalous dispersion at wavelengths as short as 500 nm [5], and HFs have been shown to be capable of supporting soliton propagation over a distance of ~3 soliton periods when seeded from a Ti:Sapphire laser operating at 800nm [3]. Whilst the bulk Ti:Sapphire systems used to seed the initial demonstrations of soliton and supercontinuum effects in HF are suitable for research, they are far from ideal if one wishes to develop practical sources based on HF technology. The results presented in this chapter demonstrate that the Yb-doped fiber system reported in the first part of this thesis is capable of

achieving the pulse durations and energies required to exploit the unusual nonlinear properties of HFs.

This chapter is organised as follows. Section 9.2 describes the characteristics of the HF used, and our experimental setup. In Section 9.3 we describe results showing linear dispersion compensation and soliton formation. Section 9.4 describes our demonstration of soliton transmission and supercontinuum generation, and Section 9.5 presents our conclusions.

9.2 Characteristics of the holey fiber

A scanning electron microgram (SEM) image of the robust, jacketed, polarisation-maintaining HF used in our experiments is shown inset to Fig. 9.1. The fiber has a small ~1.6 μm diameter core with an effective mode area, A_{eff} ~3 μm^2 at λ=1.06 μm, which is approximately 20 times smaller than for conventional fibers at this wavelength. The small core also gives rise to the increased power densities and hence high effective nonlinearity of this fiber [4]. The fiber in Fig. 9.1 has a zero dispersion wavelength (λ_0) of ~800nm (predicted with a full vector numerical model [6], using the SEM photograph of the fiber to define the transverse refractive index distribution).

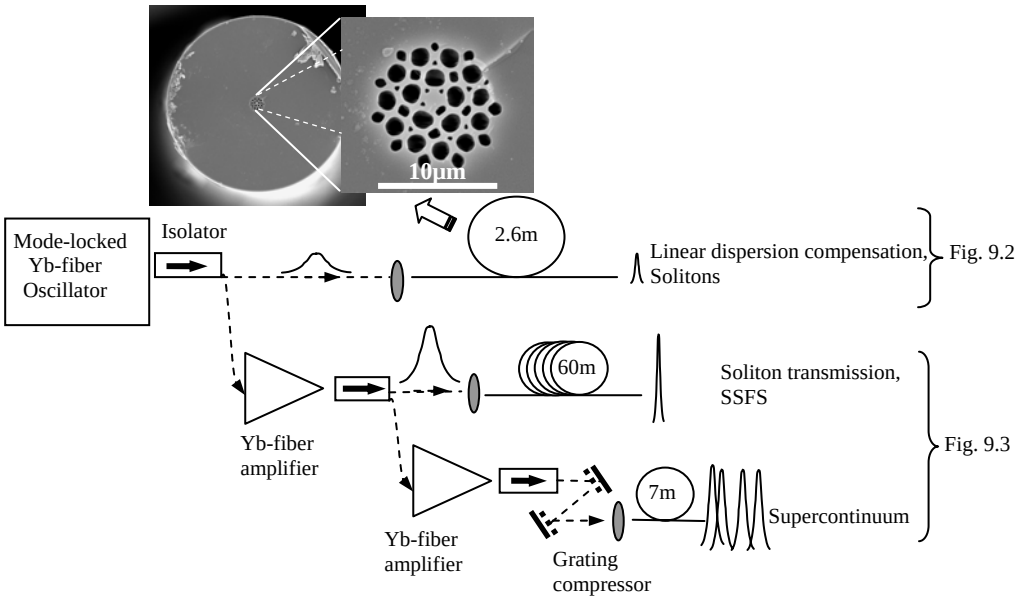

Fig. 9.1 Experimental system configuration. Inset: SEM of HF used for the pulse compression and preliminary soliton experiments.

The high (measured) transmission loss of ~1dB/m is principally due to confinement loss, and can be greatly reduced by adding more rings of holey structure around the core. This was done to produce the fiber used for the supercontinuum demonstration reported in this chapter, which had a much-reduced loss of 0.1dB/m, and similar fibers with losses as low as 0.01dB/m (at

1550 nm) have been reported [7]. The fiber is rigorously single mode at wavelengths above 1μm, but will support higher order modes at shorter wavelengths. However, the confinement losses increase rapidly at shorter wavelengths, attenuating these higher order modes, so the fiber is effectively single mode down into the visible regions of the spectrum. The fiber is highly suitable for polarisation maintaining applications, having a birefringence length of just 1.15 mm at 1.06 μm wavelength (polarisation extinction ~21dB between fiber axes). This high birefringence arises from the combination of core asymmetry, high refractive index contrast and small-scale structure.

9.3 Linear dispersion compensation and soliton formation

The mode-locked seed laser and launch arrangement are shown in Fig. 9.1. We used the Yb-doped, stretched pulse fiber laser described in Chapter 4 as our master oscillator [8]. For supercontinuum generation we amplified the pulses in diode-pumped Yb-doped fiber amplifiers. The laser output is exceptionally stable (amplitude noise ~0.05%) and therefore represents a very attractive and practical seed for Raman-soliton experiments, which are naturally highly sensitive to amplitude noise.

Fig. 9.2. shows the results obtained by launching the ~2.4 ps duration positively chirped Gaussian pulses directly from the laser into a length of the HF and recording the non-collinear SHG autocorrelations and optical spectra of the transmitted pulses. We used a half wave plate at the launch to match the pulse polarisation to a principal axis of the highly birefringent fiber. Without taking this precaution, components of the pulses launched on to the orthogonal fiber axes were observed to walk-off temporally due to the difference in dispersion between the axes, complicating the interpretation of the experiments. We present data for two launched pulse energies: 1 pJ, for which the propagation is close to linear over the propagation lengths considered, and 20 pJ, for which significant nonlinear effects become apparent. Starting with a fiber length of ~2.6 m (estimated transmission loss ~2dB) we gradually cut back the fiber length to record the evolution of the pulses as a function of propagation distance.

Fig. 9.2.a) shows a plot of the pulse FWHM vs. fiber length for pulses in both the linear (1 pJ) and nonlinear (20 pJ) regime. As expected for linear compression of an initially chirped pulse, the 1 pJ pulses are seen to initially compress, reach a minimum duration after ~1.2 m, and then to broaden again. The linearity of the compression process is confirmed by the inset spectrum Fig. 9.2.b) in which only a modest spectral broadening is observed at the point of maximum linear pulse compression. Compression by a factor of ~14 to a minimum duration of 170 fs is observed, with some higher order phase distortion remaining when compared with the minimum duration of 108 fs obtained when we compressed the pulses with a grating pair. Fitting the data

of Fig. 9.2.a) we estimate the dispersion of the fiber to be ~150 ps/(nm.km) [4]. We believe that this is the first direct demonstration of linear dispersion compensation in a HF with anomalous dispersion at wavelengths below 1.3 μm [4].

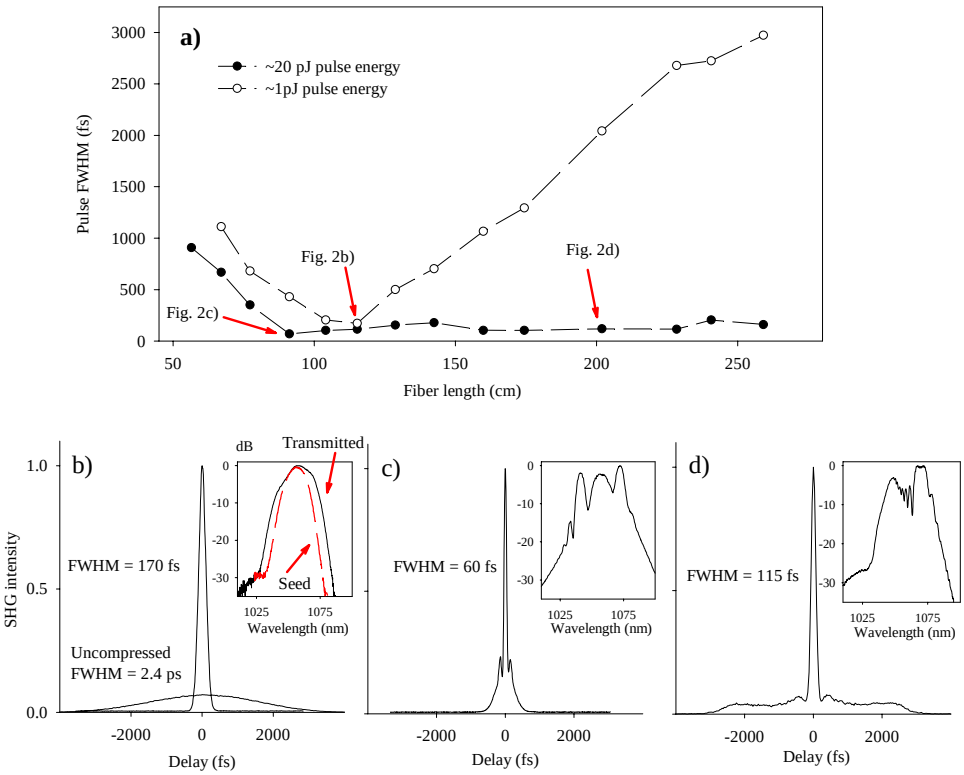

Fig. 9.2 Results obtained launching pulses directly from the laser into 2.2 m length of HF. a) Plot of transmitted pulse FWHM vs. fiber length. b)-d) Autocorrelation and inset spectra of pulses transmitted through HF: b) linear regime (1pJ pulses), fiber length = 1.15 m c) non-linear regime (20pJ pulses), fiber length = 0.92 m , d) non-linear regime, Raman scattering, fiber length = 2.02m.

In the non-linear regime (20 pJ pulses), Fig. 9.2.a) indicates soliton propagation with minimal temporal pulse broadening after transmission through ~2.6 m of fiber, which corresponds to ~ 20 soliton periods (as defined by the minimum compressed pulse width and the above estimated HF dispersion). The shortest compressed pulses have a duration of 60 fs (see autocorrelation shown in Fig. 9.2.c). The symmetric spectrum inset to Fig. 9.2.c), after propagation through 0.92 m of fiber, indicates the effects of SPM, whereas the spectrum in Fig. 9.2.d), after propagation through 2.02 m of fiber, shows a distinct peak at 1.075 μm, which is evidence of the SSFS effect. The low pulse energies (20 pJ, 200 W typical peak power) and ~1 m length of this fiber required to form solitons [1, 3, 9], are at least an order of magnitude lower than those previously required for similar experiments in conventional fiber at 1.55 μm [4], which makes these nonlinear effects readily accessible for practical applications.

9.4 Soliton transmission and supercontinuum generation

To achieve higher pulse energies we amplified the laser pulses using direct amplification in diode-pumped Yb-doped fiber amplifiers. The experimental setup is shown schematically in Fig. 9.1. The SEM of the small core, anomalously dispersive HF used for the higher pulse energy experiments is shown in Fig. 9.3.a). Although not identical to the fiber used in the earlier experiments, the fiber in Fig. 9.3.a) has very similar construction (core diameter, air fill fraction), and experimentally measured parameters (A_{eff} , λ_0) compared to the previous fiber. We believe the processes of linear and non-linear pulse compression are acting similarly in both experiments. The key difference is that by incorporating more rings of holes, the fiber shown in Fig. 9.3.a) has much lower confinement losses (~0.1dB/m).

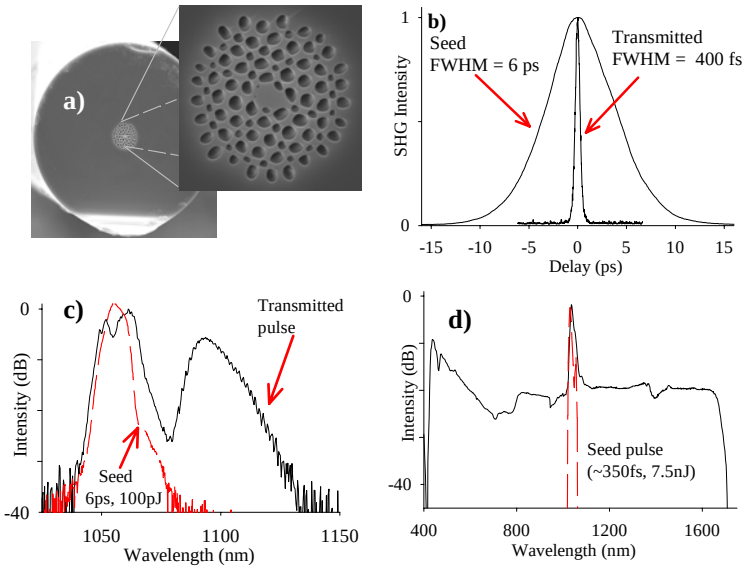

Fig. 9.3 Results obtained using amplified pulses. a) SEM of the HF used for amplified pulse experiments. b) Autocorrelation of 70 pJ pulses; at the input (positively chirped, FWHM 6ps), and after transmission through 60m of fiber (FWHM ~400fs). c) Spectra of input pulses (FWHM 6ps, 100pJ) and wavelength shifted (SSFS) pulses after transmission through 60m of fiber. d) Broadband continuum obtained by launching 20kW peak power pulses (FWHM~350fs, 7.5nJ) into 7m fiber length. The chirp of the input pulses was removed using a diffraction grating compressor.

Launching the uncompressed amplified pulses (strong positive chirp, FWHM~6ps) directly into a 60 m length of the HF shown in Fig. 9.3.a), we observed dramatic temporal pulse compression and evidence of SSFS wavelength tuning. For low launched pulse energies (below ~10 pJ), we observed that the transmitted spectrum was undistorted but the pulses were temporally broadened (beyond the ~50 ps measurement capability of our autocorrelator) due to the excess anomalous dispersion of the fiber. However, on increasing the launched pulse energy above ~20 pJ, the FWHM of the transmitted pulses reduced to below 1 ps, and for launched pulse energies around ~70 pJ, the output pulse FWHM remained constant at ~400 fs. Fig. 9.3.b) shows the SHG autocorrelation of the 400 fs transmitted pulses (solitons), and of the 6ps

launched pulses. This demonstration of soliton transmission through 60 m of fiber corresponds to ~475 soliton periods, which we believe is the longest transmission distance recorded for solitons at this wavelength. The spectrum shown in Fig. 9.3.c) clearly demonstrates single colour Raman solitons, which were tuneable with increasing launched pulse energy out to a maximum wavelength of ~1.12 μm. This complements the work on SSFS in an active Yb-doped HF described in Chapter 11 of this thesis, where we achieved a much broader tuning range 1.06-1.33 μm [10].

Finally, we increased the peak power of the launched pulses to a maximum of ~20 kW (350 fs FWHM, E~7.5 nJ) by adding a higher power cladding pumped Yb-doped fiber amplifier, a modulator to reduce the pulse repetition rate, and a diffraction grating compressor to remove the chirp. The output of the HF became a spectacular blue/white colour and the ultra-broad supercontinuum spectrum in Fig. 9.3.d) shows the enormous broadening into the visible region, especially compared to previous supercontinuum demonstrations from all fiber systems [11]. As the pulse energy was increased, the spectrum first formed a broad continuum across the infrared spectrum, and only at the highest powers did the spectrum move into the visible range. The HF length was 7 m, but we note that visible blue light was seen towards the launch end of the fiber indicating that a substantially shorter fiber length could have been used. Using an oscilloscope and detector with ~2 GHz bandwidth, the input pulses were observed to be jitter free with FWHM duration of 0.5 ns (true pulse width of ~6 ps), whereas the transmitted pulses were smeared across a 2 ns (FWHM) time window with significant jitter, which we interpreted as break-up into multiple pulses.

9.5 Conclusion

In conclusion, we have directly demonstrated, for the first time to our knowledge, linear dispersion compensation in a HF with anomalous dispersion at wavelengths less than 1.3 μm. At only 1 mW average powers (peak power ~200W), the fiber supports both soliton compression, and pulse propagation without temporal broadening, and using pulses with higher peak powers, we generated supercontinuum spectra spanning from below 400 nm to above 1750 nm. All experiments were seeded using our diode-pumped Yb-doped fiber source.

References

1. J. H. Price, W. Belardi, L. Lefort, T. M. Monro and D. J. Richardson, "Nonlinear pulse compression, dispersion compensation, and soliton propagation in holey fiber at 1 micron," Nonlinear Guided Waves and Their Applications (NLGW 2001), paper WB1-2 (2001).
2. J. H. V. Price, W. Belardi, T. M. Monro, A. Malinowski, A. Piper and D. J. Richardson, "Soliton transmission and supercontinuum generation in holey fiber, using a diode pumped Ytterbium fiber source," Optics Express **10,** 382-387 (2002).
3. W. J. Wadsworth, J. C. Knight, A. Ortigosa-Blanch, J. Arriaga, E. Silvestre and P. St.J.Russell, "Soliton effects in photonic crystal fibres at 850 nm," Electronics Letters **36,** 53-55 (2000).
4. G. P. Agrawal, *Nonlinear Fiber Optics*, Academic Press (San Diego), 2nd (1995).
5. J. C. Knight, J. Arriaga, T. A. Birks, A. Ortigosa-Blanch, W. J. Wadsworth and P. St.J.Russell, "Anomalous dispersion in photonic crystal fiber," IEEE Photonics Technology Letters **12,** 807-809 (2000).
6. T. M. Monro, D. J. Richardson, N. G. R. Broderick and P. J. Bennett, "Holey optical fibers: An efficient modal model," Journal of Lightwave Technology **17,** 1093-1102 (1999).
7. K. Suzuki, H. Kubota, S. Kawanishi, M. Tanaka and M. Fujita, "Optical properties of a low-loss polarization-maintaining photonic crystal fiber," Optics Express **9,** 676-680 (2001).
8. L. Lefort, J. H. Price, D. J. Richardson, G. J. Spuhler, R. Paschotta, U. Keller, A. Fry and J. Weston, "Practical Low-Noise stretched-pulse Yb-doped fiber laser," Optics Letters **27,** 291-293 (2002).
9. J. K. Ranka, R. S. Windeler and A. J. Stentz, "Visible continuum generation in air-silica microstructure optical fibers with anomalous dispersion at 800 nm," Optics Letters **25,** 25-27 (2000).
10. J. H. Price, K. Furusawa, T. M. Monro, L. Lefort and D. J. Richardson, "A tuneable, femtosecond pulse source operating in the range 1.06-1.33 microns based on an Yb doped holey fiber amplifier," Conference on Lasers and Electro Optics (CLEO), Vol. 56 of OSA Trends in Optics and Photonics Series (Optical Society of America, Washington, D.C., 2001) paper CPD1 (2001).
11. M. E. Fermann, M. L. Stock, D. Harter, T. A. Birks, W. J. Wadsworth, P. St.J.Russell and J. Fujimoto, "Wavelength-tunable soliton generation in the 1400-1600 nm region using an Yb fiber laser," *Conference on Advanced Solid State Lasers (ASSL), Technical Digest, Paper TuI2-1*, (2001).

Chapter 10 UV generation in a silica holey fiber

10.1 Introduction

This chapter describes our demonstration of supercontinuum generation extending to 300 nm in the UV from a pure silica holey fiber. The broad spectrum was obtained by launching ultra-short pulses (~150 fs, 10 nJ at 820 nm) from an amplified Ti:sapphire laser. The extension of HF based supercontinuum generation into the UV should prove to be of immediate application in spectroscopy. By slightly detuning the launch conditions we excited a higher order spatial mode which produced a narrower supercontinuum, but with enhanced conversion efficiency at a series of blue/UV peaks around 360 nm. We present numerical simulations, which suggest that differences in the dispersion profiles between the modes are an important factor in explaining this enhancement. In a related experiment, using the same laser source and fiber, we demonstrated visible supercontinuum from several subsidiary cores, with distinct colours in each core. The subsidiary cores were excited by appropriate input coupling. Fabrication of a fiber with a range of core sizes (dispersion profiles) for tailored supercontinuum generation can therefore be envisaged for practical applications [1].

Microstructured “holey” fibers have a unique range of optical properties [2, 3] and have enabled new applications in spectroscopy [4], metrology [5] and communications [6, 7]. Although the field of supercontinuum research using conventional fibers has been active for many years at wavelengths near 1.5 μm for telecommunications applications [8], the unique properties of HFs have enabled the demonstration of visible supercontinuum in HF pumped directly with Ti:sapphire oscillators [9]. This demonstration encouraged tremendous new research interest to both explain the origin of this remarkable spectral broadening [10, 11] and to develop further applications [12]. Visible supercontinuum spectra have previously been reported spanning 390-1600 nm using microstructured HF [9, 10], and 375-1500 nm [13] using tapered standard fiber. However, there is strong interest in extending the achievable bandwidths still further, particularly towards the ultraviolet (UV) regions of the spectrum [14, 15] for use in spectroscopy.

The dispersion profile of a HF has been shown to strongly influence the spectral shape of the supercontinuum produced [11]. We present, for the first time to our knowledge, full vector calculations based on the SEM of an actual fiber structure, of the dispersion characteristics of

the higher order spatial modes that were observed to produce enhanced UV generation. Our calculations show that the zero dispersion wavelength (λ_0) is close to the pump wavelength for the fundamental mode for our fiber, but at significantly shorter wavelengths for the higher order modes. We have used these dispersion profiles to perform numerical simulations of the continuum spectra in the fundamental and higher order modes, and which are in reasonable agreement with the measured spectra. Our observation that pumping close to λ_0 creates a broad flat spectrum, whereas pumping above λ_0 creates both red-shifted and blue-shifted spectral bands, is consistent with the investigations of other authors into the continuum spectra from the fundamental spatial mode made using fibers with different core sizes, and hence dispersion profiles [11].

Finally, using the same fiber and laser source, we demonstrated that by varying the input coupling appropriately, visible supercontinuum from several subsidiary cores could be produced. The colours of the supercontinuum spectra differed for each subsidiary core, which we consider was due to differences between the dispersion profiles of each core and also to differences between the input coupling efficiencies. This initial demonstration of supercontinuum generation in a multi-core fiber shows the potential for designing a fiber with an array of cores with different dimensions (dispersion profiles) and that could be selectively excited for tailored spectral generation from a single fiber structure.

The choice of fiber material is important for efficient UV generation in order to avoid unacceptable absorption (attenuation). High UV transmission losses affect standard silica based fibers, which are used to fabricate tapers for supercontinuum generation, because the ions typically incorporated in the fiber core in order to obtain the required transverse refractive index profile result in strong absorption in the UV (e.g. germanium doped silica has ~10,000 dB/km stronger absorption [16] at 250 nm compared to pure (undoped) silica). We expect that the comparatively low material loss of the single material pure silica HF as used in the experiments presented here should make such fibers strong candidates for efficient fiber-based UV supercontinuum sources.

This chapter is organised as follows. In Section 10.2 we describe the details of the experiment, and the properties of the HF. In Section 10.3, we describe our numerical simulations and compare the results to our experimentally measured spectra. In Section 10.4 we report our observations of supercontinuum generation in several subsidiary cores of the fiber, and in Section 10.5 we draw our conclusions.

10.2 Experimental observation of UV supercontinuum

Supercontinuum generation was produced by coupling high energy ultrashort pulses into a short length of HF. A schematic of our experimental setup is shown in Fig. 10.1. The supercontinuum generation at visible and near infrared wavelengths was recorded using a fiber-coupled optical spectrum analyser, whereas a UV optimised spectrometer and cooled CCD were used for wavelengths extending to below 300 nm. The spectral data presented in this chapter were produced using a pump wavelength λ_{pump}=820 nm. Coupling into the fundamental mode, which has λ_0 close to λ_{pump}, produced a yellow coloured supercontinuum, but by coupling into a higher order mode, we produced a dramatic change in the colour of the supercontinuum to bright blue-white, and we recorded UV spectra for the two-lobed mode showing power transferred to a series of peaks around 360 nm. By pumping at a shorter wavelength, we produced a wider variety of colours in higher order modes, as shown in Fig. 10.4.

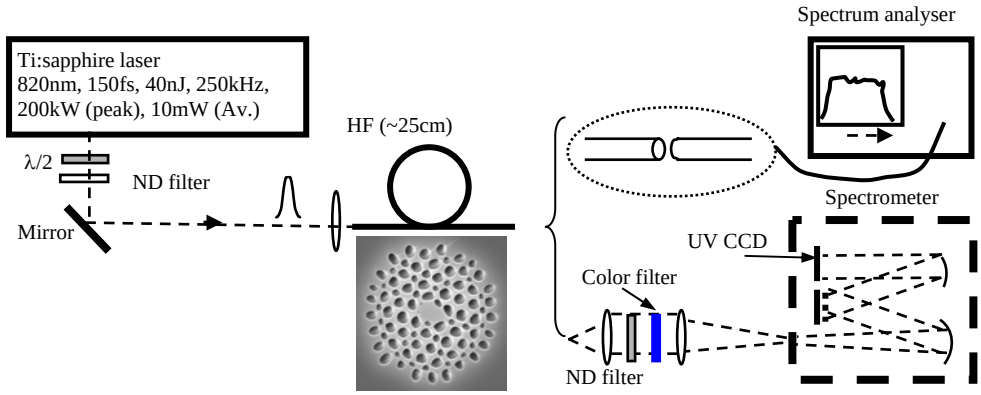

Fig. 10.1. Experimental configuration for characterising supercontinuum extending into the UV.

This section is structured as follows. Section 10.2.1 describes the characteristics of the HF. Section 10.2.2 presents the results showing UV generation to wavelengths as short as 300 nm in the UV. Section 10.2.3 shows the results obtained by coupling into higher order spatial modes (enhanced conversion efficiency into UV peaks). Section 10.2.4 is a brief report of our observations of laser induced damage to the fiber input facet.

10.2.1 Characteristics of the holey fiber

A SEM image of our robust, jacketed, polarisation-maintaining HF is shown inset to Fig. 10.1. The fiber has a ~1.6 μm diameter core, and a large air fill fraction in the cladding and this combination results in a highly confined mode with $A_{eff} \sim 2.5\ \mu m^2$. The fiber is rigorously single mode at wavelengths above 1 μm, but supports higher order modes at shorter wavelengths.

As mentioned in the introduction, we observed supercontinuum generation in higher order spatial modes, which was accompanied by enhanced spectral conversion in strong UV peaks. To further understand this process, we have calculated the mode area and dispersion properties of the fundamental and next lowest order fiber modes as shown in Fig. 10.2. The calculated dispersion profiles (Fig. 10.2(b)) show that the two polarisation modes (quasi-linearly polarised) associated with each transverse mode are not degenerate because the asymmetry of the fiber profile leads to mode splitting. (By comparison, these pairs of quasi-linearly polarised modes would remain degenerate for a fiber with an idealised hexagonal hole configuration [17].) It is therefore crucial to use a full vectorial method to calculate the properties of this small-core fiber, and we used a full vectorial implementation of the orthogonal function method [18], incorporating both odd and even functions to describe the modal fields and HF profile. The material dispersion of silica is incorporated in the calculations directly via use of the Sellmeier equation.

The numerically predicted intensity profiles of the two-lobed spatial modes, and near field photographs of continuum generation in each mode are shown in Fig. 10.2(a) and (d). A 100x microscope objective was used to image the fiber output onto a screen. The predicted intensity profiles match the observed mode shapes well, including details of the asymmetries in each direction. The dispersion predictions for the two-lobed modes and for the fundamental mode are presented in Fig. 10.2(b). The three pairs of different dispersion profiles (hence different λ_0) create distinctive supercontinuum spectral shaping. The zero dispersion wavelengths are: λ_0 = 795 nm, 838 nm (polarisation dependent) for the fundamental mode; λ_0 = 611 nm, 629 nm (polarisation dependent) for the mode of Fig. 10.2(a); and λ_0 = 671 nm, 694 nm (polarisation dependent) for the mode of Fig. 10.2(d). The injection wavelength used in our experiments (λ_{pump}= 820 nm) is shown in Fig. 10.2(b). The calculated effective mode area (A_{eff}) of the fundamental mode is shown in Fig. 10.2(c). We also calculated A_{eff} of all six modes to be: 2.32 μm^2, 2.43 μm^2 for the two principal polarisation axes of the fundamental mode; 2.01 μm^2, 2.05 μm^2 for the mode of Fig. 2(a); and 2.34 μm^2, 2.38 μm^2 for the mode of Fig. 10.2(d) (all calculated at a wavelength of 675 nm, which is close to the centre of the observed supercontinuum spectra).

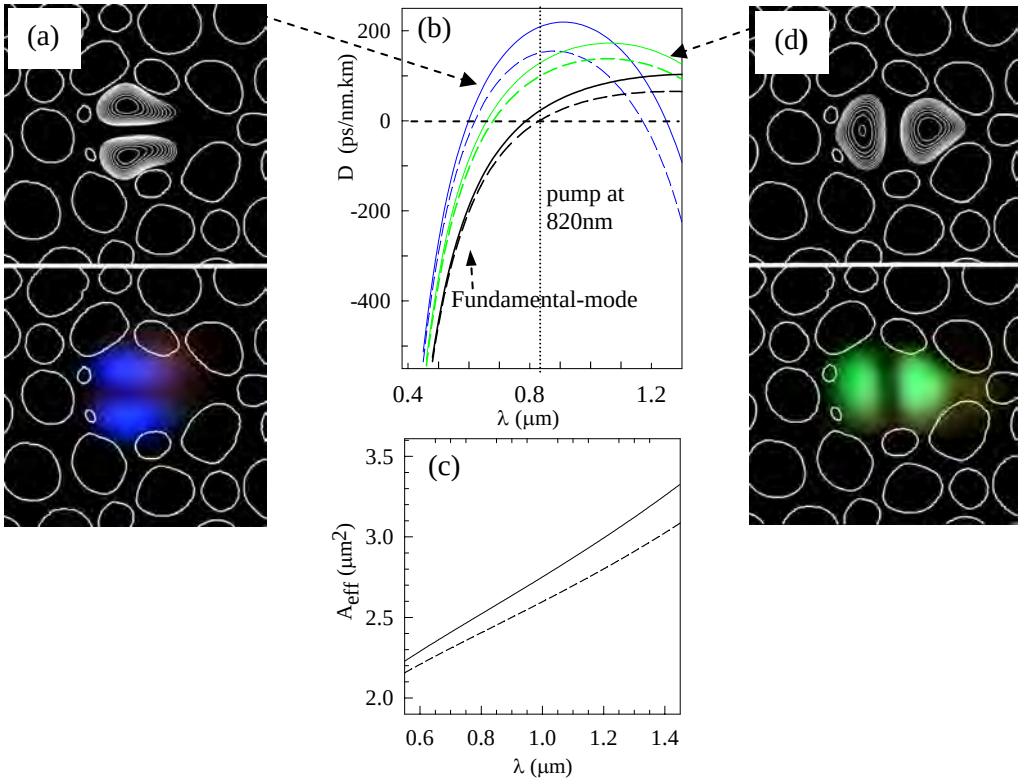

Fig. 10.2. (a),(d) Numerically predicted intensity profiles (1dB contour spacing) and corresponding near-field photographs (produced by imaging the fiber end using a 100x microscope objective) for two-lobed spatial modes. (b) Calculated dispersion for fundamental and two-lobed spatial modes. (c) Calculated A_{eff} for the fundamental spatial mode. (Similar for two-lobed modes.) The solid and dashed curves are for the two principal polarisation axes of the highly birefringent fiber.

The measured loss of the fiber (fundamental mode) is ~40dB/km at a wavelength of 1.55 μm [6]. However single material HFs with losses as low as 0.58dB/km at λ= 1.55 μm have been fabricated [19], and therefore excess loss should not be a constraint on the performance of future practical devices based on this technology. Calculations based on the multipole method [19] indicate that confinement loss provides a significant contribution toward the total measured loss in this fiber, but that it should be possible to reduce the confinement loss for this fiber to well below 0.1 dB/km simply by adding more rings of air holes. The higher order modes extend further into the cladding and it is therefore anticipated that the higher order modes would experience very large confinement loss, and so would not be observable in long fiber lengths. This effect was observed experimentally because for the mode of Fig. 10.2(a), which has λ_0 and A_{eff} furthest from those of the fundamental mode, we could much more easily observe transmitted power through a 15 cm fiber length compared to a 25 cm fiber length, whereas we observed the mode of Fig. 10.2(d) through a longer length of fiber without difficulty.

10.2.2 Supercontinuum generation into the UV

In this section we describe our experimental setup and the special precautions used to make measurements in the UV. The experimental arrangement is shown in Fig. 10.1. High energy, ultrashort (~150fs FWHM) pulses at a wavelength of 820 nm from a mode-locked Ti:sapphire laser system (TEM_{00} mode, average power~10 mW, repetition rate =250 kHz) were launched into a ~25 cm length of HF using a 40x microscope objective. By maximising the coupling efficiency, we launched ~25% of the incident power (launched energy ~10 nJ, peak power ~50 kW). The supercontinuum at the fiber output was recorded at visible and near infrared wavelengths using a fiber-coupled optical spectrum analyser (ANDO AQ6315B), and using a UV optimised spectrometer (appropriately blazed diffraction grating; UV enhanced CCD detector) for wavelengths at least as short as 300 nm. We used UV fused silica (UVFS) lenses to couple light into the spectrometer in order to avoid the poor transmission of standard BK7 glass lenses at short wavelengths.

Fig. 10.3(a) shows the observed supercontinuum extending from <300 nm to >1600 nm and combines the data from the optical spectrum analyser and spectrometer. We have considered the wavelength variation of the spectrometer efficiency, calculated from the efficiency curves of each spectrometer element shown in Fig. 10.3(b). The overall spectrometer efficiency was found to be approximately uniform from ~250 nm to 800 nm, so we have not adjusted the UV spectra of Fig. 10.3(a),(d) for instrument variation. The spectrometer slit width was held constant to minimise variations in spatial mode filtering. Scatter from higher order diffraction of the pump (820nm) and longer wavelengths was removed using a UG1 coloured filter from Schott Glass, which blocks most wavelengths >600 nm. Fig. 10.3(c) shows the overall efficiency of the spectrometer with and without the filter. The differences between the filtered and unfiltered spectra should comprise: (i) weak attenuation at the measured UV wavelength, and (ii) strong attenuation of longer wavelengths, which removes potential false counts caused by 2^{nd} order diffraction. Fig. 10.3(d) shows the UV spectra with and without the coloured filters. The differences between the filtered and unfiltered spectra match the absorption of the coloured filter at the UV wavelength, so we concluded that scatter from higher order diffraction of long wavelengths was not distorting the unfiltered spectrum. The measurements therefore confirm that the supercontinuum spectrum extends down to at least 300 nm in the UV.

For the supercontinuum produced in the fundamental mode of our fiber (λ_0 close to λ_{pump}), we interpret our observation of UV generation to 300 nm, which represents a more extreme broadening towards the UV than typically reported [9, 11], to result from differences between the precise form of the dispersion profile of our fiber compared to the fibers studied by other authors, and perhaps also from our detailed observations using a spectrometer with enhanced sensitivity in the UV.

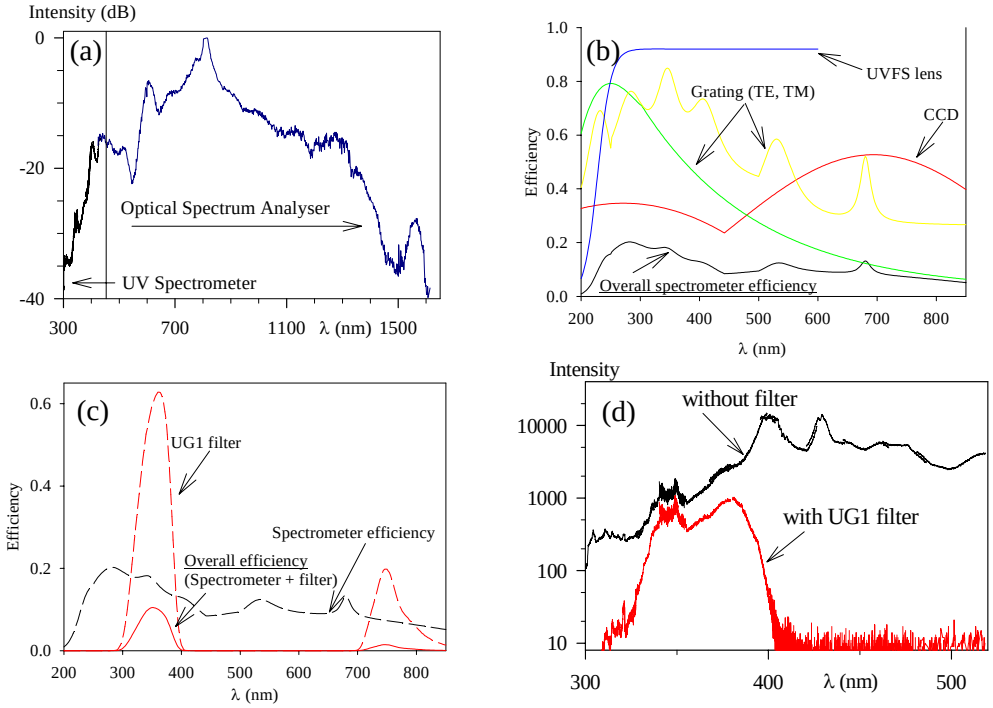

Fig. 10.3. (a) Broadband supercontinuum spectrum extending from 300nm (UV) to 1600nm (IR). (b) Calculated efficiency of the UV optimised spectrometer. The spectrometer mirror efficiency (not shown) is 92% across the spectral range considered, and is included in the overall efficiency. (c) Transmission characteristics of the coloured filter used to eliminate unwanted long-wavelength scatter. (d) UV spectra from 300nm to 500nm recorded with and without coloured filter.

10.2.3 Enhanced UV in higher order spatial modes

Despite the wide interest in supercontinuum research, there have been few previous reports of supercontinuum in higher order spatial modes [14, 20, 21]. Due to the large index difference between core and cladding modes of small core, high air fill fraction HFs, the effective index of the fundamental mode, which is mostly confined within the core, is substantially greater than for higher order modes, which extend into the holey cladding. It is therefore comparatively difficult to couple to higher order modes of these HFs, and the perturbations which couple modes in standard fibers (small variations of core diameter resulting from fabrication, and bending of the fiber) are comparatively less effective at mode-mixing. However, Fig. 10.4 illustrates that by slightly detuning the pump launch from that for optimal launch efficiency, we obtained strong coupling into higher order spatial modes accompanied by a visually stunning change in the colour of the fiber output from pale yellow (Fig. 10.4(b)(ii)) to bright white (Fig. 10.4(b)(iii)), which led us to investigate the supercontinuum spectrum into the UV.

Using a pump wavelength of ~820 nm produced only the fundamental mode of Fig. 10.4(b)(ii), or the two-lobed mode oriented as shown in Fig. 10.4(b)(i),(iii). We observed that the mode-colour of Fig. 10.4(b)(iii) was associated with the strongest UV generation. Using an OPA system to provide a pump wavelength of ~675 nm (similar pulse energy and duration

compared to 820 nm pulses), we observed a wider range of colours produced in higher-order modes and with lobes in either orthogonal orientation as shown in Fig. 10.4(b) (iv)-(vi) . The relative ease of generating supercontinuum in higher order modes when λ_{pump} = 675 nm (compared to λ_{pump} = 820 nm) could be because the pump wavelength is then closer to λ_0 of the higher order modes, although we have not identified the exact mechanism.

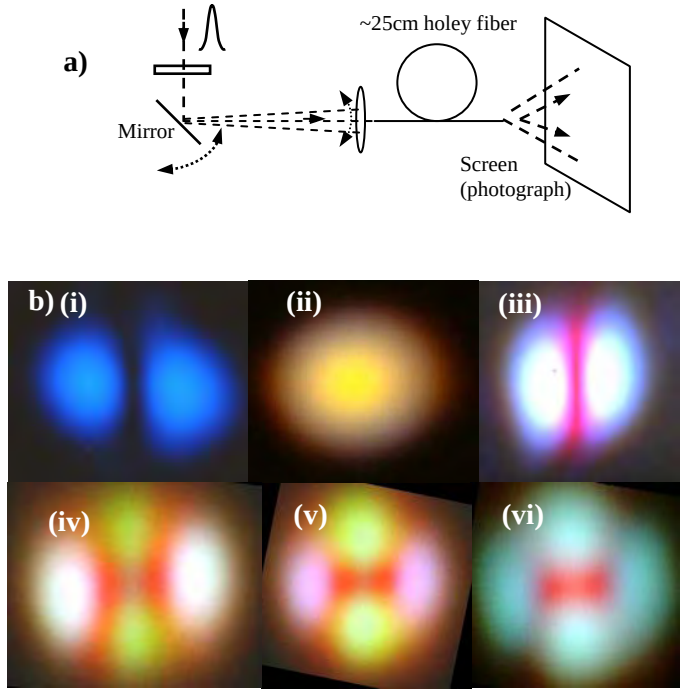

Fig. 10.4. (a) Experimental setup for detuning the launch into the HF. (b) Far-field photographs of the colours produced in higher order spatial modes. (i)-(iii) λ_{pump} = 820 nm; (iv)-(vi) λ_{pump} = 675 nm. The orientations of the modes correspond to those of the near field images in Fig. 10.2.

The average power transmitted in the higher order modes was typically ~1 mW, compared to ~2 mW in the fundamental mode. The reduction in transmitted power is due to lower launch efficiency (off-axis launch) and to somewhat higher transmission losses in this higher order mode, but high energy pulses (up to 5 nJ) could still be launched into this higher order mode. The orientation of the two-lobed mode was predominantly that shown in Fig. 10.4(b)(iii), which corresponds to the mode of Fig. 10.2 (d).

Coupling into the two-lobed mode of Fig. 10.4.(b)(iii) resulted in an enhancement of the power at wavelengths close to 360 nm, and a narrowing of the supercontinuum. Fig. 10.5 (top) shows the results from coupling into the two lobed spatial mode (shown inset). Fig. 10.5 (lower) shows the results from coupling into the fundamental mode (shown inset). The spectrum from the two lobed mode, Fig. 10.5(a)(top), was narrower when compared to the spectrum from the fundamental mode, Fig. 10.5(a)(lower), but retained strong spectral conversion to <450 nm wavelengths. Enhanced UV generation at a series of peaks near ~360 nm is demonstrated in Fig. 10.5(b) from the two-lobed mode (top plot), but the peaks are

not present in the fundamental mode spectrum (lower plot). A set of neutral density filters was used to vary the input power, and which resulted in the increasing intensity levels shown in Fig. 10.5(b). As described in Section 10.2.2, we used coloured filters to block unwanted scatter from the longer wavelengths and that could otherwise distort the UV measurements.

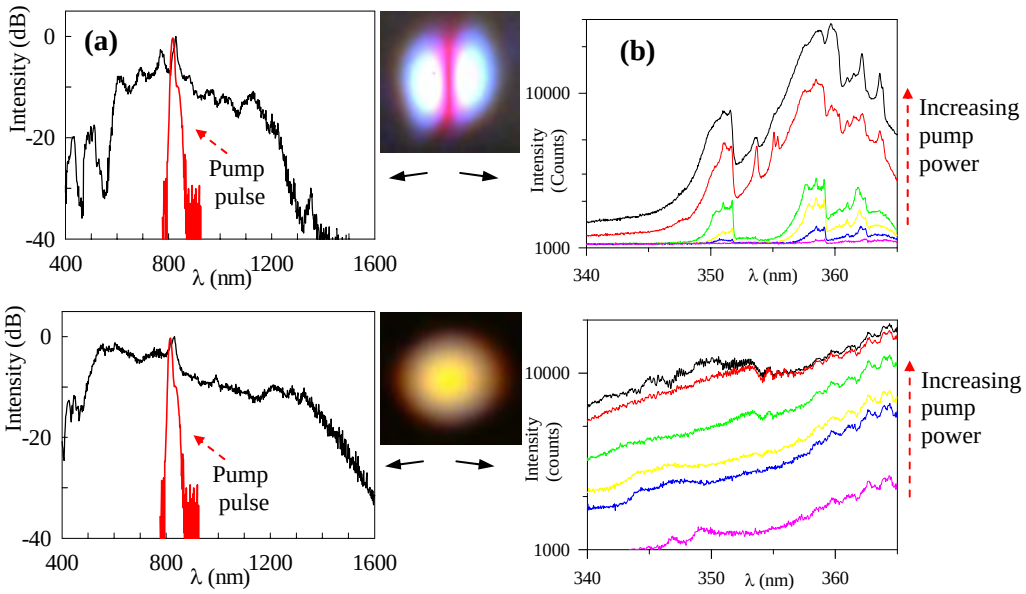

Fig. 10.5. Continuum spectra from coupling into two-lobed spatial mode (upper plots), and coupling into the fundamental mode (lower plots). Inset: photographs of corresponding far-field modes. (a) Wide span measurements. (b) Series of UV peaks at ~360 nm. The coloured lines correspond to increasing pump pulse energy: +0, 1, 2, 3, 5, 6 dB with respect to the lowest intensity trace. (Due to different signal averaging times, quantitative comparison of upper and lower plots is not possible.)

10.2.4 Laser-induced damage to the fiber tip

We observed that perturbations to the input launch conditions (e.g. caused by knocking gently on the optical table near the lens mount), could somehow change the fiber so that it was no longer possible to couple into the fundamental mode, but only into the two-lobed mode. By re-cleaving the fiber tip to reveal a new facet we could again excite the fundamental mode. We suggest that our observations are due to optically induced damage to the fiber facet, which would cause the pump light to couple into the higher order mode for all launch configurations (although we have not identified the precise damage mechanism). This explanation would be consistent with reports from other groups [14, 22] that significant UV generation was only obtained following melting of the fiber facet (as observed from SEM images) when using 1W incident average power from a high repetition rate source, but with pulse characteristics (FWHM~200 fs, energy ~ 14 nJ) similar to those used in our experiments.

10.3 Comparison of experimental results with simulations

In this section, we compare the results of our numerical modelling to the experimentally measured spectra. We performed the modelling to provide insight into the mechanisms giving rise to the enhanced UV generation in the higher order spatial mode. When considering which parameters to include in the model, we first noted that in order to excite the higher order modes it was necessary to detune the launch with respect to that used for optimum coupling into the fundamental mode. In addition, the fibers used in our experiments were quite short (25 cm), so strong coupling between modes subsequent to launch would be unlikely. We therefore considered that coupling into the two-lobed mode occurred solely at launch and not by mode-mixing from the fundamental mode after launch. This suggested that the properties (nonlinearity, dispersion) of the two-lobed mode alone could be responsible for the spectral shaping, rather than a more complex inter-modal process. As described in Section 10.2.1, the effective mode areas of the fundamental and two-lobed mode are very similar, implying similar effective nonlinearities for these modes. However, the dispersion properties are dramatically different; in particular, the two-lobed mode has λ_0~690 nm compared to λ_0~810 nm for the fundamental mode. The shorter λ_0 of the higher order mode would cause phase-matching to transfer energy further towards the UV, and would explain the general observation of enhanced UV generation.

To support our suggestion that the difference between the supercontinuum produced in different spatial modes is principally due to differences between the dispersion profiles of those modes, we performed numerical simulations based on the dispersion profiles for both the fundamental mode and for the two-lobed mode shown in Fig. 10.2(d). Our numerical model (ignoring fiber losses) uses the modified NLSE with gain, as described in Chapter 2, and shown below.

$$\frac{\partial A}{\partial z} - i\sum_{k\geq 2}\frac{i^k \beta_k}{k!}\frac{\partial^k A}{\partial t^k} = i\gamma\left(1+\frac{i}{\omega_0}\frac{\partial}{\partial t}\right)\times\left[A(z,t)\int_{-\infty}^{+t} R(t')\left|A(z,t-t')\right|^2 dt'\right]$$

where $A = A(z,t)$ is the electric field envelope, β_k are the dispersion coefficients at the center frequency ω_0, $\gamma = n_2\omega_0/(cA_{eff})$ is the nonlinear refractive index, and A_{eff} is the effective area of the fiber. The equation has been used by other authors for the numerical study of supercontinuum generation [23, 24]. To solve the propagation equation, we used a standard split-step Fourier algorithm treating dispersion in the frequency domain and the nonlinearity in the time domain, apart from the temporal derivative for the self-steepening effect, which is evaluated using Fourier transforms. In performing this modelling, I am grateful to Dr. Rüdiger

Paschotta for allowing me to use "ProPulse", which is a numerical modelling package he has written for simulating pulse propagation.

We used the dispersion and A_{eff} data from Section 10.2.1, and chose parameters for our launched pulses that would correspond to the experimentally observed average transmitted power from the fiber (E ~10 nJ, in the fundamental mode, E ~5 nJ, in the two-lobed mode; λ_{pump} = 820 nm, FWHM ~150 fs for both modes). We also performed simulations for pulses with half of these energies and the results were qualitatively similar, with only slight variations in the bandwidth. Our simulation results show the expected spectral fine structuring [23] and we have applied a rolling average to smooth the data, which is then approximately comparable to the time averaged experimental measurements. We present simulation results for one of the principal polarisation axes, but the results were qualitatively similar for the other axis. We note that there are further refinements that can be made to the above NLSE to include effects such as loss along the fiber length, ultraviolet and infrared absorption bands, polarisation coupling, and the wavelength dependence of the effective mode area. However, the simulations show reasonable qualitative agreement with the experimental spectra.

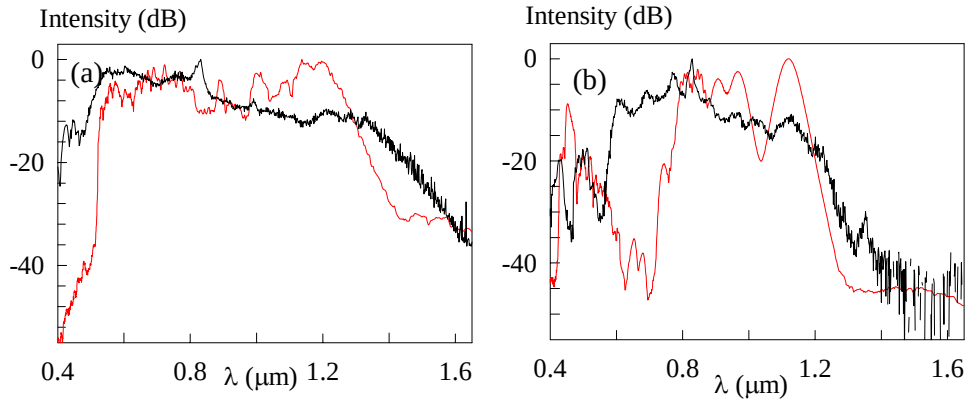

Fig. 10.6. Experimental (black) and theoretically modelled (red) supercontinuum spectra. (a) fundamental mode; (b) two-lobed mode (Fig. 10.2(d)).

The results of our simulations (red) and the experimental data (black) are shown in Fig. 10.6 for both the fundamental and the two-lobed modes. The simulation and experimental spectra show reasonable agreement: the simulation results for the fundamental mode show a broad, flat spectrum with approximate agreement to the experimentally observed bandwidth; and the simulation results for the higher order mode show a narrower spectrum, but with significant power at blue wavelengths. Given the complexity of the phenomenon of supercontinuum in higher order modes, and the approximations made in our simulations, exact agreement between simulations and experimental observations could not be expected. However, the main features observed in our simulation results are consistent with our experimental spectra. Our simulation results are also consistent with both experimental and theoretical results from other groups that

have used fibers with different λ_0 in relation to the pump wavelength, but always in the fundamental spatial mode: i.e. pumping near λ_0 produced a broad, flat spectrum, and pumping on the anomalous dispersion side of λ_0 produced discrete red-shifted and blue-shifted bands [11].

Fig. 10.6 (b) shows that the principal difference between the simulation and experimental spectrum for the higher order mode is that the simulation shows a lower intensity near λ_0 (690nm). We suspect that the higher intensity observed experimentally is likely to arise due to a non-ideal launch into the higher order mode resulting in residual excitation of the fundamental mode, as shown by the photographs of Fig. 10.4 and Fig. 10.5. Similarly, for the spectrum of the fundamental mode shown in Fig. 10.6 (a), a small fraction of the launch power coupled into the higher order mode could be responsible for the shoulder in the experimentally observed spectrum at ~450nm that is not present in the simulation result (the simulations predict a peak in the higher order mode spectrum at approximately that wavelength). The simulations predict strong pump depletion such that there is no peak remaining at the pump wavelength. This is consistent with the simulations of other authors [10, 20], and we suspect that the experimentally observed peak at the pump wavelength is due to a small fraction of the incident power guided by lossy cladding modes and observed because the fiber length is short. Overall, we believe that the simulation results provide support for our suggestion that the difference in general form of the supercontinuum spectra is principally due to the differences between dispersion profiles of the fundamental and two-lobed modes.

10.4 Supercontinuum generation in subsidiary cores

In this section we describe our observations from a related experiment that produced supercontinuum in several subsidiary cores of the fiber. Examples of multiple core HFs that have previously been reported include a dual core HF [25], and a HF containing several cores of different dimensions [26]. However, this is the first time, to our knowledge, that supercontinuum generation in secondary cores of a HF has been demonstrated. In the fiber used here, the “subsidiary” cores arise where imperfections in the structure have created relatively thicker regions of silica. In the future, it would be straightforward to envisage the systematic fabrication of multiple cores using additional solid cores in the capillary stacking process. The experimental arrangement was similar to that used for continuum generation in the higher order modes of the principal core (Fig. 10.5(a).), using the same pump pulses and HF, but with more extreme detuning of the launch.

Fig. 10.7(a) shows a typical far-field mode shape produced by continuum generation in a subsidiary core, observed as scattered light from a white card a few centimetres from the fiber

end; the six-fold symmetric pattern in a uniform colour is surprising because the fiber does not have a perfectly regular hexagonal structure, and it is substantially different from the far field images of higher order modes in the principal core (Fig. 10.4). However, the observed geometric nature of the far field modes was characteristic of our observations of continuum generation in subsidiary cores.

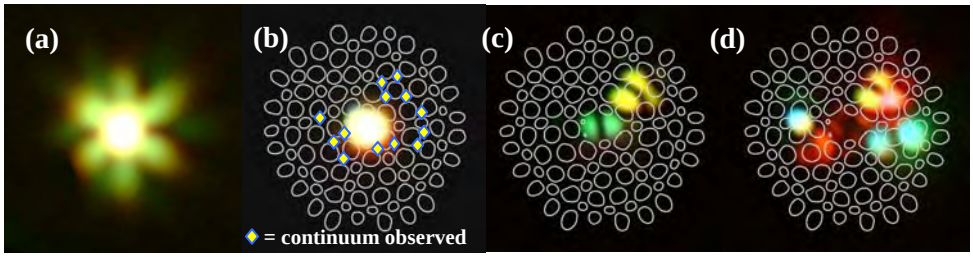

Fig. 10.7. (a) Example far-field image observed when continuum produced in a subsidiary core of this multi-core fiber. (b)-(d) Near-field pictures showing continuum in principal and subsidiary cores, with overlaid SEM of fiber structure. Note that (b) and (c) are single pictures, whereas (d) is a composite image to show the variety of colours seen in different cores. The diamond shapes in (b) indicate the subsidiary cores in which we observed continuum generation.

Fig. 10.7 (b)-(d) shows near-field pictures of supercontinuum in subsidiary cores that were recorded using a 100x microscope objective to focus the fiber output onto a screen. Using a camera on a tripod, we recorded all the near-field images from the same relative position, and we then matched the images to the subsidiary cores by overlaying those images onto the SEM of the fiber. In contrast to the far-field image, the near-field images show that the mode shapes clearly follow the fiber structure; the modes in Fig. 10.7(c) and (d) spread into neighbouring subsidiary-cores where the struts are broad, and thus the subsidiary core modes are poorly confined.

Fig. 10.7 (b)-(d) demonstrates that characteristic colours were produced by each core. The colours in any core changed when a half-wave plate was used to rotate the plane of polarisation of the input pulses. The dispersion of a HF has been shown to be a controlling factor for supercontinuum spectral broadening [11, 27], and we interpret the distinctive colours associated with each subsidiary core to be an indication of the different dispersions of these cores. The size of all the subsidiary cores (~1 μm) was of the same scale as the guided wavelengths, so we would expect the waveguide dispersion to be a sensitive function of the precise core dimensions. The strong asymmetry of the subsidiary cores also leads to substantially different dispersion properties for the orthogonal polarisation axes, which would cause the continuum colour to change with variations of the input polarisation.

We also considered the increased losses of these subsidiary cores. In an idealised HF, the average refractive index of the periodically arranged cladding, is lower than the refractive index of the solid core region, and so light is guided by this effective refractive index difference (Δn).

As explained in Section 10.2.1, reducing the confinement losses for small core HFs (to the few dB/km) requires a sufficient diameter of holey (microstructured) cladding around each core (number of rings of holes) [19]. It has previously been empirically determined that in order to confine light of wavelength λ, all fine silica struts surrounding a subsidiary core must be longer than $\sim 2\lambda$ and narrower than $\sim 1.2\lambda$ [26]. The supporting struts in our fiber were short and wide compared to the wavelength of the guided light, and the confinement losses of the subsidiary cores were therefore high. The confinement losses were evident experimentally because the fiber glowed much more brightly (unguided light) when continuum was produced in subsidiary cores compared to when continuum was produced in the main core. Furthermore, we only observed the supercontinuum in subsidiary cores using a short fiber length (15 cm as opposed to a 25 cm length for our other measurements). The average power transmitted through the fiber in subsidiary cores was ~0.5 mW compared to ~2.5 mW in the central core, due to a combination of the increased confinement losses and the reduced launch efficiency. However, we suggest that it should be possible to dramatically reduce excess losses by choosing an appropriately designed fiber structure.

Overall, we believe that this initial observation if supercontinuum generation in several subsidiary cores of a HF demonstrates the potential for fabrication of a fiber with several cores of different dimensions for tailored continuum generation from a single fiber.

10.5 Conclusion

In conclusion, we have demonstrated supercontinuum generation from 300 nm in the UV to above 1600 nm in the IR from a pure-silica HF. Care was taken to consider the efficiency of our UV enhanced spectrometer across the blue/UV spectral range, and we used coloured glass filters to block unwanted scatter from longer wavelengths. By coupling into a two-lobed spatial mode, we measured substantially enhanced UV generation in a series of blue/UV peaks at wavelengths near 360 nm. Since the fiber lengths used in our experiment were quite short (~15 cm), and because it was necessary to detune the launch in order to couple into the two-lobed mode, we believe that coupling into the two-lobed mode occurred at launch, and not by mode-mixing from the fundamental mode subsequent to launch. The enhanced UV generated would then result from differences in the dispersion profiles of the fundamental and higher order two-lobed modes. To enhance our understanding of this process, we used a full vector model based on the SEM of the fiber structure to calculate the dispersion profiles for the fundamental mode and for the two orthogonally oriented two-lobed modes, and performed numerical simulations of supercontinuum spectra produced by these dispersion profiles. The simulation and experimental results are in reasonable qualitative agreement, which provides support for our

suggestion that the enhanced UV generation is due in large part to the differences in the dispersion profiles of the distinct spatial modes.

We have also demonstrated visible supercontinuum with distinct colours produced in several subsidiary cores of our multi-core fiber. We interpret the different colours produced by each subsidiary core to result from variations in the dispersion profiles of the cores (and from the reduced launch efficiency).

We believe that the extension of HF based supercontinuum generation into the UV will prove to be of immediate practical application in spectroscopy. Following the results presented here, we could envisage the design of a fiber with optimised dispersion characteristics for enhanced UV generation. Power scaling to generate substantial UV intensity should be possible by using a higher repetition rate system compared to the 250 kHz source used in these experiments; and any such work would ideally consider new pump wavelengths in order to exploit more practical sources for supercontinuum generation based on diode-pumped Yb-doped fiber amplifiers [28]. Following our demonstration of supercontinuum in several subsidiary cores, it is now possible to consider the fabrication a fiber specifically designed with a selection of multiple cores with different dimensions to enable several tailored supercontinuum spectra to be generated from a single HF.

References

1. J. H. Price, T. M. Monro, K. Furusawa, W. Belardi, J. C. Baggett, S. J. Coyle, C. Netti, J. J. Baumberg, R. Paschotta and D. J. Richardson, "UV generation in a pure silica holey fiber," Applied Physics B-Lasers and Optics **77,** 291-298 (2003).
2. T. M. Monro, D. J. Richardson, N. G. R. Broderick and P. J. Bennett, "Holey optical fibers: An efficient modal model," Journal of Lightwave Technology **17,** 1093-1102 (1999).
3. J. C. Knight, J. Arriaga, T. A. Birks, A. Ortigosa-Blanch, W. J. Wadsworth and P. St.J.Russell, "Anomalous dispersion in photonic crystal fiber," IEEE Photonics Technology Letters **12,** 807-809 (2000).
4. R. Holzwarth, T. Udem, T. W. Hansch, J. C. Knight, W. J. Wadsworth and P. St.J.Russell, "Optical frequency synthesizer for precision spectroscopy," Physical Review Letters **85,** 2264-2267 (2000).
5. D. J. Jones, S. A. Diddams, J. K. Ranka, A. Stentz, R. S. Windeler, J. L. Hall and S. T. Cundiff, "Carrier-envelope phase control of femtosecond mode-locked lasers and direct optical frequency synthesis," Science **288,** 635-639 (2000).
6. J. H. Lee, Z. Yusoff, W. Belardi, M. Ibsen, T. M. Monro and D. J. Richardson, "Investigation of Brillouin effects in small-core holey optical fiber: lasing and scattering," Optics Letters **27,** 927-929 (2002).
7. Z. Yusoff, J. H. Lee, W. Belardi, T. M. Monro, P. C. Teh and D. J. Richardson, "Raman effects in a highly nonlinear holey fiber: amplification and modulation," Optics Letters **27,** 424-426 (2002).
8. H. Takara, T. Ohara, K. Mori, K. Sato, E. Yamada, Y. Inoue, T. Shibata, M. Abe, T. Morioka and K. I. Sato, "More than 1000 channel optical frequency chain generation from single supercontinuum source with 12.5 GHz channel spacing," Electronics Letters **36,** 2089-2090 (2000).
9. J. K. Ranka, R. S. Windeler and A. J. Stentz, "Visible continuum generation in air-silica microstructure optical fibers with anomalous dispersion at 800 nm," Optics Letters **25,** 25-27 (2000).
10. A. V. Husakou and J. Herrmann, "Supercontinuum generation of higher-order solitons by fission in photonic crystal fibers," Physical Review Letters **87,** 203901 (2001).
11. J. Herrmann, U. Griebner, N. Zhavoronkov, A. Husakou, D. Nickel, J. C. Knight, W. J. Wadsworth, P. St.J.Russell and G. Korn, "Experimental evidence for supercontinuum generation by fission of higher-order solitons in photonic fibers," Physical Review Letters **88,** 173901 (2002).
12. P. Petropoulos, T. M. Monro, W. Belardi, K. Furusawa, J. H. Lee and D. J. Richardson, "2R-regenerative all-optical switch based on a highly nonlinear holey fiber," Optics Letters **26,** 1233-1235 (2001).
13. T. A. Birks, W. J. Wadsworth and P. St.J.Russell, "Supercontinuum generation in tapered fibers," Optics Letters **25,** 1415-1417 (2000).
14. A. Efimov, F. G. Omenetto, A. J. Taylor, J. C. Knight, W. J. Wadsworth and P. St.J.Russell, "Generation of UV Light from Microstructured Fibers Pumped with Femtosecond 800nm Oscillator," *Conference on Lasers and Electro Optics*, Optical Society of America, Washington D.C., (May 19-24, 2002).
15. J. H. Price, K. Furusawa, T. M. Monro, C. Netti, A. Malinowski, J. J. Baumberg and D. J. Richardson, "Phase matched UV Generation in a silica holey fiber," Conference on Lasers and Electro Optics (CLEO), Vol. 73 of OSA Trends in Optics and Photonics Series (Optical Society of America, Washington, D.C., 2002) paper CTuB5 (2002).
16. J. S. Sanghera and I. D. Aggarwal, *Infrared Fiber Optics*, CRC Press (1998), (Fig. 2.18)

17. M. J. Steel, T. P. White, C. M. de Sterke, R. C. McPhedran and L. C. Botten, "Symmetry and degeneracy in microstructured optical fibers," Optics Letters **26,** 488-490 (2001).

18. T. M. Monro, N. G. Broderick and D. J. Richardson, "Exploring the Optical Properties of Holey Fibers," in *Nanoscale Linear and Nonlinear Optics: International School on Quantum Electronics, Erice, Sicily, July 2000*, M. Bertolotti, C. M. Bowden and C. Silbilia, Eds. Melville, NY, 2000, pp. 123-128.

19. V. Finazzi, T. M. Monro and D. J. Richardson, "Confinement loss in highly nonlinear holey optical fibers," *Optical Fiber Communications Conference*, (March 17-22, 2002).

20. J. M. Dudley, L. Provino, N. Grossard, H. Maillotte, R. S. Windeler, B. J. Eggleton and S. Coen, "Supercontinuum generation in air-silica microstructured fibers with nanosecond and femtosecond pulse pumping," Journal of the Optical Society of America B-Optical Physics **19,** 765-771 (2002).

21. F. G. Omenetto, A. J. Taylor, M. D. Moores, J. Arriaga, J. C. Knight, W. J. Wadsworth and P. St.J.Russell, "Simultaneous generation of spectrally distinct third harmonics in a photonic crystal fiber," Optics Letters **26,** 1158-1160 (2001).

22. A. Efimov, A. J. Taylor, F. G. Omenetto, J. C. Knight, W. J. Wadsworth and P. St.J.Russell, "Nonlinear generation of very high-order UV modes in microstructured fibers," Optics Express **11,** 910-918 (2003).

23. J. M. Dudley and S. Coen, "Coherence properties of supercontinuum spectra generated in photonic crystal and tapered optical fibers," Optics Letters **27,** 1180-1182 (2002).

24. G. Genty, M. Lehtonen, H. Ludvigsen, J. Broeng and M. Kaivola, "Spectral broadening of femtosecond pulses into continuum radiation in microstructured fibers," Optics Express **10,** 1083-1098 (2002).

25. B. J. Mangan, J. C. Knight, T. A. Birks, P. St.J.Russell and A. H. Greenaway, "Experimental study of dual-core photonic crystal fibre," Electronics Letters **36,** 1358-1359 (2000).

26. J. C. Baggett, T. M. Monro, W. Belardi, K. Furusawa and D. J. Richardson, "Assorted core air-clad fibre," Electronics Letters **36,** 2065-6 (2000).

27. A. L. Gaeta, "Supercontinuum generation in microstructured fibers," *Conference on Lasers and Electro Optics*, (May 6-11, 2001).

28. J. H. V. Price, W. Belardi, T. M. Monro, A. Malinowski, A. Piper and D. J. Richardson, "Soliton transmission and supercontinuum generation in holey fiber, using a diode pumped Ytterbium fiber source," Optics Express **10,** 382-387 (2002).

Chapter 11 Solitons in a holey fiber amplifier

11.1 Introduction

This chapter describes our demonstration of soliton pulse formation, amplification and soliton-self-frequency-shifting in an anomalously dispersive, Yb-doped HF amplifier seeded with pulses from our mode-locked Yb-doped, fiber oscillator described in Chapter 4. The system provides a highly practical, all diode-pumped, continuously tuneable, femtosecond pulse source operational in the important and difficult to access wavelength range from 1.06 - 1.33 μm [1, 2]. In other experiments multi-pulse, multi-coloured, soliton formation was observed with wavelength shifted pulsed output to beyond 1.58 μm. Supercontinuum generation and nonlinear pulse compression to durations of 65 fs were also obtained using other configurations.

Wavelength tuneable femtosecond optical pulse sources have a wide variety of applications, including ultrafast spectroscopy, and optical chemistry. Traditionally, femtosecond pulse sources have been based on bulk crystal materials, and extending this technology to obtain broad tuning ranges has required the use of bulk parametric nonlinear devices such as OPOs. The discovery of the soliton-self-frequency shift (SSFS) in optical fibers was first reported in 1985-1986 [3-5], and opened up the exciting possibility of obtaining widely wavelength tuneable femtosecond soliton pulses from fiber-based sources (ideally incorporating a fiber based pump laser) [6].

To obtain the SSFS effect, the frequency shifting fiber must exhibit anomalous dispersion at both the initial seed wavelength and across the required tuning range. The recent demonstration that small core HFs [7] (or less practically, it is possible to use tapered standard fibers with similarly small core dimensions [8]),can have anomalous dispersion at wavelengths shorter than 1.3 μm, where conventional silica fibers have normal disperison, has therefore extended the possible SSFS wavelength tuning range. The work presented in this chapter demonstrates wavelength tuning from 1.06-1.33 μm based on the SSFS technique.

This chapter is structured as follows. Section 11.2 describes the physical operating principles of the system, gives details of how the system was implemented, and the properties of the HF. In Section 11.3 we describe and discuss the results of our experiment, and in Section 11.4 we draw our conclusions.

11.2 System operating principles and implementation

As described above, our source comprises an Yb-doped fiber seed laser, and an Yb-doped HF amplifier. A schematic of the system is shown in Fig. 11.1. The mode-locked laser produces ultrashort pulses at 1.06 μm with a positive linear chirp. The pulses are launched into the anomalously dispersive, Yb-doped HF amplifier, together with a separate pump beam (diode laser) that controls the gain. As a result of the amplification and nonlinear pulse evolution of the pulses as they pass through the amplifier, Raman solitons form and are continuously wavelength shifted through the SSFS. The nonlinear evolution of the pulses depends critically on the pulse peak power, so the wavelength of the Raman solitons at the amplifier output is tuned by varying the gain in the amplifier (controlled by the pump laser). In this way, monocolour soliton output pulses have been wavelength tuned throughout the 1.06-1.33 μm range.

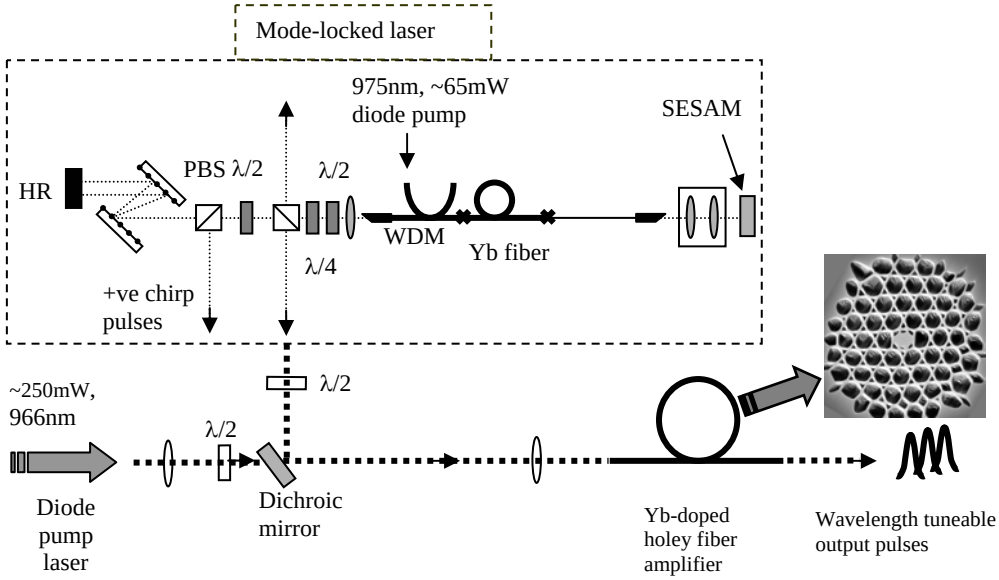

Fig. 11.1 Experimental setup, showing the in-house mode-locked Yb-fiber seed laser (diode-pumped), the launch arrangement for seeding the pulses and pump laser to the Yb-doped HF amplifier, and an inset SEM showing the HF structrure.

In this section, we describe in greater detail the system operating principles, experimental set-up and the theoretically calculated properties of the HF. Section 11.2.1, describes the operating principles of the system, and then section 11.2.2 provides details of the seed oscillator performance and the arrangement for launching seed pulses and CW pump power into the amplifier. Section 11.2.3 explains the HF characteristics.

11.2.1 Operating principles

The pulse evolution within the amplifier is governed by the complicated interplay between gain, dispersion, and nonlinear interactions. A schematic illustration of the key features of the pulse evolution, both in the spectral domain and in the time domain, is shown in Fig. 11.2.

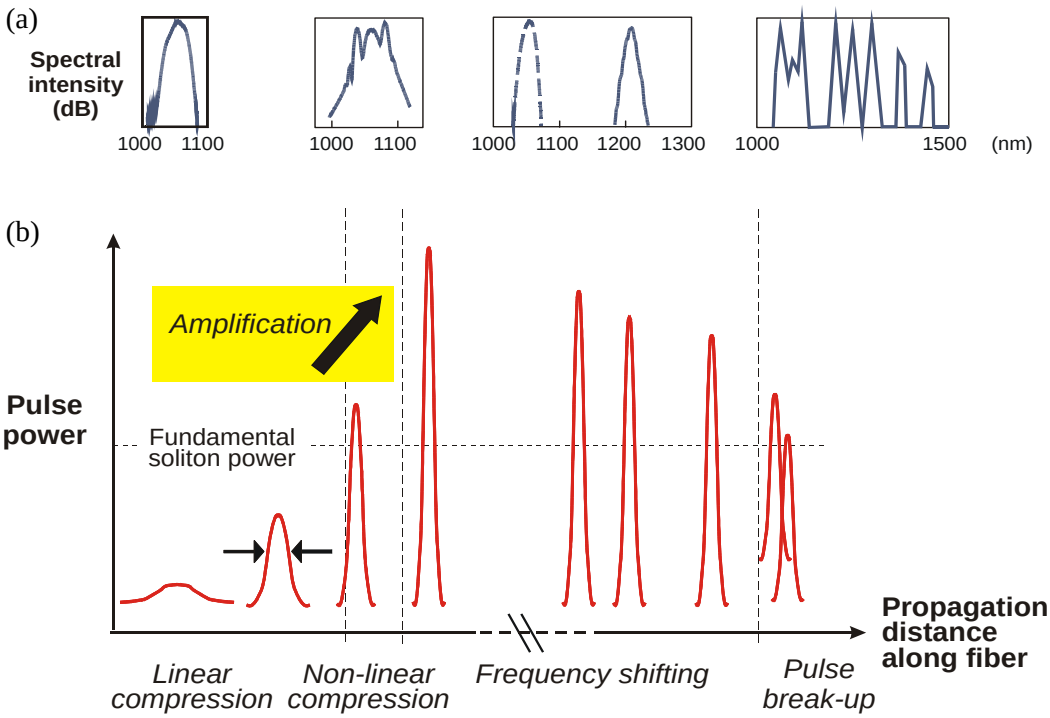

Fig. 11.2 Representation of the pulse evolution with propagation distance along the HF amplifier. (a) Frequency domain: optical spectra. (b) Time domain: pulse duration/peak power.

The pulses at the amplifier input have a positive linear chirp and a peak power below that required for soliton formation (chirped pulses have $\tau_{FWHM} = 2.4$ ps, peak power ~5 W, compressible to $\tau_{FWHM} \sim 110$ fs using a grating pair). Fig. 11.2 shows that in the time domain, the pulse duration initially decreases due to linear pulse compression over the first few tens of centimetres of the amplifier since the HF has anomalous dispersion (~100 ps/(nm.km)) which compensates the initial positive chirp. At this stage, there is no nonlinear distortion of the initial, smooth spectrum. Then as the pulse is progressively amplified and compressed the peak power rapidly increases and soon exceeds the threshold for nonlinear interactions and the formation of a fundamental, or (possibly) a higher order soliton. The higher order soliton pulse evolution is manifested in the temporal domain where the pulse undergoes soliton compression, so further increasing the peak power and accelerating the nonlinear pulse evolution.

As described in Chapter 2, the effects of intra-pulse SRS transfer the energy from the high-frequency part of the pulse spectrum to the low-frequency part. This destabilises the pulse and ultimately results in break up of the pulse into a peak and pedestal, and most importantly, to the

formation of a Raman soliton. The Raman soliton pulse is a stable entity, which, due to the SSFS effect, continuously downshifts its central frequency (moves to longer wavelengths) as it moves along the amplifier. It should be noted that the SSFS process is strongly dependent on the pulse duration ($\Delta\tau$) as the rate of frequency shift is proportional to $\Delta\tau^{-4}$ (see Chapter 2 for further discussion).

The final wavelength of the solitons at the amplifier output is sensitive to the amplifier gain settings i.e. gain distribution, pump power and the amplifier length. The gain window of the Yb-doped amplifier extends from approximately 1.03-1.12 μm, so the wavelength-shifting soliton will experience further gain after formation until either the amplifier gain is saturated, or the pulse wavelength is red-shifted beyond the gain window. Once the SSFS has shifted the wavelength of the pulses beyond the ~1.12 μm upper limit of the amplifier gain spectrum, the soliton will neither be amplified, nor suffer absorption due to the Yb-doping, and will propagate as if it was in a passive HF. However, the Yb-doped core will continue to act only on the non-Stokes-shifted pedestal of the initial pulse that is left after the Raman-soliton has been generated. By using an over-long amplifier, the excess (unpumped) length could act as an absorber for residual unshifted radiation at the seed wavelengths, whilst passing with minimal attenuation the SSFS red-shifted components, which fall outside the Yb absorption band, to leave a spectrally filtered, wavelength-shifted Raman soliton at the system output.

The maximum wavelength shift of the Raman soliton increases steadily with the length of fiber used, so the maximum obtainable wavelength will, in principle, have an upper bound set by the absorption of silica at around 2.3 μm [9]. Other factors may limit this in practice, such as the variation of the fiber dispersion over the wavelength range of interest.

Finally, it is worth noting that depending on the seed pulse energies, amplifier length, and pump power, it is possible to enter a more complicated regime of pulse evolution where the pulse breaks up into multicoloured solitons at the amplifier output. In our experiments we managed to form pulse-bursts with as many as six individual multicoloured pulses, and in some instances wavelengths approaching 1.58 μm were observed. Here, the seed pulse (or a previously formed Raman soliton) breaks up into several Raman solitons, each of which will have somewhat different characteristics at the point of formation and that will evolve separately with further propagation. A burst of multi-coloured solitons is thus observed at the end of the amplifier.

For simplicity, in the above discussion we have considered only the case of a forward pumped amplifier and positively chirped seed pulses, as this was the configuration that we studied in the greatest detail experimentally, and which gave the best tuning characteristics. We note that in other configurations e.g. a forward pumped amplifier with close to transform limited

seed pulses, the general features of the pulse formation processes would not change dramatically.

While the description given above is purely qualitative, it should be noted that detailed models have been applied numerically to describe Raman soliton formation in fiber amplifiers. For example, an approach based on a modified NLSE, which incorporated terms to describe a gain medium with a Lorentzian line shape and allowing for the effects of gain saturation along the amplifier length has been reported previously [10]. This model treats the stimulated Raman scattering using an optically driven molecular vibration model. The model was used to simulate the amplification of ~500fs pulses in an Er-doped fiber amplifier and good quantitative agreement between the experimental and theoretical data was obtained. Others have performed simulations of the propagation of pulses having a width approximately equal to the inverse bandwidth of the amplifier, and suggest that the Maxwell-Bloch equations are necessary if an accurate quantitative analysis of the system is required [11]. These theoretical approaches, with the inclusion of appropriate gain spectrum as a function of amplifier length, could readily be adapted to model our experiments in HF, although we have not done this at the time of writing, and we expect to return to this in the future

11.2.2 System implementation

Our experimental set up is shown in Fig. 11.1. The two principal components are a mode-locked seed laser emitting ultrashort pulses at 1.06 μm, and an anomalously dispersive Yb-doped HF amplifier. The characteristics of our diode-pumped Yb-doped fiber oscillator are presented in Chapter 4.

The positively chirped pulses from our oscillator were launched into a length of Yb-doped HF amplifier, which for the majority of experiments undertaken was co-directionally pumped using a 966 nm diode based MOPA (maximum output power of ~250 mW). We achieved approximately 20% coupling efficiency into the HF for both the seed pulses and the pump radiation, giving a maximum launched pulse energy of ~10 pJ, and up to 50 mW of launched pump. We used a half wave plate to match the laser output polarisation to a principal axis of the highly birefringent Yb-doped HF. We note that our results were insensitive to the orientation of the 966 nm diode pump polarisation relative to the fiber polarisation axes. The pulses emerging from the output end of the amplifier were characterised in the frequency domain using an optical spectrum analyser, and in the time domain using a non-collinear, second harmonic intensity autocorrelator with ~10 fs resolution. For our experiments the HF amplifier had a length between 1.7 m and 9 m.

11.2.3 Characteristics of the Yb -doped holey fiber

A SEM of the transverse cross section of the Yb-doped HF used in these experiments is shown in Fig. 11.3(a). The holey cladding region was fabricated using standard capillary stacking techniques [12], and an Yb-doped solid rod was used to form the core. The core of this fiber is approximately 2 μm in diameter, and the surrounding cladding is largely composed of air. The fiber was observed to be strictly single mode for all wavelengths considered here (including the 966 nm pump wavelength).

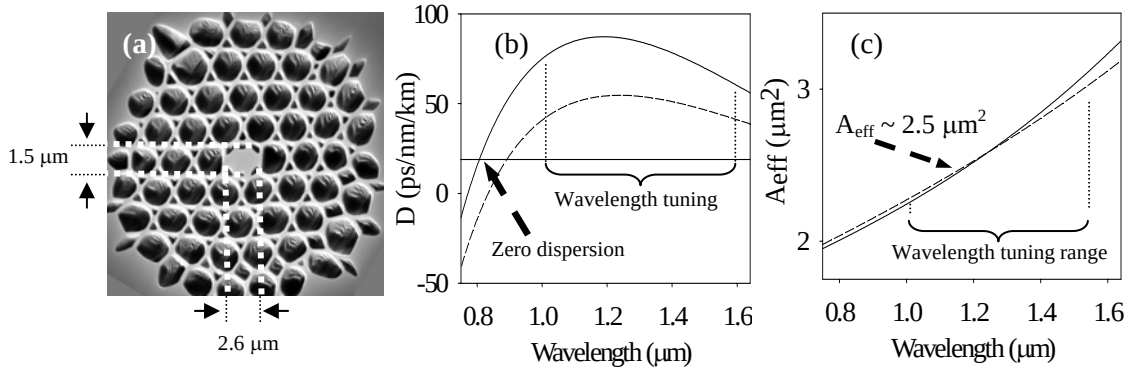

Fig. 11.3 Characteristics of the Yb-doped HF: (a) SEM of the structure, showing the dimensions of the elliptical core. (The metallic coating required for producing SEM images enlarges the fine silica silica bridges by ~ 50 nm. This is taken into account when calculating the fiber characteristics.); (b) Dispersion predictions for the two principal polarisation axes; (c) Effective mode area predictions for the two principal polarisation axes.

Yb^{3+} ions are incorporated across the central 1.7 μm of the core, to a concentration of 2000-3000 ppm, as estimated from white light measurements on fibers drawn from the unetched Yb-doped fiber preform used to fabricate the core rod. The HF used in the present experiment was recently used to make the first demonstration of a mode-locked HF laser, and a slope efficiency of > 60% was achieved [13].

We use a full vector model based on the SEM of the actual HF structure to predict the fiber's characteristics (dispersion and effective area). The model's predictions for the mode area (A_{eff}) and dispersion (D) as a function of wavelength are shown in Fig. 11.3. To demonstrate the effect of the fiber asymmetry we have shown results for both polarisation axes. Unsurprisingly, the A_{eff} does not differ greatly on the separate polarisation axes. A_{eff} is ~2.5 μm^2 at a wavelength of 1.55 μm, which is approximately 30 times smaller than for a standard single mode fiber (eg. Corning SMF28). We also note that A_{eff} increases with increasing wavelength, indicating that the mode is more tightly confined to the fiber core at shorter wavelengths. To give an indication of its exceptional nonlinear properties, we note that for a 200 fs (FWHM) pulse (1.06 μm wavelength) propagating within this fiber, the fundamental soliton power and

soliton period are approximately 50W and 60cm, respectively. As mentioned previously, these values are significantly lower than the comparable values for experiments performed by other authors in standard fiber (λ~1.5 μm). The dispersion properties of the two axes are markedly different, which indicates that the dispersion is much more sensitive to the hole arrangement compared to A_{eff}. The zero dispersion wavelengths for the separate polarisation axes are at 770 nm and 830 nm respectively, and at a wavelength of 1.06 μm the dispersion on the two axes differs by ~35 ps/(nm.km). The relatively flat dispersion curves, particularly in the 1.0-1.3 μm wavelength range combined with the high effective nonlinearity of the fiber, facilitate good wavelength tuning through the SSFS effect.

As a consequence of the combination of core asymmetry, high refractive index contrast and the small scale of the structure, this fiber is extremely birefringent (strongly polarisation maintaining). In Fig. 11.4 we plot the transmission characteristics of polarised broadband light at 1540 nm through crossed polarisers and 1.2 m of the fiber. From a measurement of the spectral period of the transmission we estimate a birefringent beat length of just 0.3 mm at 1.54 μm. This agrees well with our prediction of 0.27 mm from the model described in Chapter 9. As far as we are aware this is one of the shortest beat-lengths ever obtained for an optical fiber.

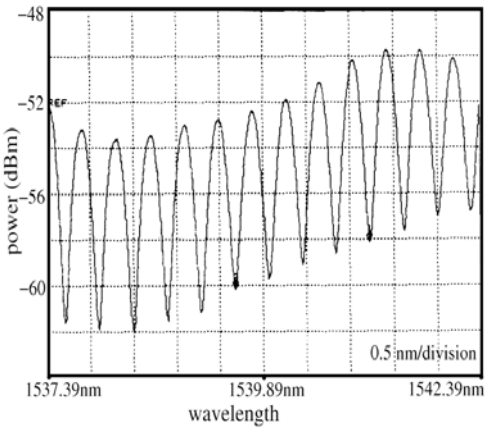

Fig. 11.4 Transmission spectrum (after a polarisation beam splitter) showing the high birefringence of this elliptical core HF (1.2m length).

11.3 Results and discussion

The output characteristics of our system were of three distinct types. Perhaps the most useful from a practical perspective is the single colour, wavelength tuneable soliton regime. Here, we obtained high quality pulses at a distinct wavelength tuneable from 1.06 – 1.33 μm, with the wavelength controlled by varying the pump power of the amplifier. We could also obtain more complex spectral output, which we characterised as multi-colour solitons and also broadband

continuous spectra. These spectra were observed when we used seed pulses with ~25% higher energy (the oscillator has a variable output coupling) compared to the single colour soliton regime, and (generally) at the highest pump powers. Finally, by using as shorter length amplifier and reducing the chirp of the seed pulses, we could avoid the pulse break-up and wavelength shifting effects and observe temporal compression of the seed pulses. We describe each regime of operation in greater detail below.

11.3.1 Single colour, wavelength tuneable solitons

We found that forward pumping an approximately 4 m length of HF amplifier was the optimal configuration for producing single colour, wavelength tuneable solitons. In particular, we used a 4.7 m length of amplifier fiber, and measured the output spectra and autocorrelations of the pulses emerging from the amplifier as a function of pump power. In Fig. 11.5 (a) we show the superposed spectra of the pulse emerging from the amplifier as the incident pump power delivered to the amplifier is increased. As can be seen in Fig. 11.5(a) a single, spectrally distinct Raman soliton of ~20 nm bandwidth is generated at the system output for pump powers above the minimum threshold power required to obtain appreciable SSFS effects (>50 mW incident pump power). As the pump power is increased, the final wavelength of the pulses progressively increases. Residual radiation at the original seed wavelength of ~1056 nm remains in each instance. The dependence of the final pulse wavelength on the amplifier pump power is shown in Fig. 11.5 (b). The final central wavelength of the pulses is seen to vary in an almost linear fashion with the level of incident pump power.

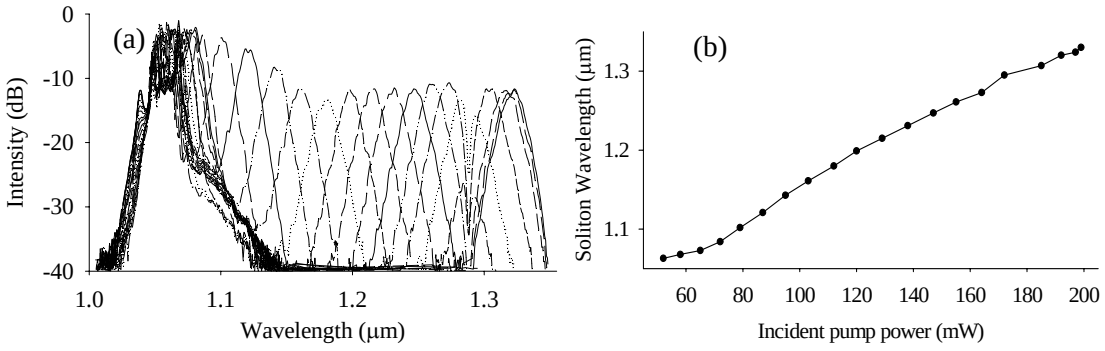

Fig. 11.5 Tuneable single colour solitons: (a) Superimposed spectra of the solitons shifted to progressively longer wavelengths (1.06–1.33 μm); (b) Plot of the soliton wavelength vs. amplifier (incident) pump power.

We attribute the increase in soliton wavelength with pump power to the fact that at higher pump powers the resultant change in gain distribution causes the Raman solitons to form earlier within the amplifier, thereby leaving them a greater length of fiber within which to walk-off to longer wavelengths through SSFS.

We also performed pulse autocorrelation measurements for pulses at various output wavelengths (amplifier pump powers), to establish how the pulse quality varied across the tuning range. The results of these measurements are shown in Fig. 11.6. To illustrate the typical pulse quality, we show in Fig. 11.6(a) the autocorrelation function and spectrum at a wavelength of 1212 nm. The pulse duration in this instance was 150 fs, and the time bandwidth product was 0.48. By comparison, the time bandwidth product for a transform limited soliton ($\mathrm{sec}h^2(T/T_0)$ intensity profile) is 0.32. The measurements plotted in Fig. 11.6(b) show that pulse duration remains approximately constant ~ 180 fs FWHM as the wavelength is tuned, and that the pulse quality as defined by the time.bandwidth product remains high across the full tuning range.

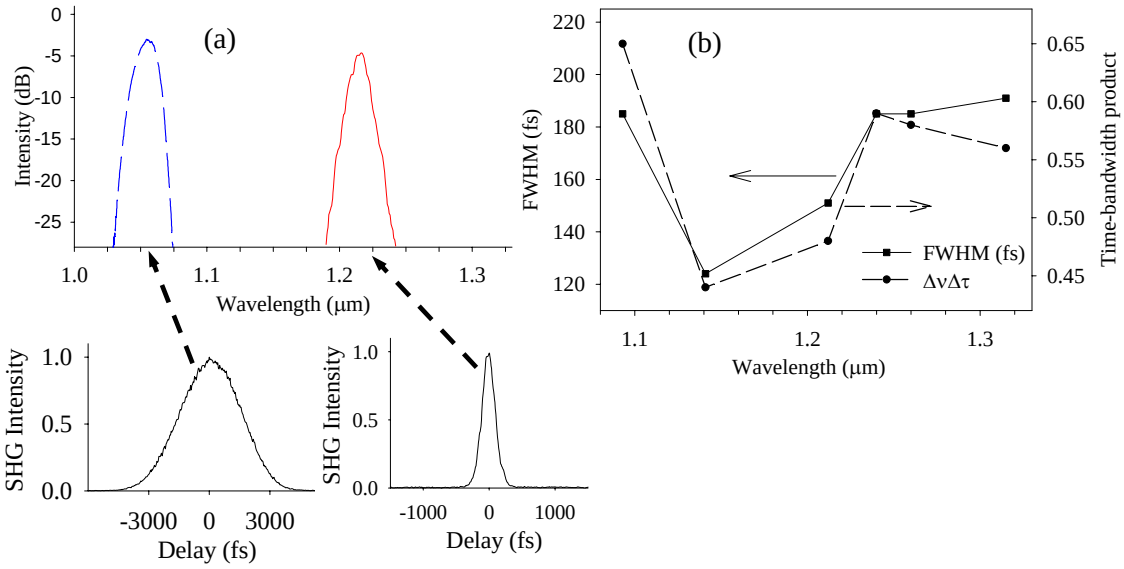

Fig. 11.6 Autocorrelation measurements of the wavelength shifted solitons: (a) Spectrum and corresponding autocorrelation traces for the seed pulse for a wavelength shifted pulse at 1.24 μm; (b) Plot of the pulse duration and Time Bandwidth product vs. soliton pulse wavelength.

Lastly, we investigated the effect of reversing the amplifier pump direction. Using the 2.4 ps, linearly chirped pulses directly from the mode-locked laser as a seed for a 1.7 m length of amplifier fiber, we obtained a similar SSFS tuning curve but obtained a maximum wavelength shift to only 1.12 μm. The wavelength tuning range was therefore much narrower when compared to that achieved for the forward-pumped amplifier. The reduction in wavelength tuning range is understandable since in this backward-pumping configuration any unbleached length of Yb-doped fiber at the front of the amplifier absorbs the signal, thereby frustrating soliton formation early within the fiber. The effective length of fiber available for wavelength shifting through SSFS is therefore reduced compared to the forward-pumping configuration.

Note that due to the practical difficulties of working with such small core fibers, compounded by the issue of pulse break up and wavelength shift within the amplifier, it was not possible for us to quantify the precise gain experienced by a given pulse for a given pump power and amplifier configuration. All that we are really able to say is that the maximum overall single pass gain through the system was greater than approximately 17 dB. This estimate considers the amplifier setup used in the experiments i.e. a flat cleaved facet at the input (to maximise the launched signal), which would provide 4% feedback; and an angle cleaved (reducing feedback to <1%) at the exit end of the amplifier. In every amplifier configuration we were able to increase the pump power sufficiently in order to obtain laser operation (at some wavelength within the Yb bandwidth) from the system, so for the end-reflections as stated above, this indicates at least 17 dB gain.

11.3.2 Multi-colour solitons and continuous spectra

It did not prove possible for us to extend the single pulse tuning range beyond 1.33 μm. Instead, when we maximised the output power of our seed oscillator, to increase the launched pulse energy to ~12 pJ (compared to ~9 pJ for the single-colour soliton experiments) we observed the generation of multicolor pulses (separated in wavelength and time) which increased in number as we increased the pump power, as shown in Fig. 11.7.

Using a longer (9m) length of amplifier fiber, and operating at the highest pump powers, we observed more complex spectra, including increased numbers of multi-colour solitons, and a broadband continuous (time-averaged) optical spectrum - similar to that achieved in supercontinuum generation experiments in passive HF [7]. Fig. 11.8(a) shows that for the most complex multi-colour soliton spectra, a far greater maximum wavelength shift up to 1.58 μm could be seen (measuring the peak with the maximum red-shift). A typical example of a broadband continuous spectrum, is shown in Fig. 11.8(b) with wavelengths extending from 1.03 μm to 1.62 μm. This broad spectrum could be useful for applications such as optical coherence tomography. At present this mode of operation is not fully understood.

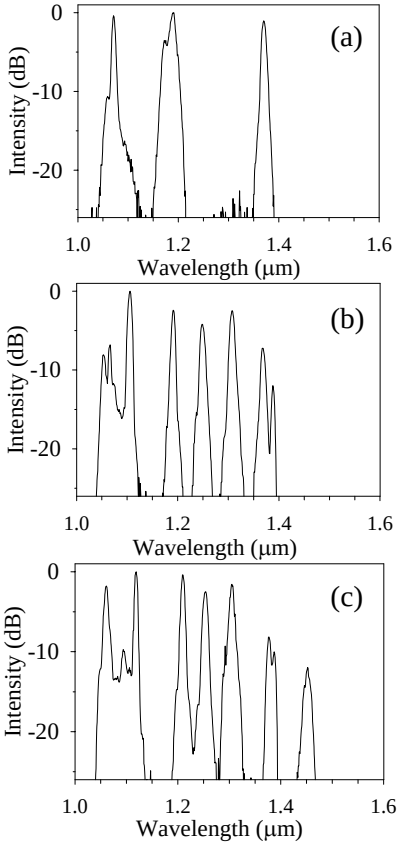

Fig. 11.7 Multicolour solitons showing (a)–(c) increasingly complex spectra as the amplifier pump power is increased.

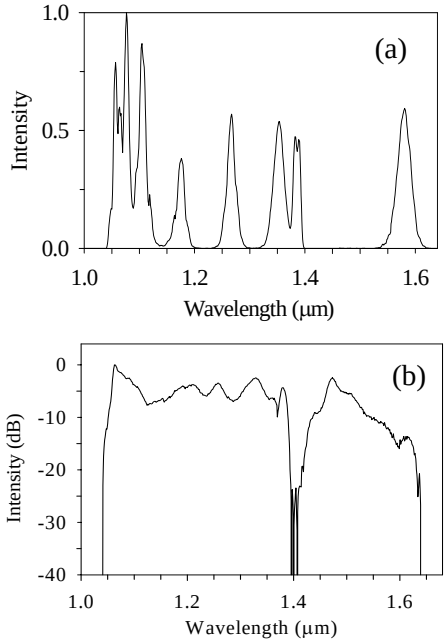

Fig. 11.8 (a) Typical example of complex multi-coloured soliton spectra, extending out to λ~1.58 μm. (b) Broadband continuous spectrum extending out to λ~1.62 μm.

11.3.3 Temporal compression

We also investigated the conditions required to produce temporal compression of the input pulses (through multi-soliton effects) as a function of amplifier pump power. By changing both the chirp of the input pulses, and the length of amplifier fiber we investigated the optimum conditions for pulse compression. The chirp of the input pulses was optimised by extracting negatively chirped pulses from the oscillator (previously we had selected the output port for positively chirped pulses), and transforming these pulses to have a small positive chirp by propagation through a length of standard fiber. Cutback measurements were performed to obtain pulses of the desired duration and hence chirp. In a similar fashion we optimised the amplifier length with respect to the minimum pulse duration at the amplifier output by measuring the output pulse duration in a series of cutback measurements on the amplifier fiber. By launching the optimally chirped pulses (~0.02 ps/nm) pulses into a 2.8 m long HF amplifier, we obtained compressed pulses down to 67 fs FWHM. The autocorrelation and spectrum of the compressed pulses is shown in Fig. 11.9 (a), (b) respectively. Although we expect the soliton

formation process in this case to be broadly similar to that described previously, since the chirp of the input pulses is smaller it is more rapidly compensated (by the anomalous dispersion of the HF) in a shorter length of amplifier fiber. Break-up into multiple solitons is prevented because the pulses exit the amplifier before evolving beyond the temporally compressed state.

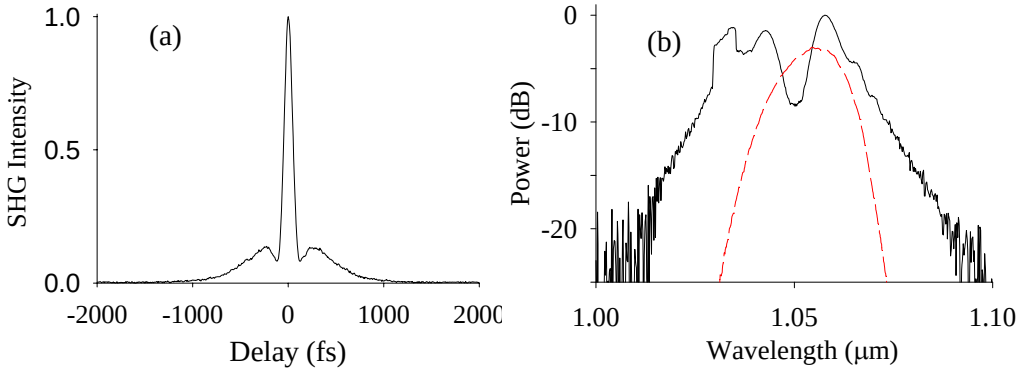

Fig. 11.9 Temporally compressed pulses: (a) Autocorrelation trace (pulse FWHM~67 fs); (b) Spectra of seed pulse (dashed line) and compressed pulse (solid line).

11.4 Conclusion

In conclusion, we have developed a continuously tuneable soliton source based on diode-pumped active microstructured HF seeded using pulses from a femtosecond, mode-locked fiber source. Tuning of the output wavelength is controlled by changing the amplifier pump power. Discrete single colour solitons are demonstrated to be of high quality ($\Delta\nu\Delta\tau \sim 0.55$), and the central wavelength is tuneable across the range 1.06-1.33 μm. Multicoloured solitons are demonstrated at wavelengths up to 1.58 μm, and continuous spectra are demonstrated spanning from 1.03 μm to 1.62 μm. We demonstrated temporal compression of the pulses to 67 fs (FWHM), compared to the minimum pulse duration of 110 fs obtainable using linear dispersion compensation of pulses directly from our oscillator (using a diffraction grating pair).

We have modelled the dispersion properties of the HF using the exact fiber structure (recorded using SEM photographs) and we have presented a brief overview of the relevant physical processes on which the system is based. Note, that our present results, combined with previously reported results from SSFS systems [9] mean that it is now possible to generate femtosecond pulses at any wavelength from 1 μm to 2.2 μm using fiber based techniques. Furthermore, it is likely that with detailed quantitative modelling and optimisation of our present system, it may well be possible to develop this single source to give SSFS wavelength tuneable output anywhere in the range from 1 - 2 μm. We believe this to be an exciting

development of fiber technology, providing a device with potential for widespread practical applications.

References

1. J. H. V. Price, K. Furusawa, T. M. Monro, L. Lefort and D. J. Richardson, "Tunable, femtosecond pulse source operating in the range 1.06- 1.33 microns based on an Yb^{3+}-doped holey fiber amplifier," Journal of the Optical Society of America B-Optical Physics **19,** 1286-1294 (2002).
2. J. H. Price, K. Furusawa, T. M. Monro, L. Lefort and D. J. Richardson, "A tuneable, femtosecond pulse source operating in the range 1.06-1.33 microns based on an Yb doped holey fiber amplifier," Conference on Lasers and Electro Optics (CLEO), Vol. 56 of OSA Trends in Optics and Photonics Series (Optical Society of America, Washington, D.C., 2001) paper CPD1 (2001).
3. F. M. Mitschke and L. F. Mollenauer, "Discovery of the soliton self-frequency shift," Optics Letters **11,** 659-661 (1986).
4. J. P. Gordon, "Theory of the soliton self-frequency shift," Optics Letters **11,** 662-664 (1986).
5. E. M. Dianov, A. Y. Karasik, P. V. Mamyshev, A. M. Prokhorov, V. N. Serkin, M. F. Stel'makh and A. A. Fomichev, "Stimulated-Raman conversion of multisoliton pulses in quartz optical fibers," JETP Lett. **41,** 294-297 (1985).
6. N. Nishizawa and T. Goto, "Compact system of wavelength-tunable femtosecond soliton pulse generation using optical fibers," IEEE Photonics Technology Letters **11,** 325-327 (1999).
7. J. K. Ranka, R. S. Windeler and A. J. Stentz, "Visible continuum generation in air-silica microstructure optical fibers with anomalous dispersion at 800 nm," Optics Letters **25,** 25-27 (2000).
8. T. A. Birks, W. J. Wadsworth and P. St.J.Russell, "Supercontinuum generation in tapered fibers," Optics Letters **25,** 1415-1417 (2000).
9. M. E. Fermann, A. Galvanauskas, M. L. Stock, K. K. Wong, D. Harter and L. Goldberg, "Ultrawide tunable Er soliton fiber laser amplified in Yb-doped fiber," Optics Letters **24,** 1428-1430 (1999).
10. D. J. Richardson, V. V. Afanasjev, A. B. Grudinin and D. N. Payne, "Amplification of Femtosecond Pulses in a Passive, All-Fiber Soliton Source," Optics Letters **17,** 1596-1598 (1992).
11. J. T. Manassah and B. Gross, "Propagation of Femtosecond Pulses in a Fiber Amplifier," Optics Communications 10031 **122,** 71-82 (1995).
12. P. J. Bennett, T. M. Monro and D. J. Richardson, "Toward practical holey fiber technology: fabrication, splicing, modeling, and characterization," Optics Letters **24,** 1203-1205 (1999).
13. K. Furusawa, T. M. Monro, P. Petropoulos and D. J. Richardson, "Modelocked laser based on ytterbium doped holey fibre," Electronics Letters **37,** 560-561 (2001).

Chapter 12 Conclusions

12.1 Introduction

The work presented in this thesis lies in two distinct research areas. First, the development of an Yb-fiber based CPA system was described in Chapters 3-7, and the characteristics of a direct amplification system (based on shared components from the CPA system) were described in Chapter 8. In the second part of this thesis, investigations of nonlinear effects in small core holey fibers were described in Chapters 9-11. In this chapter, each topic is briefly summarised and suggestions for potential future research are considered.

12.2 High power Yb-fiber systems

12.2.1 Yb-fiber oscillator

The oscillator development for our industrially sponsored contract has been completed. The oscillator is stable (<0.05% amplitude jitter), self starting, and represents a suitable source for a range of applications [1, 2]. The sponsoring company has already sold a clone of the prototype oscillator (standard mounts on a breadboard). It is now for the sponsoring company to develop suitable packaging in order to create a successful product for a broader market. The oscillator incorporated a telecommunications grade, grating-stabilised pump diode with pigtailed output, which was spliced directly to at WDM coupler and then to the Yb-doped fiber to create a robust, all-fiber gain block. The cavity used a simple Fabry-Perot design to enable straightforward manufacturing, and incorporated a SESAM in order to obtain robust self-start mode-locking.

Whilst we are fully satisfied that the oscillator meets the requirements of our sponsor, there are several possible improvements we may wish to implement. Andy Piper (co-worker) and I have recently developed an environmentally stable version of the oscillator that incorporated Faraday rotators at both ends of the fiber gain section. The Faraday rotators cause the polarisation of the pulses to be rotated by 90 degrees when traveling in opposite directions along the fiber, so any linear polarisation changes in the cavity caused by twisting the fiber or thermal fluctuations should average to zero over a round trip [3]. With the Faraday rotators included in the cavity, mode-locking is maintained while the fiber is disturbed, and also over a wide temperature range.

In future, timing jitter may be reduced by putting the oscillator in a housing, and perhaps by using a more rigid end-mirror mount. We would also like to move towards an all fiber cavity by replacing the bulk grating pair with a length of anomalously dispersive HF, and by replacing the PBS with a fiber polariser (indeed, first results in this direction have been reported by other groups [4, 5]). We may also experiment with using a 90:10 fiber coupler for the output. Moving to an all-fiber-pigtailed cavity should lead to timing jitter limited only by thermal effects and quantum noise, as has been demonstrated from recent investigations into the ultimate stability limits of Er-fiber ring lasers by researchers in the metrology community [6].

To increase the range of potential applications for the oscillator, it would also be useful to investigate the possibility of exploiting the potential Yb-bandwidth (>50 nm) to generate shorter (e.g. <50 fs) pulses, for example by including a prism-based DDL for reduced 3rd order dispersion. Further research could consider cavities based on cladding-pumped Yb-fiber to achieve much higher average powers and pulse energies. In addition, the parabolic pulse concept could enable 'similariton' lasers to produce high power, large bandwidth pulses for very high performance future Yb-fiber lasers.

12.2.2 CPA System

This thesis described the development of a CPA system that produced ~16 μJ pulses at a repetition rate of 100 kHz (average power 1.6 W), and with pulses that could be recompressed to ~500 fs (see Chapter 7). The maximum pulse energy was limited by the onset of SRS. Numerical predictions were presented, which demonstrated that by using a fiber for the final amplifier with a larger core diameter (29 μm) and shorter length (1.5 m), the system should be capable of generating 100 μJ pulses that could be recompressed to <500 fs duration. Such pulses should prove useful for a wide range of practical applications. The CPA included a CFBG stretcher incorporating both the 2nd and 3rd order dispersion to compensate the chirp of the bulk-grating compressor. The CFBG stretcher research included the development of a procedure for annealing the grating after writing in order to control the cladding-mode losses. We also designed a future-generation compressor-stretcher combination, that would reduce the 3rd order dispersion to enable a broader bandwidth CFBG to be used. The proposed design should be suitable for generating <300 fs recompressed pulses.

To further enhance the system capabilities, perhaps it would be useful to perform further modelling (using the methods described in Chapter 2) in order to optimise the gain and noise figure of the amplifiers. It is not yet clear whether such work would be most appropriately performed by researchers at the ORC, or by our industrial sponsor as they fully develop the CPA system into a commercial product.

Since the start of the CPA system development work presented in this thesis, other groups [7] have demonstrated Yb-fiber CPA systems producing 1.2 mJ pulses (repetition rate 1.7 kHz) with 380 fs duration, and M^2=1.16, using a 50 μm core (length = 2.6 m) fiber for the final amplifier. The maximum pulse energy was limited by the onset of SRS, so obtaining higher energy pulses will require use of larger core fiber. It therefore appears that significant further increases in pulse energy may not be practical if high beam quality is to be maintained. Fibers are, however, well suited to high average power operation, and perhaps the most interesting avenue for future research is to maintain the pulse energy at ~100 μJ but to exploit the ever-increasing power and reducing cost of pump laser diodes to develop a much higher average power CPA system operating at a higher repetition rate e.g. 100 μJ at 1 MHz implies 100 W average power. Yb-fiber technology is advantageous in this area because Yb has a low quantum defect, and fiber has a favourable geometry for heat dissipation. These advantages have been fully exploited for CW operation where industrial research has led to a commercial Yb-fiber laser with an average power of 6 kW [8].

The extreme fields possible by focussing diffraction limited 100 μJ, <200 fs pulses, would have power density ~10^{16} W/cm^2, which could enable future application in new areas including femtosecond high harmonic generation extending into the UV and x-ray spectral regions. Fiber pumped, ultrashort pulse, x-ray sources could be envisaged for the rapidly developing science of single molecule biological imaging.

12.2.3 Direct amplification system

The direct amplification system described in Chapter 8 of this thesis produced pulses with energy of 330 nJ at an average power 0.9 W. The pulses were recompressed to a duration of ~300 fs. The system was robust and stable, and these attributes were demonstrated by using the system to pump a femtosecond OPO [9]. The still unique, to our knowledge, aspect of the direct amplification system as presented in this thesis, is that the system used a cascade of amplifiers. Much higher total gain should therefore be possible compared to the single stage amplifier systems demonstrated by other authors [10, 11]. By using initially chirped pulses from the oscillator combined with low gain in the smaller core pre-amplifiers, the system was operated so as to avoid excessive SPM distortion to the pulses (i.e. mostly linear evolution under influence of GVD). The limiting effects of SRS were not observed.

Theoretical work reported by other groups suggests that through an appropriate combination of gain, SPM and GVD and after sufficient propagation distance, the nonlinear effects can generate pulses with a parabolic temporal and spectral profile and which have linear chirp. Therefore these parabolic pulses can be recompressed to sub-picosecond durations despite the significant influence of nonlinear effects [11]. Parabolic pulses have been demonstrated

experimentally at high average powers (17 W at 75 MHz repetition rate) in single stage amplifier systems [10].

As suggested above in relation to the possible further CPA development, the increasing availability of affordable, and very high power pump laser diodes suggests that it would be interesting to investigate multi-stage direct amplification systems producing >100 W average power, and with pulse energies ultimately limited by the onset of SRS. (The maximum pulse energy limit set by the onset of SRS increases in proportion to the pulse duration, and therefore we would expect that the maximum energy of pulses from a direct amplification system would be approximately two orders of magnitude smaller compared to those from a high average power CPA system.) Dr. Andrew Malinowski (co-worker) has recently performed initial experiments at such high average power levels using our Yb-fiber oscillator and a cascade of two Yb-fiber amplifiers. Pulse energies of ~500 nJ pulses were demonstrated at an average power of 25 W (repetition rate 50 MHz), with recompressed pulse duration ~250 fs.

A robust high-repetition rate fiber-based source of high peak power pulses could be envisaged for high speed microstructuring of materials, and would enable dramatic improvements in processing times for industrial processing applications. Frequency doubling/quadrupling of the pulses into the visible/UV would be interesting for ultrafast chemical and biological studies, and for ultra-fast imaging.

12.3 Nonlinear effects in holey fiber

12.3.1 Holey fiber based supercontinuum generation

The work presented in Chapter 10 of this thesis demonstrated supercontinuum generation extending to wavelengths below 300 nm in the UV from a small core HF. Enhanced UV generation was obtained by launching the seed pulses into a higher order transverse mode. Numerical simulations suggested that differences in the dispersion profiles between the fundamental and higher order mode could explain the enhanced UV generation. We note that in recent work, Efimov et al. [12] have demonstrated UV generation in a high-order mode of a microstructured fiber, extending to 260nm in the UV.

As with previous demonstrations of HF based supercontinuum generation [13], our high energy ultrashort seed pulses were generated from a Ti:Sapphire laser system. There appears to be an opportunity to develop practical sources of HF based supercontinuum generation, since collimated (bright) sources of broadband radiation, and the ability of HF to be a waveguide for such supercontinuum could be useful for a wide range of applications that use spectroscopic techniques. The demonstration of supercontinuum generation from a HF pumped by a fiber

based direct amplification system, as presented in Chapter 9, is one step towards such a practical source.

It has been shown that supercontinuum generation using ~100 fs pulses occurs through the mechanism of soliton fission, which results in a low degree of temporal coherence of the continuum [14]. Recent research has concentrated on reducing the amplitude noise of the supercontinuum by using input pulses with much shorter pulse durations (e.g. <30 fs pulses from Ti:Sapphire lasers), and shorter lengths of HF [15, 16] The primary mechanism of spectral broadening is then SPM and four-wave-mixing, and this short pulse / short fiber approach therefore leads to an increases the temporal coherence of the continuum. (The threshold energy for forming a higher order soliton increases for shorter pulses, and soliton fission is therefore avoided.) Further practical development of highly coherent, low noise supercontinuum appears to be dependent on the commercial development of lower cost ultra-short pulse sources. Fiber technology is an attractive alternative to bulk crystal devices, offering a route to power scaling of the average output power.

12.3.2 Wavelength tuneable holey fiber amplifier source

The work presented in Chapter 11 of this thesis demonstrated a novel source of ultrashort pulses, continuously wavelength tuneable from 1.06-1.33 μm. The pulse durations were <250 fs and the pulse energies were ~50pJ (average power ~3mW). The system was based on the SSFS in an Yb-doped HF amplifier that was seeded from our Yb-fiber oscillator. Sources of wavelength tuneable ultra-short pulses are useful for many applications, and systems based on the SSFS and have potential for practical devices because they use low cost components, and do not require external pulse compressors. Following interest in our HF amplifier system from a commercial enterprise, a patent application has been submitted based on the results presented in this thesis [17-19]. Further numerical and practical work (exploiting latest developments in HF fabrication expertise) would be appropriate to extend the tuning range of the system to the silica water absorption peak at 2.1 μm, and to increase the output pulse energy. Future research could include extending the range of accessible wavelengths by frequency doubling into the visible region of the spectrum.

References

1. D. J. Richardson, J. Nilsson, L. Lefort, J. H. Price, A. Malinowski and M. Ibsen, "Pulsed Light Sources," U.S. Patent Application 10/146,219 (May 13, 2002).
2. J. H. Price, L. Lefort, D. J. Richardson, G. J. Spuhler, R. Paschotta, U. Keller, C. Barty, A. Fry and J. Weston, "A practical, low noise, stretched pulse Yb^{3+}-doped fiber laser," Conference on Lasers and Electro-Optics (CLEO 2001), paper CTuQ6 (2001).
3. M. E. Fermann, L. M. Yang, M. L. Stock and M. J. Andrejco, "Environmentally Stable Kerr-Type Mode-Locked Erbium Fiber Laser Producing 360-fs Pulses," Optics Letters **19,** 43-45 (1994).
4. H. Lim, F. O. Ilday and F. W. Wise, "Generation of 2-nJ pulses from a femtosecond ytterbium fiber laser," Optics Letters **28,** 660-662 (2003).
5. A. V. Avdokhin, S. V. Popov and J. R. Taylor, "Totally fiber integrated, figure-of-eight, femtosecond source at 1065 nm," Optics Express **11,** 265-269 (2003).
6. H. Hundertmark, C. Fallnich, N. Haverkamp, J. Stenger and H. R. Telle, "Sub-fs pulse-to-pulse jitter from a 60 MHz repetition rate all-fiber passively mode-locked Erbium laser," *OSA Annual Meeting*, OSA, (28 September - 3 October, 2002).
7. A. Galvanauskas, Z. Sartania and M. Bischoff, "Millijoule femtosecond fiber CPA system," *Advanced Solid-State Lasers, Proceedings*, (2001).
8. *IPG Photonics press release, Dec16 2002 (http://www.ipgphotonics.com).*
9. M. V. O'Connor, M. A. Watson, D. P. Shepherd, D. C. Hanna, J. H. V. Price, A. Malinowski, J. Nilsson, N. G. R. Broderick and D. J. Richardson, "Synchronously pumped optical parametric oscillator driven by a femtosecond mode-locked fiber laser," Optics Letters **27,** 1052-1054 (2002).
10. J. Limpert, T. Schreiber, T. Clausnitzer, K. Zollner, H. J. Fuchs, E. B. Kley, H. Zellmer and A. Tünnermann, "High-power femtosecond Yb-doped fiber amplifier," Optics Express **10,** 628-638 (2002).
11. M. E. Fermann, V. I. Kruglov, B. C. Thomsen, J. M. Dudley and J. D. Harvey, "Self-similar propagation and amplification of parabolic pulses in optical fibers," Physical Review Letters **84,** 6010-6013 (2000).
12. A. Efimov, A. J. Taylor, F. G. Omenetto, J. C. Knight, W. J. Wadsworth and P. St.J.Russell, "Nonlinear generation of very high-order UV modes in microstructured fibers," Optics Express **11,** 910-918 (2003).
13. J. K. Ranka, R. S. Windeler and A. J. Stentz, "Visible continuum generation in air-silica microstructure optical fibers with anomalous dispersion at 800 nm," Optics Letters **25,** 25-27 (2000).
14. J. Herrmann, U. Griebner, N. Zhavoronkov, A. Husakou, D. Nickel, J. C. Knight, W. J. Wadsworth, P. St.J.Russell and G. Korn, "Experimental evidence for supercontinuum generation by fission of higher-order solitons in photonic fibers," Physical Review Letters **88,** 173901 (2002).
15. J. M. Dudley and S. Coen, "Coherence properties of supercontinuum spectra generated in photonic crystal and tapered optical fibers," Optics Letters **27,** 1180-1182 (2002).
16. K. L. Corwin, N. R. Newbury, J. M. Dudley, S. Coen, S. A. Diddams, K. Weber and R. S. Windeler, "Fundamental noise limitations to supercontinuum generation in microstructure fiber," Physical Review Letters **90,** art. no.-113904 (2003).
17. D. J. Richardson, T. M. Monro, J. H. Price and K. Furusawa, "Sources of, and Methods for Generating, Optical Pulses," U.S. Patent Application 10/120,965 (February 05, 2002).

18. D. J. Richardson, T. M. Monro, J. H. Price and K. Furusawa, "Sources of, and Methods for Generating, Optical Pulses," U.K. Patent Application GB 0109082.8 (April 11, 2001).

19. J. H. V. Price, K. Furusawa, T. M. Monro, L. Lefort and D. J. Richardson, "Tunable, femtosecond pulse source operating in the range 1.06- 1.33 microns based on an Yb^{3+}-doped holey fiber amplifier," Journal of the Optical Society of America B-Optical Physics **19,** 1286-1294 (2002).

Appendix I Measuring noise characteristics of CW mode-locked lasers

This Appendix describes the method used to measure the amplitude noise and timing jitter of a CW mode-locked laser [1].

The output pulses of a mode-locked laser are not perfectly periodic, but have random fluctuations in intensity (amplitude noise), and timing (temporal jitter).

If F_0 is the output intensity of a perfectly mode-locked laser:

$$F_0(t) = \sum_{\mu} f(t + \mu T)$$

(where $f(t)$ is the temporal intensity of an individual pulse in the train, and T = the period between pulses), then the noisy laser output $F(t)$, can be written:

$$F(t) = F_0(t) + F_0(t)A(t) + \dot{F}_0(t)T\,J(t).$$

The second term represents the random amplitude fluctuations, and the third term represents fluctuations in repetition rate ($f(t_\mu + \Delta t_\mu) \approx f(t_\mu) + \dot{f}(t_\mu)\Delta t_\mu$, with a fractional jitter so that $\Delta t_\mu = TJ(t)$).

The RF power spectrum of the laser intensity is given by the Fourier transform of the autocorrelation function of $F(t)$ (pure real), and can be expressed as

$$P_F(\omega) = (\Delta\omega)^2 \left| f(\omega) \right|^2 \sum_{\mu} \left[\delta(\omega_\mu) + P_A(\omega_\mu) + (2\pi\mu)^2 P_J(\omega_\mu) \right].$$

$P_A(\omega)$ and $P_J(\omega)$ are the power spectra of $A(t)$ and $J(t)$ respectively, $\Delta\omega = 2\pi f_r = 2\pi/T$ is the spacing between the frequency bands, $f(\omega)$ is the Fourier transform of the amplitde-profile of the individual ideal pulses (considered to remain constant), and μ is an integer running from minus infinity to plus infinity.

The sum represents a series of frequency bands, and each ideal peak is modified by the amplitude noise and time jitter terms. Fig I.1. is a sketch indicating the individual contributions from the amplitude noise and time jitter. P_C is the peak of the δ-function contribution, P_B is the peak of the timing jitter contribution, and P_A is the peak of the amplitude jitter contribution.

As the jitter term is proportional to μ^2, this contribution increases for higher harmonics, so we can distinguish the two noise contributions.

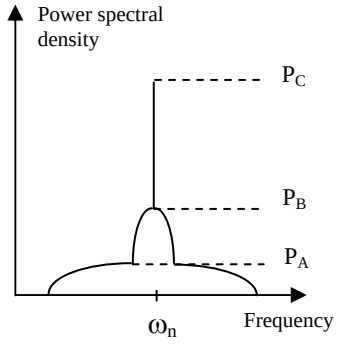

Fig. I.1. Noise bands around the n[th] harmonic of a mode-locked laser, indicating amplitude fluctuations (P_A) and temporal jitter (P_B).

The RMS intensity fluctuations (deviation ΔE of pulse energy E) and temporal jitter (deviation Δt from the pulse repetition time T) can be determined as:

$$(\Delta E/E)^2 = \int_{-\infty}^{+\infty} P_A(\omega)\,d\omega, \qquad \text{and}$$

$$(\Delta t/T)^2 = \int_{-\infty}^{+\infty} P_J(\omega)\,d\omega.$$

The integrals can be approximated as the product of the frequency width (FWHM) and the maximum power of the n[th] harmonic peak:

$$\int_{-\infty}^{+\infty} P(\omega)\,d\omega \approx 2\pi\,\Delta f\; P(\omega_n).$$

We then obtain the following formula for the amplitude jitter (Δf_{res} = selected resolution bandwidth of spectrum analyser):

$$\Delta E/E = \left[(P_A/P_C)_{n=0}\,\Delta f_A/\Delta f_{res}\right]^{1/2}.$$

As we do not see any pedestal on the fundamental peak, we estimate an upper bound on the amplitude noise by taking Δf_J = 395 Hz = width at base of peak, and P_A/P_C = -80dB = 10^{-8}, giving $\Delta E/E$ = 0.04% as stated in Chapter 4.

As the amplitude noise is much smaller that the time jitter term, we ignore it when calculating the time jitter, and obtain:

$$\Delta t / T = (2\pi n)^{-1} \left[(P_B / P_C)_n \, \Delta f_J / \Delta f_{res} \right]^{1/2},$$

where n is the order of the harmonic, ($\omega_n = n \times \Delta\omega$). From the pedestal on the 7th harmonic, we can estimate Δf_J = 23.53 kHz (FWHM of pedestal), and P_B / P_C = -58 dB = $10^{-5.8}$, giving $\Delta t / T \approx 10^{-4}$.

References

1. Von der linde, D., *Characterization of the Noise in Continuously Operating Mode-Locked Lasers.* Applied Physics B-Photophysics and Laser Chemistry, 1986. **39**(4): p. 201-217.

Appendix II SESAM selection for mode-locked Yb-fiber laser

As explained in Chapter 4, we included a SESAM in the laser cavity in order to obtain reliable self-start mode-locking. Professor U. Keller of ETH Zurich was kind enough to lend us a selection of 11 SESAMs with different modulation depths and recovery time constants, and before finally deciding which SESAM to use, we characterised the performance of the laser with the entire range of SESAMs. There are three different families of SESAMS, the performance of the laser with each SESAM is described in this appendix.

The SESAMs tested were of the low-finesse Antiresonant Fabry-Perot Saturable Absorber (A-FPSA) type, illustrated schematically in Fig. AII.1 [1]. Constructing the FPSA to operate at antiresonance makes the device broadband, and hence suitable for use in ultrafast lasers. Bandgap engineering and modern semiconductor growth technology have allowed for accurate control of the device parameters such as absorption wavelength, saturation energy, and recovery time. The reflectivity spectrum is determined by the number of layers in the bottom mirror (typically ~35 for our SESAMs), and by the dimension of the Fabry-Perot cavity. Low finesse A-FPSA devices use the air-InGaAs interface as the top-mirror (~30% reflection), which avoids post-growth processing. The absorber recovery time is controlled by growth temperature; a lower growth temperature produces a faster recovery time. The semiconductor used is III-V (InGaAs), and electron trapping is to point defects created by the excess group V atoms [1].

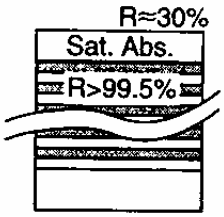

Fig. AII.1.Schematic of A-FPSA structure. The bottom mirror is a Bragg mirror formed by pairs of AlAs-AlGaAs (or AlAs-GaAs) quarter-wave layers. (From [1].)

When investigating the laser performance with the various SESAMs, we also varied the grating separation to control the net cavity dispersion. With excess negative dispersion, we observed soliton mode-locking, where the pulses were sustained because of a balance between GVD and SPM, and excess energy transferred to the low intensity wings of the pulse was removed by nonlinear polarisation rotation switching after each cavity round trip. With approximately nil net cavity dispersion, the cavity operated in stretch-pulse configuration (pulses again maintained by nonlinear polarisation rotation switching). The pulses produced in

the stretch-pulse configuration were spectrally broader and had a shorter duration compared to solitons. We also observed SESAM mode-locking (i.e. not assisted by nonlinear polarisation rotation switching), which produced much longer duration pulses that were unsuitable for our requirements.

F842, F843, F844, F845, F846

This family of SESAMs are low modulation depth (1% – 4%) devices with fast recovery times. Plots of the recovery time and reflectivity data for F844 are shown in Figures AII.2 and AII.3. The SESAMs were tested with the fiber directly butted to the front surface. We observed SESAM, soliton, and stretch-pulse mode-locking with all of these SESAMs except F842 (which did not initiate mode-locking). In every case the stretch-pulse operation showed significant (~40%) amplitude fluctuations. The mode-locking was most robust to cavity perturbation with F846. A consistent problem with using these SESAMs was that the fiber end burned quite regularly, requiring re-cleaving, and re-butting.

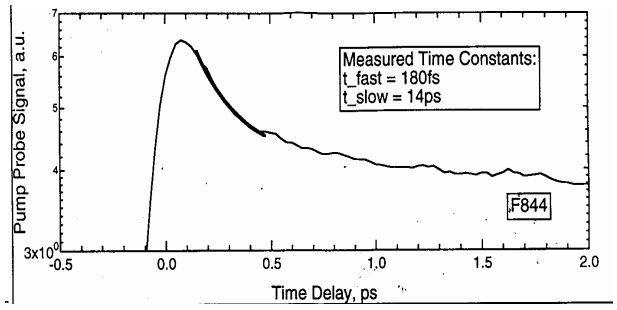

Fig. AII.2. Pulse probe reflectivity curve used to measure the recovery time of F844. (Figure provided by Professor U. Keller, ETH, Zurich.)

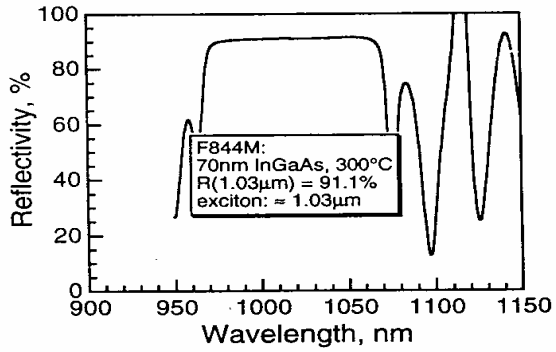

Fig. AII.3. Measured reflectivity spectrum of F844. (Figure provided by Professor U. Keller, ETH, Zurich.)

Z273, Z274, Z276 and Z365, Z367, Z384

These two families are both of a similar construction. They are high modulation depth (10% - 17%) devices with slow recovery time of ~3 ps and fast recovery time of ~100 fs. (A plot of the reflectivity of Z273 is shown in Chapter 4.) All were tested initially with matched focal length lens pair coupling. SESAMs Z274, Z365, and Z384 did not initiate stretch-pulse mode-locking, and were not investigated further. SESAMs Z273, Z276, and Z367 did initiate single pulse stretch-pulse mode-locking, but because the operation with Z276 was not as robust and required higher pump power for self-start, we chose only to investigate further the SESAMs Z273 and Z367.

Final operation of Z367, Z273

We found that excellent single pulse stretch-pulse mode-locked self-start operation was obtained with both of these SESAMs. We focussed the beam more tightly onto the SESAMs by using lenses with focal lengths of 11.0 mm nearest to the fiber and 6.24 mm nearest to the SESAM. The pulses at the cavity output were compressed by an external grating pair, to produce pulses as short as 108 fs (assuming a Gaussian profile).

Although we did not make detailed measurements, our qualitative opinion was that the operation with Z367 was slightly more robust, had a shorter self-start time, and produced a smoother spectrum at the 'rejected' output port of the laser compared to operation with Z273. Z367 was used in the optimised and fully characterised laser.

References

1. U. Keller, K. J. Weingarten, F. X. Kartner, D. Kopf, B. Braun, I. D. Jung, R. Fluck, C. Honninger, N. Matuschek and J. A. derAu, "Semiconductor saturable absorber mirrors (SESAM's) for femtosecond to nanosecond pulse generation in solid-state lasers," IEEE Journal of Selected Topics in Quantum Electronics **2,** 435-453 (1996).

Appendix III List of publications

Journal publications

1. J. H. V. Price, W. Belardi, T. M. Monro, A. Malinowski, A. Piper and D. J. Richardson, "Soliton transmission and supercontinuum generation in holey fiber, using a diode pumped Ytterbium fiber source," Optics Express 10, 382-387 (2002).
2. L. Lefort, J. H. Price, D. J. Richardson, G. J. Spuhler, R. Paschotta, U. Keller, A. Fry and J. Weston, "Practical Low-Noise stretched-pulse Yb^{3+} -doped fiber laser," Optics Letters 27, 1-3 (2002).
3. J. H. V. Price, K. Furusawa, T. M. Monro, L. Lefort and D. J. Richardson, "Tunable, femtosecond pulse source operating in the range 1.06- 1.33 μm based on an Yb^{3+}-doped holey fiber amplifier," Journal of the Optical Society of America B-Optical Physics 19, 1286-1294 (2002).
4. M. V. O'Connor, M. A. Watson, D. P. Shepherd, D. C. Hanna, J. H. V. Price, A. Malinowski, J. Nilsson, N. G. R. Broderick and D. J. Richardson, "Synchronously pumped optical parametric oscillator driven by a femtosecond mode-locked fiber laser," Optics Letters 27, 1052-1054 (2002).
5. K. Furusawa, A. Malinowski, J. H. V. Price, T. M. Monro, J. K. Sahu, J. Nilsson and D. J. Richardson, "Cladding pumped Ytterbium-doped fiber laser with holey inner and outer cladding," Optics Express 9, 714-720 (2001).
6. J. H. Price, T. M. Monro, K. Furusawa, W. Belardi, J. C. Baggett, S. J. Coyle, C. Netti, J. J. Baumberg, R. Paschotta and D. J. Richardson, "UV generation in a pure silica holey fiber," Applied Physics B-Lasers and Optics 77, 291-298 (2003).

Conference publications

7. **INVITED** J. H. Price, W. Belardi, L. Lefort, T. M. Monro and D. J. Richardson, "Nonlinear pulse compression, dispersion compensation, and soliton propagation in holey fiber at 1 micron," Nonlinear Guided Waves and Their Applications (NLGW 2001), paper WB1-2 (2001).
8. **POST DEADLINE** J. H. Price, K. Furusawa, T. M. Monro, L. Lefort and D. J. Richardson, "A tuneable, femtosecond pulse source operating in the range 1.06-1.33 microns based on an Yb-doped holey fiber amplifier," Conference on Lasers and Electro Optics (CLEO), Vol. 56 of OSA Trends in Optics and Photonics Series (Optical Society of America, Washington, D.C., 2001) paper CPD1 (2001).
9. **INVITED** J. H. Price, K. Furusawa, T. M. Monro, A. Malinowski, J. K. Sahu, J. Nilsson and D. J. Richardson, "Ultrashort pulse laser and amplifier systems based on Yb-doped holey fiber," OSA Annual Meeting, 2002, OSA (28 September - 3 October 2002)
10. J. H. Price, K. Furusawa, T. M. Monro, C. Netti, A. Malinowski, J. J. Baumberg and D. J. Richardson, "Phase matched UV Generation in a silica holey fiber," Conference on Lasers and Electro Optics (CLEO), Vol. 73 of OSA Trends in Optics and Photonics Series (Optical Society of America, Washington, D.C., 2002) paper CTuB5 (2002).
11. J. H. Price, L. Lefort, D. J. Richardson, G. J. Spuhler, R. Paschotta, U. Keller, C. Barty, A. Fry and J. Weston, "A practical, low noise, stretched pulse Yb^{3+} doped fiber laser," Conference on Lasers and Electro-Optics (CLEO 2001), paper CTuQ6 (2001).

12. W. Belardi, T. M. Monro, J. H. Lee, Z. Yusoff, J. H. Price, A. Malinowski, A. Piper and D. J. Richardson, "Silica holey fibres: fabrication and nonlinear effects," Photon, 2002, (2002)
13. W. Belardi, T. M. Monro, J. H. Price, J. H. Lee, P. Petropoulos and D. J. Richardson, "Fabrication and applications of highly nonlinear silica holey fibres," QEP 15, 2002, (3-6 September 2002)
14. K. Furusawa, A. Malinowski, J. H. Price, T. M. Monro, J. K. Sahu, J. Nilsson and D. J. Richardson, "A highly efficient all-glass double clad Ytterbium doped holey fiber laser," Conference on Lasers and Electro-optics (CLEO), 2002, OSA (2002)
15. K. Furusawa, J. H. Price, T. M. Monro, P. Petropoulos and D. J. Richardson, "Development and applications of Ytterbium doped highly-nonlinear holey optical fibres," International Workshop on Nonlinear Photonic Crystals -, 2001, (25-26 October 2001)
16. K. Furusawa, J. H. Price, T. M. Monro, P. Petropoulos and D. J. Richardson, "A small core Yb-doped holey fiber laser and amplifier," IoP Meeting 'In-fibre Bragg gratings and special fibres', Photonex, 2002, (2001)
17. **INVITED** T. M. Monro, J. C. Baggett, W. Belardi, K. Furusawa, J. H. V. Price and D. J. Richardson, "Holey fibres: Properties, applications and future directions," in Icton 2001: 3rd International Conference on Transparent Optical Networks, Conference Proceedings. New York, 2001, pp. 88-91.
18. M. V. O'Connor, M. A. Watson, D. C. Hanna, D. P. Shepherd, L. Lefort, J. H. V. Price, A. Malinowski, J. Nilsson, N. G. Broderick and D. J. Richardson, "Fibre-laser pumped femtosecond PPLN OPO," Quantum Electronics and Photonics 15 (QEP 15), 2001, Institute of Physics
19. M. V. O'Connor, M. A. Watson, D. C. Hanna, D. P. Shepherd, L. Lefort, J. H. V. Price, A. Malinowski, J. Nilsson, N. G. R. Broderick and D. J. Richardson, "Fibre-laser-pumped femtosecond PPLN optical parametric oscillator," Leos 2001: 14th Annual Meeting of the IEEE Lasers & Electro- Optics Society, Vols 1 and 2, Proceedings, 2001, IEEE
20. **INVITED** D. J. Richardson, W. Belardi, K. Furusawa, J. H. Price, A. Malinowski and T. M. Monro, "Holey fibers: fundamentals and applications," Conference on Lasers and Electro-optics, 2002, OSA (2002)
21. **INVITED** D. J. Richardson, B. H. Lee, Z. Yusoff, W. Belardi, K. Furusawa, J. H. Price, M. Kiang, K. Frampton, D. W. Hewak, J. A. Tucknott, R. C. Moore, H. N. Rutt and T. M. Monro, "Holey fibers for nonlinear fiber devices," Optical Amplifiers and Their Applications (OAA), 2002, (14 -17 July 2002)
22. **INVITED** D. J. Richardson, J. Nilsson, J. H. Price, J. A. Alvarez-Chavez and C. C. Renaud, "Pulsed fibre laser and amplifier systems," CLEO Europe - EQEC, 2002, (18-22 July 2002)

Workshops and Symposiums

23. Rank Prize Funds: Mini-Symposium on Broadband Optical Amplifiers (18-21 June, 2001), Grasmere, UK
24. Optical Soliton Workshop (22-24 March, 2001), School of Optics CREOL, Orlando, USA

Chapter 1 Introduction

This PhD thesis presents research aimed at broadening the technology base available for practical fiber based sources of ultrashort pulses. The first part of this thesis reports the development of a high-power, short pulse source based on Yb-doped fiber components. The second part of this thesis reports research on the use of Holey Fiber (HF) for ultrashort pulse applications including broadband continuum generation, and to generate wavelength tuneable ~200 fs pulses. Much of the HF based research used the short pulse source, described in the first part of this thesis, for the seed pulses.

There are a wide variety of applications that rely on nonlinear interactions with materials, for example two-photon absorption, nonlinear frequency generation in Optical Parametric Oscillators (OPOs) and supercontinuum generation in nonlinear small core fibers. For these nonlinear applications, the powers must be sufficient to excite the relevant nonlinear process, and obtaining sufficient power is generally only possible using pulsed sources. Recently, basic investigations on laser–matter interaction [1, 2] have shown that ultra-short (mode-locked) laser sources are advantageous in comparison to nano-second sources (Q-switched) for machining various solid materials with high precision [3]. This is because ultrashort pulses can ablate the material before heat has time to diffuse away from the exposed region, resulting in improved resolution and reduced collateral damage (e.g. melting, or micro-cracking). Given sufficiently high beam quality and amplitude stability, it is also possible to detect (2-photon microscopy) and ablate (material processing) features of a dimension less than the wavelength, by arranging that only in the centre of the focal volume is the intensity high enough to excite the required nonlinear processes [4]. Meeting the requirements for a wide variety of existing and emerging applications therefore requires pulses with: (i) sub-picosecond duration, (ii) megawatt peak power (μJ pulse energy), (iii) M^2 ~1 beam quality, and (iv) low amplitude noise.

Regenerative amplifiers using the chirped pulse amplification (CPA) technique [5] have generally been applied to realise the above parameters with repetition rates of up to 10 kHz [6]. However, ultrashort-pulse bulk crystal solid-state lasers are typically very complex systems, with a large number of components inside a long free-space optical cavity. The performance of such bulk crystal lasers is critically dependent on the thermal and modal conditions in the gain medium. Therefore, there are significant intrinsic limitations on the long-term stability and compactness of such laser systems, which hampers the successful implementation of the

Patent Applications

25. D. J. Richardson, J. Nilsson, L. Lefort, J. H. V. Price, A. Malinowski and M. Ibsen, "Pulsed Light Sources" UK patent application number 0203798.4 filed on 18/02/02, US patent application number 10/146,219 filed on 13/05/02.

26. D. J. Richardson, T. M. Monro, J. H. Price and K. Furusawa, "Sources of, and methods for generating, optical pulses", US patent application number 10/120,965 filed on 10/04/02.

Publications from Masters Degree Research

27. J. H. V. Price, "X-ray Study of the Smectic Layer Stability of a Mechanically Vibrated Liquid Crystal Film," Masters Thesis, Cornell University (2000).

28. Y. Li, S. G. Lemay, J. H. Price, K. Cicak, K. O'Neill, K. Ringland, K. D. Finkelstein, J. D. Brock and R. E. Thorne, "Imaging field-dependent structure in charge-density waves by X- ray diffraction topography," Journal de Physique IV 9, 151-152 (1999).

29. Y. Li, S. G. Lemay, J. H. Price, K. Cicak, K. O'Neill, K. Ringland, K. D. Finkelstein, J. D. Brock and R. E. Thorne, "Imaging shear in sliding charge-density waves by X-ray diffraction topography," Physical Review Letters 83, 3514-3517 (1999).

30. Y. Li, D. Y. Noh, J. H. Price, K. L. Ringland, J. D. Brock, S. G. Lemay, K. Cicak, R. E. Thorne and M. Sutton, "Observation of dynamic coupling between the Q(1) and Q(2) charge-density waves in $NbSe_3$ - art. no. 041103," Physical Review B 63, 041103 (2001).